Institut für Geodäsie und Geoinformation
Professur für Theoretische Geodäsie

Development of a one-step three dimensional approach for the phase unwrapping process in a differential InSAR stack based on Small BAseline Subset (SBAS) interferograms

Dissertation
zur Erlangung des Grades
Doktorin der Ingenieurwissenschaften (Dr.-Ing.)
der Landwirtschaftlichen Fakultät
der Rheinischen Friedrich-Wilhelms-Universität Bonn

von

Christina Esch

aus Mechernich

Bonn 2020

Referent:	Prof. Dr. tech. Wolf-Dieter Schuh
Korreferenten:	Prof. Dr.-Ing. Jan-Henrik Haunert
	Univ.-Prof. Dipl.-Forstw. Dr. Mathias Schardt
Tag der mündlichen Prüfung:	16. Juli 2020

Angefertigt mit Genehmigung der Landwirtschaftlichen Fakultät der Universität Bonn

Development of a one-step three dimensional approach for the phase unwrapping process in a differential InSAR stack based on Small BAseline Subset (SBAS) interferograms

Abstract

Differential Interferometric Synthetic Aperture Radar (D-InSAR) is a unique technique to detect and map deformations of the Earth's surface over large temporal and spatial scales. Processing a whole stack of multitemporal data allows the generation of multidimensional deformation time series. One of the most important and critical steps in the analysis is the determination of phase ambiguities which is called phase unwrapping. The development of the phase unwrapping step in the context of the Small BAseline Subset (SBAS) method to analyze interferograms is the main focus of this work. In addition to the Permanent Scatterer Interferometry (PSI), the SBAS method is one of the most widely used methods for the multitemporal analysis of a D-InSAR stack. The SBAS method is especially suitable for noisy data because it provides a spatially more dense result. State of the art in the SBAS analysis is the Minimum Cost Flow (MCF) algorithm to spatially unwrap one single interferogram and the extended MCF (EMCF) algorithm to multitemporally unwrap a D-InSAR stack in two steps. Therefore, the problem is divided into two problems of smaller dimension, the temporal and the spatial phase unwrapping, which in turn can be solved as a two dimensional MCF problem. The MCF problem can be defined as a Linear Program (LP). The first contribution of this thesis is based on a detailed and consistent overview and discussion of the different formulations and solution methods of the MCF problem in order to find the most efficient solution for the problem in the context of SBAS.

Methodologically, the two-step algorithm is not optimal as the spatial phase unwrapping which follows in the second step destroys the temporal constraints which are fulfilled after the temporal phase unwrapping. So the goal of this thesis is the development of a one-step three dimensional approach. The number of papers that solve the phase unwrapping multitemporally in one step with help of the MCF problem is limited. Existing theoretical considerations and basic frameworks have not been resulting in an optimal solution. In particular the problem of temporal inconsistency, which occurs with spatially filtered so called multilooked interferograms, remains unsolved. The spatial filter is of particular importance especially with noisy data as it reduces the noise and makes phase unwrapping easier.

The second contribution of this thesis provides analysis and further refinements of the two-step EMCF algorithm. Based on these results a multitemporal one-step phase unwrapping procedure is finally developed. This approach is specifically designed for multilooked and multitemporally filtered SBAS interferograms. Both, simulated and real data are used to validate this approach. The test region is the Lower-Rhine-Embayment in the southwest of North Rhine-Westphalia, Germany, a very rural region with noisy data. Thus, there are only very few stable scatterers that can be evaluated. However, this region requires regular monitoring observations since one of the largest brown coal occurrences in Europe within this area leads to continuous movements of the Earth's surface. This work shows that the new approach provides more consistent results so that the deformation time series of the analyzed pixels can be improved. The performed simulations also demonstrate that the new approach leads to an improvement, especially in the case of very noisy data. In conclusion, using the methods developed in this work besides the stable scatterers, distributed scatterers can also be included in the analysis leading to a spatially increased density of the deformation time series.

Entwicklung eines einstufigen dreidimensionalen Ansatzes zur Lösung der Phasenmehrdeutigkeiten in einem differentiellen InSAR Stapel basierend auf Small BAseline Subset (SBAS)-Interferogrammen

Zusammenfassung

Das differentielle interferometrische Radarverfahren mit synthetischer Apertur (D-InSAR) ist eine bewährte Technik zur Erkennung und Abbildung von Deformationen der Erdoberfläche über große zeitliche und räumliche Skalen. Die Auswertung eines ganzen Stapels von multitemporalen Daten ermöglicht die Erzeugung von mehrdimensionalen Deformationszeitreihen. Einer der wichtigsten und kritischsten Schritte bei der Analyse ist die Auflösung der Phasenmehrdeutigkeiten. Die Untersuchung der Phasenabwicklung im Kontext der Small BAseline Subset (SBAS) Methode steht im Mittelpunkt dieser Arbeit. Neben der Permanent Scatterer Interferometry (PSI) ist die SBAS Methode eine der am weitesten verbreitetsten Methoden für die multitemporale Analyse eines D-InSAR Stapels. Die SBAS Methode ist besonders für verrauschte Daten geeignet, da sie ein räumlich dichteres Ergebnis liefert.

Stand der Technik in der SBAS Analyse ist der Minimum Cost Flow (MCF) Algorithmus zur Lösung der Phasenmehrdeutigkeiten eines einzelnen Interferogramms und der erweiterte MCF (EMCF) Algorithmus zur multitemporalen Phasenabwicklung eines D-InSAR Stapels in zwei Schritten. Dabei wird das Problem in zwei einfachere Probleme mit kleinerer Dimension unterteilt, die zeitliche und die räumliche Phasenmehrdeutigkeitslösung, die wiederum als zweidimensionales MCF Problem gelöst werden können. Das MCF Problem kann als lineares Programm definiert werden. Der erste Beitrag dieser Arbeit beruht auf einer detaillierten und konsistenten Übersicht und Diskussion der verschiedenen Formulierungsarten und Lösungsmethoden des MCF Problems, um die für dieses Problem effizienteste Lösungsmethode zu finden.

Methodisch ist der zweistufige Algorithmus nicht optimal, da die im zweiten Schritt durchgeführte räumliche Phasenabwicklung die zeitlichen Bedingungen, die während der zeitlichen Phasenabwicklung erfüllt werden, wieder zerstört. Das Ziel dieser Arbeit ist daher die Entwicklung eines einstufigen dreidimensionalen Ansatzes. Die Anzahl der Arbeiten, die die dreidimensionale Phasenmehrdeutigkeitslösung in einem Schritt mit Hilfe des MCF Problems lösen, ist begrenzt. Existierende theoretische Überlegungen und Grundgerüste haben zu keiner optimalen Lösung geführt. Insbesondere das Problem der zeitlichen Inkonsistenz, das bei räumlich gefilterten Interferogrammen auftritt, bleibt ungelöst. Das räumliche Filtern ist jedoch gerade bei verrauschten Daten von großer Bedeutung, da es das Rauschen reduziert und das Lösen der Phasenmehrdeutigkeiten somit erleichtert.

Der zweite Beitrag dieser Arbeit liefert Analysen und weitere Verfeinerungen des zweistufigen EMCF Algorithmus, so dass die Phasenmehrdeutigkeiten letztendlich in einem Schritt multitemporal mittels eines selbst entwickelten Ansatzes gelöst werden können. Dieser Ansatz ist speziell für räumlich und multitemporal gefilterte SBAS-Interferogramme entwickelt. Zur Überprüfung dieses Ansatzes werden sowohl simulierte als auch reale Daten verwendet. Die Testregion ist die Niederrheinische Bucht im Südwesten Nordrhein-Westfalens, eine sehr ländliche Region mit verrauschten Daten. Daher gibt es nur sehr wenige stabile Rückstreuer, die ausgewertet werden können. Die Region erfordert jedoch eine regelmäßige Überwachung, da eines der größten Braunkohlereviere Europas innerhalb des Gebietes zu kontinuierlichen Bewegungen der Erdoberfläche führt. Die Arbeit zeigt, dass der neue Ansatz konsistentere Ergebnisse liefert, so dass die Deformationszeitreihen der analysierten Pixel verbessert werden können. Anhand der simulierten Daten kann zudem gezeigt werden, dass der neue Ansatz insbesondere bei sehr stark verrauschten Daten zu einer deutlichen Verbesserung führt. Zusammenfassend lässt sich sagen, dass mit den in dieser Arbeit entwickelten Methoden neben den stabilen auch noch verrauschte Rückstreuer in die Analyse einbezogen werden können, sodass flächendeckender Deformationszeitreihen resultieren.

Contents

1. Introduction

1.1 General Aspects and Motivation

The Earth‘s surface is subject to continuously occurring geophysical phenomena from geological as well as anthropogenic origin. To detect and monitor these deformations globally, satellites equipped with Synthetic Aperture Radar (SAR) systems have been orbiting the Earth since 1978. The measured differential interferometric phases (D-InSAR) between two acquisition times contain information about relative topography changes (Bamler and Hartl, 1998, p. R2). Since it is a satellite based imaging system, large scale deformations can be recorded efficiently compared to the pointwise leveling and Global Navigation Satellite System (GNSS) measurements. Analyzing repeated orbits, allows the creation of deformation time series. Therefore, typically data from several decades are used and evaluated together in a so called D-InSAR image stack.

There are two most commonly used methods for the multitemporal analysis of a D-InSAR stack, the Permanent Scatterer Interferometry (PSI) (Ferretti et al., 2001) and the Small Baseline Subset (SBAS) (Berardino et al., 2002) method. Both methods aim to circumvent the two main limitations of SAR interferometry, spatial and temporal decorrelation. With increasing temporal and spatial baselines between the two repeating orbits, the noise in the interferogram becomes larger. To overcome this, the PSI method uses only pixels that have stable backscattering characteristics over time and therefore low noise. However, these pixels are very rare. They only occur in urban areas or by man-made corner reflectors. The SBAS method, on the other hand, prevents decorrelation effects by limiting the maximum allowed temporal and spatial baseline between the SAR images. Thus, interferograms are only generated between SAR images if the maximum temporal or spatial baseline is not exceeded. Especially in rural areas, the SBAS method is better suited to obtain a spatially more dense result.

The test region investigated here is the Lower-Rhine-Embayment in the southwest of North Rhine-Westphalia, Germany. It is a very rural area with many forests in the south. Within this region there is one of the largest brown coal occurrences in Europe with the still active open-cast mines Hambach, Garzweiler and Inden and the closed coal mines Sophia-Jakoba in the mining region Erkelenz and Emil Mayrisch in the mining region Aachen. To extract the brown coal, the groundwater must be constantly pumped out so that the Earth’s surface subsides in the area around the active open-cast mines. After the cessation of the mines, the groundwater rises again which causes the Earth’s surface to elevate again. Consequently, the test region is subjected to continuous ground movements which require regular monitoring observations (Boje et al., 2008). To detect the deformations at a large scale, the SBAS method should be used, as stable scatterers are very rare in this region.

The SBAS analysis performed in this work is done in cooperation with Joanneum Research Digital, where the Remote Sensing Software Graz (RSG) is developed. One of the most critical steps in the SBAS processing chain is the resolution of the phase ambiguities which is done in the context of phase unwrapping. Due to the sinusoidal nature of the signal, the phase can only be measured modulo 2π. State of the art in the SBAS analysis is the Minimum Cost Flow (MCF) (Costantini and Rosen, 1999) algorithm. Originally, the algorithm was developed to solve phase ambiguities of a single interferogram. An Extended MCF (EMCF) (Pepe and Lanari, 2006) algorithm exists which takes the temporal information between the interferograms into account. Thus, it is possible to solve the phase ambiguities multitemporally in a D-InSAR stack. In the context of this work the EMCF algorithm was also implemented in RSG. The EMCF algorithm works in two steps. However, methodologically this stepwise approach is not optimal so the aim of this thesis is the development of a one-step approach in order to unwrap the phase multitemporally.

1.2 Scientific Context

In many imaging systems, such as Fringe Projection Profilometry (FPP), Magnetic Resonance Imaging (MRI) or radar interferometry (InSAR), the phase is used to get information about physical and geometrical properties of the measured objects. In FPP the phase is related to the surface geometry of objects, in MRI to the degree of magnetic field inhomogeneity and in InSAR to the height of the Earth's surface. In all cases the phase unwrapping is required as the phases can only be measured modulo 2π.

Phase unwrapping is a process to reconstruct the absolute phase ϕ from the measured wrapped phase ψ. Given a phase image at a special time t_α, the problem at a given pixel x_j is stated as

$$\phi_{x_j}^{t_\alpha} = \psi_{x_j}^{t_\alpha} + 2\pi k_{x_j}^{t_\alpha} \tag{1.1}$$

with the unknown integer number of phase ambiguities k. To unwrap the phase, the 2π discontinuities have to be identified and removed by adding or subtracting multiple integer numbers of 2π. However, this is an ill-posed problem as there is no unique solution if no further assumption is made (e.g. Hanssen, 2001, p. 55). Most phase unwrapping algorithms estimate finite differences between adjacent pixels and assume that these are smaller than half of the wavelength. If this assumption is true, the phase unwrapping problem can be considered as a finite difference integration problem (Tribolet, 1977). In reality, however, this is rarely the case due to a sub-sampling of the signal or noise. Then, the phase unwrapping gets more complex as it depends on the integration path.

The phase image provides information in two dimensions. When measuring changes over time, a third dimension is added: the time. Thus, measurements are available on a sparse multidimensional grid of points. Phase unwrapping methods can be classified into two categories: spatial and temporal phase unwrapping. The former one solves the phase ambiguities in one phase image at one special time by estimating phase differences between adjacent pixels of this image. There are local and global optimization approaches for this purpose. Ghiglia and Pritt (1998) provide a review of a number of spatial phase unwrapping methods. A commonly used local method is the quality-guided phase unwrapping algorithm. Starting from a reference pixel, an integration path is chosen based on a quality map, so that the highly qualified pixels are unwrapped first. A number of robust quality-guided phase unwrapping algorithms are summarized and discussed in Su and Chen (2004). Temporal phase unwrapping methods, in contrast, unwrap the phase at one pixel by analyzing information at different times. The knowledge of phase values of other pixels in the phase image is not required. Depending on the application, there are specially developed and already proven algorithms. In contrast to radar interferometry, where the signal is predetermined by the satellites, FPP systems can generate differently structured patterns. Commonly used methods are the binary coding method (e.g. Sansoni et al., 1999, Zheng et al., 2017) or the multifrequency method (e.g. Liu et al., 2010, Zhang et al., 2017). However, all these procedures cannot be transferred to D-InSAR data.

Interesting for this work are three dimensional phase unwrapping algorithms, which jointly solve the spatial and temporal phase unwrapping. Several algorithms have recently been developed that include the temporal information as a third dimension as shown in Huntley (2001), Su and Zhang (2010) for FPP data or in Cusack et al. (2001), Salfity et al. (2006) for MRI data. However, these algorithms cannot be applied directly to D-InSAR data (Hooper and Zebker, 2007).

D-InSAR data already represent temporal differences as an interferogram always consists of the phase difference between two SAR images. As it is a satellite based system, the interferometric phases include disturbing signals such as atmospheric effects or influences due to incorrect satellite orbits. These disturbing effects can be reduced by generating differences between adjacent pixels in one phase image but not by generating differences between the phase measurements in time. Therefore, the observations entering the phase unwrapping represent double differences in time and space (Costantini et al., 2012). This reminds of Global Navigation Satellite System (GNSS) signals where the problem of phase ambiguities occurs as well. The carrier phase measurement is only measurable modulo 2π and the whole number of complete wave cycles is unknown. By forming differences in space and time atmospheric effects, clock errors and orbital errors can be eliminated (Teunissen, 1995). To solve the phase ambiguities, either the more inaccurate but unambiguous code measurement can be added or, in case of permanent measurements, observations over a certain time epoch can be used assuming constant ambiguities. Afterwards, the station coordinates and the ambiguity factors can be estimated in an overdetermined system by using the least squares adjustment. First of all, a float solution with real-valued phase ambiguity factors is obtained. A fixing, for example by means of the Least Squares Ambiguity Decorrelation Adjustment (LAMBDA) method (Teunissen, 1995) or the Ambiguity Function Method (AFM) (Counselman and Gourevitch, 1981), results in integer factors. However, the interferometric data differ from the GNSS data so that these methods cannot be easily applied to D-InSAR data. In contrast to GNSS the interferometric observations are only available in a single frequency and the measurements are not continuous as the sampling time depends on the satellite repeat orbit cycle.

Three dimensional approaches specifically for D-InSAR data already exist. However, these approaches either work in several steps (Pepe and Lanari, 2006, Hooper et al., 2007) or they are not based on the double differences and therefore cannot be integrated into the SBAS workflow (Shanker and Zebker, 2010, Costantini et al., 2012). At the moment, there is a lack of a three dimensional phase unwrapping approach in the literature that works in one step and that is specifically applicable to SBAS interferograms and to go one step further that is specifically applicable to spatially filtered so called multilooked SBAS interferograms.

1.3 Main Objectives and Challenges

The aim of this work is the development of a one-step phase unwrapping approach that includes the multilooked double differences in time and space as input data. State of the art is the EMCF algorithm which was developed specifically for SBAS interferograms and can be easily integrated into the SBAS workflow. Without going into too much detail at this point, the EMCF algorithm works in two steps. First, each spatial phase gradient is temporally unwrapped. This temporal phase unwrapping is done iteratively for a predefined set of modified observations. These modified observations consist of a linear motion model, whereas the motion model parameters are unknown. The results of the temporal phase unwrapping are then used in the second step to spatially unwrap the phases independently for each image. The temporally unwrapped results serve on the one hand as a starting solution for the spatial phase unwrapping and on the other hand they are used to weight the phase gradients for the spatial phase unwrapping. Three dimensional phase unwrapping is thus performed by solving two simpler and less dimensional problems. The problems themselves are formulated as Integer Linear Programs (ILPs), to be more precise as temporal ILPs during the temporal phase unwrapping and as spatial ILPs during the spatial phase unwrapping. The special properties of the problems lead to the fact that they can be solved as Linear Programs (LPs) without considering the integer constraints and thus much more efficiently than ILPs in general. The solutions are always integer values. If several smaller LPs are replaced by one single LP, the consequence is that the problem is of a much larger dimension and an efficient solution is required. The LP within the MCF algorithm can be set up in different ways and solved with different methods. The first main objective of this thesis is a detailed and consistent overview and discussion of these different types of solutions.

Intuitively, the problem seems to be solved simply by putting all the individual LPs into one large LP with a single large constraint matrix. The problem, however, is that the temporal phase unwrapping is performed iteratively to estimate the optimal motion model parameters which are absolutely necessary to detect the motion of a phase gradient in time. Furthermore, the results of the temporal LPs are required to define the weights of the spatial LPs. Therefore, the EMCF algorithm has to be modified so that the motion model parameters and the weights of the spatial LP are estimated independently of the solution of the temporal LP. This is the second challenge of this work.

In addition to the challenges already mentioned, multilooked data poses another problem. Spatial filtering is carried out individually for each interferogram. This leads to the fact that the temporal constraints which are established between the individual interferograms during the temporal phase unwrapping are not completely fulfilled by the data. This is called temporal inconsistency and must be taken into account. Otherwise, the temporal and spatial constraints, now combined in one single large LP, will lead to conflicts. The aspect of temporal inconsistency is already mentioned in the literature (e.g. Imperatore et al., 2015) and is also considered in the two-step EMCF algorithm by a rounding operator. However, there is no solution in the literature for considering this aspect when setting up a one-step phase unwrapping method with one large constraint matrix which includes both, the spatial as well as the temporal constraints. Thus, the consideration of the temporal inconsistency in a one-step three dimensional algorithm is the third and last challenge in this work.

The main objectives of this work can thus be summarized in the following three points:

1. Detailed and consistent overview of the different formulations and solutions of the LP within the MCF algorithm
2. Modifications of the EMCF algorithm so that the motion model is no longer estimated by an iterative solution of the temporal LP and so that the spatial weights can be set up independently of the temporal LP
3. Formulation of a one-step three dimensional algorithm that takes into account the temporal inconsistencies of the multilooked data

1.4 Outline

The observations represent double differences in space and time. Therefore, a clear index notation is necessary. The temporal assignment is always represented as a superscript index where $\Delta t_{\alpha\beta}$ represents a difference between the points in time t_α and t_β. The spatial assignment is done by a subscript index where Δx_{kl} represents a difference between the two pixels x_k and x_l. A detailed list of all used symbols and terms can be found at the end of this thesis, cf. Appendix B. Furthermore, the observations are presented in two independent graphs which are referred to throughout the work. A graph is defined in the azimuth/ range plane and consists of a set $\mathcal{M}$ of nodes, a set $\mathcal{N}$ of arcs between which a set $\mathcal{R}$ of triangles are constructed. The second graph is in the temporal plane and consists of a set $\mathcal{M}'$ of nodes, a set $\mathcal{N}'$ of arcs between which a set $\mathcal{R}'$ of triangles are constructed. For a better overview the graphs are also defined at the end of the work, cf. Appendix B, so that the reader can always refer to them. Finally, the list also includes definitions of the various problem formulations, methods and weight functions analyzed in this thesis so that it is always possible to look up which problem, method or weight function is meant.

The work is divided into a fundamental part, a review and evaluations of already existing methods and a part containing own modifications and developments. All methods are tested on both simulated and real data.

Chapter 2 starts with basics on differential SAR interferometry and multitemporal D-InSAR analysis. Since the work focuses on a specific part of the analysis, it is important to know exactly what happens before and after this step. This chapter is intended to provide an understanding of the input data of the phase unwrapping process.

State of the art is the formulation of the phase unwrapping problem as an LP. For this reason, Chapter 3 provides a basic knowledge about solving LPs. In this context terms like primal and dual problem are treated and general LP solvers like the simplex method and the interior point method are explained. The special property of total unimodularity is discussed, where the result obtains an integer value even without considering the integer constraint. Finally, an LP can also be solved as a network flow problem if certain preconditions are given. This chapter ends with the description of network flow problems.

Chapters 4 and 5 include a review and an evaluation of existing methods. Chapter 4 deals with the spatial phase unwrapping algorithms based on a single interferogram with special focus on the MCF algorithm which represents the state of the art in the SBAS analysis. At this point, a detailed and consistent overview of the different formulation and solution types of the LP in the context of the MCF problem is provided. Using simulated data, these different approaches are evaluated to find the most efficient way to solve the problem. Chapter 5, on the other hand includes three dimensional phase unwrapping algorithms which include both spatial and temporal phase unwrapping. Again, the currently used two-step EMCF algorithm is examined in more detail and evaluated using simulated data.

With regard to the merging of the two-step EMCF algorithm into a one-step approach, some modifications are necessary. These include the estimation of the motion model independent of the solution of the temporal LP and the definition of spatial weights that are independent of the temporal phase unwrapping. Ideas of improvement are presented in Chapter 6 which are then evaluated using both simulated and real data. The Lower-Rhine-Embayment serves as a case study. A conscious decision was made to use data from the European Remote Sensing (ERS) satellites 1 and 2. These are older data which detect the deformation of the Earth's surface in the past. But especially with these older data, which have a lower spatial and temporal resolution compared to newer sensors, phase unwrapping errors occur more often, so that especially with these sensors there is an increased potential for improvement. Moreover, these older data are of great interest especially for a long-term evaluation. It should be noted, however, that all the methods presented in this work can easily be transferred to other newer sensors, like Sentinel-1 or TerraSAR-X.

Based on the findings of the previous chapters, a one-step procedure can finally be developed in Chapter 7. Here, the problem of temporal inconsistency is specifically addressed and a corresponding solution is worked out by introducing slack variables. This self-developed method is also evaluated using simulated and real data.

The work ends with a conclusion and an outlook in Chapter 8 where the main findings are summarized and some thoughts for further works are developed.

2. Background: Multitemporal D-InSAR Analysis

Differential Interferometric Synthetic Aperture Radar (D-InSAR) is a unique technique to detect and map deformations of the Earth's surface over large temporal and spatial scales with an accuracy in the centimeter and even millimeter range (Bamler and Hartl, 1998, p. R2). Processing a whole stack of multitemporal data allows the generation of deformation time series. As it is an active system, it provides an all-weather and day/night capability. This chapter gives an overview of the D-InSAR processing steps and later on of the multitemporal D-InSAR processing whereas the focus is on the Small BAseline Subset (SBAS) method. One of the most challenging steps in the SBAS analysis is the solution of the phase ambiguities as the phase can only be measured modulo 2π. This is done in the context of phase unwrapping. The aim of this thesis is to optimize the phase unwrapping step which represents one special step in the middle of the D-InSAR processing chain. Therefore, it is important to know and understand what happens before and after this step. However, this chapter will not give an holistic summary of the complete processing steps. There is enough literature, cf. Bamler and Hartl (1998), Curlander and McDonough (1991), Currie and Brown (1992), Bamler and Schättler (1993), Schwaebisch (1995), Hanssen (2001), which is also mentioned at given points in order to refer to further details. This chapter is intended to provide a basic understanding of the input data for the phase unwrapping step, the meaning of the output data and how it is to be interpreted. Nevertheless, it is necessary to briefly describe the basics of radar and synthetic aperture radar (SAR) first.

2.1 Radar and Synthetic Aperture Radar

The abbreviation radar comes from radio detection and ranging. An antenna emits a series of short radio pulses towards the Earth, which are reflected from scatterers and received by the antenna again. As it is an active system and operates in the microwave region, it is almost independent of meteorological conditions and sun illumination (Bamler and Hartl, 1998, p. R1). One distinguishes between monostatic and bistatic radar. In the case of a monostatic radar, transmitter and receiver share one common antenna. Against that, a bistatic radar employs two separate antennas. Both types result in a considerably different radar characteristic (Skolnik, 1980). Since the satellite data used in this work were acquired with only one antenna, a monostatic radar is assumed in the following.

Once satellites were equipped with radar systems, radar became a useful method to measure the Earth's surface. The first radar images of the Earth were obtained in 1978 with the American satellite Seasat[1]. The spatial resolution of the image was 25 m. For this, the Synthetic Aperture Radar (SAR) was used which is a specific class of radar systems. The side-looking imaging geometry, pulse compression techniques as well as the synthetic aperture concept enable geometric resolutions in the order of some meters to tens of meters with a real antenna length of modest size (Bamler and Hartl, 1998, p. R1). This chapter deals with the imaging geometry, the resolution in azimuth and range direction and backscattering characteristics to provide a basic understanding of SAR systems. More information about SAR in general, signal processing for image formation or focusing can be found in several publications for example in Schreier (1993), Curlander and McDonough (1991), Bamler and Schättler (1993) or Bamler and Hartl (1998).

---

[1] `https://directory.eoportal.org/web/eoportal/satellite-missions/s/seasat` last accessed on August 4, 2020

The main focus of this thesis is the phase unwrapping problem which is one of the main error sources in the D-InSAR analysis. Especially with older sensors, which have a lower spatial and temporal resolution, phase unwrapping gets more complex and phase unwrapping errors often occur. So especially with these sensors there is an increased potential for improvement. This work therefore focuses on European Remote Sensing (ERS) satellites 1 and 2 from the European Space Agency (ESA)[2,3]. The ERS-1 mission started in July 1991 and ended in March 2000. The almost identically constructed ERS-2 satellite was launched in April 1995 which enabled a so called tandem mission. For a period of nine months the ERS-2 satellite passed the same point on the Earth's surface one day later than the ERS-1 satellite. An error in the gyroscope degraded the data provided by the ERS-2 satellite in February 2001. The mission ended in September 2011. The most important technical data of the satellites are listed in Table 2.1.

2.1.1 Imaging Geometry and Signal

A typical imaging mode of SAR systems is represented in Fig. 2.1. The signal is transmitted in slant range or Line Of Sight (LOS) direction. The satellite itself moves perpendicular to it in azimuth direction. As the pulse duration τ is a tenth of magnitude smaller than the satellite speed, it is permitted to suppose that the satellite retains its position during signal propagation (Bamler and Hartl, 1998, p. R4). The transmitted signal is reflected from scatterers and received by the antenna again. Measurements are the amplitude $A_{x_j}^{t_\alpha}$ and the phase change $\phi_{x_j}^{t_\alpha}$ between the transmitted and received signal for one pixel x_j and one epoch t_α. One pixel represents a resolution cell with a number of scatterers. The measurement at one pixel thus represents the sum of several scatterers. More information about this is given in Section 2.1.3. The amplitude $A_{x_j}^{t_\alpha}$ depends on the backscattering coefficient which varies with changing surface roughness and soil moisture. The phase change

$$\phi_{x_j}^{t_\alpha} = \frac{2\pi \cdot 2r_{x_j}^{t_\alpha}}{\lambda} + \phi_{\mathrm{scat},x_j}^{t_\alpha} \tag{2.1}$$

is proportional to the two-way distance $2r_{x_j}^{t_\alpha}$ from the antenna to the Earth's surface and divided by the wavelength λ. The additive scattering phase $\phi_{\mathrm{scat},x_j}^{t_\alpha}$ depends on the specific backscattering

Table 2.1: Technical data for the ERS-1/-2 satellites

technical parameters	value
altitude H_S	780 km
satellite speed v	7.43 km/sec
antenna size	10 m long, 1 m wide
period	100 minutes
repeat cycle	35-day
frequency f_0	5.3 GHz (C-band)
wavelength λ	5.6666 cm
bandwidth BW	15.55 MHz
incidence angle θ	23°
resolution in azimuth $\delta_{x_{az}}$	5 m
resolution in range $\delta_{x_{rg}}$	25 m
swath width	100 km

---

[2] `https://directory.eoportal.org/web/eoportal/satellite-missions/e/ers-1` last accessed on August 4, 2020

[3] `https://directory.eoportal.org/web/eoportal/satellite-missions/e/ers-2` last accessed on August 4, 2020

characteristic of this pixel. Due to the almost sinusoidal nature of the signal, the phase can only be measured modulo 2π. The measured so called wrapped phase $\psi_{x_j}^{t_\alpha}$ is given by

$$\psi_{x_j}^{t_\alpha} = \langle \phi_{x_j}^{t_\alpha} \rangle_{2\pi} \tag{2.2}$$

with the modulo 2π operator $\langle . \rangle_{2\pi}$. In order to reconstruct the real so called unwrapped phase, the integer number of 2π jumps must be estimated. The unwrapped phase is given by

$$\phi_{x_j}^{t_\alpha} = \psi_{x_j}^{t_\alpha} + 2\pi k_{x_j}^{t_\alpha} \tag{2.3}$$

with the integer ambiguity factor $k_{x_j}^{t_\alpha}$. This factor is solved in the context of phase unwrapping which is the main focus of this work and will be addressed in Chapters 4 and following. So far, it is assumed that the unwrapped phase $\phi_{x_j}^{t_\alpha}$ is known. In general, the total signal $u_{x_j}^{t_\alpha}$ is represented in a complex way by

$$u_{x_j}^{t_\alpha} = A_{x_j}^{t_\alpha} \cdot \exp\left(i\phi_{x_j}^{t_\alpha}\right) \tag{2.4}$$

with the imaginary unit i.

As seen in Fig. 2.1, the SAR system is a side-looking radar. The radar looks with the incidence angle θ in slant range direction and therefore is an imaging radar with azimuth and slant range coordinates. The echos of near range scatterers are received before the echos of far range scatterers. The incidence angle θ refers to the flat-earth or the ellipsoid. Due to the presented geometry, the signal illuminates an elliptical area on the Earth‘s surface which is called footprint. For the ERS-1 and ERS-2 satellites the size of the footprint is 100 km in ground range and 5 km in azimuth

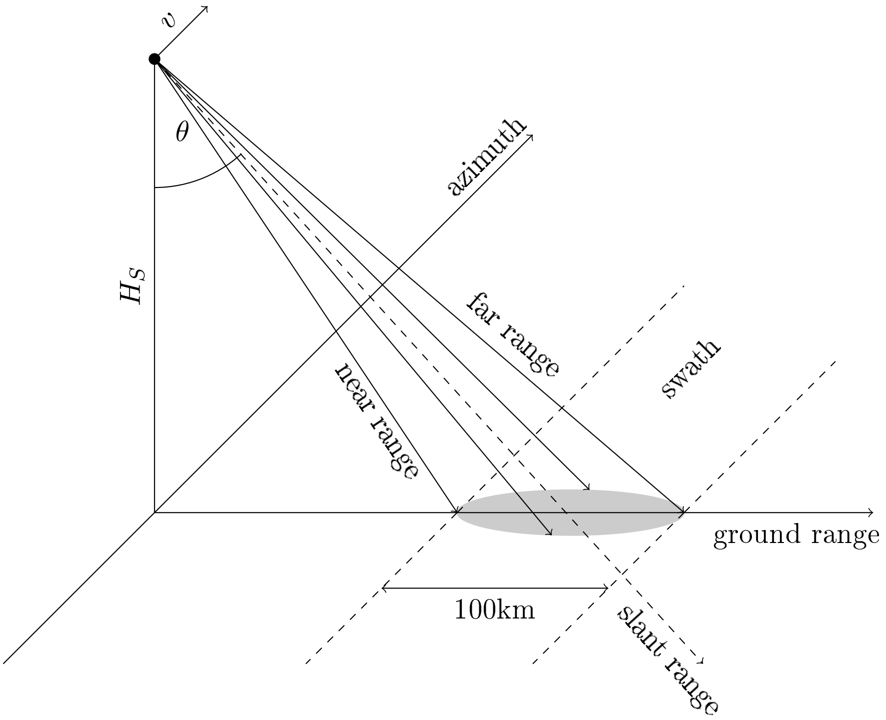

Figure 2.1: Geometry of side-looking radar. The satellite looks with the incidence angle θ in slant range direction to the Earth’s surface. Near range scatterers are received before far range scatterers. The gray area symbolizes the footprint illuminated by the signal on the Earth’s surface. The satellite moves with speed v in azimuth direction, so that the footprint traces the so called swath. Figure based on Bamler and Schättler (1993, p. 55).

direction. Using a fixed antenna, the footprint moves at the satellite speed along its orbit and traces the so called swath.

The imaging geometry described so far is called stripmap mode. Beside this mode, there are other imaging modes, like the scanning SAR (ScanSAR) (Moore et al., 1981, Currie and Brown, 1992) and the spotlight SAR (Carrara et al., 1995) where the antenna is moving. In ScanSAR mode the antenna is switching periodically in range direction to increase the swath width but the resolution in azimuth direction is simultaneously reduced. In spotlight mode the resolution is increased by steering the antenna electronically backwards in azimuth direction. This results in a longer illumination time but a continuous operation is no longer possible. More recent satellites like TerraSAR-X and Sentinel-1 have another newer acquisition mode called Terrain Observation with Progressive Scans (TOPS) mode. With the TOPS technique, in addition to steering the beam in range as in ScanSAR, the beam is also electronically steered from backward to forward in the azimuth direction. This results in very wide swaths with homogeneous image quality (De Zan and Monti Guarnieri, 2006). However, for the ERS-1/-2 satellites used here, the stripmap mode is still the most commonly used mode(Hanssen, 2001, p. 11), so that all following considerations refer to this mode.

2.1.2 Resolution in Range and Azimuth Direction

The resolution in range direction depends on the duration τ of the transmitted pulse, see Fig. 2.2. Projected on the Earth's surface the ground range resolution has got an inverse relationship with the incidence angle θ and results in

$$\delta_{x_{rg}} = \frac{c \cdot \tau}{2 \cdot \sin(\theta)} \tag{2.5}$$

with the speed of light c. The factor 1/2 results from the fact that the signal travels twice the distance between antenna and scatterer. Consequently, a short pulse duration is needed. However, reducing the pulse duration τ at the same power leads to a reduced energy

$$E = \int_0^\tau P(t) dt \tag{2.6}$$

which is the integral over the transmitted power P. Accordingly the power P must increase to keep the energy E constant. However, high-power transmitters present technical challenges as they are larger, heavier and more expensive. One way to further improve the resolution in range direction is the use of a linear frequency modulated pulse over a certain bandwidth BW. This pulse is called a chirp. With a chirp the bandwidth BW can be increased without reducing the pulse duration τ. Using a matched filter, the received signal is compressed afterwards so that the signal is as if a short pulse was transmitted. This matched filter is called range compression which can be computed efficiently by the use of Fast Fourier Transformations (Curlander and McDonough, 1991, pp. 182ff). Expressed with the bandwidth BW, the resolution in range direction becomes

$$\delta_{x_{rg}} = \frac{c}{2 \cdot BW \cdot \sin(\theta)}. \tag{2.7}$$

With an incidence angle of $\theta = 23°$ and a bandwidth of $BW = 15.55\,\mathrm{MHz}$ the range resolution for the ERS-1 and ERS-2 satellites results in $\delta_{x_{rg}} = 25\,\mathrm{m}$.

The resolution in azimuth direction for a real antenna depends on the altitude H_S, the incidence angle θ and the real aperture beamwidth Θ_r which is the fraction of the wavelength λ and the real antenna size length d_r. Thus, the resolution in azimuth direction is given by

$$\delta^r_{x_{az}} = \frac{H_S}{\cos(\theta)} \cdot \Theta_r = \frac{H_S}{\cos(\theta)} \cdot \frac{\lambda}{d_r}. \tag{2.8}$$

For ERS-1 and ERS-2 satellites this results in an unusable resolution of about 5 km which represents the size of the footprint in azimuth direction. As the wavelength and the altitude for measurements with microwave signals are predetermined and an extension of the antenna length to a few kilometer is not feasible, SAR is used to improve the resolution in azimuth direction. Therefore, the movement of the antenna platform is exploited to extend the real antenna length synthetically.

As the antenna moves, one target is measured from several satellite positions, see Fig. 2.3. All these measurements are combined as if they where measured at the same time from a synthetic antenna with the length d_s. The synthesis is based on the Doppler shift which occurs due to the relative movement between antenna and scatterer. The frequency of the signal gets higher when the distance between antenna and scatterer gets smaller and the other way around. If antenna and scatterer are perpendicular to each other the Doppler shift gets zero. As the footprint passes over the point target in Fig. 2.3, the distance between antenna and scatterer varies. It decreases to a minimum and then increases again. Thus, one target traces a hyperbolic line in azimuth/ range plane. In a further compression step all points of this curve are combined to one single pixel (Curlander and McDonough, 1991, pp. 187ff.). This technique allows an improvement of the resolution in azimuth direction. This step is therefore also called azimuth compression. Requirement is that the signal is coherent over time. It is mentioned that the antenna is not always steering perpendicular to the flight direction. Sometimes a slight squint angle occurs. This results in a Doppler centroid frequency, representing the frequency at the minimum distance between antenna and scatterer which is unequal to zero. This fact has to be considered in the azimuth compression step. This is done in a so called zero-Doppler processing step where the data is deskewed, implying that the phase values correspond with the zero-Doppler phase (Hanssen, 2001, p. 30). The length of the synthetic antenna d_s is equal to the size of the footprint in azimuth direction and therefore equal to the resolution in azimuth direction for a real antenna $\delta^r_{x_{az}}$

$$d_s = \delta^r_{x_{az}} = \frac{H_S}{\cos(\theta)} \cdot \frac{\lambda}{d_r}. \tag{2.9}$$

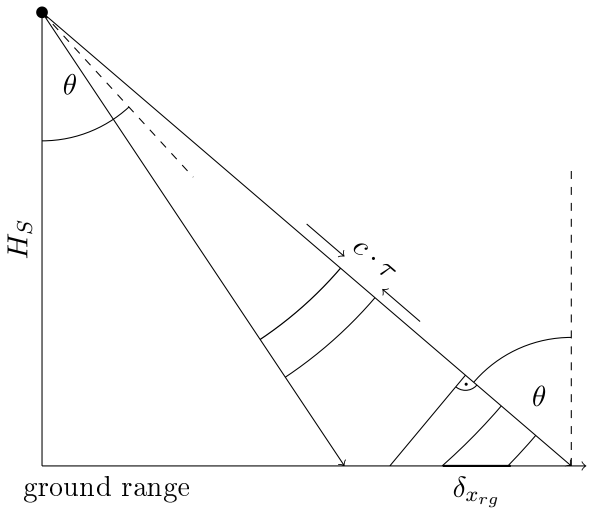

Figure 2.2: Resolution in range direction depends on the pulse duration τ and is independent of the satellite altitude H_S. With the use of pulse compression techniques the resolution can be improved to some meters.

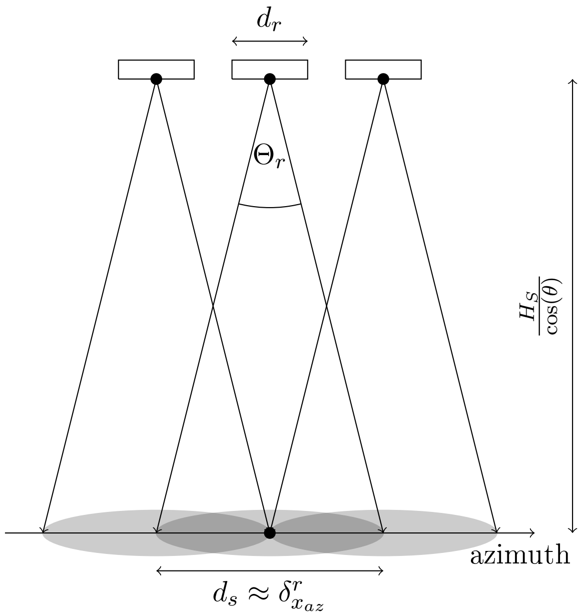

Figure 2.3: Resolution in azimuth direction for a real antenna depends on the altitude H_S and is inversely proportional to the real antenna length d_r. However, for a synthetic antenna with length d_s the resolution gets one half of the real antenna length d_r.

So on the one hand, the resolution in azimuth direction for a real antenna gets worse with increasing altitude H_S, but on the other hand the synthetic antenna length d_s also gets bigger. At the bottom line the resolution in azimuth direction for the synthetic antenna is independent of the altitude and results in

$$\delta^s_{x_{az}} = \frac{H_S}{\cos(\theta)} \cdot \Theta_s = \frac{H_S}{\cos(\theta)} \cdot \frac{\lambda}{2d_s} = \frac{H_S \cdot \lambda}{\cos(\theta) \cdot 2\frac{H_S \cdot \lambda}{\cos(\theta) \cdot d_r}} = \frac{d_r}{2}. \tag{2.10}$$

The antenna beamwidth of a synthetic aperture Θ_s can be represented similar to the real aperture, cf. (2.9), besides a factor of two. This factor results from the different measurements. In case of a real aperture the signals for each measurement are transmitted at the same time. Therefore, differences between transmitted and received signal occur only at the way back from the scatterer to the antenna. In case of a synthetic aperture the signals are not transmitted simultaneously. So differences occur twice, at the way from the antenna to the scatterer as well as at the way back from the scatterer to the antenna.
So at last, the resolution in azimuth direction is one half of the real antenna length d_r. However, the real antenna length is also limited as the signal power of the antenna gets smaller with decreasing length. For the ERS-1 and ERS-2 satellites the real antenna length is set to 10 m so that the resolution in azimuth direction results in 5 m.

2.1.3 Persistent Scatterers and Distributed Scatterers

After compression in range and azimuth direction the raw data is focused to an image. These so called SAR single look complex products include the measurements, amplitude $A^{t_\alpha}_{x_j}$ and phase $\phi^{t_\alpha}_{x_j}$ for one pixel x_j at one time t_α. These products provide standard level 1 data intended for the use in interferometric processing (Hanssen, 2001, p. 42).
One pixel represents a resolution cell of 25 m × 5 m for the ERS missions. So the measurements for one pixel are the sum of many individual scatterers located in this resolution cell. The returning waves interfere randomly in a constructive or destructive way, depending on the relative phase of each scattered waveform. This causes a pixel-to-pixel variation in amplitude and phase which can be recognized as a salt and pepper effect, called speckle (Goodman, 1975). There exist two extreme cases of scattering objects: a distributed scatterer and a persistent scatterer.

A distributed scatterer, also known as Gaussian scatterer, has a high number of random subscatterers within the resolution cell. There is no single subscatterer which dominates. This is true for most natural scatterers, as forests, agriculture fields or rock surfaces. The observation can be defined as a Gaussian random variable (Hanssen, 2001, p. 89). Relative movements of these individual scatterers or changes in the looking angle causes the scatterer contributions to sum differently (Hooper, 2006, p. 13). This can be seen in Fig. 2.4a. The phase of the pixel varies randomly with the number of iterations. This effect is known as decorrelation.
In contrast, if one subscatterer dominates in the resolution cell, the phase varies little even if the other subscatterers move with respect to the dominant scatterer or the looking angle changes, see Fig. 2.4b. This pixel is known as persistent scatterer. Examples for persistent scatterers are urban objects as corners of a house, bridges or streets. Moreover, there exist artificial constructed objects with a very stable backscattering characteristic, known as corner reflectors.

As the speckle effect makes image interpretation difficult, various ways have been evolved to suppress it. These techniques are known as speckle filtering algorithms. There are several standard speckle filters that are widely used in the SAR community. The common technique is the spatial domain

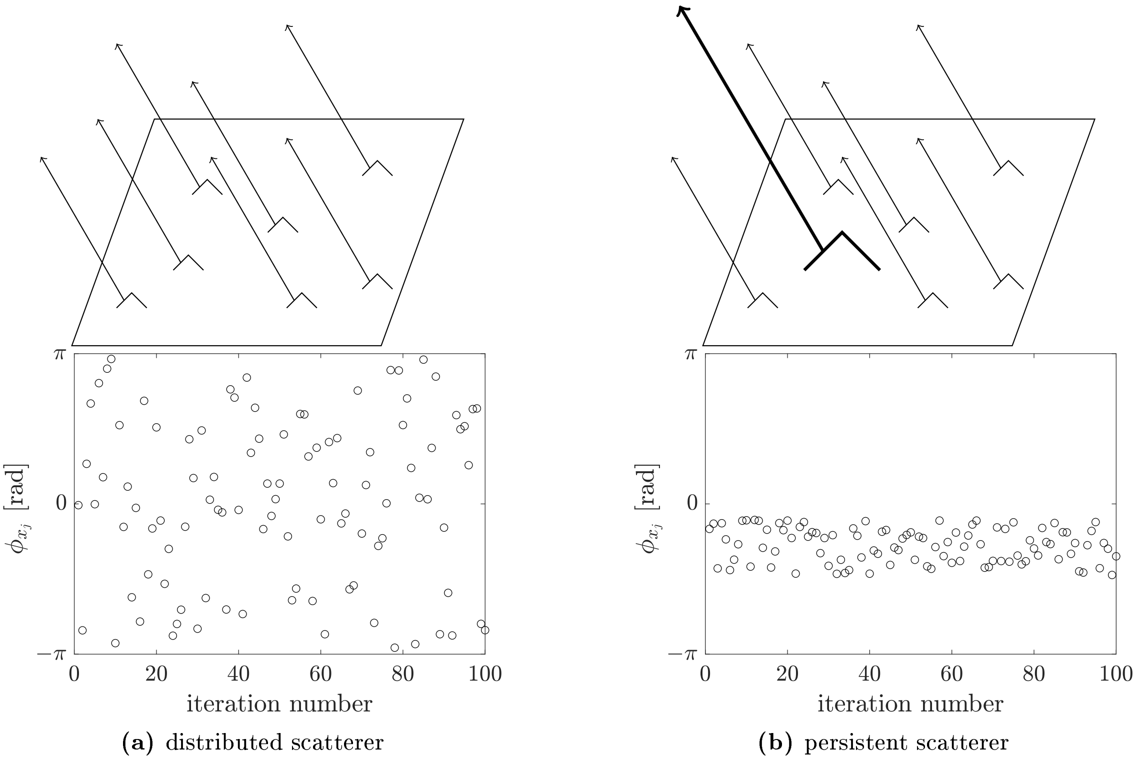

(a) distributed scatterer **(b)** persistent scatterer

Figure 2.4: Simulated phase for a distributed and a persistent scatterer. The simulation is done for 100 iterations. The above pictures show the different contributions of the individual scatterers in one resolution cell. Figures based on Hooper (2006, p. 14).

multilooking. Several independent pixels are averaged in the spatial domain resulting in a spatially compressed multilooked image. As an average filter smooths the image and removes edges, adaptive filter windows are much better. Some examples are the local statistical filters by Lee (1980), Frost et al. (1982), Kuan et al. (1985) or Lopes et al. (1990). Alternative techniques are wavelet based filters (Ranchin and Cauneau, 1993, Odegard et al., 1995). The idea is that speckle noise is a high-frequency component of the image and appears in wavelet coefficient. A good comparison of spatial and wavelet based filters is provided in Hervet et al. (1998).

2.2 Differential Interferometric Synthetic Aperture Radar

As is shown in Fig. 2.5 for one single SAR image, it is impossible to distinguish two objects at the same range. Point P_{x_k} on the reference surface and point P_{x_j} with height $H_{P_{x_j}}$ are at the same distance from the antenna. The solution to distinguish these two points is the use of a second SAR image which measures the same point by a slightly different geometry, see Fig. 2.6. The two points can now be distinguished from each other due to different incidence angles. The two SAR images can be acquired either by two different antennas operating simultaneously, known as single-pass interferometry or by using a single SAR system which images the area twice from slightly different orbits at different times, known as repeat-pass interferometry. As this study works with ERS-1 and ERS-2 data which only have single SAR systems on board, the repeat-pass interferometry is discussed here.

The phase difference of the two SAR signals, known as interferometric phase, includes information about the topography and surface deformations. The use of interferometric data for topography mapping was first reported by Graham (1974). Today, Interferometric Synthetic Aperture Radar

(InSAR) is an extremely powerful method for mapping Earth's land topography. Furthermore, the so called differential InSAR (D-InSAR) method is a unique method for detection and mapping surface displacements over large temporal and spatial scales with an accuracy in the centimeter and even millimeter range (Bamler and Hartl, 1998, p. R2). The following sections will give an overview of the most important steps to create an interferogram and the idea behind the differential interferometry to detect ground deformations.

2.2.1 Interferogram Generation

Figure 2.6 shows the InSAR configuration for a repeat-pass interferometry. The satellite passes the same point at the Earth's surface after a special time difference $\Delta t_{\alpha\beta} = t_\beta - t_\alpha$, whereas the two sensor positions S^{t_α} and S^{t_α} differ by a spatial baseline $\Delta b_{\alpha\beta}$. For the ERS-1 and ERS-2 satellites the time difference for the tandem mission is one day and otherwise 35 days or a multiple of 35 days. This time difference is also known as temporal baseline. The point $H_{P_{x_j}}$ is observed from two different incidence angles θ^{t_α} and θ^{t_β} and thus with two different distances $r_{x_j}^{t_\alpha}$ and $r_{x_j}^{t_\beta}$. The path length difference $r_{x_j}^{\Delta t_{\alpha\beta}}$ is measured by determining the phase difference according to

$$r_{x_j}^{\Delta t_{\alpha\beta}} = \frac{\lambda}{4\pi}(\phi_{x_j}^{t_\beta} - \phi_{x_j}^{t_\alpha}) = \frac{\lambda}{4\pi}\phi_{x_j}^{\Delta t_{\alpha\beta}}. \tag{2.11}$$

The phase difference, also known as interferometric phase $\phi_{x_j}^{\Delta t_{\alpha\beta}}$, is sensitive against height differences according to the relation (Hanssen, 2001, p. 37)

$$\partial H_{P_{x_j}} \sim \frac{\lambda \cdot r_{x_j}^{t_\alpha} \cdot \sin(\theta^{t_\alpha})}{4\pi \cdot \Delta b_{\alpha\beta,\perp}} \cdot \phi_{x_j}^{\Delta t_{\alpha\beta}} \tag{2.12}$$

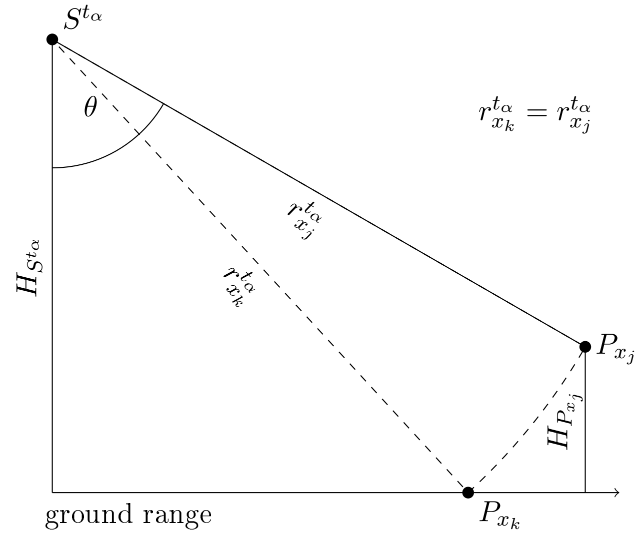

Figure 2.5: Single SAR configuration. The point P_{x_k} on the reference surface and the point P_{x_j} with $H_{P_{x_j}}$ cannot be distinguished in one single SAR image. They show the same distance to the antenna. Figure based on Hanssen (2001, p. 34).

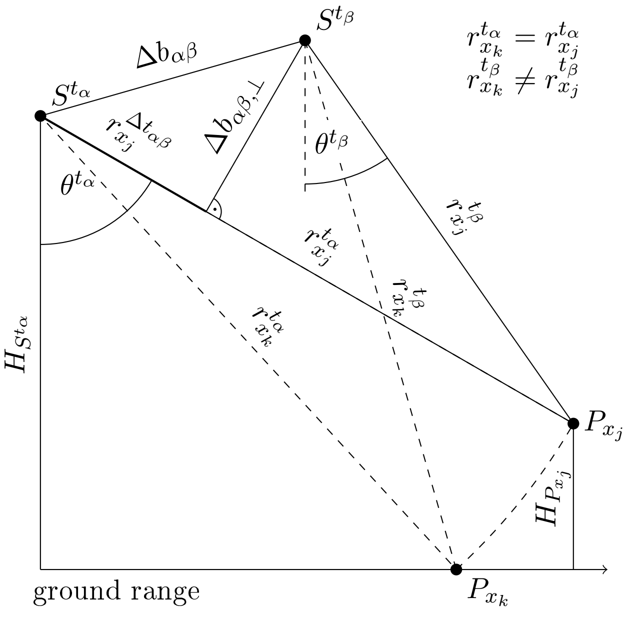

Figure 2.6: Interferometric configuration. Using two SAR images at times t_α and t_β, the topography can be determined. Therefore, the slant range difference $r_{x_j}^{\Delta t_{\alpha\beta}}$ between the two SAR images at times t_α and t_β is measured in form of the interferometric phase which is related to the height $H_{P_{x_j}}$. Figure based on Hanssen (2001, p. 34).

with the orthogonal spatial baseline $\Delta b_{\alpha\beta,\perp}$ which is the projection of the spatial baseline $\Delta b_{\alpha\beta}$ to the slant range, see Fig. 2.6. It is assumed that the wavefront of the signal arrives as a plane at the antennas since the distances between the satellite positions S^{t_α} and S^{t_β} and the point P_{x_j} on the Earth's surface are very large. The equation implies that with a larger baseline the height gets more sensitive to phase changes. According to Schwaebisch (1995, p. 72) an orthogonal spatial baseline of 50 m leads to a height error of about 25 m with an assumed phase variance of 0.7 rad. In contrast, an orthogonal spatial baseline of 300 m causes a height error of 3 m only. However, the orthogonal spatial baseline cannot be increased arbitrarily. This will be discussed in the following sections which deal with necessary preprocessing steps for generating the interferogram. In addition, the interferometric phase and a measurement to describe the quality of the phase are presented and some postprocessing steps are discussed to further improve the quality of the interferogram.

2.2.1.1 Preprocessing Steps: Bandwidth Filter and Coregistration

Before the interferometric phase between the two SAR images at times t_α and t_β can be estimated, some preprocessing steps are necessary. Starting from the two focused SAR images, one image is defined as the master image and remains unchanged during the preprocessing step. The other image is defined as slave image. In the following, the SAR image at time t_α is defined as master and the other SAR image at time t_β is defined as slave scene.
As the two SAR images are measured from slightly different incidence angles, the received spectral bands do not completely overlap both in range and in azimuth direction. This can be considered as noise in the interferometric phase. In range direction the shift is directly associated with the orthogonal spatial baseline $\Delta b_{\alpha\beta,\perp}$ between the two SAR antennas. The frequency shift in range direction $\Delta f_{r_{x_j}}$ at one pixel x_j is given by

$$\Delta f_{r_{x_j}} = -\frac{2\Delta b_{\alpha\beta,\perp}}{\lambda r_{x_j}^{t_\alpha} \tan(\theta - \zeta)} \tag{2.13}$$

with the terrain slope ζ (Bamler and Hartl, 1998, p. R13). Consequently, the frequency shift increases with a larger spatial baseline $\Delta b_{\alpha\beta,\perp}$. This will be taken into account when dealing with the conditions for interferometry later on. Due to the different squint angles, the two Doppler centroid frequencies, mentioned in Section 2.1.2 differ from each other. This causes an additional frequency shift in azimuth direction. Common bandwidth filters are used in range and azimuth direction to guarantee a maximum spectral overlap in both images. More about the spectral filtering can be found in Gabriel and Goldstein (1988) or Schwaebisch (1995, pp. 31–37) for example.

Beside the spectral shift, the slightly different geometry of the two SAR images also causes a shift of up to several thousands of pixels (Hanssen, 2001, p. 45). So a coregistration is necessary to geometrically match the images. Just and Bamler (1994) have shown that a misregistration introduces phase variance. Based on these investigations, a coregistration error of 0.1 to 0.2 pixel has become widely accepted (Schwaebisch, 1995, p. 27).
The procedure of coregistration is usually separated in two steps: coarse and fine coregistration. The coarse coregistration is for pixel level accuracy. It is implemented by using orbital information and image matching. For a point grid which refers to the master scene, the corresponding pixel coordinates for the slave scene are determined. The cross-correlation coefficient is a common parameter for evaluating the matching results (Li and Goldstein, 1990). As already said, the coarse coregistration occurs with an accuracy of approximately one pixel. However, this is not enough. So, in a second step a fine coregistration is done. For subpixel tie points a transformation equation is fitted and the slave image is resampled with help of a bilinear or bicubic interpolation. More detail on coregistration can be found in Gabriel and Goldstein (1988), Lin et al. (1992), Schwaebisch (1995, pp. 28–31) and Schwaebisch and Geudtner (1995).

2.2.1.2 Interferometric Phase and Coherence Estimation

When both SAR images resemble the same geometry and contain completely overlapping object spectra, the interferogram is computed according to

$$I_{x_j}^{\Delta t_{\alpha\beta}} = u_{x_j}^{t_\alpha} \cdot u_{x_j}^{t_\beta *} \tag{2.14}$$

with the complex conjugate of the second image $u_{x_j}^{t_\beta *}$. The interferometric phase results in

$$\phi_{x_j}^{\Delta t_{\alpha\beta}} = \phi_{x_j}^{t_\beta} - \phi_{x_j}^{t_\alpha}. \tag{2.15}$$

Self-explanatory the interferometric phase can also only be measured modulo 2π only and the measured so called wrapped phase is defined as

$$\psi_{x_j}^{\Delta t_{\alpha\beta}} = \langle \phi_{x_j}^{\Delta t_{\alpha\beta}} \rangle_{2\pi}. \tag{2.16}$$

In order to reconstruct the unwrapped interferometric phase which is given by

$$\phi_{x_j}^{\Delta t_{\alpha\beta}} = \psi_{x_j}^{\Delta t_{\alpha\beta}} + 2\pi k_{x_j}^{\Delta t_{\alpha\beta}}, \tag{2.17}$$

the unknown integer ambiguity factor $k_{x_j}^{\Delta t_{\alpha\beta}}$ has to be estimated in the phase unwrapping step. However, this problem will be treated in Chapters 4 and following so that it is assumed that the unwrapped interferometric phase $\phi_{x_j}^{\Delta t_{\alpha\beta}}$ is known at this moment.

A direct measure for the similarity between the two observations $\phi_{x_j}^{t_\beta}$ and $\phi_{x_j}^{t_\alpha}$ is the degree of coherence. An appropriate estimator for the coherence is the complex correlation coefficient

$$\gamma_{x_j} = \frac{\sum\limits_{j=1}^{m} u_{x_i}^{t_\alpha} \cdot u_{x_i}^{t_\beta}}{\sqrt{\sum\limits_{j=1}^{m} |u_{x_j}^{t_\alpha}|^2 \cdot \sum\limits_{j=1}^{m} |u_{x_j}^{t_\beta}|^2}} \tag{2.18}$$

which is a spatial averaging over a number m of pixels (Seymour and Cumming, 1994). This space-averaged coherence is biased. The bias decreases with the number m of pixels. Touzi et al. (1999) derived an analytical expression for the coherence γ as a function of the unbiased coherence and the number m of pixels. With help of a piecewise-linear model the unbiased coherence can be estimated from the biased one. The coherence values range from zero, the interferometric phase is just noise, to one, the two signals are fully coherent without any noise.

Typically a loss of coherence, known as decorrelation, has several causes. The two main sources are due to spatial and temporal decorrelation effects. As already mentioned, larger spatial baselines lead to an increased spectral shift in range direction. In extreme cases the spatial baseline is too large resulting in a non-overlapping part of the spectrum and therefore completely uncorrelated signals. Too large different Doppler centroid frequencies lead to an increased spectral shift in azimuth direction and to a further decorrelation effect. For the ERS data the critical baseline $\Delta b_{\perp,\mathrm{crit}}$ occurs at approximately 1100 m and the critical different Doppler centroid frequencies Δf_{crit} are at approximately 1380 Hz (Hooper, 2006, p. 36). The second major limitation for the interferogram generation is the temporal baseline Δt between the two SAR images. Weather, vegetation or anthropogenic activities lead to temporal decorrelation effects as the backscattering characteristics of the individual scatterers in one pixel change. The ideal temporal baseline Δt depends on the expected deformation rate or whether the deformation is instantaneous. Then a very short temporal baseline is ideal (Hanssen, 2001, p. 43). If no further information is available, according to Hooper (2006, p. 36) a typical value for the critical temporal baseline Δt_{crit} is 5 years.

2.2.1.3 Flattening and A Posteriori Filtering

The interferometric phase generated with (2.15) contains some disturbing signals which make the interpretation of the topography and surface deformation more difficult. As seen in Fig. 2.7a, pixels on the flat-earth occur at different slant ranges $r_{x_j}^{\Delta t_{\alpha\beta}}$ and $r_{x_k}^{\Delta t_{\alpha\beta}}$. Due to the side-looking geometry an additional phase effect arises which is not induced by the topography or deformation. This effect is known as the effect of the flat-earth. A schematic representation of the flat-earth phase is shown in Fig. 2.7b. Therefore, the interferogram of a flat area will show corresponding periodic interferometric fringes which have nothing to do with topography or surface deformation. It is recommended to eliminate the effect of the flat-earth. This reduces the number of fringes in the interferogram which makes the phase unwrapping process and further processing steps easier. Common methods calculate the flat-earth phase with help of orbit parameters and the use of an external Digital Elevation Model (DEM). Another commonly used algorithm utilizes the frequency information of the interferogram and subtracts constant or dominant rates of fringes in azimuth and range direction (Li and Goldstein, 1990).

After subtracting the flat-earth, the quality of the interferogram can be further enhanced by filtering techniques. Due to decorrelation effects the interferogram is disturbed by noise. A standard method to decrease the noise is the so called multilooking. The complex data are simply averaged in a specified window as already discussed in Section 2.1.3. As the resolution in azimuth direction is better than in range direction the pixels are often averaged along the azimuth axis to get square pixels. For the ERS-1 and ERS-2 satellites, therefore, five time more pixels are included during averaging in the azimuth direction than in the range direction. To preserve edges and local structure adaptive filters are recommended, like the Goldstein filter (Goldstein and Werner, 1998).

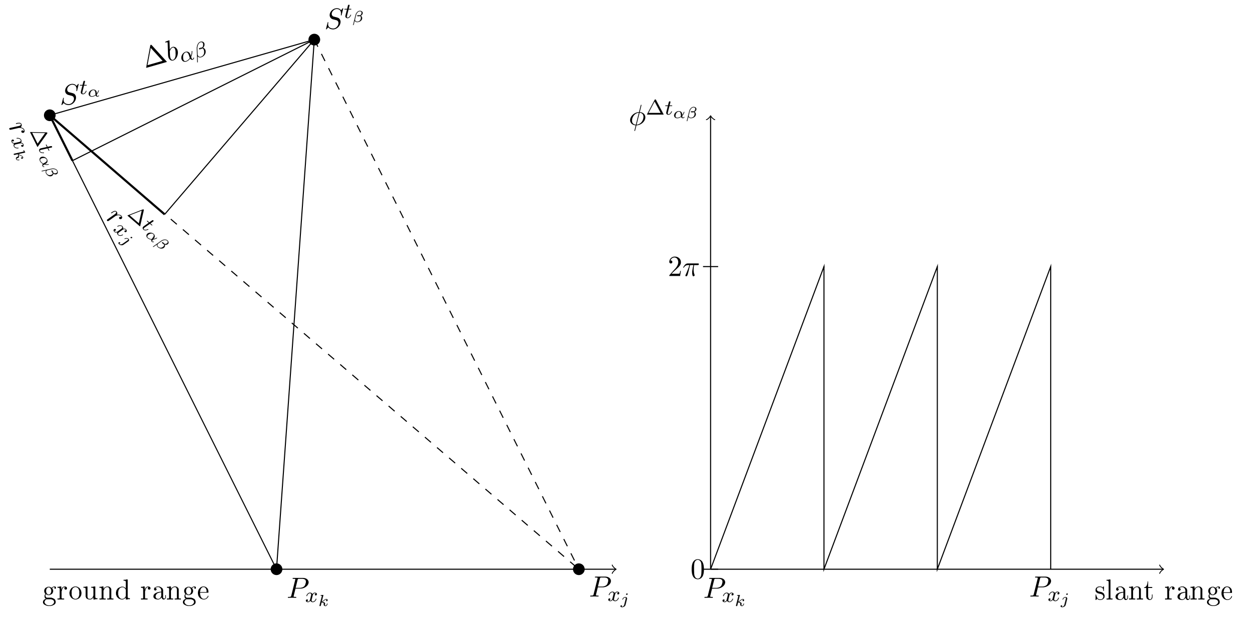

(a) scenario for the effect of the flat-earth

(b) schematic representation of the flat-earth phase

Figure 2.7: Effect of the flat-earth. Due to the side-looking geometry pixels P_{x_j} and P_{x_k} on the flat-earth occur at different slant ranges $r_{x_j}^{\Delta t_{\alpha\beta}}$ and $r_{x_k}^{\Delta t_{\alpha\beta}}$. Figures based on Schwaebisch (1995, p. 40).

2.2.2 Differential Interferometry

In reality, the interferometric phase does not only depend on different slant ranges due to the topography. Atmospheric effects, erroneous orbit parameters leading for example to incorrect flat-earth phases, or noise also cause phase changes. An additional effect is the deformation which occurs between the temporal baseline Δt of the two SAR images. Hence, the interferometric phase between the two SAR images at time t_α and t_β at pixel x_j is composed of several different parts

$$\phi_{x_j}^{\Delta t_{\alpha\beta}} = \phi_{x_j,\text{topo}}^{\Delta t_{\alpha\beta}} + \phi_{x_j,\text{defo}}^{\Delta} + \phi_{x_j,\text{orbit}}^{\Delta t_{\alpha\beta}} + \phi_{x_j,\text{atmo}}^{\Delta t_{\alpha\beta}} + \phi_{x_j,\text{noise}}^{\Delta t_{\alpha\beta}} \tag{2.19}$$

including the topographic phase $\phi_{x_j,\text{topo}}^{\Delta t_{\alpha\beta}}$, a possible deformation phase $\phi_{x_j,\text{defo}}^{\Delta t_{\alpha\beta}}$, orbit errors $\phi_{x_j,\text{orbit}}^{\Delta t_{\alpha\beta}}$, the atmosphere $\phi_{x_j,\text{atmo}}^{\Delta t_{\alpha\beta}}$ and noise $\phi_{x_j,\text{noise}}^{\Delta t_{\alpha\beta}}$. It is often difficult to distinguish between the different parts because this is depending on prior knowledge.
In order to derive deformations of the Earth's surface, the phase part $\phi_{x_j,\text{defo}}^{\Delta t_{\alpha\beta}}$ is the target quantity. Therefore, a differential interferogram is derived by subtracting the effect of the topography $\phi_{x_j,\text{topo}}^{\Delta t_{\alpha\beta}}$. This method was first applied by Gabriel et al. (1989), using Seasat data to an imaging site in Imperial Valley, California, where the expansion of water-absorbing clays led to deformations of the Earth's surface. The effect of the topography is removed by using a reference DEM coming from an external source, like the Shuttle Radar Topography Mission (SRTM [4]) or alternatively by generating tandem SAR image pairs or image pairs where no displacement is expected during the acquisition time.

Afterwards, the so provided differential interferogram can be used to detect deformations of the Earth's surface. However, the phase also contains disturbances due to errors in the reference DEM, known as topographic errors, orbit errors, atmospheric effects as well as noise. To reduce orbit errors a baseline optimization is possible. This can be either done by an adjustment based on ground control points or by a deramping, as orbit errors occur as spatial ramps in the interferograms. The other effects can be removed by analyzing a whole stack of interferograms instead of one single SAR pair. The temporal information allows the separation of the different parts as they all show an individual spatial and temporal behavior. Moreover, the analysis of a whole stack of interferograms allows the generation of deformation time series. This leads to multitemporal D-InSAR processing which will be addressed in the next section.

2.3 Multitemporal D-InSAR Processing

Multitemporal D-InSAR processing is used to generate deformation time series with respect to one reference time where the deformation is initialized to be zero. Considering a set $\mathcal{M}'$ with m' SAR images of the same scene measured at times $\boldsymbol{t}_{[m'\times 1]}$. In order to process these data altogether in a multitemporal way several methods were adopted. The following section gives a short overview of the most widely used methods. This work concentrates on the Small BAseline Subset (SBAS) method (Berardino et al., 2002) which will be described in more detail.

2.3.1 Processing Methods: Overview

The aim of multitemporal D-InSAR processing is the estimation of the deformation and the topographic errors as well as the separation of the atmospheric effects. The most widely used

---

[4] `https://www2.jpl.nasa.gov/srtm/` last accessed on August 4, 2020

methods are the Permanent Scatterer Interferometry (PSI) and the Small BAseline Subset (SBAS) method. The two main limitations of SAR interferometry are the spatial and temporal decorrelation effects which increase with larger baseline sizes, cf. Section 2.2.1.2. To overcome these effects, the PSI method, first proposed by Ferretti et al. (2001), only uses persistent scatterers which show consistent backscattering characteristics over the time series, see Fig. 2.4b. To identify them Ferretti et al. (2001) analyze the time series of the amplitude values as a measure of phase stability. However, good persistent scatterers are rare and mostly occur at urban areas. Over the years other persistent scatterer processing methods have been developed to get a more dense result even in non-urban areas. Two examples are SqueeSAR (Ferretti et al., 2011) where persistent and distributed scatterers are jointly processed or the Stanford Method for Persistent Scatterers (StaMPS) (Hooper et al., 2004, 2007) where the pixel selection is based on phase characteristics rather than on amplitudes.

Figure 2.8 shows an example of a multitemporal D-InSAR stack based on ERS-1/-2 data from May 1992 to December 2000 as used in the numerical studies, cf. Sections 6.3 and 7.4. The D-InSAR stack can be visualized as a graph in the temporal/ orthogonal spatial baseline plane. The white dots are the nodes represented by the set $\mathcal{M}'$ with m' SAR scenes at one special time and with the corresponding orthogonal spatial baseline relating to the master scene. The black lines are the arcs of the graph represented by the interferograms between the corresponding SAR images.

Here, the master scene is at the end of 1997. The master scene is chosen so that the so called stack coherence, cf. (Kampes, 2005, p. 6),

$$\gamma^{t_\alpha} = \frac{1}{m'-1} \sum_{\forall t_\beta \in \boldsymbol{t}, t_\beta \neq t_\alpha} g(\Delta b_{\alpha\beta,\perp}, \Delta b_{\perp,\mathrm{crit}}) \cdot g(\Delta t_{\alpha\beta}, \Delta t_{\mathrm{crit}}) \cdot g(\Delta f_{\alpha\beta}, \Delta f_{\mathrm{crit}}) \tag{2.20}$$

with

$$g(x,c) = \begin{cases} 1 - \frac{|x|}{c} & |x| \leq c \\ 0 & |x| > c \end{cases} \tag{2.21}$$

is maximized. As mentioned in Section 2.2.1.2, typical values for the critical orthogonal spatial baseline are $\Delta b_{\perp,\mathrm{crit}} = 1100\,\mathrm{m}$, for the critical temporal baseline Δt_{crit} =5 years and for the critical different Doppler centroid frequencies $\Delta f_{\mathrm{crit}} = 1380\,\mathrm{Hz}$ (Hooper, 2006, p. 36).

The PSI method only processes persistent scatterers which do not suffer from decorrelations as they remain coherent in all interferograms. Thus, there are no limitations on the size of the spatial and temporal baselines. Therefore, the interferograms are generated with respect to one master scene resulting in the star-like single-master stack with $m'-1$ interferograms, shown in Fig. 2.8a.

By applying the SBAS method a set $\mathcal{N}'$ with n' interferograms is generated under the condition that the maximum temporal and spatial baselines are not exceeded. Thereby, the decorrelation effects are reduced. This leads to a network with more than one master scene. Figure 2.8b shows an optimized network for the ERS-1/-2 data set following Pepe et al. (2015).

The SBAS method was first proposed by Berardino et al. (2002) based on multilooked images to reduce phase noise and a coherence based pixel selection criterion. This results in an increased spatial sampling with respect to the original PSI approach (Crosetto et al., 2016). Furthermore, it includes an approach to link independent baseline subsets which can occur due to

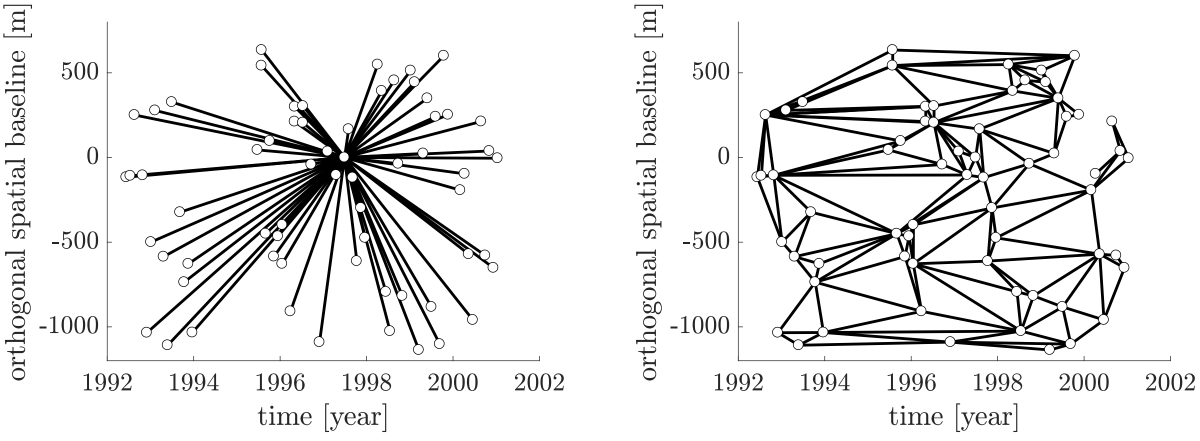

(a) PSI method with $m' - 1$ interferograms **(b)** SBAS method with n' interferograms

Figure 2.8: Multitemporal SAR data representation as a graph in the temporal/ orthogonal spatial baseline plane for the ERS-1/-2 data from May 1992 to December 2000 covering the test region of the Lower-Rhine-Embayment. All scenes are coregistrated to one master scene at the end of 1997. The white dots are the nodes of the graph represented by the set $\mathcal{M}'$ with m' SAR images at one time with corresponding orthogonal spatial baseline relating to the master scene. The black lines are the arcs of the graph represented by the interferograms. The interferogram selection is represented once for the PSI and once for the SBAS method.

the limitations of baseline sizes. Lanari et al. (2004) extended the SBAS approach to work with full-resolution interferograms which are not multilooked in order to detect local deformations as well.

The aim is to detect the deformation of the test region in the Lower-Rhine-Embayment. This region is characterized by a very rural area with many forests in the south. Moreover, within this region there is one of the largest brown coal occurrences in Europe. The groundwater extraction and the flooding after the closing of the open-cast mines lead to extensive Earth's surface motions. To detect them in a large scale the SBAS method is used in this work as persistent scatterers are very rare in this region.

2.3.2 Small BAseline Subset Method

The aim of the SBAS method is to estimate a deformation time series by processing a series of SAR images multitemporally. Therefore, a D-InSAR stack is generated according to Fig. 2.8b under the condition that the maximum temporal and spatial baselines are not exceeded. The resulting differential interferometric phases include the deformation signal, orbit and topographic errors, atmospheric effects and noise. To reduce the noise which is effected by decorrelation effects, only so called coherent pixels are analyzed. These are pixels with a stable backscattering characteristic. The identification is based on the coherence, cf. (2.18). Hence, only pixels that show a coherence value greater than a specific threshold in a minimum number of interferograms are taken into account. In the following m' SAR images are considered resulting in n' D-InSAR images based on the SBAS method.

2.3.2.1 Preprocessing Steps

Before the SBAS workflow is applied, two preprocessing steps based on Pepe et al. (2015) are inserted in order to improve the resulting deformation time series. These preprocessing steps imply an effective noise filtering and an efficient interferogram selection procedure.

A posteriori filtering steps, like the multilooking are performed individually for each interferogram, cf. Section 2.2.1.3. This leads to the fact that the interferometric phases are not fully time consistent. Due to the multilooking, the so called loop closure phase, expressed here for the three SAR images at times t_α, t_β and t_γ

$$\phi_{x_j}^{\Delta t_{\alpha\beta}} + \phi_{x_j}^{\Delta t_{\beta\gamma}} + \phi_{x_j}^{\Delta t_{\gamma\alpha}} \neq 0 \tag{2.22}$$

is unequal to zero. This is called temporal inconsistency. With help of the overdetermined system, the unknown wrapped phases at each SAR image (see white nodes in Fig. 2.8b) are estimated to reconstruct new time consistent SBAS interferograms. To overcome the rank defect, the phase of the first SAR image is assumed to be zero. Nevertheless, in some cases the phase quality of the new reconstructed interferogram gets worse. To further increase the quality of the whole stack the observed and reconstructed interferograms are combined through a weighted averaging operation. This new stack of SBAS interferograms offers an increased level of coherence compared to the original interferograms and the time consistency gets better. However, it has to be mentioned that the interferograms are not fully time consistent.

The second step identifies the optimum set of previously filtered interferograms. Therefore, a Delaunay triangulation in the temporal/ orthogonal spatial baseline plane based on the m' SAR images is used. For this purpose, a normalized length is defined for each arc $\Delta t_{\alpha\beta}$

$$L^{\Delta t_{\alpha\beta}} = \sqrt{(\frac{\Delta t_{\alpha\beta}}{\delta t})^2 + (\frac{\Delta b_{\alpha\beta,\perp}}{\delta b_\perp})^2} \tag{2.23}$$

with the normalization factors $\delta t = 1500\,\text{days}$ and $\delta b_\perp = 300\,\text{m}$ (Pepe and Lanari, 2006). Along each arc the interferograms are generated whereas all arcs with too large baselines are removed. Starting from this reduced Delaunay triangulation an averaged coherence value is calculated and maximized by a simulated annealing algorithm. This searching procedure mutates the current triangulation by performing a so called edge flip operation (Aichholzer et al., 2003). Therefore, one inner arc is randomly selected and replaced with the other diagonal of the quadrilateral around this arc. If the averaged coherence of this new triangulation is larger it is accepted and a new mutation is done until an abort criterion is achieved. However, if the averaged coherence of the new triangulation is lower, it is not directly rejected. It is accepted with a defined acceptance probability. This guarantees that the algorithm does not immediately end at a local optimum. The acceptance probability decreases with the iterations and finally reaches zero meaning that a worse state is not accepted anymore. Simulated annealing will also be used in Section 6.1 where it will be described in more detail. The identified optimum set of multitemporally filtered interferograms is used as input for the SBAS workflow which is described in the next section.

2.3.2.2 SBAS Workflow

The SBAS workflow is shown in Fig. 2.9 and the following derivations are based on Berardino et al. (2002). Starting point is the multitemporal D-InSAR stack of multilooked and multitemporally filtered SBAS interferograms. Due to the sinusoidal nature of the signal the differential interferometric phase is ambiguous. These phase ambiguities are solved in the context of phase unwrapping which represents the main focus of this work and will be addressed in Chapters 4 and following in more detail. After the phase unwrapping, the unwrapped phases are used to estimate the deformation and the topographic error for each pixel. Removing the deformation and the topographic error, applying a further phase unwrapping step and adding the deformation back leads to the modified unwrapped and corrected phases. An inversion step offers the single epoch phases for one epoch.

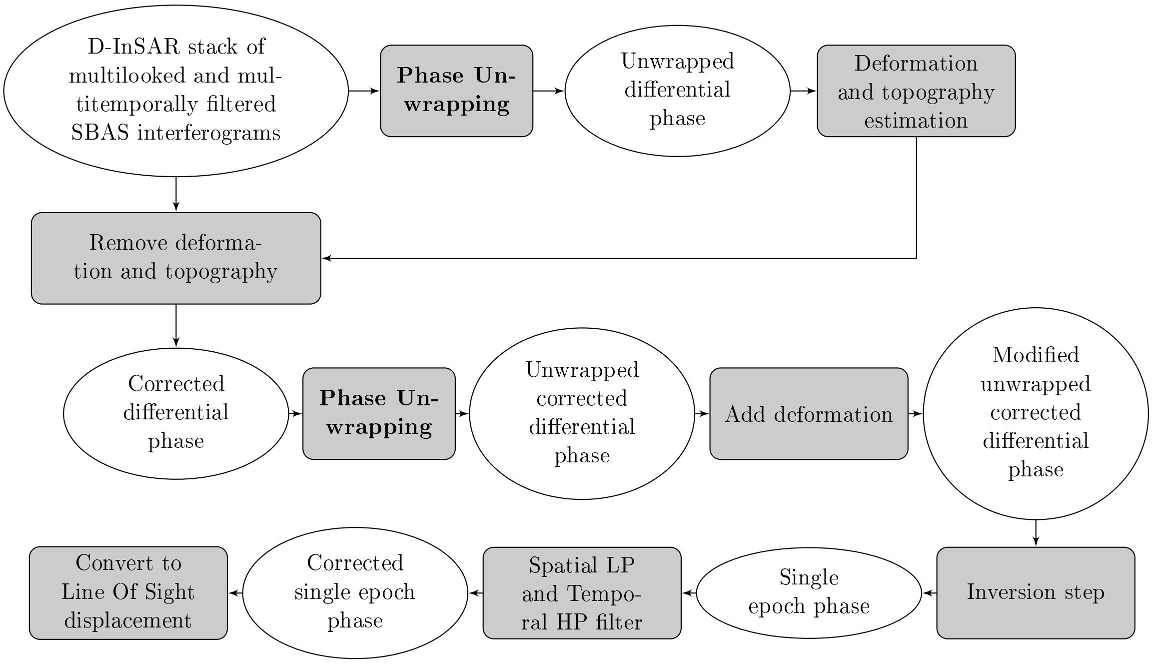

Figure 2.9: SBAS Workflow according to Berardino et al. (2002) starting from multitemporally filtered SBAS interferograms, cf. Pepe et al. (2015).

Beside the deformation, these phases include variations caused by the atmosphere. A spatial and temporal filter allows the separation of these two effects leading to the deformation time series in slant range direction. The individual steps are shortly described in the following.

Deformation and Topography Estimation

The unwrapped differential phase is temporally low-pass filtered by estimating a mean deformation and a topographic error for each pixel over the entire stack. If, for example, the pixel x_j in the entire D-InSAR stack is considered

$$\boldsymbol{\phi}_{x_j}^{\Delta \boldsymbol{t}} = \left[\phi_{x_j}^{\Delta t_1} \quad \dots \quad \phi_{x_j}^{\Delta t'_n}\right]^T, \tag{2.24}$$

the functional model results in

$$\boldsymbol{\phi}_{x_j}^{\Delta \boldsymbol{t}} = \frac{4\pi}{\lambda}\Delta\boldsymbol{t} \cdot v_{x_j} + \frac{4\pi}{\lambda}\frac{\Delta\boldsymbol{b}_\perp}{r\sin\theta} \cdot \Delta h_{x_j} \tag{2.25}$$

with the temporal and orthogonal spatial baselines $\Delta\boldsymbol{t}$ and $\Delta\boldsymbol{b}_\perp$, the unknown mean velocity v_{x_j} and the unknown topographic error Δh_{x_j}. Considering more than two D-InSAR images, the parameters $\tilde{v}_{x_j}$ and $\Delta\tilde{h}_{x_j}$ can be estimated by using the least squares adjustment. The observations are assumed to be equal weighted and uncorrelated. The estimated phase components for the deformation and the topographic error are given by

$$\tilde{\boldsymbol{\phi}}_{x_j,\text{defo}}^{\Delta \boldsymbol{t}} = \frac{4\pi}{\lambda}\Delta\boldsymbol{t} \cdot \tilde{\boldsymbol{v}}_{x_i}^{\Delta \boldsymbol{t}} \tag{2.26}$$

$$\tilde{\boldsymbol{\phi}}_{x_j,\text{topo}}^{\Delta \boldsymbol{t}} = \frac{4\pi}{\lambda}\frac{\Delta\boldsymbol{b}_\perp}{r\sin\theta}\Delta\tilde{h}_{x_j} \tag{2.27}$$

and respectively, the complete estimated differential interferometric phase results in

$$\tilde{\boldsymbol{\phi}}_{x_j}^{\Delta \boldsymbol{t}} = \tilde{\boldsymbol{\phi}}_{x_j,\text{defo}}^{\Delta \boldsymbol{t}} + \tilde{\boldsymbol{\phi}}_{x_j,\text{topo}}^{\Delta \boldsymbol{t}}. \tag{2.28}$$

Modified Unwrapped Corrected Differential Phase

After the initial deformation and topography estimation, the complete estimated phase $\widetilde{\boldsymbol{\phi}}^{\Delta \boldsymbol{t}}_{x_j}$ is subtracted from the observed wrapped phase $\boldsymbol{\psi}^{\Delta \boldsymbol{t}}_{x_j}$ modulo 2π resulting in the corrected differential phase

$$\boldsymbol{\psi}^{\Delta \boldsymbol{t}}_{x_j,\mathrm{corr}} = \langle \boldsymbol{\psi}^{\Delta \boldsymbol{t}}_{x_j} - (\widetilde{\boldsymbol{\phi}}^{\Delta \boldsymbol{t}}_{x_j,\mathrm{defo}} + \widetilde{\boldsymbol{\phi}}^{\Delta \boldsymbol{t}}_{x_j,\mathrm{topo}}) \rangle_{2\pi}. \tag{2.29}$$

This step minimizes the phase ambiguities and makes the phase unwrapping step easier. The corrected differential phase includes possible phase unwrapping errors as well as atmospheric and noise effects. In order to correct supposed phase unwrapping errors, the corrected differential phases are unwrapped again resulting in the unwrapped corrected differential phases $\boldsymbol{\phi}^{\Delta \boldsymbol{t}}_{x_j,\mathrm{corr}}$. These phases are extended by the before subtracted deformation part, leading to the so called modified unwrapped corrected differential phases

$$\boldsymbol{\phi}^{\Delta \boldsymbol{t}}_{x_j,\mathrm{mod}} = \boldsymbol{\phi}^{\Delta \boldsymbol{t}}_{x_j,\mathrm{corr}} + \widetilde{\boldsymbol{\phi}}^{\Delta \boldsymbol{t}}_{x_j,\mathrm{defo}}. \tag{2.30}$$

Inversion Step

The modified unwrapped corrected differential phases $\boldsymbol{\phi}^{\Delta \boldsymbol{t}}_{x_j,\mathrm{mod}}$ are further regarded for each pixel x_j over the entire stack. One phase between the two SAR images at times t_α and t_β at pixel x_j is given by the difference of the two phases of the corresponding SAR images $\phi^{t_\beta}_{x_j,\mathrm{mod}}$ and $\phi^{t_\alpha}_{x_j,\mathrm{mod}}$

$$\phi^{\Delta t_{\alpha\beta}}_{x_j,\mathrm{mod}} = \phi^{t_\beta}_{x_j,\mathrm{mod}} - \phi^{t_\alpha}_{x_j,\mathrm{mod}}. \tag{2.31}$$

The task is to estimate the unknown m' phase values $\boldsymbol{\phi}^{\boldsymbol{t}}_{x_j,\mathrm{mod}}$ with help of the n' modified unwrapped corrected differential phases $\boldsymbol{\phi}^{\Delta \boldsymbol{t}}_{x_j,\mathrm{mod}}$. As the observations are relative values, the system has a rank defect. To overcome this, it is assumed that the phase and thus the deformation at the first time t_1 is zero. With help of the functional model which is already given in (2.31), the system results in

$$\boldsymbol{\phi}^{\Delta \boldsymbol{t}}_{x_j,\mathrm{mod}} = \boldsymbol{A} \boldsymbol{\phi}^{\boldsymbol{t}}_{x_j,\mathrm{mod}} \tag{2.32}$$

with the design matrix $\boldsymbol{A} \in \mathbb{Z}^{n' \times m'-1}$. Each row of $\boldsymbol{A}$ represents one interferogram and is filled with two entries: one and minus one at the respective positions of the corresponding SAR images. Providing $n' > m' - 1$, the system is overdetermined and the solution is given by the least squares adjustment and results in

$$\widetilde{\boldsymbol{\phi}}^{\boldsymbol{t}}_{x_j,\mathrm{mod}} = (\boldsymbol{A}^T \boldsymbol{P} \boldsymbol{A})^{-1} \boldsymbol{A}^T \boldsymbol{P} \boldsymbol{\phi}^{\Delta \boldsymbol{t}}_{x_j,\mathrm{mod}} \tag{2.33}$$

with the weight matrix $\boldsymbol{P}$ which is set to a unit matrix.

Due to the limitations of baseline sizes independent baseline subsets can occur. Figure 2.10 shows such an example. Seven SAR images are used to produce eight differential interferograms resulting in two independent subsets. The design matrix $\boldsymbol{A}$ has a rank defect resulting in a singular matrix $\boldsymbol{A}^T \boldsymbol{A}$. The linear equation system in (2.32) can be solved by using a Singular Value Decomposition (SVD) and the pseudo inverse of $\boldsymbol{A}$. However, this results in large discontinuities in the cumulative deformations which cannot be physically interpreted.

As solution Berardino et al. (2002) replaces the unknown phase values by the mean velocity occurring between neighboring SAR scenes. The mean velocity represents the slope between two following SAR scenes, see Fig. 2.11. This results in the new parameter vector

$$\boldsymbol{v}^{\Delta \boldsymbol{t}}_{x_j} = \begin{bmatrix} v^{\Delta t_1}_{x_j} & \dots & v^{\Delta t_{m'-1}}_{x_j} \end{bmatrix}^T = \begin{bmatrix} \frac{\phi^{t_2}_{x_j,\mathrm{mod}}}{t_2 - t_1} & \dots & \frac{\phi^{t_{m'}}_{x_j,\mathrm{mod}} - \phi^{t_{m'-1}}_{x_j,\mathrm{mod}}}{t_{m'} - t_{m'-1}} \end{bmatrix}^T. \tag{2.34}$$

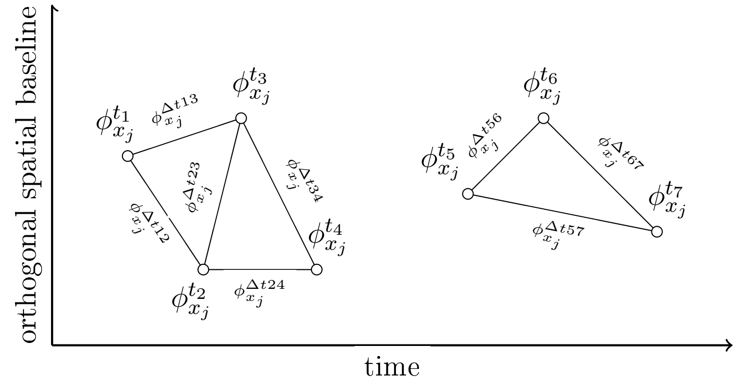

Figure 2.10: Temporal/ orthogonal spatial baseline network with subsets. In order to reduce decorrelation effects, large baselines are avoided after the SBAS method. This may lead to independent subsets.

Considering the differential interferometric phase $\phi_{x_j,\mathrm{mod}}^{\Delta t_{13}}$, the functional model is given by

$$\phi_{x_j,\mathrm{mod}}^{\Delta t_{13}} = (t_2 - t_1) \cdot v_{x_j}^{\Delta t_{12}} + (t_3 - t_2) \cdot v_{x_j}^{\Delta t_{23}} \tag{2.35}$$

or to be general, the differential interferometric phase $\phi_{x_j,\mathrm{mod}}^{\Delta t_{\alpha\beta}}$ is represented by

$$\phi_{x_j,\mathrm{mod}}^{\Delta t_{\alpha\beta}} = \sum_{i=\alpha}^{\beta} (t_{i+1} - t_i) v_{x_j}^{\Delta t_i}. \tag{2.36}$$

With the design matrix $\boldsymbol{A'} \in \mathbb{Z}^{n' \times m'-1}$ the functional model can be formulated as

$$\boldsymbol{\phi}_{x_j,\mathrm{mod}}^{\boldsymbol{\Delta t}} = \boldsymbol{A'} \boldsymbol{v}_{x_j}^{\boldsymbol{\Delta t}}. \tag{2.37}$$

To link independent subsets, the system can also be solved by using the SVD and the pseudo inverse of $\boldsymbol{A'}$ in this case. The individual phases $\boldsymbol{\phi}_{x_j,\mathrm{mod}}^{\boldsymbol{t}}$ result from an additional integration of the estimated velocities $\boldsymbol{v}_{x_j}^{\boldsymbol{\Delta t}}$.

Estimation of the Atmosphere

Beside the deformation, the single phases $\boldsymbol{\phi}_{x_j,\mathrm{mod}}^{\boldsymbol{t}}$ include an atmospheric effect. The atmosphere is considered to be uncorrelated in time and therefore temporally very highly frequented. In contrast, it correlates in space and is therefore spatially low frequented. Using a spatial low-pass and a temporal high-pass filter, the atmosphere can be separated from the deformation. Therefore, the single phases are averaged over a defined window, for example 25 pixels, in space in order to reduce the noise. The averaged signal $\boldsymbol{\phi}_{x_j,\mathrm{LP}}^{\boldsymbol{t}}$ is then averaged individually in time for each pixel. In time the window can be set to 300 days for example. The spatial low-pass and temporal high-pass filtered signal represents the noise and atmospheric corrected signal and therefore consists of a deformation signal only.

Estimation of the cumulative deformation time series

Using the spatial low-pass and temporal high-pass filtered signal $\phi_{\boldsymbol{x}}^{\boldsymbol{t}}$, the cumulative deformation in LOS can be estimated for each pixel x_j and each time t_α according to

$$d_{x_j}^{t_\alpha} = \frac{\lambda}{4\pi} \phi_{x_j}^{t_\alpha} \tag{2.38}$$

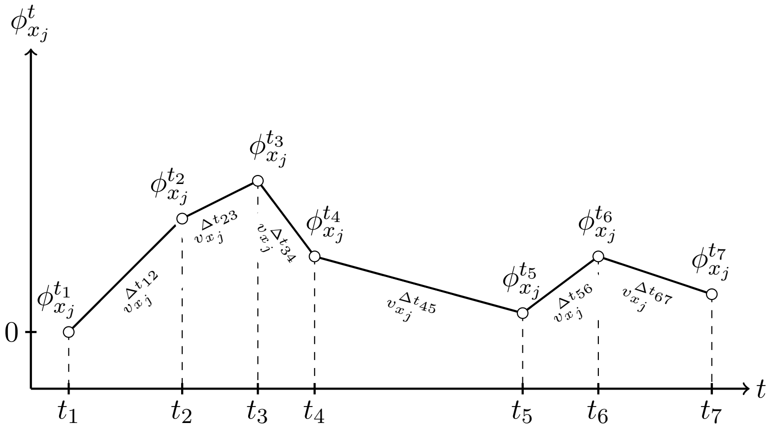

Figure 2.11: Replacing the unknown phase values $\boldsymbol{\phi}_{x_j}^{\boldsymbol{t}}$ with the mean velocity $\boldsymbol{v}_{x_j}^{\Delta \boldsymbol{t}}$ between neighboring SAR scenes. Figure based on Berardino et al. (2002).

with respect to time t_1 where the deformation is set to zero. This time series can be used to estimate a trend where the slope represents the mean deformation velocity at the corresponding pixel x_j.

However, it has to be considered that the deformation refers to LOS direction. In reality the movement takes place in the three dimensional space. Based on a one dimensional measurement, it is impossible to derive the entire three dimensional ground motion. Radar satellites have either an almost north-south direction for descending orbits or an almost south-north direction for ascending orbits. Combining ascending and descending orbits, as it is possible with the recently available Sentinel-1A/B[5] data free of charge, a division into a vertical elevation and an east-west movement component can be made, see Yin and Busch (2018). The north-south component must be neglected due to the poor intersection condition of the ascending and descending orbits. If there is only one data set, ascending or descending, the LOS motion can be converted into a height change with the help of the angle of incidence

$$\Delta H_{x_j}^{t_\alpha} = \frac{d_{x_j}^{t_\alpha}}{\cos(\theta^{t_\alpha})}. \tag{2.39}$$

However, this is based on the assumption that no horizontal movement takes place.

---

[5] `https://directory.eoportal.org/web/eoportal/satellite-missions/content/-/article/sentinel1` last accessed on August 4, 2020

3. Linear Programming

A rather popular phase unwrapping operation to solve the phase ambiguity factors $\boldsymbol{k}_{\boldsymbol{x}}^{\Delta t_{\alpha\beta}}$ of the interferometric phases between the two SAR images t_α and t_β is the Minimum Cost Flow (MCF) algorithm (Costantini, 1997). It is the current state of the art in the SBAS analysis for spatial phase unwrapping and will also be the main focus of this work. The phase unwrapping task is defined as a weighted L_1-norm minimization problem where the unknown parameters are the integer values $\boldsymbol{k}_{\boldsymbol{x}}^{\Delta t_{\alpha\beta}}$. Thus, the problem is defined as an Integer Linear Program (ILP). However, due to its special characteristic, the problem can be solved as a Linear Program (LP) without considering the integer constraints. Before the phase unwrapping problem is solved in detail, the general solution of an LP is discussed. In this context, an overview of the interaction between primal and dual problems is given. Moreover, LP solvers (Dantzig, 1963, Karmarkar, 1984) are summarized and the solution with network flow algorithms (Fulkerson, 1961, Bertsekas and Tseng, 1988) is explained. Detailed information about LP and ILP can be found in Schrijver (1986) or Vanderbei (2001), for example.

3.1 Primal/ Dual Form

In a general LP a linear objective function has to be minimized subject to a set of linear $\geq$- inequalities with respect to the variables $\boldsymbol{x}$ which should not be negative. Any LP can be transformed into this standard form. Maximizing problems or $\leq$- inequalities are multiplied by minus one and every equality can be represented by two inequalities. An LP in standard form is written as

$$\boxed{\begin{array}{rl} \text{Objective function:} & \boldsymbol{c}^T\boldsymbol{x}\ldots\min \\ \text{Constraint:} & \boldsymbol{B}^T\boldsymbol{x} \geq \boldsymbol{b} \\ \text{Variable:} & \boldsymbol{x} \in \mathbb{R}_{\geq 0} \end{array}} \tag{3.1}$$

with the target function vector $\boldsymbol{c} \in \mathbb{R}^n$, the parameter vector $\boldsymbol{x} \in \mathbb{R}^n$ which should be non-negative, the constraint matrix $\boldsymbol{B}^T \in \mathbb{R}^{r\times n}$ and the right-hand side vector $\boldsymbol{b} \in \mathbb{R}^r$. Figure 3.1 shows a two dimensional example of an LP subject to three linear inequality constraints. Geometrically, the linear inequalities define a convex polytope over which the objective function should be minimized. The optimal solution always lays on one of the corner points of the polytope or, if the solution is ambiguous, on an arc. In this case the optimal solution is in the bottom left corner.

The initial form of an LP is always named as primal program. Associated with the primal problem is another LP, the dual one (Dantzig, 1963, p. 123). Therefore, the example in Fig. 3.1 is considered once again. A valid solution for the primal problem can be $x_1 = 5$ and $x_2 = 2$ with an objective function value of $\Phi(\boldsymbol{x}) = 7$. However, obviously the first two constraints indicate a maximum lower bound so that $x_1 = 3$ and $x_2 = 2$ with an objective function value of $\Phi(\boldsymbol{x}) = 5$ seems to be the optimal solution. This is exactly the idea of the dual problem. It should represent a maximum lower bound, see Fig. 3.2 for clarification. This maximum lower bound is obtained by a linear combination of the primal constraints by multiplying them from both sides with the vector $\boldsymbol{y}^T$

$$\boldsymbol{y}^T\boldsymbol{B}^T\boldsymbol{x} \geq \boldsymbol{y}^T\boldsymbol{b}. \tag{3.2}$$

For the example shown in Fig. 3.1 this results in $y_1 = 1$, $y_2 = 2$ and $y_3 = 0$. Since a maximum lower bound for the primal minimization problem is required, it follows:

$$\min\ldots\Phi(\boldsymbol{x}) = \boldsymbol{c}^T\boldsymbol{x} \geq \boldsymbol{y}^T\boldsymbol{B}^T\boldsymbol{x} \geq \boldsymbol{y}^T\boldsymbol{b} = \Phi(\boldsymbol{y})\ldots\max. \tag{3.3}$$

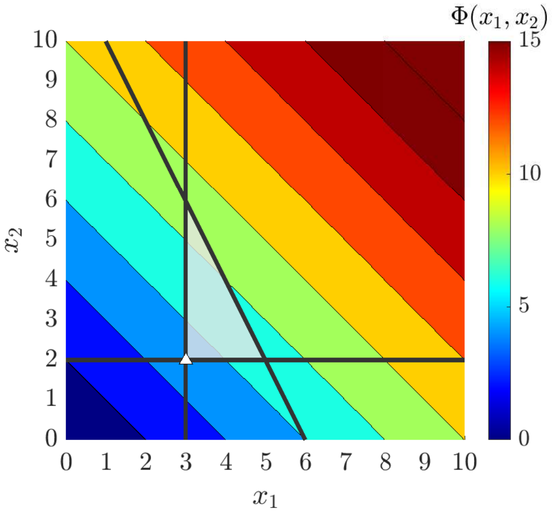

primal:

$$\begin{aligned}\text{Objective function:}\quad & \Phi(\boldsymbol{x}) = x_1 + x_2 \ldots \min\\ \text{Constraint:}\quad & x_1 \geq 3\\ & x_2 \geq 2\\ & -2x_1 - x_2 \geq -12\\ \text{Variable:}\quad & \boldsymbol{x} \in \mathbb{R}_{\geq 0}\\ \text{LP}_{\text{opt}}:\quad & x_1 = 3, \quad x_2 = 2\end{aligned}$$

dual:

$$\begin{aligned}\text{Objective function:}\quad & \Phi(\boldsymbol{y}) = 3y_1 + 2y_2 - 12y_3 \ldots \max\\ \text{Constraint:}\quad & y_1 - 2y_3 \leq 1\\ & y_2 - y_3 \leq 1\\ \text{Variable:}\quad & \boldsymbol{y} \in \mathbb{R}_{\geq 0}\\ \text{LP}_{\text{opt}}:\quad & y_1 = 1, \quad y_2 = 1, \quad y_3 = 0\end{aligned}$$

Figure 3.1: Two dimensional example for an LP. The linear inequality constraints define a feasible region represented as gray filled polygon. The white triangle minimizes the objective function. The problem is defined in its primal and its dual form.

The vector $\boldsymbol{y}$ consists of the dual variables. The number of dual variables is equal to the number of primal constraints. The conversion between primal and dual LPs can also be derived from the Tucker diagram in Table A.1 in the Appendix A. Accordingly, the following dual problem results for the primal problem described in (3.1)

$$\boxed{\begin{aligned}\text{Objective function:}\quad & \Phi(\boldsymbol{y}) = \boldsymbol{y}^T\boldsymbol{b} \ldots \max\\ \text{Constraint:}\quad & \boldsymbol{B}\boldsymbol{y} \leq \boldsymbol{c}\\ \text{Variable:}\quad & \boldsymbol{y} \in \mathbb{R}_{\geq \boldsymbol{0}}.\end{aligned}} \tag{3.4}$$

The dual LP is again a linear optimization program and taking the dual of the dual LP returns to the primal LP with the variables $\boldsymbol{x}$, again. As the dual LP gives a maximal lower bound for the primal LP, the objective value $\Phi(\boldsymbol{x})$ of the primal LP is always greater than or equal to the solution of the dual LP $\Phi(\boldsymbol{y})$. This results in the relationship

$$\Phi(\boldsymbol{x}) \geq \Phi(\boldsymbol{y}) \tag{3.5}$$

which is also known as weak duality (Vanderbei, 2001, pp. 55ff). The sentence of strong duality (Vanderbei, 2001, pp. 57ff) intensifies this relationship. Strong duality means that for both, the primal and the dual LP, the optimal solutions have the same objective values:

$$\Phi(\boldsymbol{x}) = \Phi(\boldsymbol{y}). \tag{3.6}$$

With (3.3) follows

$$\boldsymbol{c}^T\boldsymbol{x} = \boldsymbol{y}^T\boldsymbol{B}^T\boldsymbol{x} = \boldsymbol{y}^T\boldsymbol{b} \tag{3.7}$$

and consequently

$$\boldsymbol{c}^T\boldsymbol{x} = \boldsymbol{y}^T\boldsymbol{B}^T\boldsymbol{x} \quad \Leftrightarrow (\boldsymbol{c}^T - \boldsymbol{y}^T\boldsymbol{B}^T)\boldsymbol{x} = \boldsymbol{0} \tag{3.8}$$

$$\boldsymbol{y}^T\boldsymbol{B}^T\boldsymbol{x} = \boldsymbol{y}^T\boldsymbol{b} \quad \Leftrightarrow \boldsymbol{y}^T(\boldsymbol{B}^T\boldsymbol{x} - \boldsymbol{b}) = \boldsymbol{0}. \tag{3.9}$$

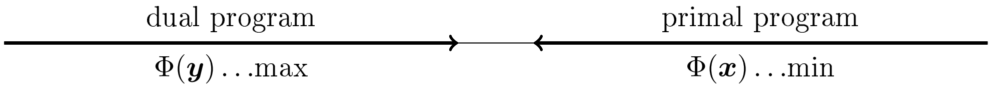

Figure 3.2: Relationship between primal and dual LP. The primal objective function $\Phi(\boldsymbol{x})$ should be minimized and the dual one $\Phi(\boldsymbol{y})$ maximized. The dual program is a maximum lower bound for the primal one. The dual objective function value is therefore less than or equal to the primal objective function value. Figure based on Vanderbei (2001, p. 56).

Defining so called primal slacks $\boldsymbol{s}_x$ and dual slacks $\boldsymbol{s}_y$, so that

$$\boldsymbol{B}^T\boldsymbol{x} - \boldsymbol{s}_x = \boldsymbol{b} \tag{3.10}$$

$$\boldsymbol{B}\boldsymbol{y} + \boldsymbol{s}_y = \boldsymbol{c} \tag{3.11}$$

holds, the optimality constraints can be formulated as

$$\boldsymbol{B}^T\boldsymbol{x} - \boldsymbol{s}_x = \boldsymbol{b} \tag{3.12}$$

$$\boldsymbol{B}\boldsymbol{y} + \boldsymbol{s}_y = \boldsymbol{c} \tag{3.13}$$

$$x_j s_{y_j} = 0 \quad \forall j \in n \tag{3.14}$$

$$y_j s_{x_j} = 0 \quad \forall j \in n \tag{3.15}$$

$$\boldsymbol{x}, \boldsymbol{y}, \boldsymbol{s}_x, \boldsymbol{s}_y \geq \boldsymbol{0} \tag{3.16}$$

with the so called complementary slackness condition defined in (3.14) and (3.15).

3.2 Solving Linear Programs

There are two main classes of LP solvers, the simplex method and the interior point method. Both classes exploit the primal and dual form of the program and its relationship to verify the optimality of a solution. Their main features are described in the following. For further information on this matter Vanderbei (2001) or Vanderbei (2001) can be consulted.

3.2.1 Simplex Method

The simplex method was one of the first algorithm used for the solution of an LP and was introduced by Dantzig (1963). The approach uses a simplex tableau to perform row operations on the LP model as well as to check a solution for optimality. As a reminder, the optimal solution always lays on a corner point of the polytope or on an arc if the solution is ambiguous. The simplex method takes advantage of this fact and starts at one feasible corner, not necessary the optimal one. This is done by choosing r basic variables with a feasible solution unequal to zero and consequently $n - r$ nonbasic variables equal to zero, provided that the matrix $\boldsymbol{B}^T \in \mathbb{R}^{r \times n}$ has a rank of r. In a next step, the optimal solution is found by base changes. Geometrically, the approach iteratively moves from corner to corner and tests for the optimal solution. The solution is optimal when the objective function cannot be reduced further by a basis substitution.

The standard simplex method always starts with a program in canonical form, specifying a unique representation for the r basic variables with a feasible primal solution. In practice, it is often difficult to find a starting feasible canonical form. One possibility is the two phase simplex method or alternatively the dual simplex algorithm (Lemke, 1954). There also exist primal-dual simplex methods which simultaneous try to get a primal feasible solution while optimizing the dual program. However, these methods have limited success for general LPs (Curet, 1993).

Although it is established that the primal or dual simplex method is very efficient and works in linear time for the most cases, there exists a number of LPs for which the algorithm runs in exponential time. This motivates the development of the polynomial-time interior point method described in the following.

3.2.2 Interior Point Method

The interior point method, also referred to as barrier method, follows a different approach. The algorithm moves across the interior of the feasible region and not along the boundary like the simplex method. The first interior point method was invented by Karmarkar (1984), known as ellipsoid algorithm. Many variations have been proposed afterwards, including the primal-dual interior point method which is known as the most common. Under the assumption that the primal and the dual LP are bounded and feasible, a solution is optimal if it fulfills the optimality constraints defined in (3.12) to (3.16). The optimal solution is found in an iterative way by temporarily ignoring the non-negative constraints and relaxing the complementary slackness conditions with a tolerance. This tolerance gets smaller after each iteration. So the method starts with a non-negative solution and iteratively generates a new point in an update step where the search direction is obtained by solving (3.12), (3.13) and the relaxed complementary slackness conditions with help of Newton's method (Nocedal and Wright, 2006, p. 51).

The interior point method is a competitive alternative to the simplex method, especially for LPs with a high number of parameters and constraints (Gondzio, 2012). However, the performance depends on the specific LP. So it is often a good idea to try both methods and then decide which works best for the given problem.

3.3 Solving Integer Linear Programs

An Integer Linear Program (ILP) has the same structure as an LP with the additional condition that the variables must take integer values. An ILP in standard form is written as

$$\boxed{\begin{array}{rl} \text{Objective function:} & \boldsymbol{c}^T\boldsymbol{x}\ldots\min \\ \text{Constraint:} & \boldsymbol{B}^T\boldsymbol{x} \geq \boldsymbol{b} \\ \text{Variable:} & \boldsymbol{x} \in \mathbb{Z}_{\geq 0} \end{array}} \tag{3.17}$$

with the target function vector $\boldsymbol{c} \in \mathbb{R}^n$, the parameter vector $\boldsymbol{x} \in \mathbb{Z}^n$ which should be non-negative and take on integer values, the constraint matrix $\boldsymbol{B}^T \in \mathbb{R}^{r \times n}$ and the right-hand side vector $\boldsymbol{b} \in \mathbb{R}^r$. If only some of the variables are constrained to be integers, the problem is known as a Mixed Integer Linear Program (MILP).

The computational complexity of ILPs is much higher than for LPs. In general, solving ILPs is NP-hard (Schrijver, 1986, p. 20). Figure 3.3 shows a two dimensional example of an ILP subject

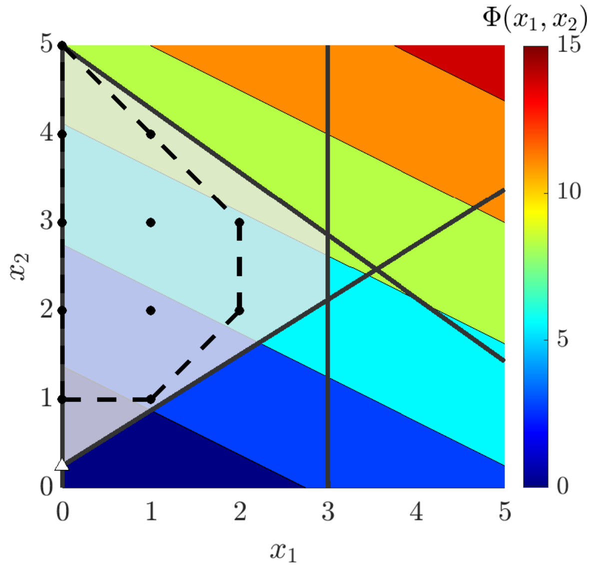

Objective function: $\Phi(\boldsymbol{x}) = x_1 + 2x_2 \ldots \min$
Constraint: $-x_1 \geq -3$
$-5x_1 - 7x_2 \geq -35$
$-5x_1 + 8x_2 \geq 2$
Variable: $x_1, x_2 \in \mathbb{Z}_{\geq 0}$

$\mathrm{LP_{opt}}$: $x_1 = 0, \quad x_2 = 0.25$
$\mathrm{ILP_{opt}}$: $x_1 = 0 \quad , \quad x_2 = 1$

Figure 3.3: Two dimensional example for an ILP. The linear inequality constraints define a feasible region represented as gray filled polygon. Without integer constraints the white triangle minimizes the objective function, also known as the solution of the LP relaxation. However, the feasible integer points are shown in black with their convex hull represented as dashed line. This is the smallest feasible region that contains these points. The point with the smallest objective function value is thus at $x_1 = 0$ and $x_2 = 1$. So the solution of ILP cannot be achieved by simply rounding the solution of the LP.

to three linear inequality constraints. Due to the additional condition that the variables should be integers, the feasible region is restricted to a discrete set of points. A naive way to solve the problem is to simply disregard the integer constraints and solve the so called LP relaxation problem and then round the solution to the next integer values. For the example in Fig. 3.3 this leads to the solution $x_1 = 0$ and $x_2 = 0$. This solution provides an optimal solution with regard to minimizing the objective function, however, one constraint is violated.

3.3.1 Total Unimodularity and Totally Dual Integrality

Solving ILPs is not an easy task. Fortunately, there are LPs whose solutions are automatically integers, see for example the LP given in Fig. 3.1. Even without the integer constraints, the parameters are integers. One sufficient condition is the total unimodularity of the constraint matrix $\boldsymbol{B}^T \in \mathbb{Z}^{r \times n}$ and additionally the vectors $\boldsymbol{c} \in \mathbb{Z}^n$ and $\boldsymbol{b} \in \mathbb{Z}^r$ must have all integer entries. A matrix is totally unimodular if every square submatrix has a determinant of zero, plus or minus one. Since the smallest square submatrix is the entry itself, this implies that the matrix itself may only have ones, minus ones or zeros as entries. Given these conditions, the solutions of the LP will be integers (Schrijver, 1986, p. 266). Besides total unimodularity, there is another category of LPs whose solutions are integers, the so called totally dual integrality systems. A linear system with rational constraint matrix $\boldsymbol{B}^T \in \mathbb{R}^{r \times n}$ and rational right-hand vector $\boldsymbol{b} \in \mathbb{R}^r$ is totally dual integral if for each integer cost vector $\boldsymbol{c} \in \mathbb{Z}^n$ an optimal dual integer solution exists. If the system is totally dual integral and the right-hand side vector $\boldsymbol{b} \in \mathbb{Z}^r$ consists of integer values, then the corner points of the matching polytope which describe the convex hull of the perfect matches are automatically integers and therefore the primal solution is also an integer value (Edmonds and Giles, 1977).

3.3.2 Integer Linear Programming Solver

When the total unimodularity or the totally dual integrality is not given and the solution needs to be an integer value, an ILP solver is necessary. If only some of the parameters are constrained to be integers an MILP solver is required. The optimal solution may not be achieved at a corner point of the polytope. It is found at one corner of the convex hull of all feasible points. In the following, no distinction is made between ILP and MILP solver, as an MILP solver can be used if some or even all of the variables are constrained to be integers.

One class of solvers is the cutting plane method. It starts with the solution of the LP relaxation and iteratively adds some linear constraints, known as cutting planes, to drive the solution or a part of the solution towards integer values without eliminating any feasible integer solution. Therefore, the cutting plane should be placed between the solution of the LP relaxation and the convex hull of the feasible points. Gomory's cutting plane method (Gomory, 1958) was the first MILP solver and until today all cutting plane methods are based on this method.

Another class of algorithms is the branch and bound method, first proposed by Land and Doig (1960). It also starts with the solution of the LP relaxation. Then some variable, say x_j, is picked that is restricted to be integer and its value in the LP relaxation is fractional, say 3.2. This variable is branched by producing two new subproblems, one with the additional restriction that $x_j \leq 3$ and one with the additional restriction $x_j \geq 4$. Afterwards, the same idea is applied to the two subproblems by solving the LP relaxation and if necessary selecting new branching variables. The set of feasible solutions is partitioned into smaller more restricted subsets of the solution resulting in a search tree. The search tree ends when all required variables are integers. Cutting planes can be used to speed up the process of finding the optimal solution. This combination is known as branch and cut algorithm.

3.4 Network Flow Problems

Many LPs can be considered as network flow problems. A special type of a network flow problem is called the Minimum Cost Flow (MCF) problem which will be addressed here. A network or sometimes called a graph $\mathcal{G}$ consists of a set $\mathcal{M}$ with m nodes which are connected by a set $\mathcal{N}$ with n directed arcs. Fig. 3.4 shows an example of a small network. It consists of $m = 4$ nodes and $n = 5$ arcs. Each node j offers an amount b_j of flow, whereas a positive amount is understandable as a supply and a negative amount as a demand. Based on the flow conservation, the sum of the incoming and outcoming flow Π has to satisfy the supply/demand at each node, meaning that

$$\sum_{\{k|(kj)\in\mathcal{N}\}} \Pi_{kj} - \sum_{\{k|(jk)\in\mathcal{N}\}} \Pi_{jk} = b_j \quad \forall j \in \mathcal{M}. \tag{3.18}$$

Moreover, the total sum of all supplies and demands has to be zero

$$\sum_{j\in\mathcal{M}} b_j = 0. \tag{3.19}$$

Each arc (jk) is associated with a cost c_{jk} that arises when the flow Π_{jk} moves from node j to node k. The task is to minimize the total cost

$$\sum_{(jk)\in\mathcal{N}} c_{jk}\Pi_{jk} \ldots \min. \tag{3.20}$$

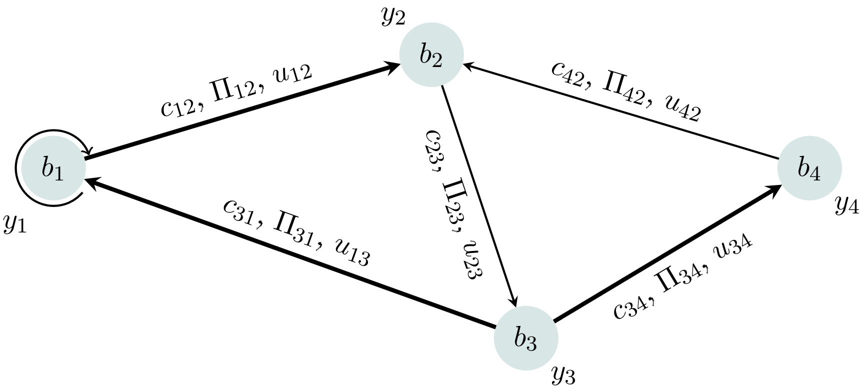

Figure 3.4: Example of a small network flow problem consisting of $m = 4$ nodes and $n = 5$ arcs. Each node j offers an amount b_j which should be satisfied by the incoming and outcoming primal flows $\mathbf{\Pi}$. Each arc (jk) is weighted with a cost value c_{jk} which represents an arc capacity for the dual flow $y_k - y_j$. The thick arcs represent a possible spanning tree.

Moreover, each arc (jk) can have an upper capacity u_{jk} for the flow. Together with the non-negative constraint, the minimum cost flow problem is defined as

$$\boxed{\begin{array}{rl} \text{Objective function:} & \Phi(\mathbf{\Pi}) = \boldsymbol{c}^T\mathbf{\Pi} \ldots \min \\ \text{Flow conservation:} & \boldsymbol{A}^T\mathbf{\Pi} = \boldsymbol{b} \\ \text{Variable:} & \mathbf{0} \leq \mathbf{\Pi} \leq \boldsymbol{u} \end{array}} \tag{3.21}$$

with the constraint matrix $\boldsymbol{A}^T \in \mathbb{Z}^{m \times n}$ also called the node-to-arc incidence matrix of the graph. One row of $\boldsymbol{A}^T$ represents one node with zeros except the columns belonging to the outcoming and incoming arcs. These are filled with ones for the incoming ones and minus ones for the outcoming ones. For the small network in Fig. 3.4 the flow conservation results in

$$\underbrace{\begin{bmatrix} -1 & 1 & 0 & 0 & 0 \\ 1 & 0 & -1 & 1 & 0 \\ 0 & -1 & 1 & 0 & -1 \\ 0 & 0 & 0 & -1 & 1 \end{bmatrix}}_{\boldsymbol{A}^T} \underbrace{\begin{bmatrix} \Pi_{12} \\ \Pi_{31} \\ \Pi_{23} \\ \Pi_{42} \\ \Pi_{34} \end{bmatrix}}_{\mathbf{\Pi}} = \underbrace{\begin{bmatrix} b_1 \\ b_2 \\ b_3 \\ b_4 \end{bmatrix}}_{\boldsymbol{b}} . \tag{3.22}$$

Assuming integer values for the costs, the upper capacity and the supply/demand vector, the values for the flow $\mathbf{\Pi}$ are integers as the matrix $\boldsymbol{A}^T$ fulfills the characteristics of a totally unimodular matrix, cf. Section 3.3.1. The network flow problem defined in (3.21) is called the primal problem. A flow is primal feasible if the conservation in (3.21) is fulfilled and all flows are in the capacity bounds. With the help of the Tucker diagram in Table A.1 in the Appendix A, the associated dual problem can be established which is helpful to verify the optimality of the solution. The dual problem is defined as

$$\boxed{\begin{array}{rl} \text{Objective function:} & \Phi(\boldsymbol{y}, \boldsymbol{z}_u) = \boldsymbol{b}^T\boldsymbol{y} - \boldsymbol{u}\boldsymbol{z}_u \ldots \max \\ \text{Capacity contraint:} & \boldsymbol{A}\boldsymbol{y} - \boldsymbol{z}_u \leq \boldsymbol{c} \\ \text{Variable:} & \boldsymbol{z}_u \geq \mathbf{0} \end{array}} \tag{3.23}$$

with the dual variable $\boldsymbol{y}$ which represents the node potential and $\boldsymbol{z}_u$ which is the bound of the variable. The dual problem is a maximal flow network with the arc capacities represented by the costs. The solution is dual feasible if it fulfills the capacity constraints, meaning that the difference of the node potentials $y_k - y_j$ along one arc (jk) minus the bound of the variable $z_{u_{jk}}$ is not allowed to exceed the arc capacity c_{jk}. The solution is optimal when the complementary slackness conditions

$$\boldsymbol{A}^T\boldsymbol{\Pi} = \boldsymbol{b} \tag{3.24}$$

$$\boldsymbol{A}\boldsymbol{y} - \boldsymbol{z}_u + \boldsymbol{s}_y = \boldsymbol{c} \tag{3.25}$$

$$\Pi_{jk}s_{y_{jk}} = 0 \quad \forall jk \in n \tag{3.26}$$

$$z_{u_{jk}}(u_{jk} - \Pi_{jk}) = 0 \quad \forall jk \in n \tag{3.27}$$

$$\boldsymbol{\Pi}, \boldsymbol{s}_y, \boldsymbol{z}_u \geq \boldsymbol{0} \tag{3.28}$$

are fulfilled. The dual slack

$$s_{y_{jk}} = c_{jk} - (y_k - y_j - \boldsymbol{z}_{u_{jk}}) \tag{3.29}$$

gives a statement how much capacity is left.

Network flow problems can be solved efficiently due to the specific network form. The simplex algorithm for example always starts with a feasible basic solution with for this case $m-1$ basic variables which are unequal to zero as the matrix $\boldsymbol{A}^T \in \mathbb{Z}^{m\times n}$ has a rank of $m-1$. Assuming that the network is connected, a spanning tree $\mathcal{T}$ is related to a base of the simplex method. A subnetwork is called a spanning tree if it connects every node without containing any cycle. For the small network in Fig. 3.4 the thick arcs are corresponding to a spanning tree. Starting at a root node, the flows can successively be solved for the arcs $(jk) \in \mathcal{T}$ belonging to the spanning tree with help of the flow conservation. All other flows along the arcs $(jk) \notin \mathcal{T}$ are set to zero. Analogously, the dual variables can be solved relating to the spanning tree. The node potential for the root node is set to zero and the $m-1$ other variables can be solved corresponding to the capacity constraints. Along each arc $(jk) \in \mathcal{T}$ corresponding to the spanning tree the dual slack has to be zero so that the difference of the node potentials $y_k - y_j$ has to be maximal and equals the arc capacity.

Depending on whether the solution is primal or dual feasible, the primal or dual network simplex method is used. The basic idea of the primal network simplex method is to pick an arc $(jk) \notin \mathcal{T}$ that is dual infeasible and let it enter the tree. Therefore, the tree has cycles. To reconstruct a new spanning tree, the arc on the cycle with the opposite direction to the entering arc and with the smallest flow has to leave the tree. Contrary, the basic idea of the dual network simplex method is to pick an arc $(jk) \in \mathcal{T}$ that is primal infeasible and let it leave the spanning tree. Therefore, the tree is split into two subtrees. To reconstruct a new spanning tree the arc with the opposite direction than the leaving arc and with the smallest dual slack is entered to the basis.
Well-known network flow algorithms are the out-of-kilter algorithm by Fulkerson (1961) or the relaxation method by Bertsekas and Tseng (1988).

Most network flow algorithms assume non-negative flows. However, in some cases there are non-zero lower capacities $\boldsymbol{l}$ resulting in

$$\boxed{\begin{array}{rl} \text{Objective function:} & \Phi(\boldsymbol{\Pi}) = \boldsymbol{c}^T\boldsymbol{\Pi}\ldots\min \\ \text{Flow conservation:} & \boldsymbol{A}^T\boldsymbol{\Pi} = \boldsymbol{b} \\ \text{Variable:} & \boldsymbol{l} \leq \boldsymbol{\Pi} \leq \boldsymbol{u}. \end{array}} \tag{3.30}$$

For this case, the problem can be transformed to

$$\boxed{\begin{array}{rl} \text{Objective function:} & \Phi(\mathbf{\Pi}') = \boldsymbol{c}^T\mathbf{\Pi}' \ldots \min \\ \text{Flow conservation:} & \boldsymbol{A}^T\mathbf{\Pi}' = \boldsymbol{b} + \boldsymbol{A}^T\boldsymbol{l} \\ \text{Variable:} & \mathbf{0} \leq \mathbf{\Pi}' \leq \boldsymbol{u} + \boldsymbol{l} \end{array}} \tag{3.31}$$

with the non-negative transformed flow $\mathbf{\Pi}'$. Afterwards, the solution of $\mathbf{\Pi}'$ has to be retransformed to the origin flow

$$\mathbf{\Pi} = \mathbf{\Pi}' - \boldsymbol{l}. \tag{3.32}$$

4. Spatial Phase Unwrapping – Review and Evaluation of Methods

The main problem of interferometric data is that the interferometric phase $\psi_{x_j}^{\Delta t_{\alpha\beta}}$ of two SAR images at times t_α and t_β at pixel x_j can only be measured modulo 2π. To derive the information of interest, for instance the deformation, the phase ambiguities have to be solved. This is done in the context of phase unwrapping. According to Pepe and Lanari (2006) this part remains a critical task in the analysis as phase unwrapping errors may lead to misinterpretations in the deformation.

This chapter will address the problem of unwrapping the observed interferometric phase. It starts with an overview of existing phase unwrapping approaches based on one single interferogram. An interferogram provides information in two dimensions represented by the azimuth and range direction. As there are many phase unwrapping algorithms, only the widespread techniques are mentioned here. In this work, the focus is set to the rather popular Minimum Cost Flow (MCF) approach, which is the state of the art in the SBAS analysis. The problem is formulated as a weighted L_1-norm problem. In this work, the multitemporal D-InSAR processing is done with the Remote Sensing Software Graz (RSG). Currently, RSG solves the weighted L_1-norm problem using a standard LP solver, cf. Section 3.2. Due to its structure the MCF problem can also be solved very efficiently as a network flow problem, cf. Section 3.4. This chapter focuses on different ways of formulating the MCF problem. The basic idea can already be found in the literature, but there is no detailed and precise comparison of the different formulations. This work should help to demonstrate and discuss different ways to solve the phase unwrapping problem. The different approaches are applied to a simulated D-InSAR stack and validated afterwards.

4.1 Problem Formulation

The problem is that the interferometric phase $\psi_{x_j}^{\Delta t_{\alpha\beta}}$ of two SAR images at times t_α and t_β at pixel x_j can only be measured within an interval from $[-\pi, \pi]$. Consequently, if the surface displacement is greater than a quarter of the radar wavelength (equal to 1.42 cm for the ERS satellites) or other effects, like topographic errors, atmosphere or noise occur, the interferogram cannot be uniquely inverted. This ambiguous phase is called the wrapped phase. The absolute, so called unwrapped phase

$$\phi_{x_j}^{\Delta t_{\alpha\beta}} = \psi_{x_j}^{\Delta t_{\alpha\beta}} + 2\pi k_{x_j}^{\Delta t_{\alpha\beta}} \quad \forall\, x_j \in \mathcal{M} \tag{4.1}$$

is obtained by adding an integer multiple $k_{x_j}^{\Delta t_{\alpha\beta}}$ of 2π to the wrapped phase. This has to be done for each pixel of the set $\mathcal{M}$ of pixels in the interferogram. Fig. 4.1a represents an example for a simulated settlement depression for one interferogram. The absolute unwrapped phases exceed the measurable range so that the measured wrapped phases, shown in Figure 4.1b, include the typical phase fringes due to the phase ambiguities. To obtain the absolute unwrapped phases the so called unknown phase ambiguity vector $\boldsymbol{k}_{\boldsymbol{x}}^{\Delta t_{\alpha\beta}} \in \mathbb{Z}$ has to be solved. This is done during the process called phase unwrapping and is a critical task in D-InSAR analysis (Pepe and Lanari, 2006).

Several methods to estimate the unknown phase ambiguity factors exist. Basically all of them start with the measured wrapped D-InSAR phases and consider the unwrapped phase as a continuous

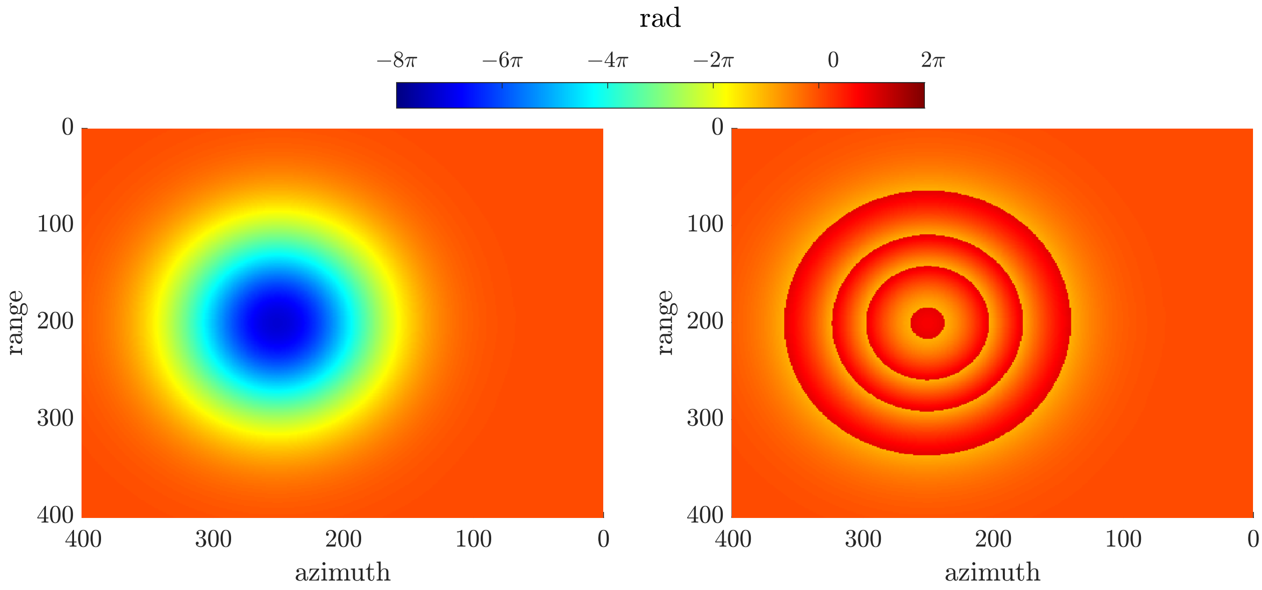

(a) reference phase $\hat{\phi}_x^{\Delta t_{\alpha\beta}}$ **(b)** measured wrapped phase $\psi_x^{\Delta t_{\alpha\beta}}$

Figure 4.1: Simulated ground settlement depression for one interferogram with a temporal baseline of $\Delta t_{\alpha\beta} = 315\,\mathrm{days}$ and an orthogonal spatial baseline of $\Delta b_{\perp,\alpha\beta} = 76.322\,\mathrm{m}$.

curve. Under the assumption that there are no 2π phase jumps between neighboring pixels, the unwrapped phase can be considered as an integral of the phase gradients (Tribolet, 1977). A preliminary estimate of the unwrapped phase gradient between two adjacent pixels x_k and x_l is defined via the numerical differentiation (Costantini, 1998)

$$\psi_{\Delta x_{kl}}^{\Delta t_{\alpha\beta}} = \langle \psi_{x_l}^{\Delta t_{\alpha\beta}} - \psi_{x_k}^{\Delta t_{\alpha\beta}} \rangle_{-\pi,\pi} \quad \forall\, \Delta x_{kl} \in \mathcal{N} \tag{4.2}$$

with the modulo 2π operator $\langle . \rangle_{-\pi,\pi}$ and the set $\mathcal{N}$ of phase gradients in the interferogram. The modulo operator is necessary to transform the gradient in a range from $-\pi$ to π according to the above assumption that the unwrapped phase will not change by as much as half a cycle between adjacent pixels. If the assumption is true, there are no discontinuities and both wrapped and unwrapped gradients do not differ from each other, meaning that

$$\phi_{\Delta x_{kl}}^{\Delta t_{\alpha\beta}} = \psi_{\Delta x_{kl}}^{\Delta t_{\alpha\beta}} \tag{4.3}$$

holds true. The unwrapped phase $\phi_{x_j}^{\Delta t_{\alpha\beta}}$ at pixel x_j can then be easily reconstructed up to an additive constant by integrating the wrapped phase gradients along any set $\mathcal{N}_{x_j}$ of phase gradients that connect a reference point x_0 and the pixel x_j

$$\phi_{x_j}^{\Delta t_{\alpha\beta}} = \sum_{\forall \Delta x_{kl} \in \mathcal{N}_{x_j}} \psi_{\Delta x_{kl}}^{\Delta t_{\alpha\beta}} + \phi_{x_0}^{\Delta t_{\alpha\beta}}. \tag{4.4}$$

The integral is replaced by a sum due to the pixel based representation. The solution is path-independent and does not depend on the set $\mathcal{N}_{x_j}$ of phase gradients.

In reality, assumption (4.3) is not generally true. Phase noise, atmospheric effects, sub-sampling or topographic effects lead to inconsistencies, meaning that the oriented sum of the phase gradients, cf. (4.2), in one loop is unequal zero in some cases. This oriented sum is referred to as residue. The residues are assumed to be located at the centroids of the corresponding loops. Figure 4.2 shows an inconsistency with a corresponding positive residue on a square of four sampled pixels. The task is to correct or to avoid these inconsistencies. To better detect at which arc the inconsistency exactly

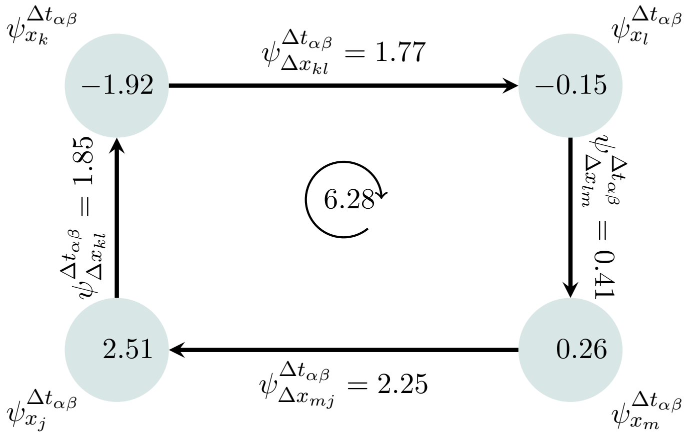

Figure 4.2: Example for one spatial inconsistency. The oriented sum over the spatial wrapped phase gradients is unequal to zero and leads to a positive residue: $\psi_{\Delta x_{kl}}^{\Delta t_{\alpha\beta}} + \psi_{\Delta x_{kl}}^{\Delta t_{\alpha\beta}} + \psi_{\Delta x_{lm}}^{\Delta t_{\alpha\beta}} + \psi_{\Delta x_{mj}}^{\Delta t_{\alpha\beta}} = 6.28$.

occurs, it is also possible to investigate redundant loops. Costantini et al. (2012) has done this and found that the phase unwrapping result is more reliable and accurate. However, this leads to overlapping arcs which can be problematic with specific formulation types of the phase unwrapping problem. The different types of formulations and solutions of the phase unwrapping problem will be presented and discussed later.

4.2 Most Popular Approaches

One of the first phase unwrapping algorithm was introduced by Tribolet (1977). Since then several algorithms have been developed. This section will give an overview of the existing spatial phase unwrapping algorithms.

Spatial phase unwrapping approaches are based on the analysis of one single interferogram. In the following an interferogram between the two SAR images at times t_α and t_β with a set $\mathcal{M}$ of m pixels and accordingly a set $\mathcal{N}$ of n gradients between these pixels is assumed. To unwrap the measured interferometric phases one classifies local and global methods which are described in the next subsections.

4.2.1 Local Methods

Local unwrapping algorithms are also known as path following methods as they find a suitable integration way and unwrap each pixel locally, starting from a reference point. The phase of the reference point is either known a priori or assumed to be zero.

Sequential paths are the simplest paths as they do not use quantities to define a preferred way. One of the first and classic path following algorithm for spatial phase unwrapping is Goldstein's algorithm (Goldstein et al., 1988). So called branch cuts are defined by connecting residues with opposite sign so that the cut is neutralized. The phases can then be unwrapped in a consistent way if the branch cuts are not crossed. The algorithm works well for images with high coherence values. However, areas which are trapped by branch cuts are inaccessible for the algorithm resulting into spatially incomplete and disconnected solutions. If the branch cuts become very dense, the algorithm also fails. Zebker and Lu (1998) illustrate this with help of simulated data.

Beside the sequential way another class of path following methods exists that uses quality maps which show the quality of individual pixels. The quality can be defined by the coherence, the phase difference between neighboring pixels, the signal-to-noise ratio or the spatial frequency of the fringe pattern for example. The integration path is then chosen in such a way that the high quality pixels are unwrapped first. Su and Chen (2004) present a review on reliability guided phase unwrapping algorithms. The success of these algorithms strongly depends on the quality map.

4.2.2 Global Methods

Global methods find a global solution by minimizing a certain measure of misfit between the wrapped data and the unwrapped solution

$$\sum_{\forall \Delta x_{kl} \in \mathcal{N}} g(\phi_{\Delta x_{kl}}^{\Delta t_{\alpha\beta}}, \psi_{\Delta x_{kl}}^{\Delta t_{\alpha\beta}}) \ldots \min \tag{4.5}$$

with a general cost function $g(.)$. The advantage of this global method is that it does not depend on path following approaches.

Ghiglia and Romero (1994) suggest a minimum-norm method, so that the cost function results in

$$g(\phi_{\Delta x_{kl}}^{\Delta t_{\alpha\beta}}, \psi_{\Delta x_{kl}}^{\Delta t_{\alpha\beta}}) = |\phi_{\Delta x_{kl}}^{\Delta t_{\alpha\beta}} - \psi_{\Delta x_{kl}}^{\Delta t_{\alpha\beta}}|^p \tag{4.6}$$

which is known as the L_p-norm. A typical algorithm is the least squares method for the case $p = 2$. The least squares phase unwrapping problem is mathematically identical to the solution of the discrete form of Poisson's Equation which can be efficiently solved by a discrete cosine transform approach (Ghiglia and Romero, 1994). The major difference to the local methods is that any value may be added to the measurements to ensure a continuity in the solution. It has the advantage that the phase can be unwrapped everywhere in the image. However, the solution underestimates the phase gradients as shown in Zebker and Lu (1998). The algorithm tends to distribute unwrapping errors globally instead of isolating the residues to a small set of points. If some points are more reliable than others, weighting strategies may be used. However, the solution of the weighted least squares approach cannot be reduced to the simple Poisson's Equation and requires iterative methods using repeated discrete cosine transforms (Ghiglia and Romero, 1994). The weights can be defined by functions of the signal-to-noise ratio or coherence values. Various methods for selecting weights are described by Pritt (1996).

A second technique to unwrap the phase in a global way is the Minimum Cost Flow (MCF) algorithm. Costantini (1997) developed a branch cut based algorithm to solve the regular sampled spatial phase unwrapping problem. Costantini and Rosen (1999) adapted the algorithm to solve sparse networks by using a Delaunay triangulation of a set of pixels. The MCF approach deals with the assumption that the wrapped phase gradients differ from the unwrapped ones by an unknown multiple of 2π

$$\phi_{\Delta x_{kl}}^{\Delta t_{\alpha\beta}} = \psi_{\Delta x_{kl}}^{\Delta t_{\alpha\beta}} + 2\pi k_{\Delta x_{kl}}^{\Delta t_{\alpha\beta}} \tag{4.7}$$

with the phase ambiguity factor of the phase gradient $k_{\Delta x_{kl}}^{\Delta t_{\alpha\beta}}$.

According to the MCF approach, the phase unwrapping is seen as the weighted L$_1$-norm minimization problem of the deviation between the estimated and unknown phase gradients of the unwrapped phases under the above assumption that both differ by an integer multiple of 2π. This assumption prevents the errors from spreading effects (Costantini, 1997). The cost function can therefore be summarized as

$$g(\phi_{\Delta x_{kl}}^{\Delta t_{\alpha\beta}}, \psi_{\Delta x_{kl}}^{\Delta t_{\alpha\beta}}) = |p_{\Delta x_{kl}}^{\Delta t_{\alpha\beta}} k_{\Delta x_{kl}}^{\Delta t_{\alpha\beta}}| \tag{4.8}$$

with the weights $p_{\Delta x_{kl}}^{\Delta t_{\alpha\beta}}$. Considering the structure, the problem can be transformed into a network searching for the weighted minimum cost flow defined by the unknown phase ambiguity factors. This will be discussed in more detail in the next section.

The weight $p_{\Delta x_{kl}}^{\Delta t_{\alpha\beta}}$ defines the probability of a branch cut (Costantini, 1998). If the weights are constant, the MCF approach minimizes the total length of branch cuts. However, usually the costs are defined by the user or quality maps relating to information extracted from the data (Costantini, 1998). The choice of the weights is an essential quality factor for the phase unwrapping solution (Even and Schulz, 2014). There are different kinds of methods to extract them from coherence values, amplitudes, residue densities or flatness (Costantini, 1998, Eineder et al., 1998). Based on this approach, Chen (2001) extended the problem by generalized statistical cost functions $g(.)$. These generalized costs can be represented as a conditional probability density function of the unwrapped phase gradients depending on the observed wrapped phase, the image intensity and the coherence. Although these individually adapted costs suggest great promise (Chen, 2001), the statistical model must be modified according to the application so that there is no universally valid model for generating the costs. The generalized costs also lead to a non-linear optimization problem which can be seen as a maximum a posteriori probability estimation approach. To get an approximated solution Chen (2001) developed an iterative non-linear network flow solver technique, implemented in the open source software Statistical cost Network flow Algorithm for PHase Unwrapping (SNAPHU) [1].

This work will focus on the weighted L$_1$-norm minimization problem with linear cost functions based on the MCF approach by Costantini and Rosen (1999). The MCF approach is a rather popular spatial phase unwrapping operation and will be described in more detail in the next section.

4.3 Minimum Cost Flow Approach

The Minimum Cost Flow (MCF) algorithm by Costantini and Rosen (1999) only uses so called coherent pixels in the analysis to reduce the noise. These are pixels with a stable backscattering characteristic identified by the coherence values, cf. (2.18). Figure 4.3 shows the coherent pixels for the above mentioned simulated settlement depression. In this case, one pixel is defined as coherent when its coherence value is greater than or equal to 0.7. Based on the set $\mathcal{M}$ with m coherent pixels a Delaunay triangulation in the azimuth/ range plane with the set $\mathcal{N}$ of n spatial arcs and the set $\mathcal{R}$ of r defined triangles is computed. The corresponding triangulation of the simulation is shown in Fig. 4.4.

It is not necessarily required to use a Delaunay triangulation. As investigated in Costantini et al. (2012), redundant loops are also possible. It is only important that loops exist to locate the inconsistencies. The Delaunay Triangulation has the advantage that no arcs overlap and the graph

---

[1] `https://web.stanford.edu/group/radar/softwareandlinks/sw/snaphu/` last accessed on August 4, 2020

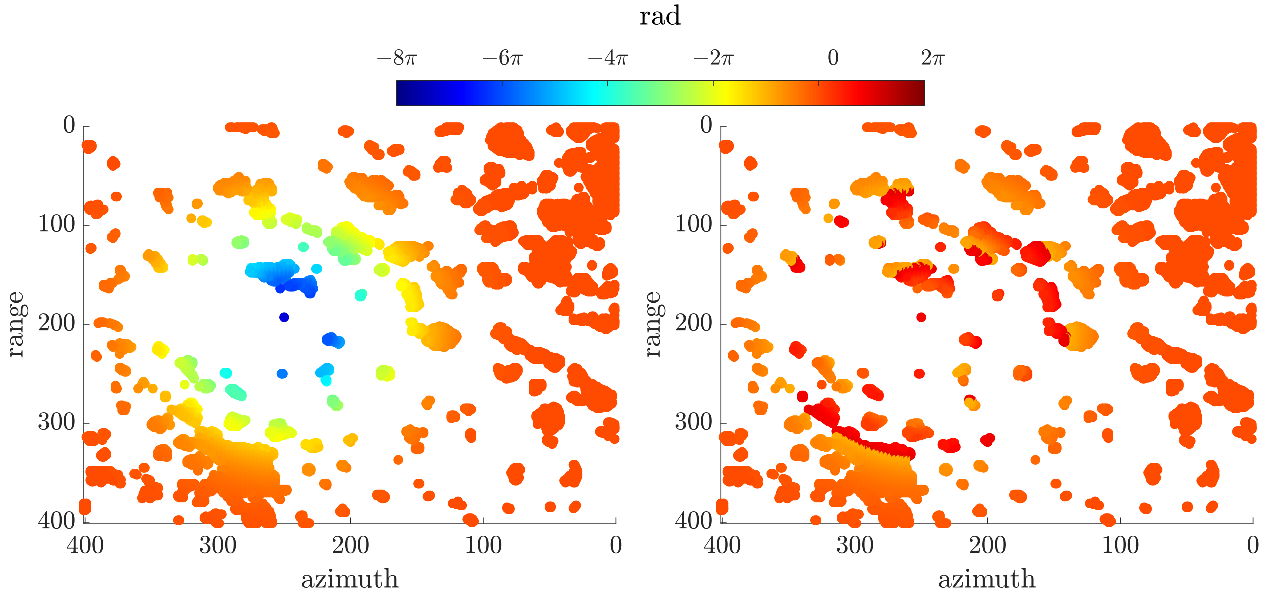

(a) coherent pixels of reference phase $\hat{\phi}_x^{\Delta t_{\alpha\beta}}$ **(b)** coherent pixels of measured wrapped phase $\psi_x^{\Delta t_{\alpha\beta}}$

Figure 4.3: Coherent pixels of simulated settlement depression for one interferogram with a temporal baseline of $\Delta t_{\alpha\beta} = 315$ days and an orthogonal spatial baseline of $\Delta b_{\perp,\alpha\beta} = 76.322$ m. A pixel is defined as coherent if its coherence value is greater than or equal to 0.7.

is therefore plane. This allows a special formulation of the problem which can be solved with very efficient algorithms. Before these different formulations and solutions are discussed in Section 4.3.1, the problem is defined, in the following.

Along each arc the wrapped phase gradient $\psi_{\Delta x_{kl}}^{\Delta t_{\alpha\beta}} \forall \Delta x_{kl} \in \mathcal{N}$ is calculated, cf. (4.2). To ensure that the solution of the minimization problem does not depend on the integration path, following constraint

$$\phi_{\Delta x_{kl}}^{\Delta t_{\alpha\beta}} + \phi_{\Delta x_{kl}}^{\Delta t_{\alpha\beta}} + \phi_{\Delta x_{lj}}^{\Delta t_{\alpha\beta}} = 0 \tag{4.9}$$

in each of the r Delaunay triangles, here referred to the triangle shown in Fig. 4.5, has to be fulfilled. Using the relation expressed in (4.7) this results in the constraint

$$k_{\Delta x_{kl}}^{\Delta t_{\alpha\beta}} + k_{\Delta x_{kl}}^{\Delta t_{\alpha\beta}} + k_{\Delta x_{lj}}^{\Delta t_{\alpha\beta}} = -\lfloor \frac{\psi_{\Delta x_{kl}}^{\Delta t_{\alpha\beta}} + \psi_{\Delta x_{kl}}^{\Delta t_{\alpha\beta}} + \psi_{\Delta x_{lj}}^{\Delta t_{\alpha\beta}}}{2\pi} \rceil \tag{4.10}$$

with the round symbol $\lfloor . \rceil$ to ensure that the estimated phase ambiguity factors are integer numbers. As the phase gradients are consistent in space, the rounding operator is only necessary for numerical issues. The problem is carried out by choosing the weighted L$_1$-norm for the error criterion

$$\sum_{\forall \Delta x_{kl} \in \mathcal{N}} |p_{\Delta x_{kl}}^{\Delta t_{\alpha\beta}} k_{\Delta x_{kl}}^{\Delta t_{\alpha\beta}}| \ldots \text{min}. \tag{4.11}$$

The weights $p_{\Delta x_{kl}}^{\Delta t_{\alpha\beta}}$, the wrapped phase gradients $\psi_{\Delta x_{kl}}^{\Delta t_{\alpha\beta}}$ and the phase ambiguity factors $k_{\Delta x_{kl}}^{\Delta t_{\alpha\beta}}$ for all $\Delta x_{kl} \in \mathcal{N}$ are collected in the vectors $\boldsymbol{p}_{\boldsymbol{\Delta x}}^{\Delta t_{\alpha\beta}}$, $\boldsymbol{\psi}_{\boldsymbol{\Delta x}}^{\Delta t_{\alpha\beta}}$ and $\boldsymbol{k}_{\boldsymbol{\Delta x}}^{\Delta t_{\alpha\beta}}$, respectively. For the representation of the L$_1$-norm the unknown phase ambiguity vector $\boldsymbol{k}_{\boldsymbol{\Delta x}}^{\Delta t_{\alpha\beta}}$ is split into a positive and a negative part

$$\boldsymbol{k}_{\boldsymbol{\Delta x}}^{\Delta t_{\alpha\beta}} = \boldsymbol{k}_{\boldsymbol{\Delta x}}^{\Delta t_{\alpha\beta},+} - \boldsymbol{k}_{\boldsymbol{\Delta x}}^{\Delta t_{\alpha\beta},-} \quad \text{with:} \quad \boldsymbol{k}_{\boldsymbol{\Delta x}}^{\Delta t_{\alpha\beta},+}, \boldsymbol{k}_{\boldsymbol{\Delta x}}^{\Delta t_{\alpha\beta},-} \in \mathbb{Z}_{\geq 0} \tag{4.12}$$

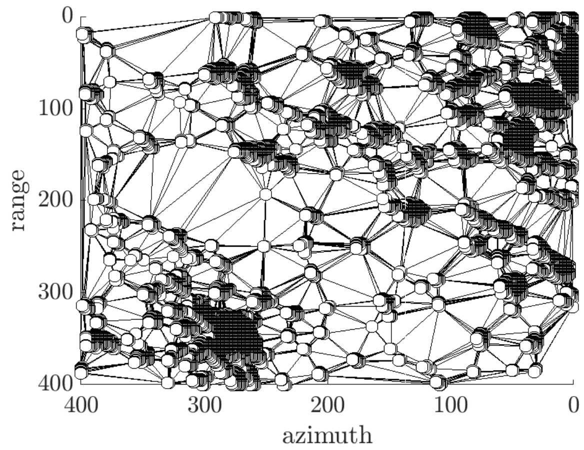

Figure 4.4: Spatial Delaunay triangulation of coherent pixels shown in Fig. 4.3.

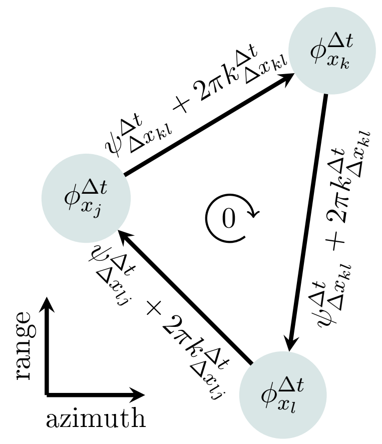

Figure 4.5: Spatial Delaunay triangulation for an example of three pixels. To ensure that the solution is rotation-free, the sum of the unwrapped phase gradients in one triangle has to be zero.

characterized by a superscript plus and a superscript minus. This leads to the constrained weighted MCF L$_1$-norm problem

$$\boxed{\begin{array}{rl} \text{Objective function:} & C(\boldsymbol{k}_{\boldsymbol{\Delta x}}^{\Delta t_{\alpha\beta},+}, \boldsymbol{k}_{\boldsymbol{\Delta x}}^{\Delta t_{\alpha\beta},-}) = \begin{bmatrix} \boldsymbol{p}_{\boldsymbol{\Delta x}}^{\Delta t_{\alpha\beta}T} & \boldsymbol{p}_{\boldsymbol{\Delta x}}^{\Delta t_{\alpha\beta}T} \end{bmatrix} \begin{bmatrix} \boldsymbol{k}_{\boldsymbol{\Delta x}}^{\Delta t_{\alpha\beta},+} \\ \boldsymbol{k}_{\boldsymbol{\Delta x}}^{\Delta t_{\alpha\beta},-} \end{bmatrix} \dots \min \\ \text{Constraint:} & \begin{bmatrix} \boldsymbol{B}_{\text{spatial}}^T & -\boldsymbol{B}_{\text{spatial}}^T \end{bmatrix} \begin{bmatrix} \boldsymbol{k}_{\boldsymbol{\Delta x}}^{\Delta t_{\alpha\beta},+} \\ \boldsymbol{k}_{\boldsymbol{\Delta x}}^{\Delta t_{\alpha\beta},-} \end{bmatrix} = \underbrace{-\left\lfloor \frac{\boldsymbol{B}_{\text{spatial}}^T \boldsymbol{\psi}_{\boldsymbol{\Delta t}}^{\Delta t_{\alpha\beta}}}{2\pi} \right\rceil}_{\boldsymbol{b}_{\text{spatial}}} \\ \text{Variable:} & \boldsymbol{k}_{\boldsymbol{\Delta x}}^{\Delta t_{\alpha\beta},+}, \boldsymbol{k}_{\boldsymbol{\Delta x}}^{\Delta t_{\alpha\beta},-} \in \mathbb{Z}_{\geq 0} \end{array}} \tag{4.13}$$

with the constraint matrix $\boldsymbol{B}_{\text{spatial}}^T \in \mathbb{Z}^{r \times n}$ and the right-hand side vector $\boldsymbol{b}_{\text{spatial}} \in \mathbb{Z}^r$. One row of $\boldsymbol{B}_{\text{spatial}}^T$ contains zeros except the columns which belong to the defining arcs of the actual triangle. These are filled with one or minus one depending on the orientation of the arc.

In general, the solution of an ILP problem is NP-hard (Schrijver, 1986, p. 20). There often are different formulations and solution types of the problem which differ in the number of parameters, the number of constraints and the performance. For this reason, it is useful to analyze the different solution types in some more detail in the next section.

4.3.1 Solving the L$_1$-norm Phase Unwrapping Problem

In this section the principles of linear programming described in Chapter 3 are applied to the phase unwrapping problem. Figure 4.6 shows a small network consisting of $m = 5$ nodes which correspond to the stable pixels where the unwrapped phase values are measured. In the following a Delaunay triangulation is assumed, since a plane graph is necessary in a later formulation of the problem. The Delaunay triangulation of these pixels results in $n = 8$ arcs along which the phase gradients are estimated and $r = 4$ triangles. First, the phase unwrapping problem is solved with help of an LP solver and afterwards as a network flow problem. Therefore, the phase unwrapping problem is seen as a graph, where the graph of the network shown in Fig. 4.6 is called the primal graph.

4.3.1.1 Solution as a Linear Program

The phase unwrapping problem is similar to a leveling network with the unknown phase ambiguity factors equal to the residues. The adjustment problem can be solved by minimizing the weighted L$_1$-norm of the phase ambiguity factors subject to the constraint, that in each triangle the sum of the adjusted observations, here of the unwrapped phase gradients, should be zero. For the network in Fig. 4.6 four constraints are necessary, symbolized by the colored loops. The corresponding constrained weighted L$_1$-norm problem is defined in (4.13). As already said, the solution of the LP relaxation is an integer solution if the target function vector $\boldsymbol{c}^T$ and the right-hand side vector $\boldsymbol{b}$ have only integer entries and if the matrix $\boldsymbol{B}^T$ is totally unimodular. The target function vector $\boldsymbol{c}^T$ has integer entries when choosing integer weights and the right-hand side of the constraints $\boldsymbol{b}_{\text{spatial}}$ consists of integer values due to the rounding operator. The constraint matrix $\boldsymbol{B}^T_{\text{spatial}}$ for the network in Fig. 4.6 in an outwritten form has the structure

$$\boldsymbol{B}^T_{\text{spatial}} = \begin{bmatrix} 1 & -1 & 0 & 1 & 0 & 0 & 0 & 0 \\ 0 & 0 & 0 & -1 & 1 & 0 & -1 & 0 \\ 0 & 1 & -1 & 0 & 0 & 1 & 0 & 0 \\ 0 & 0 & 0 & 0 & 0 & -1 & 1 & 1 \end{bmatrix} \tag{4.14}$$

with

$$\boldsymbol{k}^{\Delta t_{\alpha\beta}}_{\boldsymbol{\Delta x}} = \begin{bmatrix} k^{\Delta t_{\alpha\beta}}_{\Delta x12} & k^{\Delta t_{\alpha\beta}}_{\Delta x13} & k^{\Delta t_{\alpha\beta}}_{\Delta x14} & k^{\Delta t_{\alpha\beta}}_{\Delta x23} & k^{\Delta t_{\alpha\beta}}_{\Delta x25} & k^{\Delta t_{\alpha\beta}}_{\Delta x34} & k^{\Delta t_{\alpha\beta}}_{\Delta x35} & k^{\Delta t_{\alpha\beta}}_{\Delta x54} \end{bmatrix}^T . \tag{4.15}$$

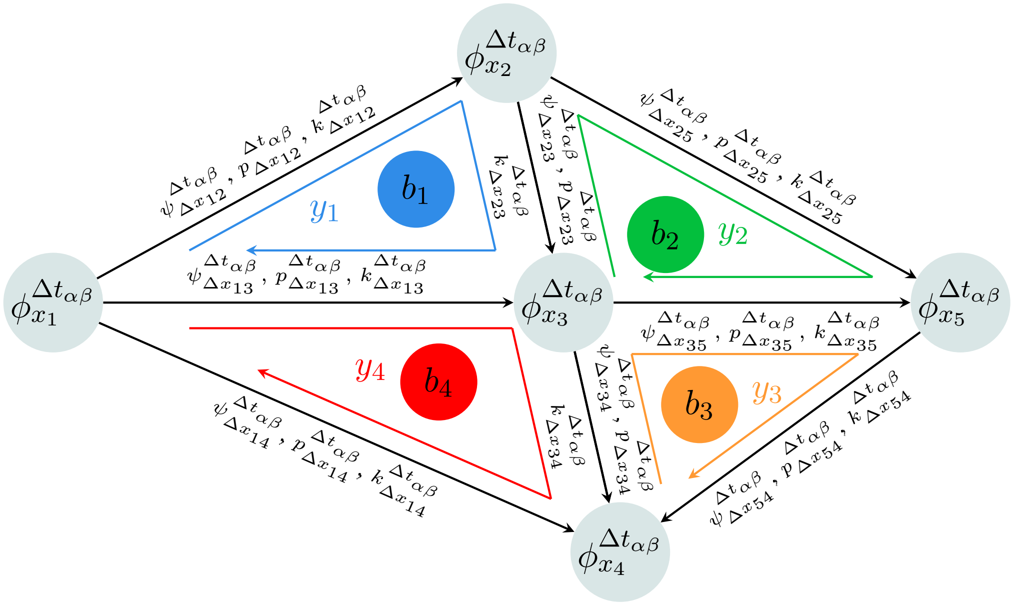

Figure 4.6: Small phase unwrapping network consisting of $m = 5$ nodes/ pixels with unknown unwrapped phases $\boldsymbol{\phi}^{\Delta t_{\alpha\beta}}_{\boldsymbol{x}}$, $n = 8$ arcs with unwrapped phase gradients $\boldsymbol{\phi}^{\Delta t_{\alpha\beta}}_{\boldsymbol{\Delta x}}$, weights $\boldsymbol{p}^{\Delta t_{\alpha\beta}}_{\boldsymbol{\Delta x}}$ and unknown phase ambiguity vectors $\boldsymbol{k}^{\Delta t_{\alpha\beta}}_{\boldsymbol{\Delta x}}$. This results in a redundance of $r = n - m = 4$ resulting in four independent constraints with the right-hand side vector $\boldsymbol{b}$.

It can be proven that this matrix is totally unimodular. Consequently, the constrained weighted L_1-norm phase unwrapping problem can be defined as an LP problem without considering the integer constraints. So the first considered problem formulation in its primal and dual form results in

PROBLEM 1:

$$
\begin{array}{rl}
\textit{primal:} & \\
\text{Objective function:} & C(\boldsymbol{k}_{\boldsymbol{\Delta x}}^{\Delta t_{\alpha\beta},+}, \boldsymbol{k}_{\boldsymbol{\Delta x}}^{\Delta t_{\alpha\beta},-}) = \begin{bmatrix} \boldsymbol{p}_{\boldsymbol{\Delta x}}^{\Delta t_{\alpha\beta}\,T} & \boldsymbol{p}_{\boldsymbol{\Delta x}}^{\Delta t_{\alpha\beta}\,T} \end{bmatrix} \begin{bmatrix} \boldsymbol{k}_{\boldsymbol{\Delta x}}^{\Delta t_{\alpha\beta},+} \\ \boldsymbol{k}_{\boldsymbol{\Delta x}}^{\Delta t_{\alpha\beta},-} \end{bmatrix} \ldots \min \\
\text{Constraint:} & \begin{bmatrix} \boldsymbol{B}_{\text{spatial}}^T & -\boldsymbol{B}_{\text{spatial}}^T \end{bmatrix} \begin{bmatrix} \boldsymbol{k}_{\boldsymbol{\Delta x}}^{\Delta t_{\alpha\beta},+} \\ \boldsymbol{k}_{\boldsymbol{\Delta x}}^{\Delta t_{\alpha\beta},-} \end{bmatrix} = \underbrace{-\lfloor \frac{\boldsymbol{B}_{\text{spatial}}^T \boldsymbol{\psi}_{\boldsymbol{\Delta t}}^{\Delta t_{\alpha\beta}}}{2\pi} \rceil}_{\boldsymbol{b}_{\text{spatial}}} \\
\text{Variable:} & \boldsymbol{k}_{\boldsymbol{\Delta x}}^{\Delta t_{\alpha\beta},+}, \boldsymbol{k}_{\boldsymbol{\Delta x}}^{\Delta t_{\alpha\beta},-} \in \mathbb{R}_{\geq 0} \\
\textit{dual:} & \\
\text{Objective function:} & C(\boldsymbol{y}) = \boldsymbol{b}^T \boldsymbol{y} \ldots \max \\
\text{Constraint:} & -\boldsymbol{p}_{\boldsymbol{\Delta x}}^{\Delta t_{\alpha\beta}} \leq \boldsymbol{B}_{\text{spatial}} \boldsymbol{y} \leq \boldsymbol{p}_{\boldsymbol{\Delta x}}^{\Delta t_{\alpha\beta}} \\
\text{Variable:} & \boldsymbol{y} \in \mathbb{R}
\end{array}
\tag{4.16}
$$

For the conversion between primal and dual program the reader is kindly referred to the Tucker diagram in Table A.1 in the Appendix A. The LP can be solved with the simplex method for example.

As mentioned in Costantini et al. (2012), the phase unwrapping can also be solved as parametric adjustment considering the functional model

$$
\phi_{x_k}^{\Delta t_{\alpha\beta}} - \phi_{x_l}^{\Delta t_{\alpha\beta}} - 2\pi k_{\Delta x_{kl}}^{\Delta t_{\alpha\beta}} = \psi_{\Delta x_{kl}}^{\Delta t_{\alpha\beta}} \tag{4.17}
$$

between the wrapped phase gradient $\psi_{\Delta x_{kl}}^{\Delta t_{\alpha\beta}}$ along the arc Δx_{kl} and the unwrapped phases $\phi_{x_k}^{\Delta t_{\alpha\beta}}$ and $\phi_{x_l}^{\Delta t_{\alpha\beta}}$ at pixels x_k and x_l. First, the relationship (4.1) is inserted for each pixel, resulting in

$$
\psi_{x_k}^{\Delta t_{\alpha\beta}} + 2\pi k_{x_k}^{\Delta t_{\alpha\beta}} - \psi_{x_l}^{\Delta t_{\alpha\beta}} - 2\pi k_{x_l}^{\Delta t_{\alpha\beta}} - 2\pi k_{\Delta x_{kl}}^{\Delta t_{\alpha\beta}} = \psi_{\Delta x_{kl}}^{\Delta t_{\alpha\beta}} \tag{4.18}
$$

which divided by 2π and some reformulations results in

$$
k_{x_k}^{\Delta t_{\alpha\beta}} - k_{x_l}^{\Delta t_{\alpha\beta}} - k_{\Delta x_{kl}}^{\Delta t_{\alpha\beta}} = \frac{\psi_{\Delta x_{kl}}^{\Delta t_{\alpha\beta}} - \psi_{x_k}^{\Delta t_{\alpha\beta}} + \psi_{x_l}^{\Delta t_{\alpha\beta}}}{2\pi}. \tag{4.19}
$$

As the wrapped measured phase gradient $\psi_{\Delta x_{kl}}^{\Delta t_{\alpha\beta}}$ already is a wrapped value in a range from $-\pi$ to π, inserting relationship

$$
\psi_{\Delta x_{kl}}^{\Delta t_{\alpha\beta}} = \psi_{x_k}^{\Delta t_{\alpha\beta}} - \psi_{x_l}^{\Delta t_{\alpha\beta}} - 2\pi \lfloor \frac{\psi_{x_k}^{\Delta t_{\alpha\beta}} - \psi_{x_l}^{\Delta t_{\alpha\beta}}}{2\pi} \rceil \tag{4.20}
$$

into (4.19) leads to

$$
k_{x_k}^{\Delta t_{\alpha\beta}} - k_{x_l}^{\Delta t_{\alpha\beta}} - k_{\Delta x_{kl}}^{\Delta t_{\alpha\beta}} = -\lfloor \frac{\psi_{x_k}^{\Delta t_{\alpha\beta}} - \psi_{x_l}^{\Delta t_{\alpha\beta}}}{2\pi} \rceil. \tag{4.21}
$$

For all arcs the functional model matrix $\boldsymbol{A}_{\text{primal}} \in \mathbb{Z}^{n \times m}$, also called the arc-to-node incidence matrix of the primal graph, is defined. One row contains zeros except the two columns which belong to the defining nodes of the actual arc. These are filled with one for the end node and minus one for the start node. For the graph displayed in Fig. 4.6 the matrix has the structure

$$\boldsymbol{A}_{\text{primal}} = \begin{bmatrix} -1 & 1 & 0 & 0 & 0 \\ -1 & 0 & 1 & 0 & 0 \\ -1 & 0 & 0 & 1 & 0 \\ 0 & -1 & 1 & 0 & 0 \\ 0 & -1 & 0 & 0 & 1 \\ 0 & 0 & -1 & 1 & 0 \\ 0 & 0 & -1 & 0 & 1 \\ 0 & 0 & 0 & 1 & -1 \end{bmatrix}. \tag{4.22}$$

This matrix also is totally unimodular. With this property the phase unwrapping problem can again be formulated as an LP without taking into account the integer constraints. Thus, the second formulated LP to describe the phase unwrapping problem in its primal and dual form results in

PROBLEM 2:

primal:

$$\text{Objective function:} \quad C(\boldsymbol{x}) = \underbrace{\begin{bmatrix} \boldsymbol{0}_{[1\times m]} & {\boldsymbol{p}_{\boldsymbol{\Delta x}}^{\Delta t_{\alpha\beta}}}^T & {\boldsymbol{p}_{\boldsymbol{\Delta x}}^{\Delta t_{\alpha\beta}}}^T \end{bmatrix}}_{\boldsymbol{c}^T} \underbrace{\begin{bmatrix} \boldsymbol{k}_{\boldsymbol{x}}^{\Delta t_{\alpha\beta}} \\ \boldsymbol{k}_{\boldsymbol{\Delta x}}^{\Delta t_{\alpha\beta},+} \\ \boldsymbol{k}_{\boldsymbol{\Delta x}}^{\Delta t_{\alpha\beta},-} \end{bmatrix}}_{\boldsymbol{x}} \dots \min$$

$$\text{Constraint:} \quad \begin{bmatrix} \boldsymbol{A}_{\text{primal}} & -\boldsymbol{1}_{[n\times n]} & \boldsymbol{1}_{[n\times n]} \end{bmatrix} \underbrace{\begin{bmatrix} \boldsymbol{k}_{\boldsymbol{x}}^{\Delta t_{\alpha\beta}} \\ \boldsymbol{k}_{\boldsymbol{\Delta x}}^{\Delta t_{\alpha\beta},+} \\ \boldsymbol{k}_{\boldsymbol{\Delta x}}^{\Delta t_{\alpha\beta},-} \end{bmatrix}}_{\boldsymbol{x}} = \underbrace{-\left\lfloor \frac{\boldsymbol{A}_{\text{primal}} \boldsymbol{\psi}_{\boldsymbol{x}}^{\Delta t_{\alpha\beta}}}{2\pi} \right\rceil}_{\boldsymbol{b}} \tag{4.23}$$

$$\text{Variable:} \quad \boldsymbol{k}_{\boldsymbol{x}}^{\Delta t_{\alpha\beta}} \in \mathbb{R}, \quad \boldsymbol{k}_{\boldsymbol{\Delta x}}^{\Delta t_{\alpha\beta},-}, \boldsymbol{k}_{\boldsymbol{\Delta x}}^{\Delta t_{\alpha\beta},+} \in \mathbb{R}_{\geq 0}$$

dual:

$$\text{Objective function:} \quad C(\boldsymbol{y}) = \boldsymbol{b}^T \boldsymbol{y} \dots \max$$

$$\text{Constraint:} \quad \boldsymbol{A}_{\text{primal}}^T \boldsymbol{y} = \boldsymbol{0}$$

$$\text{Variable:} \quad -\boldsymbol{p}_{\boldsymbol{\Delta x}}^{\Delta t_{\alpha\beta}} \leq \boldsymbol{y} \leq \boldsymbol{p}_{\boldsymbol{\Delta x}}^{\Delta t_{\alpha\beta}}.$$

The variable vector $\boldsymbol{x}$ is extended by the phase ambiguity factors $\boldsymbol{k}_{\boldsymbol{x}}^{\Delta t_{\alpha\beta}}$ at each pixel. This has the advantage that the integration step of the unwrapped phase gradients is no longer necessary to get the unwrapped phase values at the pixels. However, the problem is then of higher dimension. The LP can be solved again with the simplex method for example.

4.3.1.2 Solution as Network Flow Problem

Beside the LP solver, the phase unwrapping problem can be solved more efficiently as a network flow problem. Therefore, the PROBLEM 1 formulated in (4.16) is considered first. As described in Section 3.4, the network flow problem is based on a graph. To formulate PROBLEM 1 as a network flow problem, the dual graph is required. The dual graph $\mathcal{G}'$ of a plane graph $\mathcal{G}$, also called primal graph, is a graph that has a node for each face of $\mathcal{G}$ including the outside face (Wilson, 1986, p. 73). The arcs of the dual graph connect these nodes by cutting the arcs of the graph $\mathcal{G}$. The phase unwrapping problem is based on a Delaunay triangulation represented by the primal graph $\mathcal{G}$ with m nodes, n arcs and r triangles. As a Delaunay triangulation is a plane graph a corresponding dual graph $\mathcal{G}'$ with $r+1$ nodes and n arcs exists (Wilson, 1986, p. 73). The dual graph of the network shown in Fig. 4.6 is represented in Fig. 4.7. Based on this graph, the phase unwrapping problem can be formulated as a network flow problem. Each node has a potential $\boldsymbol{b}$ expressed by the right-hand side vector of the triangle constraint in (4.16). The potential of the node, corresponding to the outside face, represents the sum over the outlying arcs of the primal graph. There is a flow along each arc Δx_{kl} of the dual graph represented by the phase ambiguity factor $k^{\Delta t_{\alpha\beta}}_{\Delta x_{kl}}$ which is weighted with a cost value $p^{\Delta t_{\alpha\beta}}_{\Delta x_{kl}}$. The goal is to minimize the costs under the flow conservation that the sum of the incoming and outcoming flow has to satisfy the potential at each node. This results in the third phase unwrapping problem, this time formulated as a network flow problem. The network flow problem in its primal and dual form is given by

PROBLEM 3:

$$
\begin{array}{rl}
 & \textit{primal:} \\[1ex]
\text{Objective function:} & C(\boldsymbol{\Pi}) = \underbrace{\begin{bmatrix} {\boldsymbol{p}^{\Delta t_{\alpha\beta}}_{\Delta x_{kl}}}^T & {\boldsymbol{p}^{\Delta t_{\alpha\beta}}_{\Delta x_{kl}}}^T \end{bmatrix}}_{\boldsymbol{c}^T} \underbrace{\begin{bmatrix} \boldsymbol{k}^{\Delta t_{\alpha\beta},+}_{\boldsymbol{\Delta x}} \\ \boldsymbol{k}^{\Delta t_{\alpha\beta},-}_{\boldsymbol{\Delta x}} \end{bmatrix}}_{\boldsymbol{\Pi}} \dots \min \\[2ex]
\text{Flow conservation:} & \begin{bmatrix} \boldsymbol{A}^T_{\text{dual}} & -\boldsymbol{A}^T_{\text{dual}} \end{bmatrix} \underbrace{\begin{bmatrix} \boldsymbol{k}^{\Delta t_{\alpha\beta},+}_{\boldsymbol{\Delta x}} \\ \boldsymbol{k}^{\Delta t_{\alpha\beta},-}_{\boldsymbol{\Delta x}} \end{bmatrix}}_{\boldsymbol{\Pi}} = \underbrace{-\left\lfloor \frac{\boldsymbol{A}^T_{\text{dual}} \boldsymbol{\psi}^{\Delta t_{\alpha\beta}}_{\boldsymbol{\Delta x}}}{2\pi} \right\rceil}_{\boldsymbol{b}} \\[2ex]
\text{Variable:} & \boldsymbol{0} \leq \boldsymbol{k}^{\Delta t_{\alpha\beta},+}_{\boldsymbol{\Delta x}} \leq \boldsymbol{u}^+ \\
 & \boldsymbol{0} \leq \boldsymbol{k}^{\Delta t_{\alpha\beta},-}_{\boldsymbol{\Delta x}} \leq \boldsymbol{u}^- \\[2ex]
 & \textit{dual:} \\[1ex]
\text{Objective function:} & C(\boldsymbol{y}, \boldsymbol{z}_u^+, \boldsymbol{z}_u^-) = \boldsymbol{b}^T \boldsymbol{y} - {\boldsymbol{u}^+}^T \boldsymbol{z}_u^+ - {\boldsymbol{u}^-}^T \boldsymbol{z}_u^- \dots \max \\[2ex]
\text{Capacity contraint:} & \begin{bmatrix} \boldsymbol{A}_{\text{dual}} & \boldsymbol{1}_{[n\times n]} & \boldsymbol{0}_{[n\times n]} \\ -\boldsymbol{A}_{\text{dual}} & \boldsymbol{0}_{[n\times n]} & \boldsymbol{1}_{[n\times n]} \end{bmatrix} \begin{bmatrix} \boldsymbol{y} \\ \boldsymbol{z}_u^+ \\ \boldsymbol{z}_u^- \end{bmatrix} \leq \begin{bmatrix} \boldsymbol{p}^{\Delta t_{\alpha\beta}}_{\Delta x_{kl}} \\ \boldsymbol{p}^{\Delta t_{\alpha\beta}}_{\Delta x_{kl}} \end{bmatrix} \\[2ex]
\text{Variable:} & \boldsymbol{z}_u^+, \boldsymbol{z}_u^- \geq \boldsymbol{0}
\end{array}
\tag{4.24}
$$

with the constraint matrix $\boldsymbol{A}^T_{\text{dual}} \in \mathbb{Z}^{r+1\times n}$ also called the arc-to-node incidence matrix of the dual graph. This arc-to-node incidence matrix equals the transposed constraint matrix of (4.14) with the additional outlying loop constraint

$$
\boldsymbol{A}^T_{\text{dual}} = \begin{bmatrix} 1 & -1 & 0 & 1 & 0 & 0 & 0 & 0 \\ 0 & 0 & 0 & -1 & 1 & 0 & -1 & 0 \\ 0 & 1 & -1 & 0 & 0 & 1 & 0 & 0 \\ 0 & 0 & 0 & 0 & 0 & -1 & 1 & 1 \\ -1 & 1 & 1 & 0 & 0 & 0 & 0 & -1 \end{bmatrix}^T . \tag{4.25}
$$

Assuming integer values for the costs and the upper capacity, the values for the variables will be integers. The upper capacities $\boldsymbol{u}^+$ and $\boldsymbol{u}^-$ describe the maximum numbers of estimated phase ambiguity factors along each arc. The application of this upper capacity can reflect previous knowledge or reduce the run time but it is not mandatory (Costantini, 1998). Consequently, the phase unwrapping problem can be solved using network flow algorithms like the out-of-kilter algorithm (Fulkerson, 1961) or the relaxation method (Bertsekas and Tseng, 1988). Since this formulation depends on the

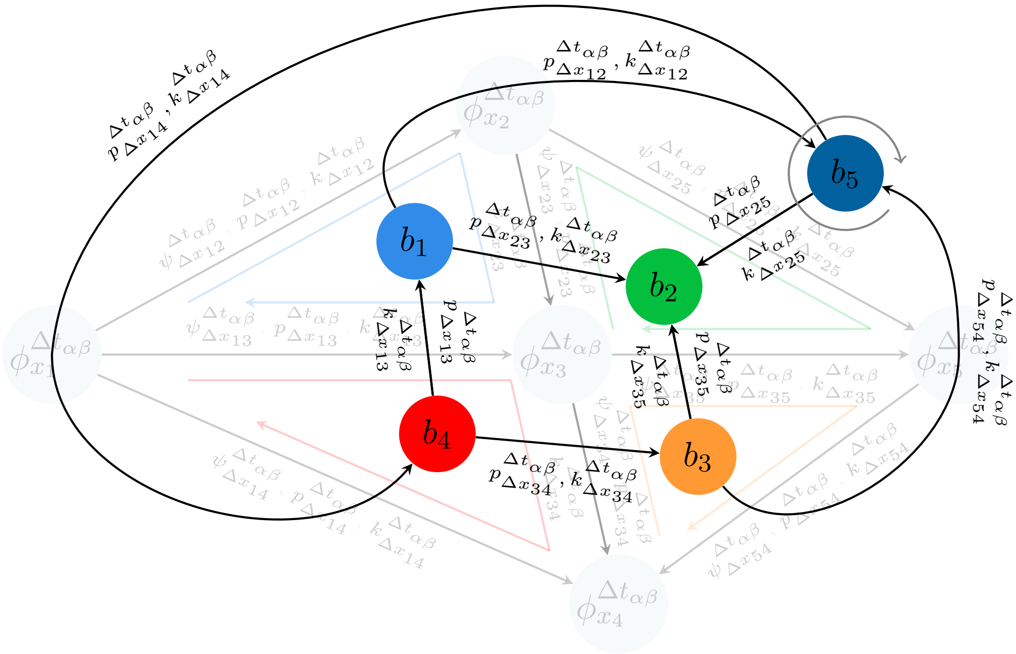

Figure 4.7: Dual graph of Fig. 4.6. The constraints of the primal problem define the new nodes with node potential $\boldsymbol{b}$. The arcs connect these nodes by cutting the arcs of the primal graph. Along the arcs runs the weighted flow in form of the phase ambiguity factors $\boldsymbol{k}_{\Delta \boldsymbol{x}}^{\Delta t_{\alpha\beta}}$. According to the flow conservation, the sum of the incoming and outcoming flow has to be equal to the node potential.

dual graph, it is only applicable if the primal graph is plane (Wilson, 1986, p. 73). Thus, redundant arcs are not allowed in this formulation.

Referring to the parametric weighted L$_1$-norm problem, formulated as PROBLEM 2 in (4.16), the problem can also be seen as a network flow problem. Therefore, the primal graph in Fig. 4.6 is regarded. The constraint in (4.23) can be seen as the capacity constraint of the dual flow problem, cf. (3.23). The phase ambiguity factors at each pixel $k_{x_k}^{\Delta t_{\alpha\beta}}$ and $k_{x_l}^{\Delta t_{\alpha\beta}}$ represent the node potential $\boldsymbol{y}$, the phase ambiguity factor along the arc $k_{\Delta x_{kl}}^{\Delta t_{\alpha\beta}}$ the bound variable $\boldsymbol{z}_u$ and the right-hand side vector the arc capacity $\boldsymbol{c}$. Altogether, the fourth phase unwrapping problem formulated again as network flow problem can be defined in its primal and dual form as

PROBLEM 4:

primal:

Objective function: $$C(\boldsymbol{z}_u) = \underbrace{\begin{bmatrix} \boldsymbol{p}_{\Delta x_{kl}}^{\Delta t_{\alpha\beta}\,T} & \boldsymbol{p}_{\Delta x_{kl}}^{\Delta t_{\alpha\beta}\,T} \end{bmatrix}}_{\boldsymbol{u}} \underbrace{\begin{bmatrix} \boldsymbol{k}_{\Delta \boldsymbol{x}}^{\Delta t_{\alpha\beta},+} \\ \boldsymbol{k}_{\Delta \boldsymbol{x}}^{\Delta t_{\alpha\beta},-} \end{bmatrix}}_{\boldsymbol{z}_u} \ldots \min$$

Capacity constraint: $$\boldsymbol{A}_{\text{primal}} \boldsymbol{k}_{\boldsymbol{x}}^{\Delta t_{\alpha\beta}} - \begin{bmatrix} \boldsymbol{1}_{[n\times n]} - \boldsymbol{1}_{[n\times n]} \end{bmatrix} \underbrace{\begin{bmatrix} \boldsymbol{k}_{\Delta \boldsymbol{x}}^{\Delta t_{\alpha\beta},+} \\ \boldsymbol{k}_{\Delta \boldsymbol{x}}^{\Delta t_{\alpha\beta},-} \end{bmatrix}}_{\boldsymbol{z}_u} = \underbrace{-\left\lfloor \frac{\boldsymbol{A}_{\text{primal}} \boldsymbol{\psi}_{\boldsymbol{x}}^{\Delta t_{\alpha\beta}}}{2\pi} \right\rceil}_{\boldsymbol{c}} \quad (4.26)$$

Variable: $\boldsymbol{z}_u \geq \boldsymbol{0}$

dual:

Objective function: $C(\boldsymbol{\Pi}) = \boldsymbol{c}^T \boldsymbol{\Pi} \ldots \max$

Flow conservation: $\boldsymbol{A}_{\text{primal}}^T \boldsymbol{\Pi} = \boldsymbol{0}$

Variable: $-\boldsymbol{p}_{\Delta \boldsymbol{x}}^{\Delta t_{\alpha\beta}\,T} \leq \boldsymbol{\Pi} \leq \boldsymbol{p}_{\Delta \boldsymbol{x}}^{\Delta t_{\alpha\beta}\,T}$

with the arc-to-node incidence matrix $\boldsymbol{A}_{\text{primal}} \in \mathbb{Z}^{n\times m}$ of the primal graph. Assuming integer values for $\boldsymbol{p}_{\Delta\boldsymbol{x}}^{\Delta t_{\alpha\beta}}$, the values for the variables will be integers. On this basis, the problem can also be solved using network flow algorithms like the out-of-kilter algorithm or the relaxation method. Compared with the before mentioned formulation as constrained L_1-norm problem, this formulation has the advantage that the generation of the dual graph is not necessary. It depends on the primal graph and therefore, redundant arcs are possible which results in more reliable and accurate solutions (Costantini et al., 2012).

4.3.2 Application to Simulated Data

4.3.2.1 Simulation Scenario

To analyze the phase unwrapping process in some more detail, a D-InSAR stack is simulated based on the ERS-1/-2 configuration in time and space. For this purpose, 64 SAR images from May 1992 to December 2000 are used which cover the test region of the Lower-Rhine-Embayment. The test region is restricted to 401 pixels. The whole workflow for generating the simulated interferometric phases is summarized in Fig. 4.8. In the center of the test region a ground settlement depression is simulated with respect to the first SAR image. The deformation consists of a linear trend and the deformation velocity is restricted to a range from 8 to 12 cm/yr reaching a dimension from 120 to 240 pixels. The deformation velocities in the Lower-Rhine-Embayment are within the ground settlement basins of the active open-cast mines at several centimeters per year, so this simulation environment represents a realistic scenario. In addition to the deformation a topographical error is modeled. In differential SAR interferometry the effect of topography is removed by subtracting a reference DEM. The modeled topography error is intended to simulate errors in the used DEM. In the simulation this error reaches values from -5 to 40 m. To make the simulation more realistic a noise per SAR image is added which is assumed to be independent and identical distributed with a standard deviation of 0.4 rad.

With respect to the SBAS method, 161 interferograms are generated, as can be seen in the corresponding temporal triangulation shown in Fig. 2.8b. Filtering operations that are applied individually to each interferogram, such as the multilooking, cause the real data to be inconsistent over time. To simulate this, an additional normally distributed noise is added to each simulated interferogram. The standard deviation depends on the unbiased coherence Lee et al. (1994) taken from the real coherence values of the ERS-1/-2 data set. These coherence values are also used to select the so called stable pixels. Pixels are defined as stable if they have a coherence value greater than or equal to 0.7 in at least 80 % of the interferograms. Within the 401 × 401 test region there are $m = 15\,347$ stable

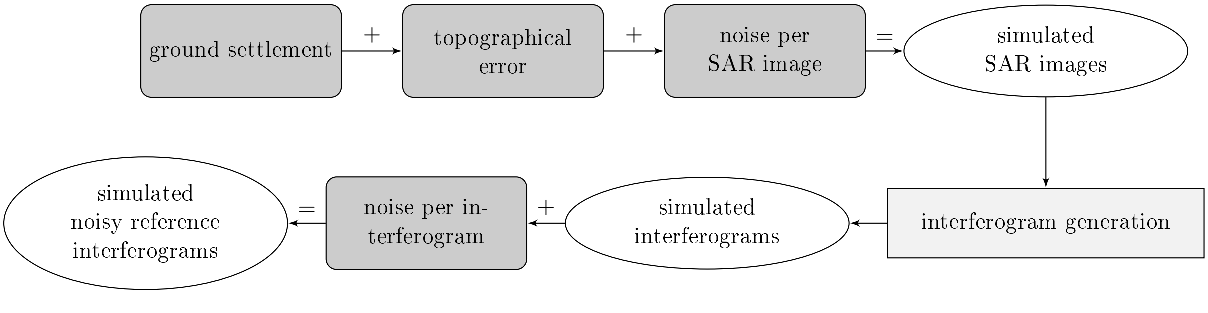

Figure 4.8: Workflow for generating simulated interferometric reference phases. The simulated SAR images consist of a ground settlement, a topographical error and a noise part. On this basis, interferograms are generated which in turn are provided with noise.

pixels defining $n = 45\,842$ arcs and $r = 30\,496$ triangles. Figure 4.9a shows the simulated phases of the stable pixels in the test region for one interferogram with a temporal baseline of $\Delta t_{\alpha\beta} = 315$ days and an orthogonal spatial baseline of $\Delta b_{\perp,\alpha\beta} = 76.322$ m. The associated measured wrapped phase in the interval from $-\pi$ to π is represented in Fig. 4.9b. The lines between the pixels in Fig. 4.9a symbolize the phase gradients that exceed the measurable value range. Dark blue indicates that a double negative 2π phase jump must be added to the measured phase gradient, the corresponding phase ambiguity factor $k_{\Delta x_{kl}}^{\Delta t_{\alpha\beta}}$ of this arc Δx_{kl} is -2, light blue means a single negative 2π phase jump ($k_{\Delta x_{kl}}^{\Delta t_{\alpha\beta}} = -1$), dark red a double positive 2π phase jump ($k_{\Delta x_{kl}}^{\Delta t_{\alpha\beta}} = 2$) and light red a single positive 2π phase jump ($k_{\Delta x_{kl}}^{\Delta t_{\alpha\beta}} = 1$).

The task of the phase unwrapping process is to estimate these phase ambiguity factors $\boldsymbol{k}_{\Delta \boldsymbol{x}}^{\Delta t_{\alpha\beta}}$. As demonstrated in Section 4.3.1, the problem can be defined in different ways see PROBLEM 1 to 4 in (4.16), (4.23), (4.24) and (4.26). This section deals with the phase unwrapping of the simulated D-InSAR stack with help of these four problem formulations. Therefore, all 161 interferograms are unwrapped individually. For the solution of PROBLEM 1 and PROBLEM 2 the commercial optimization solver Gurobi[2] is used. To solve LPs, Gurobi uses the concurrent optimizer which uses multiple algorithms simultaneously and returns the solution from the first one to finish. As standard it uses the primal simplex, the dual simplex and the interior point method. To solve PROBLEM 3 and PROBLEM 4, the open source RELAX-IV[3] implementation described in Bertsekas and Tseng (1994) is used. It is an extremely efficient solver for network flow problems with integer data. The weights $\boldsymbol{p}_{\Delta \boldsymbol{x}}^{\Delta t_{\alpha\beta}}$ of the phase ambiguity factors are all set to one.

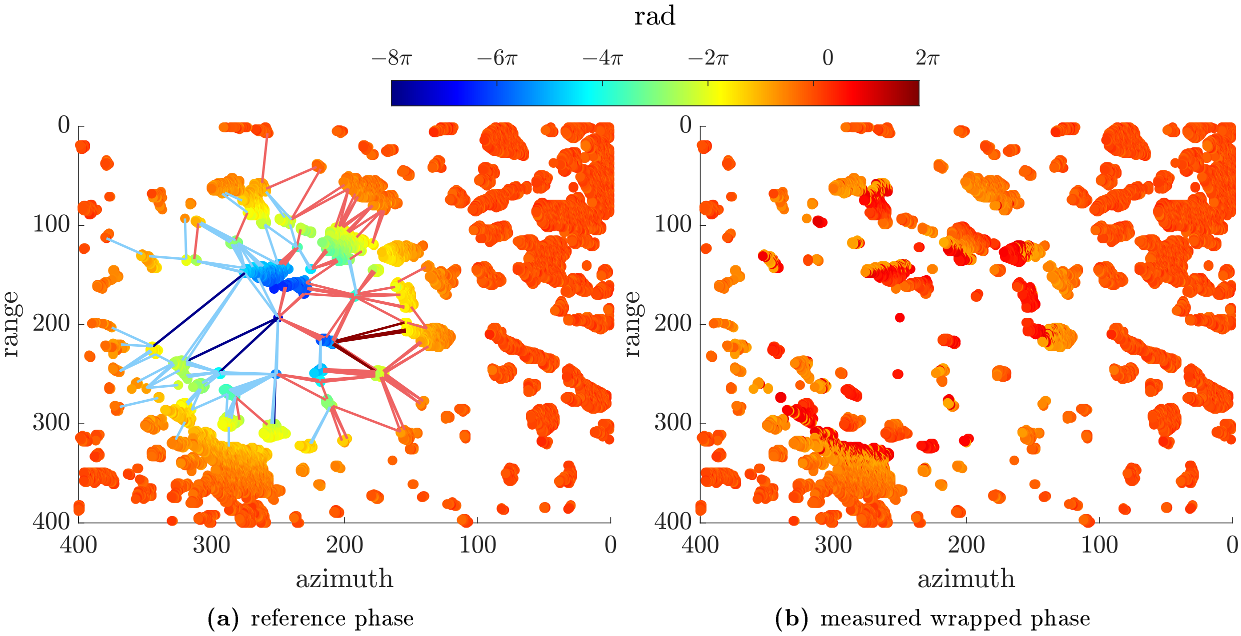

(a) reference phase **(b)** measured wrapped phase

Figure 4.9: Coherent pixels of simulated ground settlement depression for one interferogram with a temporal baseline of $\Delta t_{\alpha\beta} = 315$ days and an orthogonal spatial baseline of $\Delta b_{\perp,\alpha\beta} = 76.322$ m. The lines between the pixels in Fig. 4.9a symbolize the phase gradients that exceed the measurable value range. Dark blue indicates that a double negative 2π phase jump must be added to the measured phase gradient, the corresponding phase ambiguity factor $k_{\Delta x_{kl}}^{\Delta t_{\alpha\beta}}$ of this arc Δx_{kl} is -2, light blue means a $k_{\Delta x_{kl}}^{\Delta t_{\alpha\beta}}$ of -1, dark red a $k_{\Delta x_{kl}}^{\Delta t_{\alpha\beta}}$ of 2 and light red a $k_{\Delta x_{kl}}^{\Delta t_{\alpha\beta}}$ of 1.

---

[2] `http://www.gurobi.com/` last accessed on August 4, 2020

[3] `http://www.di.unipi.it/di/groups/optimize/Software/MCF.html` last accessed on August 4, 2020

4.3.2.2 Results of Closed Loop Simulation

Figure 4.10 shows the unwrapped phases for the interferogram already shown in Fig. 4.9. For Fig. 4.10a the phase unwrapping is solved according to the PROBLEM 1 formulation with Gurobi. For one interferogram the problem consists of $2{\cdot}45\,842$ parameters with $30\,496$ constraints. Figure 4.10b shows the solution of PROBLEM 2 solved with Gurobi, as well. The dimension of the problem extends to $2{\cdot}45\,842 + 15\,347$ parameters with $45\,842$ constraints as the phase ambiguity factor at each pixel is added. Consequently, the problem is of highest dimension resulting in a higher run time which is about twenty times larger than the solution of PROBLEM 1. In Figs. 4.10c and 4.10d the phase unwrapping is solved as a network flow problem using the RELAX-IV algorithm. Figure 4.10c shows the solution of PROBLEM 3. The problem formulation refers to the dual graph consisting of $30\,496 + 1$ nodes and $2{\cdot}45\,842$ parameters in form of the flow represented by the phase ambiguity factors. Beside this, Fig. 4.10d shows the results according to the PROBLEM 4

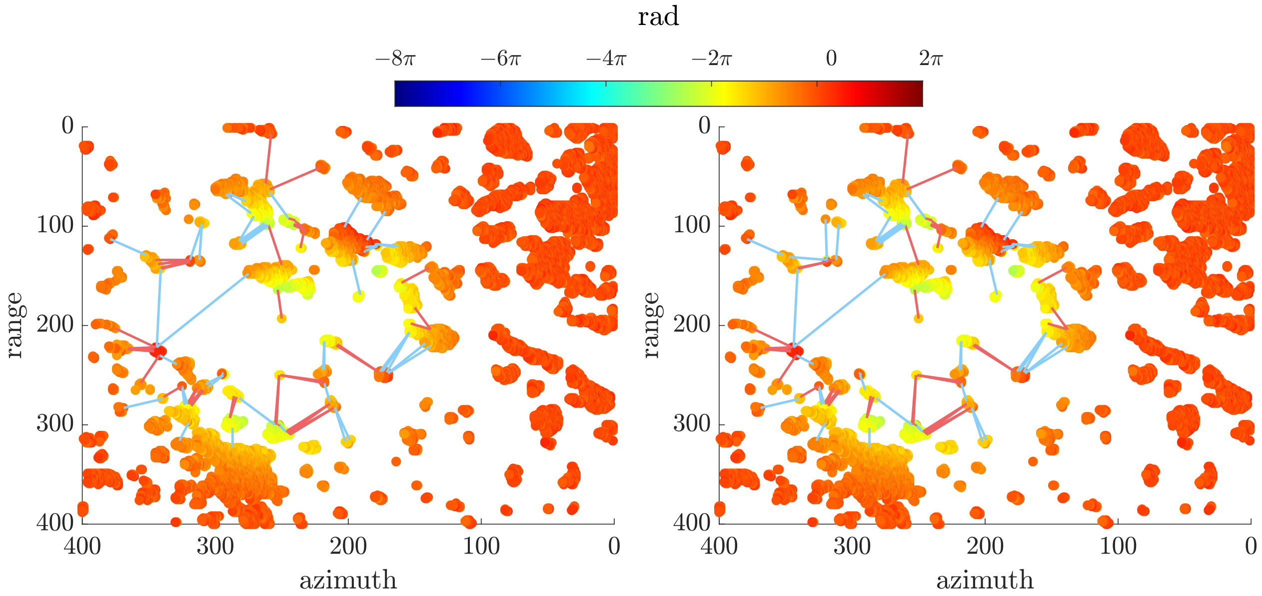

(a) solution of PROBLEM 1 solved with Gurobi

(b) solution of PROBLEM 2 solved with Gurobi

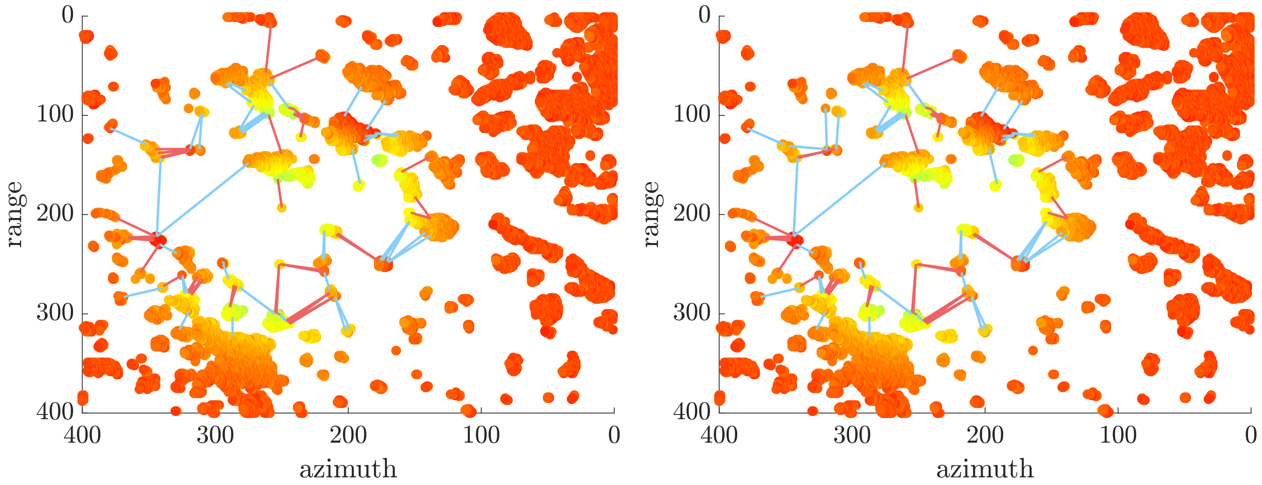

(c) solution of PROBLEM 3 solved with RELAX-IV

(d) solution of PROBLEM 4 solved with RELAX-IV

Figure 4.10: Unwrapped phases using the spatial MCF algorithm formulated in a constrained or parametric way and solved as LP or network flow problem for the interferogram already shown in Fig. 4.9. The lines between the pixels symbolizes if a phase ambiguity factor is estimated or not. Light blue mean a phase ambiguity factor of -1 and light red of 1.

formulation. The problem refers to the primal graph and consists of 15 347 nodes and 45 842 arcs. Comparing the run time between a standard LP solver which is used in Gurobi and the network flow solver, a significant reduction of run time can be observed when solving the problem as a network flow problem. On the basis of the detailed formulation presented here, the solution of the phase unwrapping problem using RELAX-IV was integrated into the current stable version of the RSG software. The utilization of the network-like structure results in a four times shorter run time.

In the following, the results will be examined in more detail. Looking at the results in Fig. 4.10, it can first of all be seen that for all four solutions the settlement depression is not correctly reconstructed compared to the reference phase shown in Fig. 4.9a. In addition to the unwrapped phases, the figures show, analogous to Fig. 4.9a, the corresponding estimated phase ambiguity factors per phase gradient. Light blue means again a phase ambiguity factor of $k_{\Delta x_{kl}}^{\Delta t_{\alpha\beta}} = -1$ and light red a phase ambiguity factor of $k_{\Delta x_{kl}}^{\Delta t_{\alpha\beta}} = 1$. Phase ambiguity factors greater than one or smaller than minus one are not estimated.

For all four problem formulations the objective function value which is equal to the weighted L$_1$-norm of the phase ambiguity factors $\boldsymbol{k}_{\Delta \boldsymbol{x}}^{\Delta t_{\alpha\beta}}$ is 107. As can already be seen in Fig. 4.9a, phase ambiguity factors greater than one or smaller than minus one occur especially in the area of the settlement depression. To reconstruct the reference phase gradients a total number of $\sum |\boldsymbol{k}_{\Delta \boldsymbol{x}}^{\Delta t_{\alpha\beta}}| = 210$ is necessary. However, to obtain spatially consistent phase gradients, a smaller number is sufficient. As a solution is sought, in which the weighted L$_1$-norm of the phase ambiguity factors should be minimal, the results shown in Fig. 4.10 are therefore optimal. If one compares the arcs for all four solutions where a phase ambiguity factor unequal zero is estimated, it can be seen that 2π phase jumps are not always inserted at exactly the same arc. Therefore, the solution is not unique. However, following the problem definition all unwrapped phase gradients in Fig. 4.10 are optimal and equivalent.

The question is why the spatial phase unwrapping is not able to reconstruct the reference phase. The considered interferogram has a temporal baseline $\Delta t_{\alpha\beta}$ of 315 days. With a wavelength of $\lambda = 5.6666\,\mathrm{cm}$, a phase gradient between the pixels x_k and x_l should have a mean deformation velocity variation $v_{\Delta x_{kl}}$ in a range from -1.65 cm/yr to 1.65 cm/yr according to the Nyquist sampling theorem so that the signal can be reconstructed exactly. In this case no inconsistencies occur. The phase gradients are within the measurable range and spatially consistent, i.e. the sum of the phase gradients in a loop is zero. In the simulation, however, the mean deformation velocity variation of the phase gradients is far above this value, especially in the area of the settlement depression values above 6 cm/yr occur. If too many phase gradients exist which exceed the measurable value range from $-\pi$ to π, as it is the case in Fig. 4.9a, it is always possible to get spatially consistent phases by inserting a smaller number of 2π phase jumps. Therefore, the methods used are not able to reconstruct the reference phase.

For interferograms with a larger temporal baseline, the problem becomes worse as the phase gradients show an even greater displacement. Figures 4.11a and 4.11b show the results for all 161 unwrapped interferograms depending on the temporal baseline between the two corresponding SAR images. Figure 4.11a represents the absolute number of phase ambiguity factors $\sum |\boldsymbol{k}_{\Delta \boldsymbol{x}}^{\Delta t_{\alpha\beta}}|$ for the corresponding interferograms which is equal to the objective function value. The results of the individual solutions are marked in different symbols and colors. The solutions of the PROBLEM 1 formulation is symbolized as dark blue squares, the solutions of the PROBLEM 2 as green squares, the solutions of the PROBLEM 3 as orange points and the solutions of the PROBLEM 4 as light blue points. Again, it is obvious that all solutions result in the same objective function values. However, comparing the individual results with the reference phase, shown as black stars, it can be seen that the unwrapped phases do not reconstruct the reference phases. The objective function values of the reference data are always higher or equal to the unwrapped results. This confirms the above statements. At mean deformation velocity variations of 5 to 6 cm/yr between the pixels and a temporal baseline of less than 100 days, the deformation can still be reconstructed exactly according to the Nyquist sampling theorem. This is also shown in Fig. 4.11b. The figure presents the percentage of correctly unwrapped phase gradients depending on the temporal baseline between the two corresponding SAR images. It can be seen that especially with larger temporal baseline it is not possible to unwrap the phase correctly with the used methods.

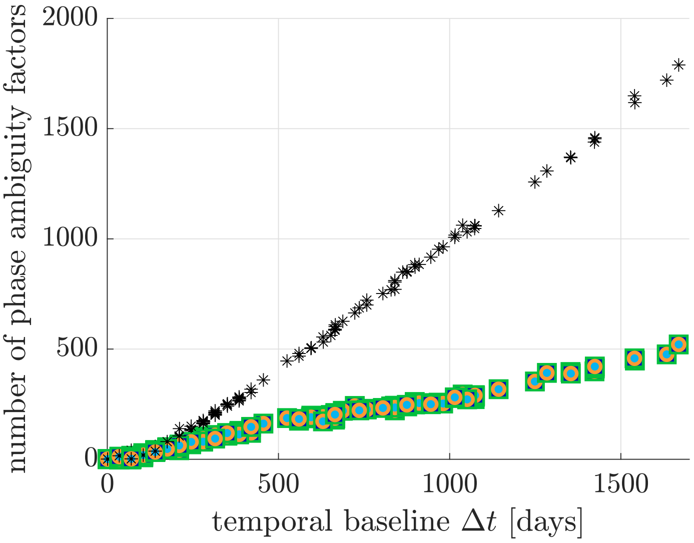

(a) absolute number of phase ambiguity factors compared to the observed phase gradients

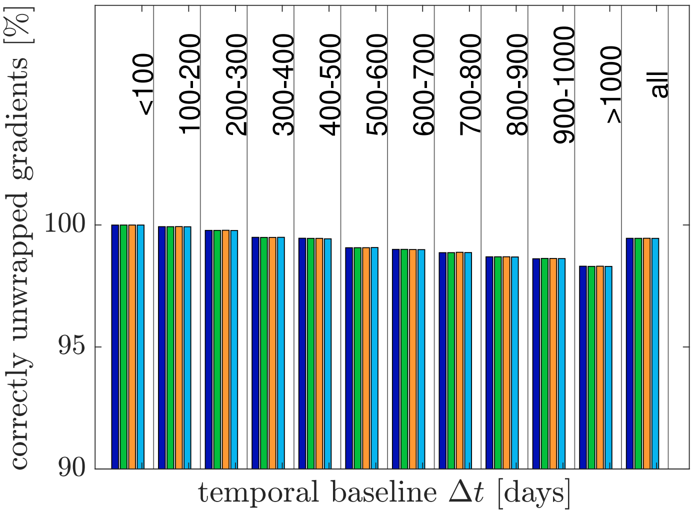

(b) percentage of correctly spatially unwrapped phase gradients

Figure 4.11: Solution of the spatially unwrapped phase gradients depending on the temporal baseline. The dark blue color represents the results of the PROBLEM 1 formulation, the orange of the PROBLEM 2 formulation, the green of the PROBLEM 3 and the light blue of the PROBLEM 4 formulation. For comparison, the black stars in Fig. 4.11a show the reference solution.

One way to avoid this problem is to distribute the data more densely so that the phase gradients are smaller and fewer phase gradients extend the measurable value range from $-\pi$ to π. The distribution of the data is, however, predetermined by the coherence. Adding pixels with less coherence means that the pixels have a higher noise level which makes phase unwrapping more complex. One possibility is to down-weight these less reliable pixels by using low weights. The choice of weights will be discussed further in Section 6.2. Another way is to refine the problem formulation and to insert additional information, like the time. The idea is not to analyze each interferogram individually, but to integrate the temporal information provided by the D-InSAR stack into the problem. By considering and applying a linear motion model, the number of phase ambiguities can be further reduced which is the idea of the so called three dimensional phase unwrapping.

4.4 Summary

It can be concluded that the phase unwrapping problem can be formulated and solved in different ways. In this thesis a total of four problem formulations to solve the LP within the MCF method are presented. Thus, the first main objective of this work is achieved. It has been shown that all formulations lead to the same objective function values. They are optimal according to the problem formulation. Differences in the results only arise if the solution is not unique. However, looking at the complexity and the dimension of the problem, the parametric L_1-norm problem, described in PROBLEM 2 and PROBLEM 4 is not recommended compared to the constrained formulations. Furthermore, on the basis of the simulated data it can be shown that the reference phase cannot be reconstructed by unwrapping each interferogram separately. Without further extensions or additional information the methods used are unable to unwrap the phase correctly. Therefore, the problem formulation has to be refined by inserting the temporal information which is given by the D-InSAR stack, for example. Figure 4.11a already hypothesized that there is a linear relationship between the temporal baseline and the total number of phase ambiguity factors. This leads to the three dimensional phase unwrapping which will be addressed in the next chapter.

5. Three Dimensional Phase Unwrapping – Review and Evaluation of Methods

So far phase unwrapping is done for one single interferogram using the spatial, two dimensional information in the azimuth/ range plane, cf. Fig. 4.4. With respect to a multitemporal D-InSAR stack a set $\mathcal{M}'$ of m' SAR images at times $t_1, t_2, \ldots, t_{m'}$ is available. The images are assembled to a set $\mathcal{N}'$ of n' D-InSAR images with respect to the SBAS method. The idea is to exploit the temporal relationship between the interferograms in order to multitemporally unwrap D-InSAR images. According to Hooper et al. (2007), the inclusion of the time as an additional information leads to an improvement in the accuracy of the solution in a similar way to which two dimensional phase unwrapping provides an improvement over one dimensional methods. This chapter starts with an overview of the most popular three dimensional approaches where the temporal relationship between the interferograms represents the third dimension. As already mentioned there are many phase unwrapping algorithms. With the growing interest towards the multitemporal D-InSAR analysis and the generation of deformation time series, especially the three dimensional phase unwrapping becomes a research focus. As discussed before for the spatial phase unwrapping, the MCF approach by Costantini (1997) is a rather popular method and an extended version for the three dimensional case, the so called Extended MCF (EMCF) algorithm exists. In the context of this work, the EMCF algorithm has become state of the art in the RSG software and will be described in more detail.

5.1 Most Popular Approaches

The main literature relating to multitemporal phase unwrapping can be found in Pepe and Lanari (2006), Hooper et al. (2007), Shanker and Zebker (2010) and Costantini et al. (2012). Three dimensional phase unwrapping can be achieved either by using multiple steps or by a one-step algorithm. The edgelist algorithm by Shanker and Zebker (2010) allows the exploitation of redundant arcs as the problem is formulated as an parametric L_1-norm problem based on the primal graph, see PROBLEM 2 formulation in Section 4.3.1. In the three dimensional case this means that temporal arcs between the interferograms are allowed. However, as described in Costantini et al. (2012) it has to be considered that disturbing signals like the atmosphere, orbit errors etc. are removed by generating differences between the phase measurements in space but not by generating differences between the phase measurements in time. Therefore, the observation remains the double differences in time and in space, resulting in the functional model

$$\phi^{t_\beta}_{x_l} - \phi^{t_\alpha}_{x_l} - (\phi^{t_\beta}_{x_k} - \phi^{t_\alpha}_{x_k}) - 2\pi k^{\Delta t_{\alpha\beta}}_{\Delta x_{kl}} = \psi^{\Delta t_{\alpha\beta}}_{\Delta x_{kl}} \tag{5.1}$$

for one phase gradient $\psi^{\Delta t_{\alpha\beta}}_{\Delta x_{kl}}$ between two pixels x_k and x_l computed from two SAR images at times t_α and t_β. The interferograms can be generated following either the SBAS or the PSI method. Compared to the spatial phase unwrapping, the functional model can be reformulated by inserting the relationship (4.1) for each pixel at each time and considering that the wrapped phase gradient $\psi^{\Delta t_{\alpha\beta}}_{\Delta x_{kl}}$ is already a wrapped value in a range from $-\pi$ to π. Consequently, the functional model for the phase unwrapping in three dimensions results in

$$k^{t_\beta}_{x_l} - k^{t_\alpha}_{x_l} - k^{t_\beta}_{x_k} + k^{t_\alpha}_{x_k} - k^{\Delta t_{\alpha\beta}}_{\Delta x_{kl}} = -\lfloor \frac{\psi^{t_\beta}_{x_l} - \psi^{t_\alpha}_{x_l} - \psi^{t_\beta}_{x_k} + \psi^{t_\alpha}_{x_k}}{2\pi} \rceil. \tag{5.2}$$

The rounding operator $\lfloor . \rceil$ is only necessary for numerical issues to ensure that the phase ambiguity factors will be integer numbers. Due to the double differences, the problem is not really described by a three dimensional graph. Moreover, there are two graphs. One is defined in the azimuth/ range plane where the nodes are represented by the m stable pixels and the arcs represent the n spatial phase gradients. The second one is represented in time where the m' SAR images represent the nodes and the n' interferograms the arcs. It should be noted that the term in the denominator on the right-hand side of (5.2) is not equal to the measured wrapped interferometric phase gradient

$$\langle \psi^{t_\beta}_{x_l} - \psi^{t_\alpha}_{x_l} - \psi^{t_\beta}_{x_k} + \psi^{t_\alpha}_{x_k} \rangle_{-\pi,\pi} \neq \psi^{\Delta t_{\alpha\beta}}_{\Delta x_{kl}} . \tag{5.3}$$

This is due to the fact that the interferograms are individually handled in a preprocessing step, for example during the multilooking. So the observations are no longer the interferometric phase gradients but rather the phases per SAR image and per pixel. Collecting all phases of each SAR image and each pixel in one vector

$$\boldsymbol{\psi}^{\boldsymbol{t}}_{\boldsymbol{x}} = \begin{bmatrix} \psi^{t_\alpha}_{x_j} & \psi^{t_\beta}_{x_j} & \ldots & \psi^{t_\alpha}_{x_k} & \psi^{t_\beta}_{x_k} & \ldots \end{bmatrix}^T , \tag{5.4}$$

the functional model, cf. (5.2), for the three dimensional case results in

$$\boldsymbol{A}_{\mathrm{3D}} \boldsymbol{k}^{\boldsymbol{t}}_{\boldsymbol{x}} - \boldsymbol{k}^{\Delta \boldsymbol{t}}_{\Delta \boldsymbol{x}} = -\lfloor \frac{\boldsymbol{A}_{\mathrm{3D}} \boldsymbol{\psi}^{\boldsymbol{t}}_{\boldsymbol{x}}}{2\pi} \rceil \tag{5.5}$$

with the functional model matrix $\boldsymbol{A}_{\mathrm{3D}} \in \mathbb{Z}^{n' \cdot n \times m' \cdot m}$. One row of the matrix contains four entries each at the corresponding position of the pixel and the SAR image which is needed to generate the interferometric phase gradient. To get a better idea how the matrix looks like, Fig. 5.1 shows a small D-InSAR stack consisting of three SAR images between which three interferograms are formed and each interferogram contains four pixels between which five phase gradients are generated. Thus, the $\boldsymbol{A}_{\mathrm{3D}}$ matrix has a size of 15×12. The phase unwrapping problem is again defined by minimizing the weighted L$_1$-norm of the phase ambiguity factors $\boldsymbol{k}^{\Delta \boldsymbol{t}}_{\Delta \boldsymbol{x}}$. If these factors are further split into a

Example:

$\boldsymbol{A}_{\mathrm{3D}} \in \mathbb{Z}^{15 \times 12}$

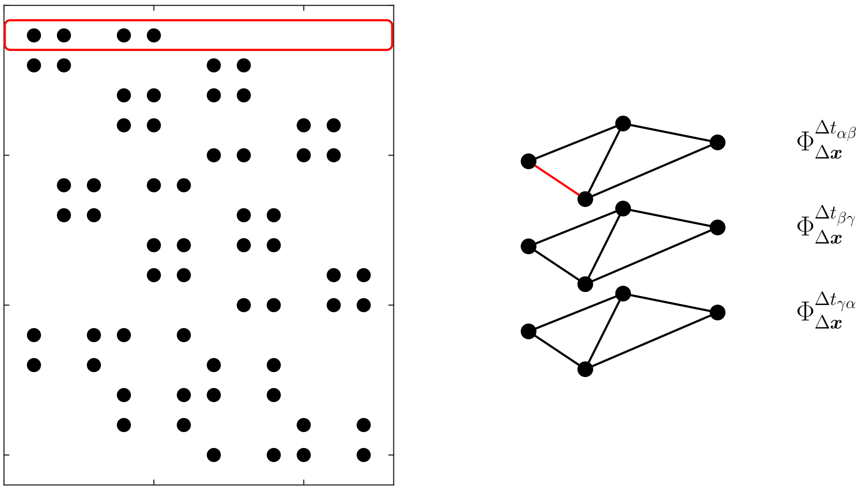

Figure 5.1: Exemplary structure of global $\boldsymbol{A}_{\mathrm{3D}}$ matrix for a small D-InSAR stack consisting of three interferograms and five spatial gradients.

positive and a negative component to represent the L_1-norm, the weighted L_1-norm problem for the three dimensional case results in

$$\boxed{\begin{array}{rl} \text{Objective function:} & C(\boldsymbol{x}) = \displaystyle\sum_{\forall \Delta t_{\alpha\beta} \in \mathcal{N}'} \sum_{\forall \Delta x_{kl} \in \mathcal{N}} p_{\Delta x_{kl}}^{\Delta t_{\alpha\beta}} k_{\Delta x_{kl}}^{\Delta t_{\alpha\beta},+} + p_{\Delta x_{kl}}^{\Delta t_{\alpha\beta}} k_{\Delta x_{kl}}^{\Delta t_{\alpha\beta},-} \ldots \min \\ \text{Constraint:} & \begin{bmatrix} \boldsymbol{A}_{\mathrm{3D}} & -\mathbf{1}_{[n'\cdot n \times n'\cdot n]} & \mathbf{1}_{[n'\cdot n \times n'\cdot n]} \end{bmatrix} \underbrace{\begin{bmatrix} \boldsymbol{k}_{\boldsymbol{x}}^{\boldsymbol{t}} \\ \boldsymbol{k}_{\boldsymbol{\Delta x}}^{\Delta \boldsymbol{t}_+} \\ \boldsymbol{k}_{\boldsymbol{\Delta x}}^{\Delta \boldsymbol{t}_-} \end{bmatrix}}_{\boldsymbol{x}} = \underbrace{-\left\lfloor \frac{\boldsymbol{A}_{\mathrm{3D}} \boldsymbol{\psi}_{\boldsymbol{x}}^{\boldsymbol{t}}}{2\pi} \right\rceil}_{\boldsymbol{b}} \\ \text{Variable:} & \boldsymbol{k}_{\boldsymbol{x}}^{\boldsymbol{t}} \in \mathbb{R}, \quad \boldsymbol{k}_{\boldsymbol{\Delta x}}^{\Delta \boldsymbol{t}_+}, \boldsymbol{k}_{\boldsymbol{\Delta x}}^{\Delta \boldsymbol{t}_-} \in \mathbb{R}_{\geq 0} \end{array}} \tag{5.6}$$

with the unknown phase ambiguity factors at each pixel and each SAR image $\boldsymbol{k}_{\boldsymbol{x}}^{\boldsymbol{t}}$ and the phase ambiguity factors at each phase gradient $\boldsymbol{k}_{\boldsymbol{\Delta x}}^{\Delta \boldsymbol{t}}$. Considering that a whole D-InSAR image with thousands of pixels and gradients will be unwrapped, the $\boldsymbol{A}_{\mathrm{3D}}$ matrix is high dimensional. Moreover, the matrix is no longer an arc-to-node incidence matrix, since the observations cannot be represented in a three dimensional graph, but rather in the two two dimensional graphs in the azimuth/range plane and the temporal plane. Thus the problem cannot be solved as a network flow problem. However, assuming integer values for the weights $\boldsymbol{p}_{\Delta \boldsymbol{x}}^{\Delta \boldsymbol{t}}$, the estimated phase ambiguity factors will be integers, as the constraint matrix is totally unimodular.

A remarkable problem is that the observations are no longer the interferometric phase gradients, but rather the phases per SAR image and per pixel. Remember that the three dimensional phase unwrapping method should be inserted into the SBAS workflow, shown in Fig. 2.9. Looking at the workflow, the phase unwrapping is applied to the multilooked interferograms. This filtering step is necessary as the here described test region is characterized by a very rural and therefore noisy area. However, this means that the one-step approach described in Costantini et al. (2012) and summarized in (5.6) cannot easily be integrated into the SBAS workflow. Assuming an equal sign in (5.3) and taking as observations the multilooked interferometric phase gradients, inconsistencies in the constraints occur so that the problem cannot be solved. However, the problem will be discussed in more detail in Chapter 7 where a one-step three dimensional approach will be developed based on the results of this and the following chapter.

In contrast, the EMCF algorithm by Pepe and Lanari (2006) works in two steps. The problem is downscaled to two simpler problems that are two dimensional and can therefore be solved easily as an LP as discussed for the spatial phase unwrapping in Section 4.3.1. It is a method which is fully compatible to the SBAS method. First, the phase gradients are individually unwrapped in the temporal space and afterwards the temporally unwrapped phase gradients are used to unwrap every single interferogram in the spatial domain. As this algorithm has become the state of the art in the RSG software, motivated by this study, it is discussed in more detail.

To conclude the most popular three dimensional phase unwrapping approaches, one last method has to be mentioned. Hooper and Zebker (2007) developed a framework by extending the branch-cut algorithm to three dimensions. Unlike the EMCF algorithm it works for both SBAS and PSI interferograms. A branch-cut line in the two dimensional case represents a branch-cut surface in three dimensions. These branch-cut surfaces can be divided into single cycle and multiple cycle discontinuity surfaces, depending on the size of the residues, one cycle for the first case and greater one for the second case. For the single cycle discontinuity surfaces they develop a minimum L$_p$-norm algorithm

$$\sum_{\forall \Delta t_{\alpha\beta} \in \mathcal{N}'} \sum_{\forall \Delta x_{kl} \in \mathcal{N}} |\phi^{\Delta t_{\alpha\beta}}_{\Delta x_{kl}} - \psi^{\Delta t_{\alpha\beta}}_{\Delta x_{kl}}|^p \ldots \min \tag{5.7}$$

whereas the constraint that unwrapped values differ from the wrapped phase values only by integer multiples of 2π is desirable. For $p = 0$ and $p = 1$ this can be the case. However, for $p = 2$ the unwrapped phase gradients are underestimated, as shown by Zebker and Lu (1998). For multiple cycle discontinuity surfaces a stepwise three dimensional algorithm is described. The phase gradients are first unwrapped in the temporal domain by low-pass filtering the complex phase gradient time series in the frequency domain. The result is then used in the second step as initial solution for unwrapping each interferogram in the two dimensional way. Similar to the EMCF algorithm, this stepwise solution is not optimal in a three dimensional case.

5.2 Extended Minimum Cost Flow Approach

The EMCF algorithm by Pepe and Lanari (2006) works in two main steps, based on two independent triangulations. One is generated in the azimuth/ range plane, analogous to the spatial MCF approach as shown in Fig. 4.4. The other one is generated in the so called temporal/ perpendicular baseline plane, see again Fig. 2.8b. As already discussed within the scope of SBAS interferogram generation, one temporal arc in the temporal/ perpendicular baseline plane represents one D-InSAR data pair. In order to avoid too strong decorrelation effects, interferograms with too long baselines or large Doppler frequency differences are removed from the triangulation.
On the basis of these two triangulations the EMCF approach can be applied according to the following two main steps: the temporal and the spatial unwrapping. To keep in mind, one interferogram consists of m stable pixels and n gradients resulting in r triangles and altogether there are m' SAR images resulting in n' interferograms and r' triangles in the temporal plane.

5.2.1 Temporal Phase Unwrapping

With time, the pixels are moving with a certain motion model. The goal is to detect these movements. In spatial phase unwrapping, it has been shown that phase unwrapping becomes difficult if the motion and the temporal baseline of the interferogram is large. The idea of the temporal phase unwrapping is to consider each phase gradient individually in all interferograms. For example, looking at the red arc in Fig. 5.1, assuming it is the arc Δx_{kl} between the two pixels x_k and x_l. The relative deformation of this phase gradient is measured three times between three different acquisition times, collected in the ambiguous observation vector $\boldsymbol{\psi}^{\boldsymbol{\Delta t}}_{\Delta x_{kl}}$. The temporal information is used to estimate the motion model of the phase gradient, whereas a linear motion model

$$\boldsymbol{M}(v_{\Delta x_{kl}}, \Delta h_{\Delta x_{kl}}) = \frac{4\pi}{\lambda} \boldsymbol{\Delta t} \cdot v_{\Delta x_{kl}} + \frac{4\pi}{\lambda} \frac{\Delta \boldsymbol{b}_\perp}{r \sin(\theta)} \cdot \Delta h_{\Delta x_{kl}} \tag{5.8}$$

is assumed with the temporal baseline $\boldsymbol{\Delta t}$ and the orthogonal spatial baseline $\Delta \boldsymbol{b}_\perp$ between the SAR images, the wavelength λ, the sensor target distance r in LOS and the incidence angle θ and the two unknown parameters, the error of the scene topography $\Delta h_{\Delta x_{kl}}$ and the deformation velocity variation $v_{\Delta x_{kl}}$ between the pixels x_k and x_l. In the following, the model $\boldsymbol{M}(v_{\Delta x_{kl}}, \Delta h_{\Delta x_{kl}})$ is briefly referred to as $\boldsymbol{M}$.
This motion model is used as preliminary information to estimate new modified observations

$$\boldsymbol{\chi}^{\boldsymbol{\Delta t}}_{\Delta x_{kl}} = \boldsymbol{M} + \langle \boldsymbol{\psi}^{\boldsymbol{\Delta t}}_{\Delta x_{kl}} - \boldsymbol{M} \rangle_{-\pi,\pi} \tag{5.9}$$

which offer a reduced number of phase ambiguities. This makes the phase unwrapping easier.

Assuming that the modified and unwrapped gradients differ again by a multiple of 2π, but this time by a smaller multiple than the original observations $\boldsymbol{\psi}_{\Delta x_{kl}}^{\boldsymbol{\Delta t}}$, the relationship is given by

$$\boldsymbol{\phi}_{\Delta x_{kl}}^{\boldsymbol{\Delta t}} = \boldsymbol{\chi}_{\Delta x_{kl}}^{\boldsymbol{\Delta t}} + 2\pi \boldsymbol{k}_{\Delta x_{kl}}^{\boldsymbol{\Delta t}} \tag{5.10}$$

with the unknown phase ambiguity factors $\boldsymbol{k}_{\Delta x_{kl}}^{\boldsymbol{\Delta t}}$.

As a reminder, in spatial phase unwrapping, spatial consistency is assumed as a constraint, i.e. the sum of the unwrapped phase gradients in a triangle of the spatial triangulation should be zero. The same applies to the temporal phase unwrapping. The unwrapped phase gradients should be consistent in time. This means that the sum of the unwrapped phase gradients in a triangle of the temporal triangulation, the so called loop closure phase should be zero. Considering again the red arc in Fig. 5.1 which is measured in a total of three interferograms. These gradients must therefore fulfill the following temporal constraint:

$$\phi_{\Delta x_{kl}}^{\Delta t_{\alpha\beta}} + \phi_{\Delta x_{kl}}^{\Delta t_{\beta\gamma}} + \phi_{\Delta x_{kl}}^{\Delta t_{\gamma\alpha}} = 0. \tag{5.11}$$

As mentioned in Section 2.3.2 in (2.22), the interferograms are not all fully consistent in time. However, this assumption is made for the temporal phase unwrapping. The temporally unwrapped phase gradients serve only as a preliminary solution which will be included in the spatial phase unwrapping, afterwards.

If (5.10) is inserted into (5.11), the temporal constraint results in

$$k_{\Delta x_{kl}}^{\Delta t_{\alpha\beta}} + k_{\Delta x_{kl}}^{\Delta t_{\beta\gamma}} + k_{\Delta x_{kl}}^{\Delta t_{\gamma\alpha}} = -\left\lfloor \frac{\chi_{\Delta x_{kl}}^{\Delta t_{\alpha\beta}} + \chi_{\Delta x_{kl}}^{\Delta t_{\beta\gamma}} + \chi_{\Delta x_{kl}}^{\Delta t_{\gamma\alpha}}}{2\pi} \right\rceil.$$

At this point, the rounding operator $\lfloor . \rceil$ is absolutely necessary and does not only serve for numerical purposes, since the right-hand side will usually not be an integer due to temporal inconsistency.

Analogous to the spatial MCF approach, the problem is defined as minimizing the L$_1$-norm of the phase ambiguity factors. So for the arc Δx_{kl} the temporal phase unwrapping results in

$$\boxed{\begin{array}{rl} \text{Objective function:} & C_{\text{temp}}(\boldsymbol{x}) = \underbrace{\begin{bmatrix} {\boldsymbol{p}_{\Delta x_{kl}}^{\boldsymbol{\Delta t}}}^T & {\boldsymbol{p}_{\Delta x_{kl}}^{\boldsymbol{\Delta t}}}^T \end{bmatrix}}_{\boldsymbol{c}_{\text{temp}}^T} \underbrace{\begin{bmatrix} \boldsymbol{k}_{\Delta x_{kl}}^{\boldsymbol{\Delta t},+} \\ \boldsymbol{k}_{\Delta x_{kl}}^{\boldsymbol{\Delta t},-} \end{bmatrix}}_{\boldsymbol{x}} \ldots \min \\ \text{Constraint:} & \begin{bmatrix} \boldsymbol{B}_{\text{temp}}^T & -\boldsymbol{B}_{\text{temp}}^T \end{bmatrix} \underbrace{\begin{bmatrix} \boldsymbol{k}_{\Delta x_{kl}}^{\boldsymbol{\Delta t},+} \\ \boldsymbol{k}_{\Delta x_{kl}}^{\boldsymbol{\Delta t},-} \end{bmatrix}}_{\boldsymbol{x}} = \underbrace{-\left\lfloor \frac{\boldsymbol{B}_{\text{temp}}^T \boldsymbol{\chi}_{\Delta x_{kl}}^{\boldsymbol{\Delta t}}}{2\pi} \right\rceil}_{\boldsymbol{b}_{\text{temp}}} \\ \text{Variable:} & \boldsymbol{x} \in \mathbb{R}_{\geq 0} \end{array}} \tag{5.12}$$

with the target function vector $\boldsymbol{c}_{\text{temp}} \in \mathbb{Z}^{2n'}$, the parameter vector $\boldsymbol{x} \in \mathbb{Z}^{2n'}$, the constraint matrix $\boldsymbol{B}_{\text{temp}}^T \in \mathbb{Z}^{r' \times n'}$ and the right-hand side vector $\boldsymbol{b}_{\text{temp}} \in \mathbb{Z}^{r'}$. One row of $\boldsymbol{B}_{\text{temp}}^T$ contains zeros except the columns which belong to the defining arcs of the actual triangle. These are filled with one or minus one depending on the orientation of the arc. For the sake of simplicity, the weights $\boldsymbol{p}_{\Delta x_{kl}}^{\boldsymbol{\Delta t}}$

are generally set to one. As the constraint matrix is totally unimodular, the estimated parameters will be integers.

Consequently, the problem can be solved with an LP solver analogous to the spatial phase unwrapping, see PROBLEM 1 formulation in Section 4.3.1. It has to be mentioned that the network in the temporal/ perpendicular baseline plane must always contain loop closure constraints for the application of the EMCF algorithm. However, this does not necessarily have to be a triangulation. Fornaro et al. (2011) allows a free choice of the network in the temporal/ perpendicular baseline plane with overlapping arcs and consequently an increased degree of freedom. The advantage of a triangulation without overlapping arcs is that the network represents a planar graph and can therefore be solved very efficiently as a network flow problem (Costantini, 1997), see PROBLEM 3 formulation in Section 4.3.1. Theoretically, it is also possible to solve the temporal phase unwrapping as a parametric L$_1$-norm problem as done in the PROBLEM 2 and PROBLEM 4 formulations in Section 4.3.1 for the spatial phase unwrapping. However, this implies that the modified observations $\boldsymbol{\chi}^{\boldsymbol{t}}_{\Delta x_{kl}}$ for every SAR image are needed and this cannot be easily integrated into the SBAS workflow. Consequently, the temporal phase unwrapping is solved as a constrained L$_1$-norm problem, see (5.12).

The problem remains that the variables $v_{\Delta x_{kl}}$ and $\Delta h_{\Delta x_{kl}}$ which are included in the sequence of modified observations $\boldsymbol{\chi}^{\boldsymbol{\Delta t}}_{\Delta x_{kl}}$ are unknown. Therefore, the parameter vector $\boldsymbol{k}^{\boldsymbol{\Delta t}}_{\Delta x_{kl}}$ is sequentially estimated for each ($v_{\Delta x_{kl}}$, $\Delta h_{\Delta x_{kl}}$)-pair in a predefined discrete search space Ω resulting in one cost function value C_{temp}. The optimal solution is obtained by the pair where the cost value is minimal. This solution is symbolized with a bar, afterwards.

5.2.2 Spatial Phase Unwrapping

So far, the unknown phase ambiguity factor $\bar{k}^{\Delta t_{\alpha\beta}}_{\Delta x_{kl}}$ and thus the corresponding unwrapped phase gradient

$$\bar{\phi}^{\Delta t_{\alpha\beta}}_{\Delta x_{kl}} = \bar{\chi}^{\Delta t_{\alpha\beta}}_{\Delta x_{kl}} + 2\pi \bar{k}^{\Delta t_{\alpha\beta}}_{\Delta x_{kl}} \tag{5.13}$$

for each spatial arc in each D-InSAR image is estimated via the temporal phase unwrapping. In a second step, the phase is unwrapped for each single interferogram separately. With this step, the previously created temporal constraint in (5.12) is destroyed again.

In the following one single D-InSAR image, computed out of the difference of two SAR acquisitions at times t_α and t_β is assumed. The phase is unwrapped along each arc via the spatial MCF approach, cf. (4.13), whereas the previously calculated temporally unwrapped phase gradients $\bar{\phi}^{\Delta t_{\alpha\beta}}_{\boldsymbol{\Delta x}}$ are used as starting point. The required weights along each spatial arc Δx_{kl} can be derived using the previously calculated cost value $\bar{C}_{\text{temp}_{\Delta x_{kl}}}$ for the corresponding arc Δx_{kl}. Large costs mean that the probability of an occurring phase ambiguity is large and therefore the unwrapped phase can be erroneous. Hence, this arc is less familiar and its influence is lowered by low weights. The weights are derived by an inverse exponential relation (Pepe and Lanari, 2006)

$$p^{\Delta t_{\alpha\beta}}_{\Delta x_{kl}} = \begin{cases} 2^S/2^{\bar{C}_{\text{temp}_{\Delta x_{kl}}}} & \bar{C}_{\text{temp}_{\Delta x_{kl}}} < \rho \\ 1 & \bar{C}_{\text{temp}_{\Delta x_{kl}}} \geq \rho \end{cases} \tag{5.14}$$

with an upper limit for the maximum cost 2^S and a threshold ρ. The quotient of two logarithmic quantities to base 2 and the integer costs ensure that the weights are also integer values. The final absolutely unwrapped phase at each pixel can be determined by integrating the unwrapped phase gradient along each arc independently of the integration path.

5.2.3 Application to Simulated Data

In this section, the EMCF algorithm discussed above will be applied to the simulated D-InSAR stack, cf. Section 4.3.2.1. To find the optimal motion model parameters, the search area is chosen in a range from $-8\,\mathrm{cm/yr}$ to $8\,\mathrm{cm/yr}$ with a step width of $0.5\,\mathrm{cm/yr}$ for the deformation velocity variation $v_{\Delta x_{kl}}$ and in a range from $-50\,\mathrm{m}$ to $50\,\mathrm{m}$ with a step width of $5\,\mathrm{m}$ for the error of the scene topography $\Delta h_{\Delta x_{kl}}$ between the pixels x_k and x_l. For every possible $(v_{\Delta x_{kl}}, \Delta h_{\Delta x_{kl}})$-pair the modified observations are estimated and the corresponding temporal LP, cf. (5.12), is solved. The pair which minimizes the cost function is defined as optimal.

Figure 5.2b shows the phase unwrapping results using the EMCF algorithm for the already analyzed interferogram with a temporal baseline of $\Delta t_{\alpha\beta} = 315\,\mathrm{days}$ and an orthogonal spatial baseline of $\Delta b_{\perp,\alpha\beta} = 76.3225\,\mathrm{m}$. Figure 4.9a shows the reference phase. Using the spatial MCF approach without considering the temporal information, the method is not able to reconstruct the settlement depression correctly, see Fig. 4.10. However, comparing the reference phase with Fig. 5.2b, it can be seen that the reference phase is reconstructed more correctly via the EMCF approach. In this case this is mainly due to the estimated motion model. Figure 5.2a shows the modified observations that include the motion model, see (5.9). The lines between the pixels symbolize the phase gradients where a phase ambiguity factor unequal zero occurs in contrast to the observed phase gradients.

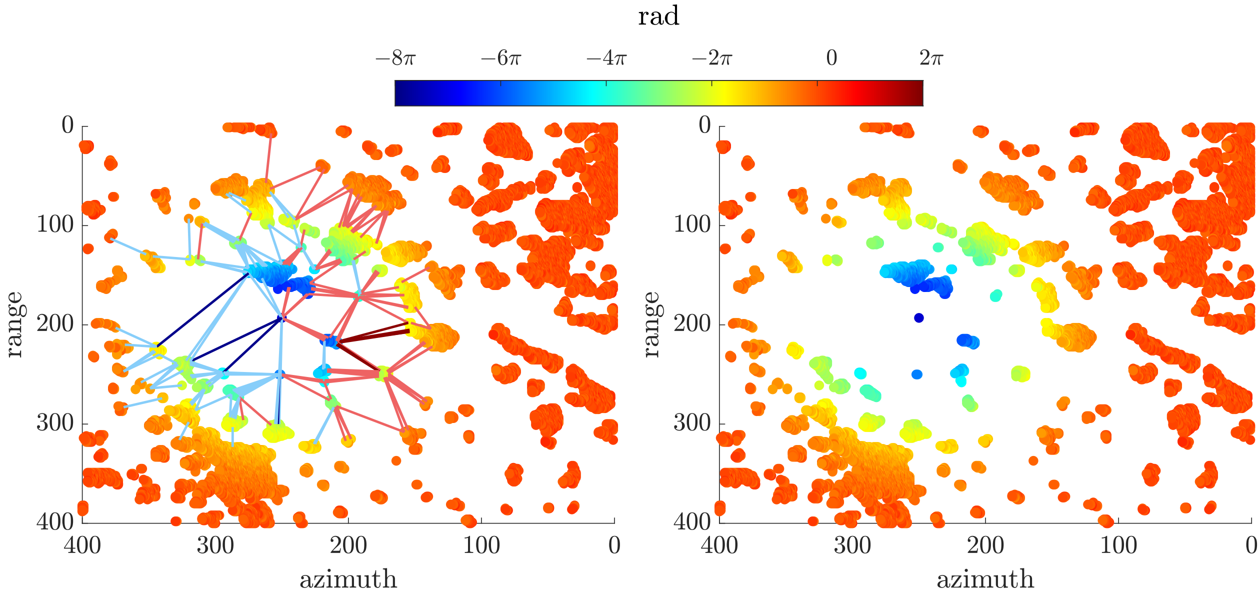

(a) modified observation **(b)** unwrapped phase using the EMCF algorithm

Figure 5.2: Phase unwrapping results of the simulated ground settlement depression for one interferogram with a temporal baseline of $\Delta t_{\alpha\beta} = 315\,\mathrm{days}$ and an orthogonal spatial baseline of $\Delta b_{\perp,\alpha\beta} = 76.322\,\mathrm{m}$ using the EMCF algorithm. The lines in Fig. 5.2a between the pixels show the phase gradients where a phase ambiguity factor unequal zero occurs in contrast to the observed phase gradients, see Fig. 4.9b. Dark blue means a phase ambiguity factor of -2, light blue of -1, dark red of 2 and light red of 1. Between the modified observation in Fig. 5.2a and the unwrapped phase in Fig. 5.2b is no longer a difference.

Dark blue means a phase ambiguity factor of -2, light blue of -1, dark red of 2 and light red of 1. These modified observations enter the temporal phase unwrapping, cf. (5.12), and then in a second step the spatial phase unwrapping is done. In these two steps, however, nothing happens anymore so that in Fig. 5.2b no lines between the pixels can be seen. Thus, the modified observations already correspond to the unwrapped phase gradients.

However, this is not always the case. In addition, a second interferogram is examined, this time with a very large temporal baseline. Figure 5.3 shows the results of an interferogram with a temporal baseline of $\Delta t_{\alpha\beta} = 1669$ days and an orthogonal spatial baseline of $\Delta b_{\perp,\alpha\beta} = 8.220$ m.

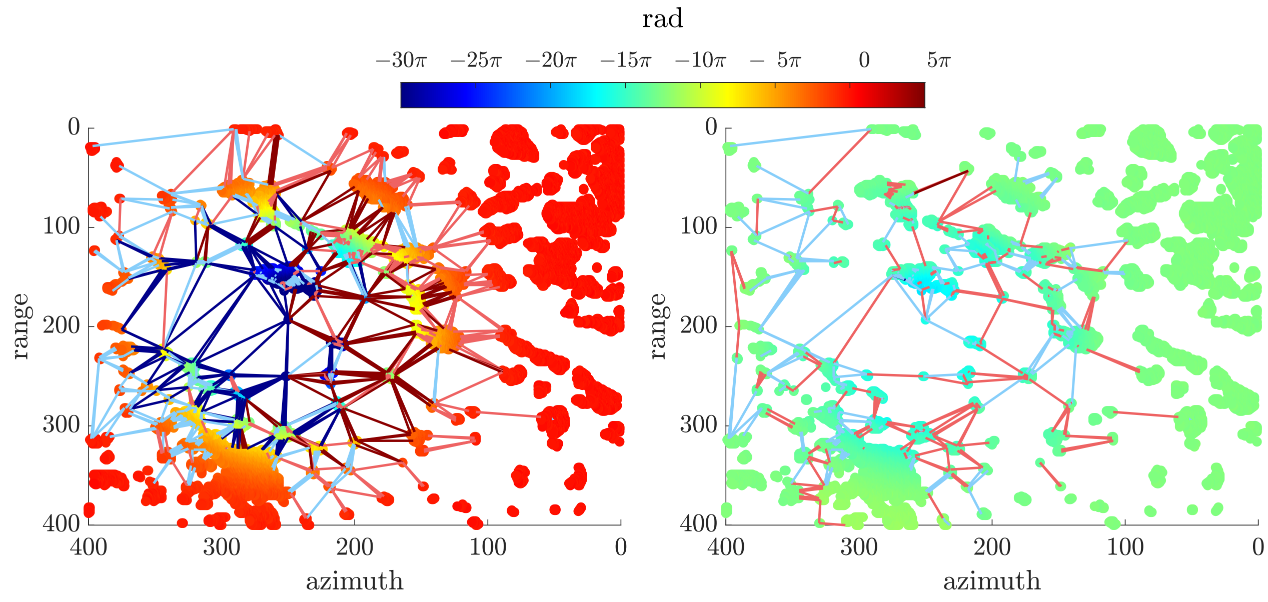

(a) reference phase

(b) unwrapped phase using the MCF algorithm without considering the temporal information

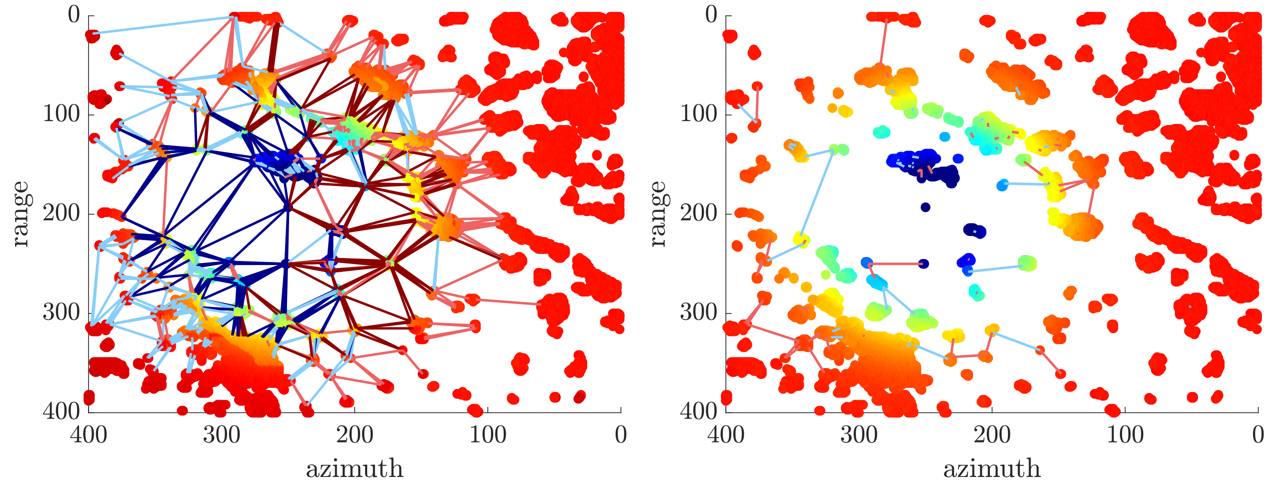

(c) modified observations

(d) unwrapped phase using the EMCF algorithm with considering the temporal information

Figure 5.3: Phase unwrapping results of the simulated ground settlement depression for one interferogram with a very large temporal baseline of $\Delta t_{\alpha\beta} = 1669$ days and an orthogonal spatial baseline of $\Delta b_{\perp,\alpha\beta} = 8.220$ m using the MCF and the EMCF algorithm. For Fig. 5.3a to Fig. 5.3c, the lines between the pixels show the phase gradients where a phase ambiguity factor unequal zero occurs in contrast to the observed phase gradients. For Fig. 5.3d the estimated phase ambiguity factors refer to the modified observations in Fig. 5.3c. Dark blue means a phase ambiguity factor smaller than -1, light blue of -1, dark red of greater than 1 and light red of 1.

Figure 5.3a shows the reference phase. This time, the phases have a much wider range of values from -30π to 2π, because of the movement resulting from the large temporal baseline. The lines again symbolize the phase gradients that exceed the measurable range of values. The dark colors indicate that the phase ambiguity factor has a value greater than 1 or less than -1. A detailed differentiation of the multiple phase jumps is omitted here for reasons of clarity. In total, the absolute sum of the phase ambiguity factors is 1789, in contrast to the observed phase. Figure 5.3b shows the results of the spatial phase unwrapping without considering the temporal information. As expected, it is not possible to reconstruct the settlement depression correctly without considering a motion model. The absolute sum of the estimated phase ambiguity factors is 521, i.e. well below the reference. Figure 5.3c shows the modified observations that include the estimated motion model. In contrast to the observed phase the absolute sum already includes 1762 estimated phase ambiguity factors. This is very close to the reference. These observations already show a reduced number of phase ambiguities. They enter into the EMCF algorithm finally resulting in the unwrapped phases displayed in Fig. 5.3d. During the phase unwrapping more phase ambiguity factors are estimated, see the lines in the figure. In the absolute sum, 1789 phase ambiguity factors are added so that the reference phase is reconstructed correctly.

For an overall comparison, Fig. 5.4a shows the total number of phase ambiguity factors in contrast to the observed phase gradients. The blue squares are the results of the MCF approach. As already seen the MCF approach is not able to reconstruct the reference shown as black stars. The results of the EMCF approach are represented as green triangles. The extension of the temporal information and the associated consideration of a motion model leads to an improvement. The results of the EMCF approach reproduce the reference. Figure 5.4b verifies this. The figure shows the percentage of correctly unwrapped phase gradients depending on the temporal baseline. Again, the blue bars are the results of the MCF approach and the green bars the results of the EMCF approach. It is obvious that the EMCF approach shows an improvement against the MCF approach. The inclusion of the temporal phase unwrapping results in a higher percentage of correctly unwrapped phase gradients which confirms the findings of Pepe and Lanari (2006). For every interferogram, even for the ones with a larger baseline and therefore larger movements, nearly 100 % of phase gradients are unwrapped correctly.

It can be concluded that the three dimensional phase unwrapping algorithm leads to an improvement in the correctness of the results. However, when implementing the EMCF algorithm and applying it to simulated and real data, it has been shown that there are aspects that can be further improved and optimized. These aspects will be discussed in the following chapter.

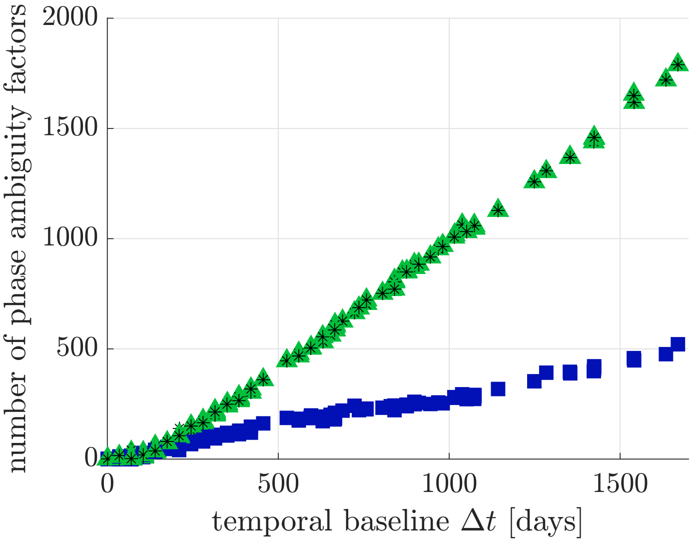

(a) absolute number of phase ambiguity factors compared to the observed phase gradients

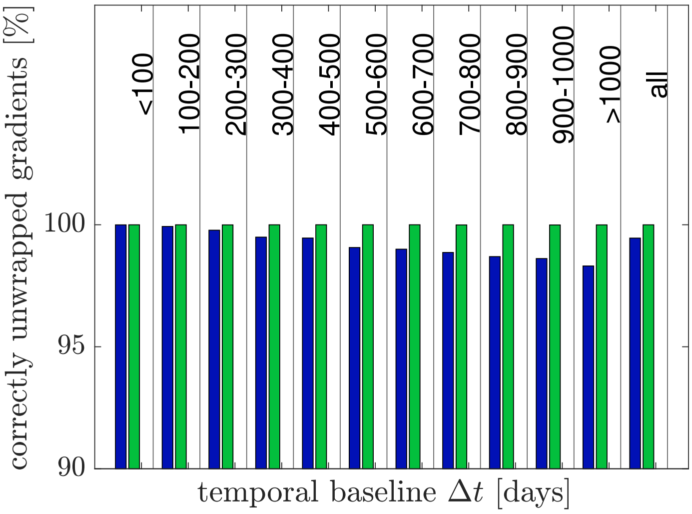

(b) Percentage of correctly unwrapped phase gradients

Figure 5.4: Solution of the unwrapped phase gradients depending on the temporal baseline. The dark blue color represents the results using the MCF approach and the green color represents the results using the EMCF approach. For comparison, the black stars in Fig. 5.4a show the reference solution.

6. Extended Minimum Cost Flow Approach – Ideas of Improvements

As shown on the basis of the simulated D-InSAR stack, the inclusion of the temporal information results in a higher percentage of correctly unwrapped gradients. However, there are some aspects which can be further improved. The first aspect involves the estimation of a suitable motion model to calculate modified observations, cf. (5.9). These modified observations contain a reduced number of phase ambiguities which makes phase unwrapping much easier. The second aspect deals with the choice of weights when setting up the LPs. In the following, some ideas of improvements are discussed and compared with the conventional EMCF approach. The aspect of estimating the motion model has already been published in Esch et al. (2019a). For a better comparison, the individual steps of the conventional EMCF algorithm are summarized in the flowchart shown in Fig. 6.1.

6.1 Estimation of the Motion Model

The estimation of the optimal motion model during the temporal phase unwrapping is an important step. Considering the spatial arc Δx_{kl}, the motion model includes the unknown deformation velocity variation $v_{\Delta x_{kl}}$ and the error of the scene topography $\Delta h_{\Delta x_{kl}}$. This model is used to estimate the modified observations $\boldsymbol{\chi}^{\boldsymbol{\Delta t}}_{\Delta x_{kl}}$, cf. (5.9), which are inserted into the temporal LP, cf. (5.12). In the conventional workflow, the optimal motion model is determined in an iterative search process. Therefore, the range of the scene topography and the deformation velocity is limited to a special search space Ω and discretized with a certain step width, see Fig. 6.1. For each $(v_{\Delta x_{kl}}, \Delta h_{\Delta x_{kl}})$-pair, the temporal LP is solved and the pair that results in the minimal cost value $\bar{C}_{\text{temp}}$ is defined as optimal. However, this procedure has some disadvantages. It is not straightforward how to select the search space and the step width effectively. Increasing the search space and refining the step width, the complexity grows. Moreover, the choice depends on the Euclidean distance between the pixels x_k and x_l of the regarded phase gradient $\psi^{\boldsymbol{\Delta t}}_{\Delta x_{kl}}$. For larger gradients the error of the scene topography and the deformation velocity variation may be greater compared to shorter gradients. Moreover, due to the discrete optimization function the solution is typically not unique. In this case it is assumed that the deformation velocity variation and the error of the scene topography of the phase gradient are as small as possible.

The problem of multiple potential local minima is also addressed in Imperatore et al. (2015). To find a robust motion model, it is proposed not to estimate the parameters directly based on the total search space, but to calculate successive solutions over a sequence of nested search spaces. For each search space, an optimal motion model is estimated and then the phase is unwrapped. The individual solutions of each search space are then combined using a weighted average. This approach has proven to be very robust against local minima of the discrete temporal cost function (Imperatore et al., 2015).

However, this procedure still has the disadvantages listed above, a search space must first be defined with a certain discretization and it remains an iterative procedure, where the temporal LP has to be solved in each iteration step. The goal is to find an estimation method for the motion model parameters that is independent of the solution of the temporal LP. This has the advantage that the temporal LP has to be solved only once for each spatial gradient. Therefore, an alternative way is

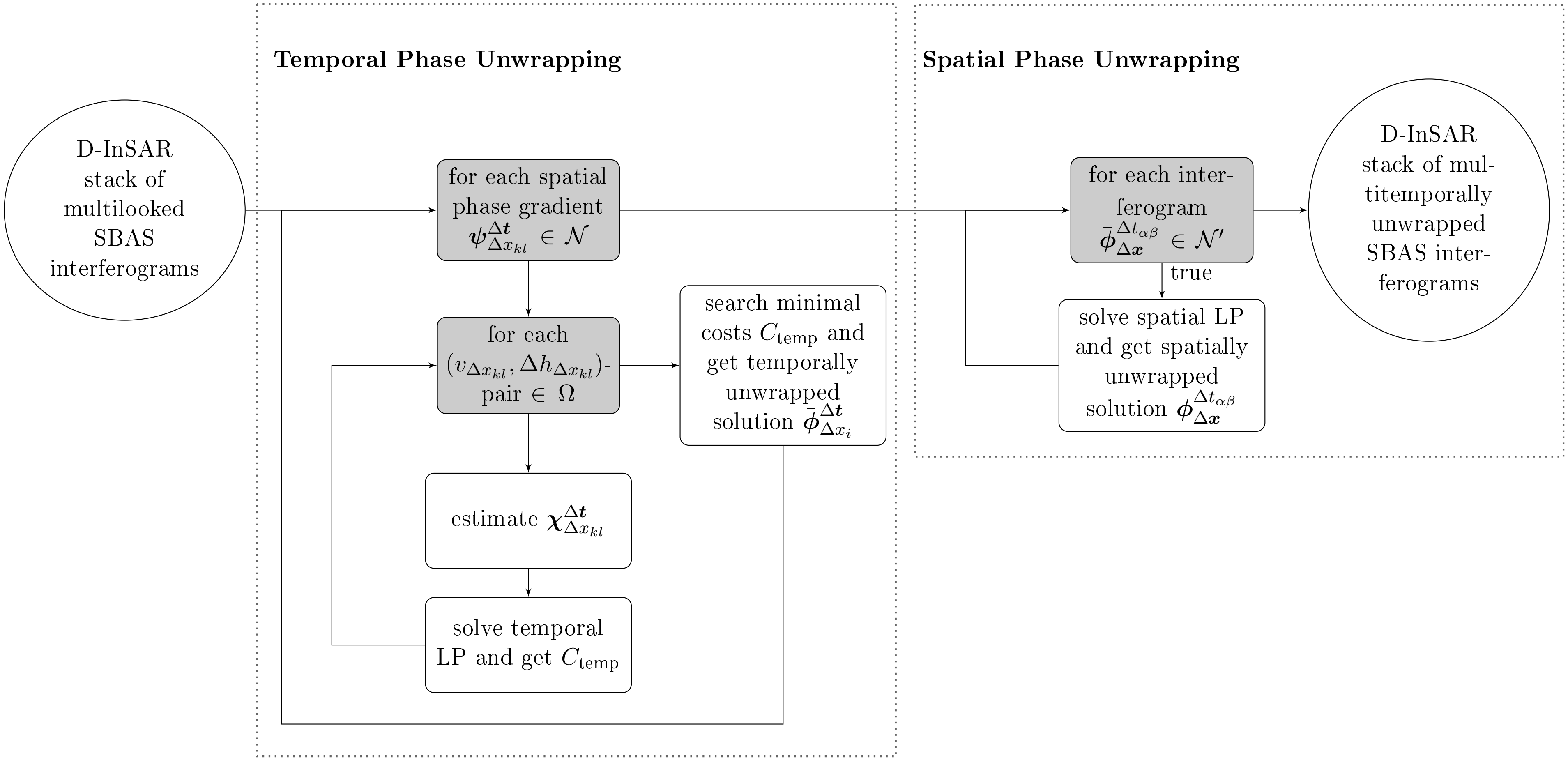

Figure 6.1: Flowchart of conventional stepwise EMCF algorithm by Pepe and Lanari (2006) for a D-InSAR stack of a set $\mathcal{N}'$ of interferograms whereas each interferogram consists of a set $\mathcal{N}$ of phase gradients. To estimate the motion model parameters a predefined search space Ω is used.

proposed here which uses the so called Ensemble Phase Coherence (EPC) (Zhang et al., 2014). The EPC gives a value for the quality of the estimated model for each phase gradient. For the arc Δx_{kl} it is defined as

$$EPC(v_{\Delta x_{kl}}, \Delta h_{\Delta x_{kl}}) = \left| \frac{1}{n'} \sum_{\forall \Delta t_{\alpha\beta} \in \mathcal{N}'} e^{i(\psi_{\Delta x_{kl}}^{\Delta t_{\alpha\beta}} - \boldsymbol{M})} \right| \tag{6.1}$$

with $\boldsymbol{M}$ from (5.8) which depends on the parameters $v_{\Delta x_{kl}}$ and $\Delta h_{\Delta x_{kl}}$. The EPC function is continuous with values between zero and one. A value of zero means that model and observation do not fit and a value of one corresponds to an optimal fit. Figure 6.2 shows the EPC function exemplary for one simulated phase gradient. It can be seen that the function shows a clear maximum. At this maximum the error of the scene topography and the deformation velocity variation fit best to the observations. The idea is to find this maximum of the EPC function and to use the corresponding parameters as optimal motion model parameters to calculate the modified observations. The modified flowchart of this alternative EMCF algorithm is shown in Fig. 6.3.

However, with an increasing noise level the maximum value of the function decreases and it gets difficult to find the global maximum. Three different methods are used for this purpose: the Nelder-Mead method (Nelder and Mead, 1965), a grid search approach and simulated annealing (Kirkpatrick et al., 1983). Some of them need a starting point which results from a two-step weighted least squares adjustment, cf. Zhang et al. (2014). First, it is assumed that the observed wrapped phase gradients do not differ from the unwrapped ones. Therefore, the functional model for one phase gradient $\boldsymbol{\psi}_{\Delta x_{kl}}^{\boldsymbol{\Delta t}}$ becomes

$$\boldsymbol{\psi}_{\Delta x_{kl}}^{\boldsymbol{\Delta t}} = \frac{4\pi}{\lambda} \boldsymbol{\Delta t} \cdot v_{\Delta x_{kl}} + \frac{4\pi}{\lambda} \frac{\boldsymbol{\Delta b}_\perp}{r \sin(\theta)} \cdot \Delta h_{\Delta x_{kl}} \tag{6.2}$$

with the temporal baseline vector $\boldsymbol{\Delta t} \in \mathbb{R}^{n'}$ and the orthogonal spatial baseline vector $\boldsymbol{\Delta b}_\perp \in \mathbb{R}^{n'}$. After applying a weighted least squares adjustment, the estimated parameters result in

$$\begin{bmatrix} \hat{v}_{\Delta x_{kl}} \\ \Delta\hat{h}_{\Delta x_{kl}} \end{bmatrix} = (\boldsymbol{A}^T \boldsymbol{P} \boldsymbol{A})^{-1} \boldsymbol{A} \boldsymbol{P} \boldsymbol{\psi}_{\Delta x_{kl}}^{\boldsymbol{\Delta t}} \tag{6.3}$$

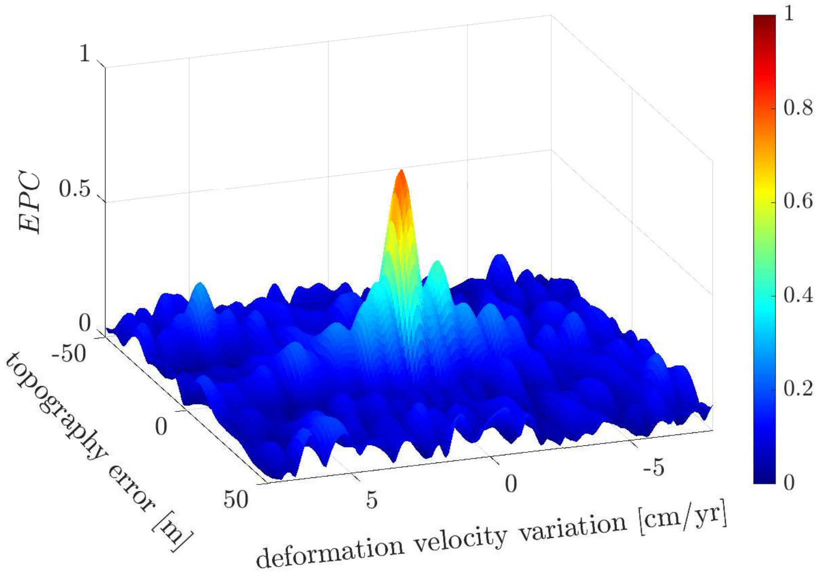

Figure 6.2: EPC function exemplary for one phase gradient depending on the error of the scene topography and the deformation velocity variation.

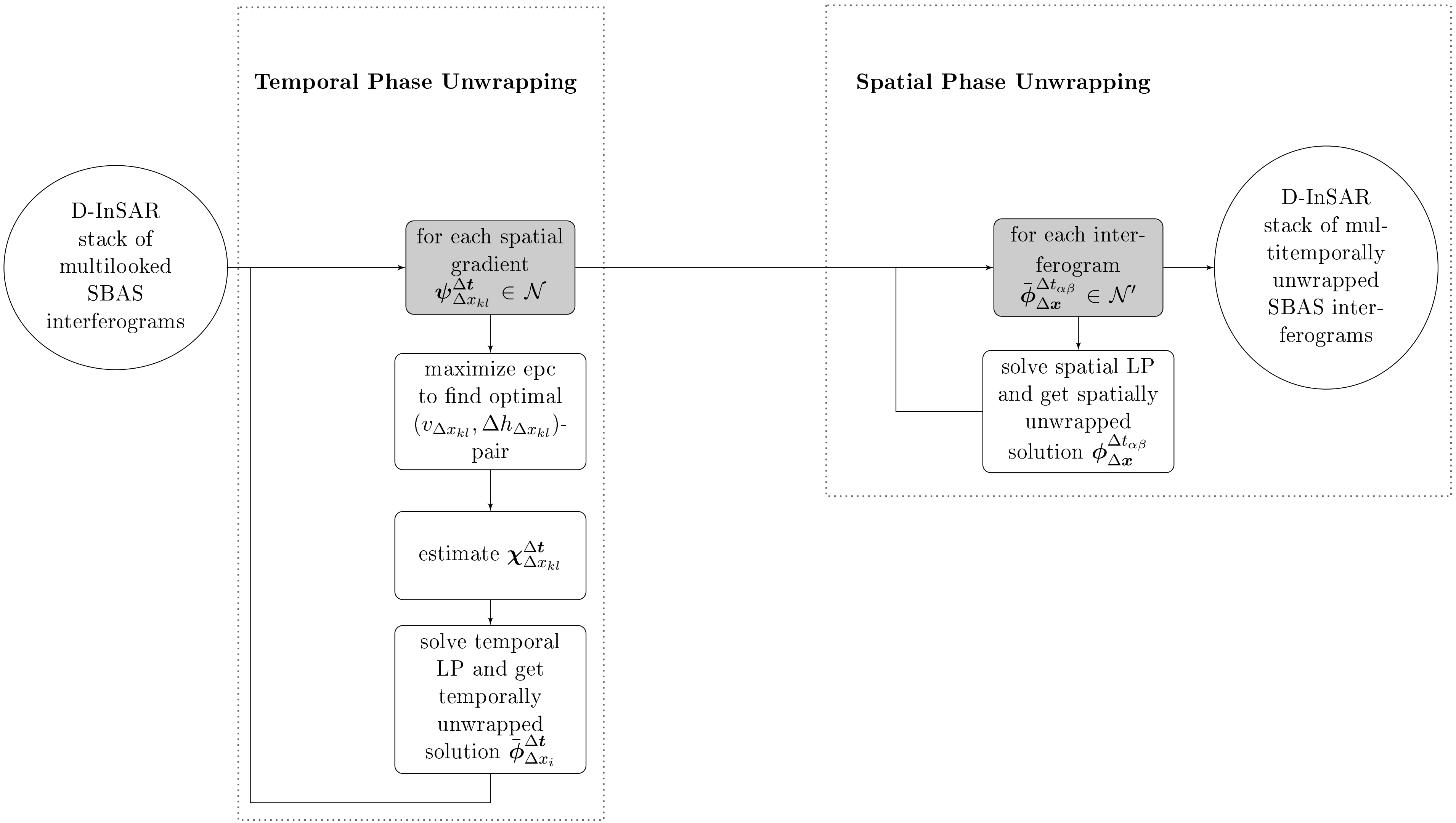

Figure 6.3: Flowchart of alternative stepwise EMCF algorithm for a D-InSAR stack of a set $\mathcal{N}'$ of interferograms whereas each interferogram consists of a set $\mathcal{N}$ of phase gradients. The optimal motion model is found by maximizing the EPC. Compared to Fig. 6.1, the sequentially solution of the LP for each $(v_{\Delta x_{kl}}$, $\Delta h_{\Delta x_{kl}})$-pair in a predefined discrete search space Ω is no longer needed.

with the design matrix

$$\boldsymbol{A} = \begin{bmatrix} \frac{4\pi}{\lambda}\boldsymbol{\Delta t} & \frac{4\pi}{\lambda}\frac{\Delta \boldsymbol{b}_{\perp}}{r\sin{(\theta)}} \end{bmatrix} \tag{6.4}$$

and the weight matrix $\boldsymbol{P} \in \mathbb{R}^{n' \times n'}$ which is a diagonal matrix with the vector

$$\boldsymbol{p} = \frac{1}{|\frac{4\pi}{\lambda}\boldsymbol{\Delta t} \cdot \frac{4\pi}{\lambda}\frac{\Delta \boldsymbol{b}_{\perp}}{r\sin{(\theta)}}|} \tag{6.5}$$

on its diagonal. The weights are chosen so that phase gradients with longer temporal and spatial baselines are considered less reliable. As the assumption that the wrapped and unwrapped phase gradients are equal is not always true in reality, the estimated parameters $\hat{v}_{\Delta x_{kl}}$ and $\Delta\hat{h}_{\Delta x_{kl}}$ might not be a feasible starting solution. Therefore, some new modified observations

$$\boldsymbol{\chi}^{\boldsymbol{\Delta t}}_{\Delta x_{kl}} = \boldsymbol{M}(\hat{v}_{\Delta x_{kl}}, \Delta\hat{h}_{\Delta x_{kl}}) + \langle \boldsymbol{\psi}^{\boldsymbol{\Delta t}}_{\Delta x_{kl}} - \boldsymbol{M}(\hat{v}_{\Delta x_{kl}}, \Delta\hat{h}_{\Delta x_{kl}}) \rangle_{-\pi,\pi} \tag{6.6}$$

are estimated. Again, it is assumed that these new observations are equal to the unwrapped phase gradients. The final estimated motion model parameters result in

$$\begin{bmatrix} \tilde{v}_{\Delta x_{kl}} \\ \Delta\tilde{h}_{\Delta x_{kl}} \end{bmatrix} = (\boldsymbol{A}^T\boldsymbol{P}\boldsymbol{A})^{-1}\boldsymbol{A}^T\boldsymbol{P}\boldsymbol{\chi}^{\boldsymbol{\Delta t}}_{\Delta x_{kl}}. \tag{6.7}$$

These parameters are used to initialize the search processes which will be described in the following.

Grid Search Method

One of the easiest search processes is the grid search process. Similar to the iterative search process a special search space is analyzed with a defined step width. At each grid the objective function is evaluated and the optimum is defined at the smallest or the highest one, depending on the optimization task. The whole algorithm is described in Algorithm 1 for a general maximization task with an objective function $f(\boldsymbol{x})$. To find the optimal motion model parameters, the EPC is calculated in each iteration step. So the problem of the definition of a search space and the step width remains. However, when compared to the conventional method the advantage is that the temporal LP has only to be solved once and not in each iteration step.

Nelder-Mead Method

The downhill simplex or Nelder-Mead method (Nelder and Mead, 1965) is a direct search algorithm to find the optimum of a non-linear unconstrained objective function without knowing the derivatives. The algorithm compares the function values at the nodes of a simplex which is a triangle for

Algorithm 1: Grid Search Method for maximizing the objective function $f(\boldsymbol{x})$

```
Data: search parameter space: $\boldsymbol{x}$
Result: best parameter vector : $\widetilde{\boldsymbol{x}}$
$f_{\max} = 0$;
for $j = 1 \dots N_x$ do
    $f = f(\boldsymbol{x}(j))$;
    if $f > f_{\max}$ then
        $f_{\max} = f$;
        $\widetilde{\boldsymbol{x}} = \boldsymbol{x}(j)$;
    end
end
```

two variables. The initial triangle is generated around a given starting point. The worst node with the smallest function value, when searching for the maximum, is rejected and replaced with a new one. This new node is placed in a direction away from the worst one. Therefore, three operations are used: reflection, contraction and expansion. In the following the best node is symbolized by $\boldsymbol{x}_1$, the second best by $\boldsymbol{x}_2$, the worst one by $\boldsymbol{x}_3$ and the centroid of the two best nodes by $\boldsymbol{x}_m$. The reflected node is defined as

$$\boldsymbol{x}_r = (1+\alpha)\boldsymbol{x}_m - \alpha\boldsymbol{x}_3 \tag{6.8}$$

with a positive reflection coefficient α. If the reflected point is better than the second best and inferior to the best one, a new triangle is generated and the algorithm starts again. Otherwise, if the reflected point is better than the best one, the expansion by the relation

$$\boldsymbol{x}_e = \gamma\boldsymbol{x}_r + (1-\gamma)\boldsymbol{x}_m \tag{6.9}$$

with the expansion coefficient γ which is greater than one is used. If this expanded point is a further improvement to the best one, the expanded one is used to generate a new triangle. Otherwise, the reflected one is used. Remains the case if the reflected point is inferior to the second best. Then, the contraction is used by the relation

$$\boldsymbol{x}_c = \beta\boldsymbol{x}_h + (1-\beta)\boldsymbol{x}_m \tag{6.10}$$

with the contraction coefficient β which lies between zero and one. Point $\boldsymbol{x}_h$ is the better point of $\boldsymbol{x}_3$ and $\boldsymbol{x}_r$. If the contracted point is better than the worst one, the worst is replaced by the contracted point. Otherwise, a new reduced triangle around the best point is generated. The algorithm stops if the abort criterion is fulfilled. According to Nelder and Mead (1965) the standard error of the objective values

$$\Delta f = \sqrt{\frac{1}{2}\sum_{i=1}^{2}(f(\boldsymbol{x}_i) - f(\boldsymbol{x}_m))^2} \tag{6.11}$$

is compared to a given threshold ϵ and it stops if Δf is below this value. The whole algorithm is described in Algorithm 2 for a general objective function $f(\boldsymbol{x})$ with a two dimensional parameter vector $\boldsymbol{x}$.

Simulated Annealing

Simulated annealing is a heuristic algorithm to find a global optimum of a given function. It finds a solution that is good enough in a reasonable amount of time. The name simulated annealing is inspired by the process of annealing in metal work. Annealing involves heating and cooling a material. With changing temperatures, the internal structure alters. A high temperature means a high dynamic and as the metal cools its new structure becomes fixed. With help of a temperature variable simulated annealing simulates this heating process. Metropolis et al. (1953) introduced the algorithm in order to simulate substances consisting of interacting molecules. Later on, Kirkpatrick et al. (1983) applied the algorithm to combinatorial optimization problems. A typical example is the traveling salesman problem. The description of simulated annealing is shown in Algorithm 3 for a general objective function $f(\boldsymbol{x})$ which has to be maximized. The algorithm works iteratively. It starts at a point $\boldsymbol{x}$ which is set to the actual optimal solution $\widetilde{\boldsymbol{x}}$. In each iteration a neighboring point $\boldsymbol{x}'$ is randomly chosen by a sampling process. If the new objective function $f(\boldsymbol{x}')$ is higher than the actual objective function $f(\widetilde{\boldsymbol{x}})$, the new sample is used in the next iteration as actual optimal solution $\widetilde{\boldsymbol{x}}$. However, if the objective function of the new point is lower, it is not directly rejected. It is accepted with a defined acceptance probability. This guarantees that the algorithm does not immediately end at a local optimum. Comparable to the annealing process, the probability decreases for lower temperature T and for larger differences between the two objective values as described in Metropolis et al. (1953). Therefore, the probability is defined as

$$P(\widetilde{\boldsymbol{x}}, \boldsymbol{x}', T) = \exp\,(\frac{-(f(\widetilde{\boldsymbol{x}}') - f(\boldsymbol{x}))}{T}). \tag{6.12}$$

The probability is compared to a random number uniformly distributed in an interval (0,1) to implement the random part of the algorithm (Kirkpatrick et al., 1983). If the probability is larger than the random sample, the new sample is selected and if not, the actual state is used to start the next iteration. Beginning with a temperature T_0, the temperature decreases according to a so called

Algorithm 2: Nelder-Mead Method for maximizing the objective function $f(\boldsymbol{x})$ with a two dimensional parameter vector $\boldsymbol{x}$

```
Data: starting simplex with the nodes: $\boldsymbol{x} = [\boldsymbol{x}_1, \boldsymbol{x}_2, \boldsymbol{x}_3]$
Result: best parameter vector : $\widetilde{\boldsymbol{x}}$
// While abort criterion $\Delta f$ is greater than a given threshold $\epsilon$
while $\Delta f > \epsilon$ do
    // evaluate the function at each point and sort the values so that
       $f(\boldsymbol{x}_1) > f(\boldsymbol{x}_2) > f(\boldsymbol{x}_3)$
    // estimate centroid of the two best points
    $\boldsymbol{x}_m = 1/2 \cdot (\boldsymbol{x}_1 + \boldsymbol{x}_2)$ ;
    // generate reflected point
    $\boldsymbol{x}_r = (1 + \alpha)\boldsymbol{x}_m - \alpha \boldsymbol{x}_3$;
    if $f(\boldsymbol{x}_1) > f(\boldsymbol{x}_r) > f(\boldsymbol{x}_2)$ then
        $\boldsymbol{x}_3 = \boldsymbol{x}_r$;
    else if $f(\boldsymbol{x}_r) > f(\boldsymbol{x}_1)$ then
        // calculate the expansion point to proof if step length for reflected point
           was to small
        $\boldsymbol{x}_e = \gamma \boldsymbol{x}_r + (1 - \gamma)\boldsymbol{x}_m$;
        if $f(\boldsymbol{x}_e) > f(\boldsymbol{x}_1)$ then
            $\boldsymbol{x}_3 = \boldsymbol{x}_e$;
        else
            $\boldsymbol{x}_3 = \boldsymbol{x}_r$;
        end
    else if $f(\boldsymbol{x}_r) < f(\boldsymbol{x}_2)$ then
        if $f(\boldsymbol{x}_r) < f(\boldsymbol{x}_3)$ then
            // Contract inside
            $\boldsymbol{x}_c = \beta \boldsymbol{x}_3 + (1 - \beta)\boldsymbol{x}_m$;
        else
            // Contract outside
            $\boldsymbol{x}_c = \beta \boldsymbol{x}_r + (1 - \beta)\boldsymbol{x}_m$;
        end
        if $f(\boldsymbol{x}_c) > f(\boldsymbol{x}_3)$ then
            $\boldsymbol{x}_3 = \boldsymbol{x}_c$ ;
        else
            // Shrink triangle around the best point
            $\boldsymbol{x}_2 = 1/2 \cdot (\boldsymbol{x}_2 + \boldsymbol{x}_1)$ ;
            $\boldsymbol{x}_3 = 1/2 \cdot (\boldsymbol{x}_3 + \boldsymbol{x}_1)$ ;
        end
    end
end
$\widetilde{\boldsymbol{x}} = \boldsymbol{x}$;
```

Algorithm 3: Simulated annealing for maximizing the objective function $f(\boldsymbol{x})$

```
Data: starting point: $\boldsymbol{x}$
Result: best parameter vector : $\widetilde{\boldsymbol{x}}$
$\widetilde{\boldsymbol{x}} = \boldsymbol{x}$;
for $j = 1 \dots N_j$ do
    $T = \boldsymbol{T}(j)$;
    $\boldsymbol{x}' = sample(\widetilde{\boldsymbol{x}})$;
    $P = P(\widetilde{\boldsymbol{x}}, \boldsymbol{x}', T)$;
    if $P \geq rand(0,1)$ then
        $\widetilde{\boldsymbol{x}} = \boldsymbol{x}'$
    end
end
```

annealing schedule. The temperature can decrease quadratically, for example. It finally reaches zero meaning that no worse state is accepted anymore. At each temperature the system must stay long enough for the system to reach a steady state (Kirkpatrick et al., 1983). Consequently, for a given number of iterations the temperature remains the same. During this temperature period the new samples are generated using a probability distribution. In the classic version of the simulated annealing uniformly distributed samples are generated within a certain search space (Kirkpatrick et al., 1983). The search space has to be increasingly restricted depending on the temperature, so that new samples are only locally generated at the end. These step sizes must be defined. In this paper, an alternative way is chosen using a Gaussian probability distribution to generate new samples (Geman and Geman, 1984). Based on all samples generated during the corresponding temperature period, mean values and standard deviations are estimated for the parameters defining a bivariate normal distribution. Since no a priori information are available an uncorrelated normal distribution is assumed. After each period the temperature is lowered thus the standard deviations for the parameters change which automatically reduces the value range of the new samples. In the first period the standard deviations are comparable to a given search space.

6.1.1 Application to Simulated Data

To examine the three search methods and to check whether maximizing the EPC is a possible alternative to the conventional process which minimizes the costs of the temporal LP, two spatial gradients of the simulated D-InSAR stack are analyzed in more detail. The arcs are chosen near the simulated settlement depression. The first one has a distance of 2 pixels and thus 160 m with a pixel size of 80 m and the second has a distance of 55 pixels and thus 4400 m. Figures 6.4a and 6.4c show the discrete and iteratively solved cost function values resulting from the temporal LP. It is obvious that there are several minima with a function value of zero. Since the assumption is made that the optimum parameters have a minimum norm, the green triangles indicate the optimum. In Fig. 6.4a the optimal parameters for arc 1 are $v_{\Delta x_{kl}} = 0.5\,\mathrm{cm/yr}$ and $\Delta h_{\Delta x_{kl}} = 0\,\mathrm{m}$ and in Fig. 6.4c $v_{\Delta x_{kl}} = 6\,\mathrm{cm/yr}$ and $\Delta h_{\Delta x_{kl}} = 0\,\mathrm{m}$ for arc 2, see also Tab. 6.1. For comparison purposes, the black stars show the reference parameters of the simulated unwrapped phase gradients which are $v_{\Delta x_{kl}} = 0.1\,\mathrm{cm/yr}$ and $\Delta h_{\Delta x_{kl}} = \text{-}1\,\mathrm{m}$ for arc 1 and $v_{\Delta x_{kl}} = 5.9\,\mathrm{cm/yr}$ and $\Delta h_{\Delta x_{kl}} = \text{-}9\,\mathrm{m}$ for arc 2. For both arcs the estimated parameters are very close to the reference. However, as the solution is not unique, it is possible that there are other optimal parameters which fit even better to the reference.

Figures 6.4b and 6.4d show the EPC function. The results of the individual search algorithms are marked in different symbols. The orange point is the maximum found with Algorithm 2, the dark blue triangle is the maximum found with Algorithm 1 and the light blue point is the result of using Algorithm 3. For Algorithm 1 the search area is chosen analogous to the conventional iterative cost minimization task. For Algorithm 2 the starting point results from the two-step weighted least squares adjustment. The black dot indicates the initial solution. This point is also used in Algorithm 3 as starting point. The black star again symbolizes the reference parameters of the simulated unwrapped phase gradients. Looking first at arc 1 in Fig. 6.4b, it becomes clear that all three search methods work and produce approximately identical results. Algorithm 3 finds the maximum EPC value of 0.80 at $v_{\Delta x_{kl}} = 0.2\,\mathrm{cm/yr}$ and $\Delta h_{\Delta x_{kl}} = \text{-}1\,\mathrm{m}$ which together with Algorithm 1 fits best to the reference parameters. For arc 2, considered in Fig. 6.4d, it becomes clear that Algorithm 2 is not able to find the global maximum. Starting from the initial solution, it stops at a local maximum. The EPC value found with Algorithm 2 is 0.17 which is smaller than the values found using Algorithm 1 (0.76) and Algorithm 3 (0.77). The estimated parameters using Algorithm 1 and 3 are very consistent with the minimum of the cost value in Fig. 6.4c. They are $v_{\Delta x_{kl}} = 6.0\,\mathrm{cm/yr}$

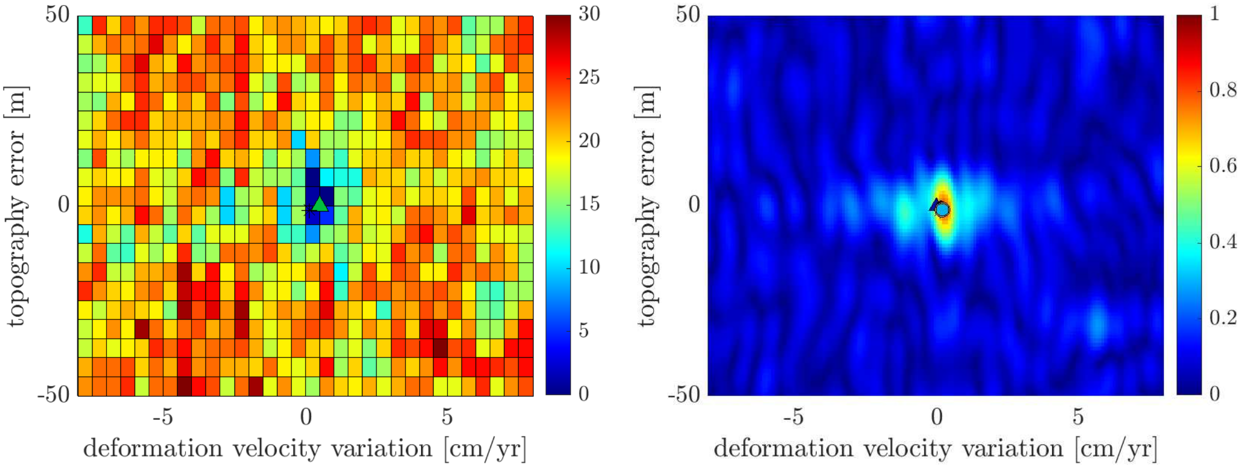

(a) cost values resulting from temporal LP for arc 1

(b) EPC for arc 1

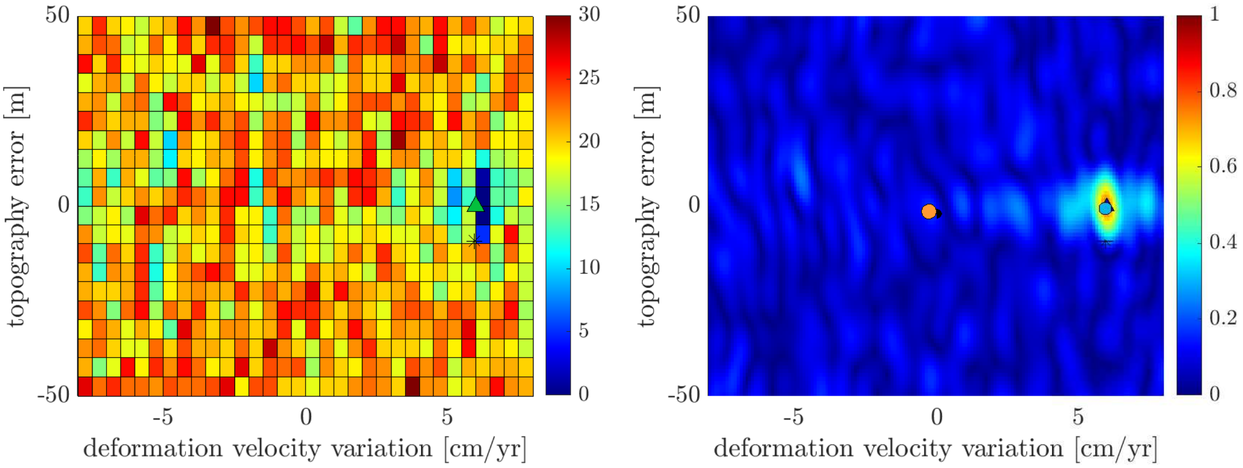

(c) cost values resulting from temporal LP for arc 2

(d) EPC for arc 2

Figure 6.4: Cost values and corresponding EPC values for two simulated spatial gradients with a noise level of 0.4 rad. The green triangles in the figures on the left symbolize the optimal point resulting from the conventional process where the costs of the temporal LP are minimized. For comparison, the black star is the reference solution. The other symbols in the figures on the right represent the optimum point from maximizing the EPC. The orange point is obtained using Algorithm 2, the dark blue triangle using Algorithm 1 and the light blue point using Algorithm 3. The black point represents the starting solution.

Table 6.1: Estimated motion model parameters during the temporal phase unwrapping using different approaches

(a) parameters for arc 1 corresponding to Figs.6.4a and 6.4b

	reference	conventional	Algorithm 1	Algorithm 2	Algorithm 3	start
$v_{\Delta x}$[cm/yr]	0.1	0.5	0.0	0.2	0.2	0.2
$\Delta h_{\Delta x}$[m]	-1	0	0	-1	-1	0
$C_{\Delta x}$	1	0	1	1	1	1
$EPC_{\Delta x}$	0.77	0.78	0.68	0.80	0.80	0.78

(b) parameters for arc 2 corresponding to Figs.6.4c and 6.4d

	reference	conventional	Algorithm 1	Algorithm 2	Algorithm 3	start
$v_{\Delta x}$[cm/yr]	5.9	6.0	6.0	-0.3	5.9	0.0
$\Delta h_{\Delta x}$[m]	-9	0	0	-2	-1	-2
$C_{\Delta x}$	5	0	0	22	0	20
$EPC_{\Delta x}$	0.29	0.12	0.76	0.17	0.77	0.12

and $\Delta h_{\Delta x_{kl}} = 0\,\text{m}$ for the Algorithm 1 and $v_{\Delta x_{kl}} = 5.9\,\text{cm/yr}$ and $\Delta h_{\Delta x_{kl}} = \text{-}1\,\text{m}$ for Algorithm 3 which are also close to the reference parameters.

In order to investigate the influence of the differently estimated parameters on the phase unwrapping results, Fig. 6.5 shows an overall comparison. First, Fig. 6.5a shows the results after the temporal phase unwrapping without considering the spatial information. The figure shows the percentage of correctly unwrapped phase gradients depending on the temporal baseline. The different colors refer to the different methods for estimating the motion model. The green bars are the results of the conventional way by minimizing the costs of the temporal LP in an iterative search process. The orange bars are the results of the alternative way by maximizing the EPC using Algorithm 2, dark blue using Algorithm 1 and light blue using Algorithm 3. All results represent a valid solution after the definition of the phase unwrapping problem. They deliver minimal costs and meet the specified constraints. The results differ only in the choice of the motion model parameters. The above statements can be confirmed on the basis of Fig. 6.5a. Maximizing the EPC using Algorithm 2 does not work well. However, if Algorithm 1 or 3 is used, it can be seen that the results are comparable to the conventional method, shown as green bars. Almost all gradients can be unwrapped correctly by the temporal phase unwrapping alone. The last few percentages are reached after applying the spatial phase unwrapping, see Fig. 6.5b. Some errors caused by wrong estimated motion model parameters using Algorithm 2 can still be fixed by the spatial phase unwrapping, but the result remains that Algorithm 2 is the worst compared to the other methods.

It can be concluded that maximizing the EPC function using Algorithm 1 or 3 is a good alternative to find a suitable motion model. The conventional method has the disadvantage that the discrete function may consist of a set of potential solutions and especially if the search area is unknown or very large, the method results in a long run time as the temporal phase unwrapping problem has to be solved sequentially for each ($v_{\Delta x_{kl}}$, $\Delta h_{\Delta x_{kl}}$)-pair. In this simulation, the cost function was evaluated sequentially in 693 steps. For a single arc the temporal LP has to be solved 693 times. Compared to this, the temporal LP only needs to be solved once with the alternative method. The run time[1] to solve the temporal phase unwrapping for one spatial phase gradient is approximately 5.57 seconds using the conventional method. If the alternative method is used the run time can be reduced on average to 0.01 seconds using Algorithm 2, to 0.02 seconds using Algorithm 1 and to 0.23 seconds using Algorithm 3. The run time of about 6 seconds does not look very critical at the first look.

---

[1] run time refers to a prototype implementation in MATLAB©. The computations were performed on a workstation equipped with two Intel Xeon E5-2650 v4 (2.20GHz) 12 core (24 threads) CPUs and 512 GB of main memory.

However, it must be considered that the times refer to the temporal phase unwrapping of one single phase gradient. In total, the temporal LP for several ten thousands of phase gradients must be solved. Figure 6.6 shows the run time required to solve the temporal phase unwrapping for each of the 45 842 phase gradients. The green triangles show the run time when using the conventional method and the other colors when using the alternative method. The orange points are the run times when using Algorithm 2, the dark blue triangles when using Algorithm 1 and the light blue points when using Algorithm 3. With the alternative method a significant run time reduction can be achieved which is essential for the implementation in the operational RSG software.

Comparing the three search algorithms to find the maximum of the EPC function, it can be summarized that Nelder-Mead (Algorithm 2) needs the shortest run time. However, it is often not able to find the global maximum as it gets stuck in a local maximum. The grid search approach (Algo-

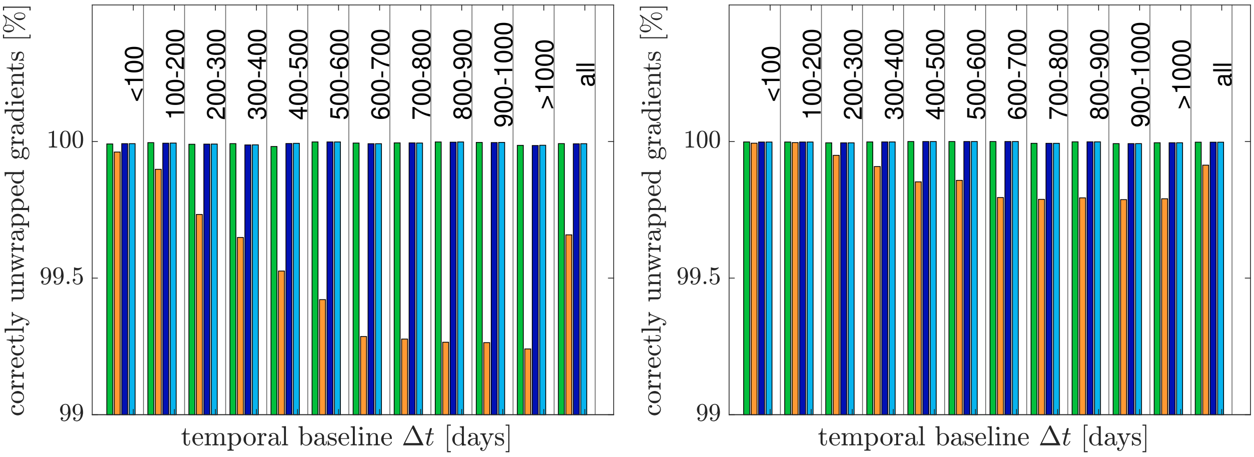

(a) results after temporal phase unwrapping **(b)** results after temporal and spatial phase unwrapping

Figure 6.5: Percentage of correctly unwrapped phase gradients for simulated D-InSAR stack depending on the temporal baseline. The motion model is estimated with different approaches. The green bars show the results of the conventional way by minimizing the costs of the temporal LP in an iterative search process. The orange bars show the results using Algorithm 2 to estimate the motion model by maximizing the EPC, the dark blue bars when using Algorithm 1 and the light blue bars when using Algorithm 3.

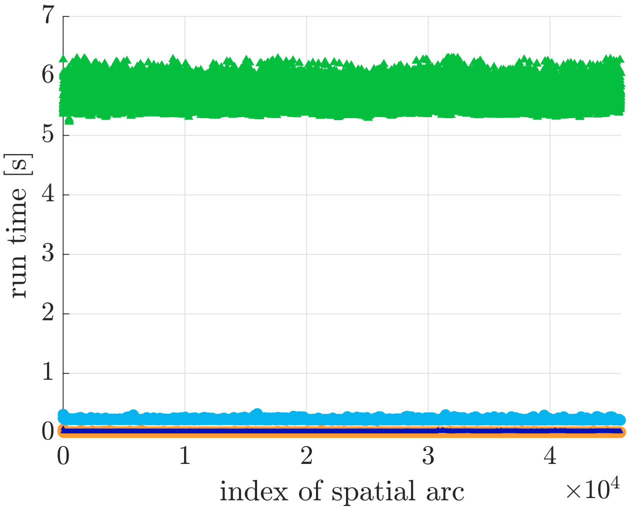

Figure 6.6: Run time of the temporal phase unwrapping for the individual spatial phase gradients. The green triangles show the run time when using the conventional method, the orange squares when using the alternative method with Algorithm 2, the dark blue triangles with Algorithm 1 and the light blue points with Algorithm 3.

rithm 1) is similar to the Nelder-Mead method regarding the run time, but it is able to find the global maximum depending on the sampling. However, this sampling has the disadvantage that the prior definition of an exact search range is necessary which is not straightforward. Although simulated annealing (Algorithm 3) requires a slightly longer run time, it delivers the largest EPC value in all cases considered here and, in contrast to the conventional method, the run time can be reduced enormously as the temporal LP only has to be solved once for each phase gradient. Moreover, simulated annealing is a very robust method which is especially important for increased noise behavior. With increasing noise, the maximum of the EPC function decreases, because model and observations do not fit together well. Thus, it becomes more difficult to find the maximum or to decide which parameters represent the optimal motion. The noise level until which the methods are still applicable is examined in the following chapter.

6.1.2 Analysis for Different Scenarios

For a more general conclusion, the studies are repeated for different simulation scenarios. As a reminder, each SAR image is provided with an independent normally distributed noise, see the workflow for the simulation scenario in Fig. 4.8. The noise was previously selected with a standard deviation of 0.4 rad. The typical signal-to-noise ratio for ERS data is 10 to 20 dB (Schwaebisch, 1995, p. 26). This corresponds to a standard deviation of 15 ° to 40 ° (Just and Bamler, 1994), equal to 0.3 to 0.7 rad. Therefore, the standard deviation of the noise per SAR image varies from 0.2 to 0.9 rad in the simulation scenario. In all cases, it can be shown that the global maximum of the EPC function can be reliably found by Algorithm 3. Figure 6.7 shows the percentage of correctly unwrapped gradients for the entire D-InSAR stack depending on the noise level. For a noise level below 0.6 rad the results described above are confirmed. For a noise level above 0.6 rad the results look different. In this case Algorithm 2, shown as orange bars, provides the best results. For a higher noise level, the EPC values become generally smaller and there is no unique global maximum anymore. Figure 6.8 shows the relative frequency of the occurring EPC values found by Algorithm 3 for the different noise levels. The darker the color of the histogram, the higher the noise.

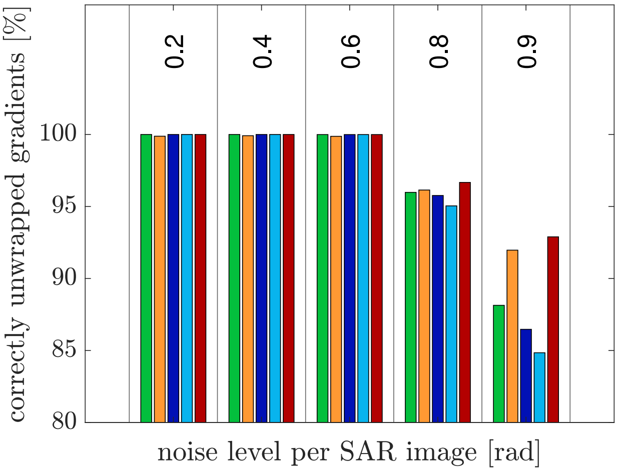

Figure 6.7: Percentage of correctly unwrapped phase gradients depending on the noise level which is added per SAR image. The motion model is estimated with different approaches. The green bars show the results of the conventional way. The orange bars show the results using Algorithm 2 to maximize the EPC, the dark blue bars using Algorithm 1, the light blue bars using Algorithm 3 and the red bars using Algorithm 4.

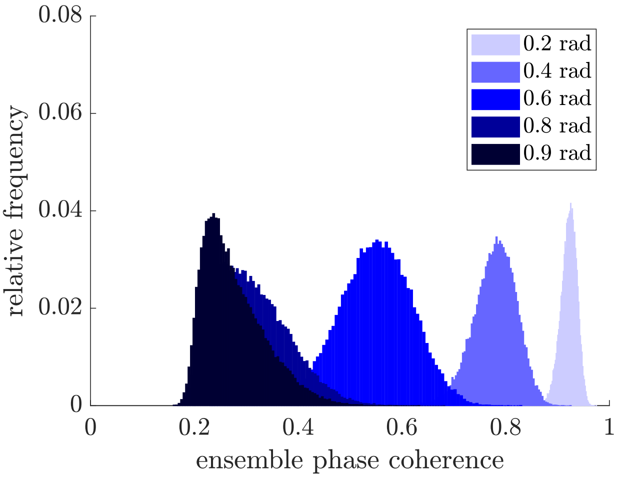

Figure 6.8: Relative frequency of occurring EPC values using Algorithm 3. The darker the color of the histogram, the higher the noise level. It varies from 0.2 rad to 0.9 rad.

Furthermore, Fig. 6.9 shows exemplary for one spatial arc of the simulated D-InSAR stack with a noise level of 0.8 rad the iteratively reduced cost function (Fig. 6.9a) and the EPC values (Fig. 6.9b). It is obvious that the EPC reaches very small values and that there is no significant maximum. Although Algorithm 3 and 1 find the global maximum at 0.24 and 0.20 with a deformation velocity variation of around 8 cm/yr and a topographic error of about 30 m. The reference values are at a slightly smaller EPC value of 0.14 with motion model parameters near zero, see also Tab. 6.2. Since there are several local maxima, Algorithm 2 ends near the starting solution, which in this case fits better to the reference.

With a higher noise level and thus smaller EPC values, the estimated motion model parameter cannot be reliably estimated. In such cases it is better to use motion model parameters that correspond to a local maximum with a small norm instead of using an extreme motion model which is very unreliable and may lead to phase unwrapping errors as it cannot be compensated by the following spatial phase unwrapping. Based on this conclusion, the idea is to use a modified search algorithm to find the optimal motion model parameters using the EPC function. The modified search algorithm is described in Algorithm 4 for a general maximization task with objective function $f(\boldsymbol{x})$. This search algorithm relies on the results of simulated annealing as long as the function value is above a certain threshold. For smaller values it is assumed that the motion model cannot be estimated reliably and instead the local maximum around zero is taken using the Nelder-Mead method. For this simulation, the threshold is set to 0.3 based on the histogram in Fig. 6.8.

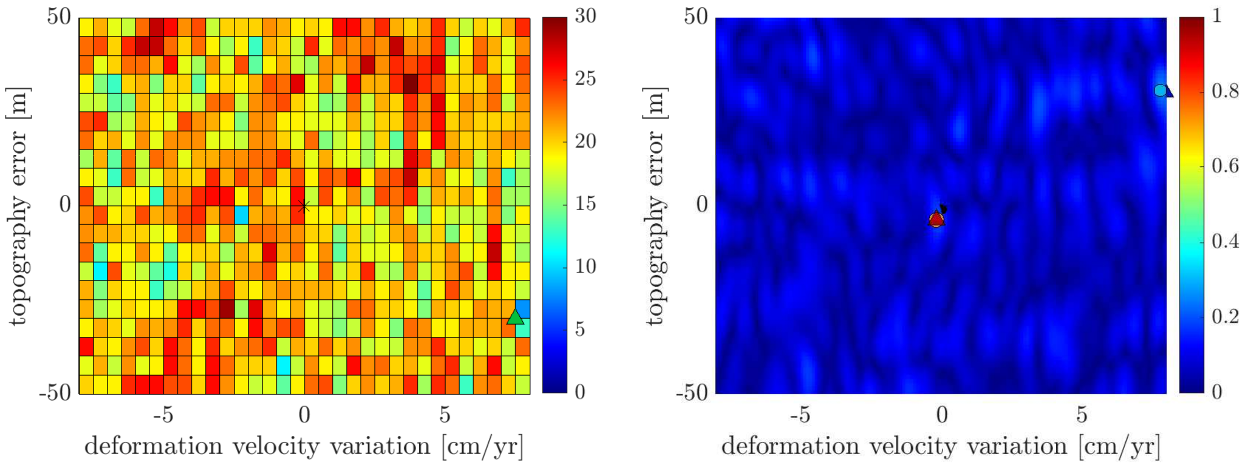

(a) cost values resulting from temporal LP

(b) EPC

Figure 6.9: Cost values and corresponding EPC values for one spatial gradient of the simulated D-InSAR stack with a noise level of 0.8 rad. The green triangle in the left figure shows the results of the conventional way by minimizing the costs of the temporal LP in an iterative search process. The black star is the reference solution. The orange point in the right figure shows the results using Algorithm 2 to maximize the EPC, the dark blue triangle when using Algorithm 1, the light blue point when using Algorithm 3 and the red triangle when using Algorithm 4. The black point represents the starting solution which is necessary for some algorithms.

Table 6.2: Parameters for phase gradient 1 corresponding to Fig.6.9

	reference	conventional	Algorithm 1	Algorithm 2	Algorithm 3	Algorithm 4	start
$v_{\Delta x}$[cm/yr]	-0.0	7.5	8.0	-0.2	7.8	-0.2	0.0
$\Delta h_{\Delta x}$[m]	-0	-30	30	-4	31	-4	-1
$C_{\Delta x}$	17	8	16	19	16	19	17
$EPC_{\Delta x}$	0.14	0.14	0.20	0.19	0.24	0.19	0.14

```
Algorithm 4: Modified Search Algorithm for maximizing the objective function $f(\boldsymbol{x})$
Data: starting point: $\boldsymbol{x}_0$
Result: best parameter vector : $\widetilde{\boldsymbol{x}}$
// Maximize $f(\boldsymbol{x})$ with simulated annealing
$\widetilde{\boldsymbol{x}} = simulated\_annealing(\boldsymbol{x}_0)$;
// if objective function is below a given threshold $\varepsilon$
if $f(\widetilde{\boldsymbol{x}}) < \varepsilon$ then
    // search local maxima around $(0,0)$ using Nelder-Mead
    $\widetilde{\boldsymbol{x}} = NelderMead(\mathbf{0})$;
end
```

For the arc analyzed in Fig. 6.9b, the optimum point found using Algorithm 4 is marked as a red triangle which fits better to the reference compared to the solution found by Algorithm 3. A corresponding overall result of the percentage of correctly unwrapped phase gradients is shown as red bars in Fig. 6.7. For a noise level below 0.6 rad the results are identical to Algorithm 3 as the EPC values are not below the threshold of 0.3, see the histogram in Fig. 6.8. However, with a noise level above 0.6 rad an improvement can be seen, also with respect to the conventional way by minimizing the costs of the temporal LP in an iterative search process.

Finally, it can be concluded that the estimation of a correct motion model plays a critical role in the temporal phase unwrapping steps. A few errors can be compensated by the spatial phase unwrapping which follows in a second step. However, as has been demonstrated, this is not always the case. Simulated annealing (Algorithm 3) reliably finds the global maximum in all examined scenarios. However, especially with higher noise levels, no unique global maximum can be obtained, since model and observation no longer fit together due to the high noise level. In such a case, the motion model can no longer be reliably estimated. Before assuming an extreme and unreliable motion model, it is better to take a local maximum with a small norm. The modified approach (Algorithm 4) shows its effect especially at a noise level above 0.6 rad. Since the standard deviation of the ERS data ranges from 0.3 to 0.7 rad, the use of the modified algorithm combining simulated annealing and Nelder-Mead is recommended.

6.2 Choice of the Weights

In general, the phase unwrapping problem is defined as an MCF problem in both time and space, see (4.13) and (5.12). The phase ambiguity factor represents the flow which is weighted with costs. The task is to search for an optimal flow which minimizes the total sum of costs. In the optimization process the weights are a critical design parameter. For the temporal phase unwrapping, the weights are assumed to be constant, cf. Pepe and Lanari (2006). For the spatial phase unwrapping different weight functions have been evolved. In general, the weights should be low in areas where the data is noisy, atmospheric, deformation or topographic effects occur and thus a phase ambiguity factor is likely. In contrast, it should be expensive to insert a phase ambiguity factor in areas with low phase noise.

Following Costantini (1998) the weights for the spatial phase unwrapping should be based on information extracted from the data, for example the coherence values or the spatial inconsistency, meaning the investigation of the spatial loop constraint. When such a priori knowledge is not available all weights should be chosen equal to one. However, this is the worst choice. It is always better to take additional information from the data into account when defining the weights. Eineder et al. (1998) generated binary cost maps, limiting the three variables of amplitude, inconsistency and flatness to estimate the costs for the optimization. Chen (2001) developed statistical models for non-linear cost functions depending on the observed wrapped phase, the image intensity and the coherence. The phase unwrapping problem is recast into a maximum a posterior probability estimation problem which can be solved in an approximate way using a non-linear network flow solver. In Fornaro et al. (2011) the weights for the spatial phase unwrapping are related to the phase gradient $\psi_{\Delta x_{kl}}^{\Delta t_{\alpha\beta}}$ and the Euclidean distance $L_{\Delta x_{kl}}$ between the two pixels x_k and x_l

$$p_{\Delta x_{kl}}^{\Delta t_{\alpha\beta}}(\psi_{\Delta x_{kl}}^{\Delta t_{\alpha\beta}}, L_{\Delta x_{kl}}) = \frac{1}{L_{\Delta x_{kl}}}(1 - \frac{|\psi_{\Delta x_{kl}}^{\Delta t_{\alpha\beta}}|}{\pi}) \tag{6.13}$$

meaning that short gradients are considered more reliable. The term in brackets reaches values close to zero as soon as there is a motion between the two considered pixels. If there is no movement, the phase gradient will be very small resulting in a large weight factor and therefore the observation will be more reliable. Furthermore, Fornaro et al. (2011) introduced a weighting based on the EPC values

$$p_{\Delta x_{kl}}(EPC_{\Delta x_{kl}}) = EPC_{\Delta x_{kl}}. \tag{6.14}$$

The higher the EPC value the better fit observation and model, and the more reliable the result should be. Another possibility are the coherence based weights. However, the coherence values are defined for the individual pixels and the weights refer to a phase gradient. Based on the variance propagation law, the coherence value per phase gradient is calculated from the sum of the coherence values per pixel resulting in the coherence based weights

$$p_{\Delta x_{kl}}^{\Delta t_{\alpha\beta}}(\gamma_{\Delta x_{kl}}^{\Delta t_{\alpha\beta}}) = \gamma_{x_k}^{\Delta t_{\alpha\beta}} + \gamma_{x_l}^{\Delta t_{\alpha\beta}}. \tag{6.15}$$

It remains to ensure that the estimated parameters in form of the phase ambiguity factors $\boldsymbol{k}_{\Delta \boldsymbol{x}}^{\Delta \boldsymbol{t}}$ must be integer values. To get an integer solution from the LP, the weights must also be integers, see Section 3.3.1. The coherence value, (6.13) and (6.14) return values between 0 and 1. A simple rounding only returns values of 0 and 1 or 2 for (6.15). In order to obtain a slightly more detailed classification, the weight factors are first increased by a factor of ten and then rounded. An increase by a further factor is not necessary. Since only integer values are allowed, the solution is less sensitive to a small change of the weights (Costantini, 1998). In order to obtain a clearer classification, the weight factor is then potentiated to base 2. This results in the following three integer weights on the basis of the coherence, the phase gradient and the length as well as on the basis of the EPC values

Weight 1:
$$p_{\Delta x_{kl}}^{\Delta t_{\alpha\beta}}(\gamma_{\Delta x_{kl}}^{\Delta t_{\alpha\beta}}) = 2^{\lfloor \gamma_{\Delta x_{kl}}^{\Delta t_{\alpha\beta}} \cdot 10 \rceil} \tag{6.16}$$

Weight 2:
$$p_{\Delta x_{kl}}^{\Delta t_{\alpha\beta}}(\psi_{\Delta x_{kl}}^{\Delta t_{\alpha\beta}}, L_{\Delta x_{kl}}) = 2^{\lfloor \frac{1}{L_{\Delta x_{kl}}}(1 - \frac{|\psi_{\Delta x_{kl}}^{\Delta t_{\alpha\beta}}|}{\pi}) \cdot 10 \rceil} \tag{6.17}$$

Weight 3:
$$p_{\Delta x_{kl}}(EPC_{\Delta x_{kl}}) = 2^{\lfloor EPC_{\Delta x_{kl}} \cdot 10 \rceil}. \tag{6.18}$$

So far, the conventional weights for the spatial phase unwrapping result from the costs of the temporal LP according to Pepe and Lanari (2006). The higher the costs, i.e. the higher the absolute number of phase ambiguity factors, the less reliable are the results from the temporal phase unwrapping. Thus, the weights for the spatial LP result from an inverse relationship to the temporal costs, see (5.14). The idea now is to test and compare the different weightings.

6.2.1 Application of the Weighting Procedures to Simulated Data

The influence of the weights is tested using the simulated D-InSAR stack, cf. Section 4.3.2.1. To estimate the motion model, the EPC function is maximized using the modified Algorithm 4. Thus, differences in the results are only the consequence of different weight choices. Therefore, *Weights 2* and *3*, cf. (6.17) and (6.18), are analyzed and compared with the conventional weighting. The simulated D-InSAR stack, designed here in a simplified way, does not allow a reliable analysis of the *Weight 1*. In general, the coherence values are calculated within the framework of the multilooking process. In the case of ERS-1/-2 data a multilooking over 80 looks, 20 in azimuth and 4 in range direction, is performed. The simulation already refers to multilooked data and the coherence values are taken from the real ERS-1/-2 data. The noise is added to the simulated data on two levels, for each SAR image and for each interferogram depending on the coherence value. The noise per SAR image is kept variable in the analysis from 0.2 to 0.9 rad. If the coherence based *Weight 1* is used, the coherence values would also have to be adjusted according to the noise level. To do this, the simulation has to start before the multilooking process in order to be able to calculate new coherence values depending on the noise level. However, since the application to real data will show that the coherence based *Weight 1* is worse than the *Weights 2* and *3*, this step is omitted and the analysis of the coherence based *Weight 1* is limited to the application to real data.

In a first step, *Weights 2* and *3* are only used for the spatial phase unwrapping. For the temporal phase unwrapping constant weights are still used. The investigation of different temporal weights will be done later.

6.2.1.1 Influence of Spatial Weights

Figure 6.10 shows the percentage of correctly unwrapped phase gradients after the temporal and spatial phase unwrapping depending on the noise level per SAR image. The temporal weights are assumed to be constant in all cases. The differences arise only in the choice of the spatial weights. The green bars represent the results using the conventional weights according to Pepe and Lanari (2006), where the spatial weights are inversely proportional to the temporal costs. For the orange bars the phase and length based *Weights 2* are used and for the blue bars the EPC based *Weights 3*. Due to the different spatial weighting, significant differences can be observed at a noise level above 0.6 rad. At a lower noise level there are no differences and in all cases the phase gradients can be unwrapped correctly at almost 100 %. However, in the case of a high noise level above 0.6 rad, *Weights 3* show the highest percentage of correctly solved phase gradients, 98.5 % for a noise level of 0.8 rad and 97.1 % for a noise level of 0.9 rad. For *Weights 2* and the conventional weights the percentage values are smaller. For *Weights 2* they are 96.3 % (noise level 0.8 rad) and 93.9 % (noise level 0.9 rad) and for the conventional weights 96.7 % (noise level 0.8 rad) and 92.9 % (noise level 0.9 rad). As a reminder a noise level of 0.9 rad is a worst case scenario as the typical values of the standard deviation for ERS data are between 0,3 and 0,7 rad.

The question is why the *Weights 2* and the conventional weights fail. Therefore, Fig. 6.11 shows the estimated mean deformation velocity per pixel for the simulated D-InSAR stack with a noise level of 0.8 rad. Figure 6.11a shows the results of the reference phase and Figs. 6.11b to 6.11d show the differences between the reference and the phase unwrapping results using different spatial weightings. It can be seen that the settlement depression in Fig. 6.11c does not represent the reference. The differences to the reference are up to -6 cm/yr in the basin of the settlement depression. The estimated motion is too small. Looking at the equation for calculating *Weight 2*, cf. (6.17), it becomes obvious that observations which involve motion and thus have large phase

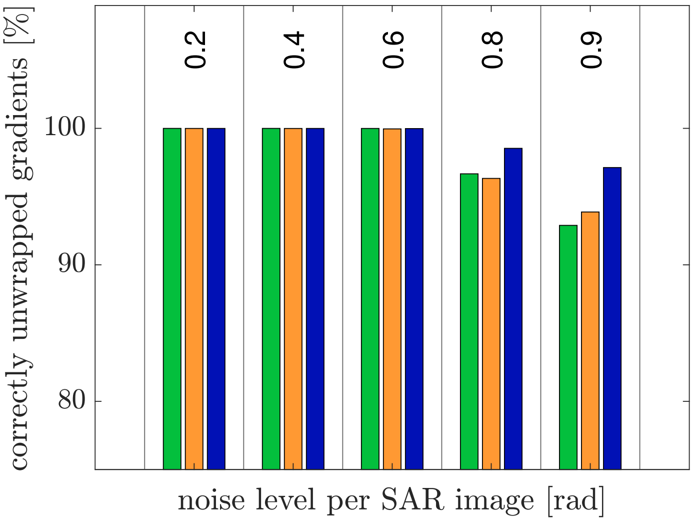

Figure 6.10: Percentage of correctly unwrapped phase gradients depending on the noise level which is added per SAR image. The motion model parameters are estimated by maximizing the EPC using the modified method. The weight factors for the spatial phase unwrapping are chosen in different ways. The green bars are the results with the conventional weights, the orange bars with *Weights 2* and the blue bars with *Weights 3*. For the temporal phase unwrapping constant weights are used.

gradients, will have small weights. Consequently, all observations close to the settlement depression will be weighted down. This weighting does not take into account that the estimated motion model may fit well and should be trusted. This leads to the fact that these phase gradients are changed during the spatial phase unwrapping and the motion cannot be reconstructed well. This works better for the conventional weights and the *Weights 3*. In this case the differences are almost zero everywhere. When using conventional weights, there are differences of 6cm/yr at individual pixels, see red boxes in Fig. 6.11b. Too much movement is assumed at these pixels. Looking at the corresponding phase gradients of these pixels, it can be seen that the estimated motion model parameters are very large. However, the motion model does not fit well to the observations. This is indicated by a low EPC value. Nevertheless, these phase gradients show low temporal costs and therefore very large spatial weights when using the conventional weighting. Consequently, these gradients are not further modified in the spatial phase unwrapping, because it is too expensive to estimate a phase ambiguity factor. Thus, the motion model that was erroneously estimated as too large is still in the data and leads to the erroneous pixels, see red boxes in Fig. 6.11b. This is different with *Weights 3*. Since the EPC values are small, this results in low spatial weights. Thus, the phase gradients which contain the incorrectly estimated motion model are changed in the spatial phase unwrapping, so that the unwrapped pixels reconstruct the reference. This is also possible with *Weights 2* at these pixels. Since, too large motion model parameters are estimated, this weighting also results in low spatial weights. But as already mentioned, with *Weights 2* it is not possible to reconstruct the deformation in the settlement depression.

For a more precise analysis, the percentage of correctly unwrapped interferograms per phase gradient is calculated for the results based on the noise level of 0.8 rad and plotted against the estimated topography error, cf. Fig. 6.12a, and the estimated deformation velocity variation, cf. Fig. 6.12b. The green triangles show the results for conventional weights, the orange points for *Weights 2* and the blue stars for *Weights 3*. As already suspected, *Weights 2* fail as soon as there are large movements or large topography errors. With conventional weights, this behavior is not as obvious. Here it is rather noticeable that the results are faulty with very small gradients which show almost no movements or topography errors. Looking at these gradients, it is evident that the temporal costs again do not match the EPC values. Gradients fulfill the temporal constraints and have low temporal

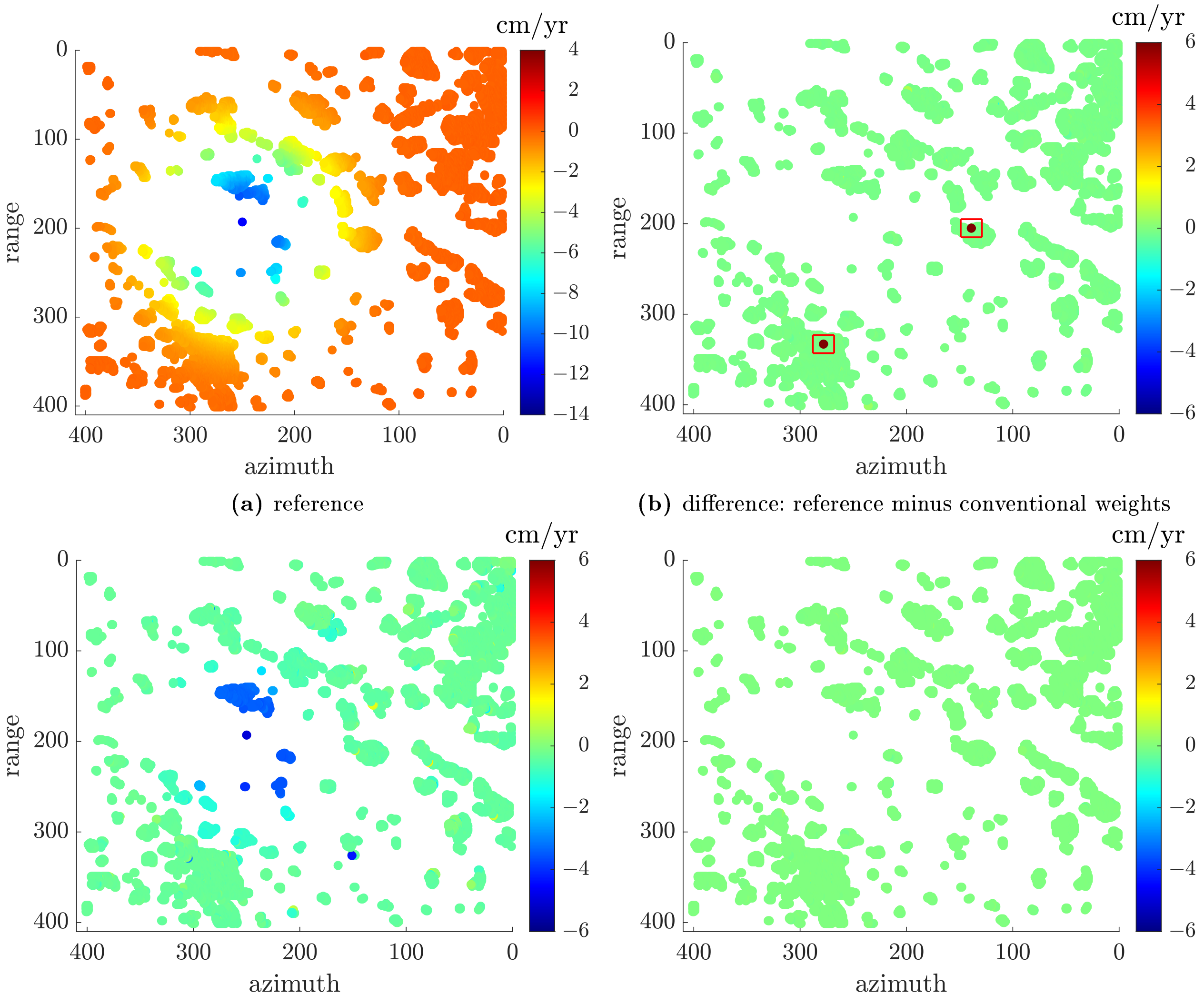

(a) reference **(b)** difference: reference minus conventional weights

(c) difference: reference minus *Weights 2* **(d)** difference: reference minus *Weights 3*

Figure 6.11: Mean deformation velocity per pixel with a noise level of 0.8 rad using different spatial weight factors. The results differ in the choice of weights for the spatial phase unwrapping. Constant weights are used for the temporal phase unwrapping.

costs, but the estimated motion model does not fit well. These gradients are therefore incorrectly strongly trusted. Just as well the opposite case can occur. The situation is different with *Weights 3*. Even with large movements and topography errors, the phase gradients are unwrapped correctly at almost 90 %. Even with smaller movements, the *Weights 3* show a clear improvement over the other two weightings. All in all, with *Weights 3* in 75 % of the cases gradients are unwrapped correctly in more interferograms than with *Weights 2*, in 12 % of cases equally and in 13 % of cases in less interferograms. Compared with the conventional weighting, the *Weights 3* are better for 57 % of gradients, for 29 % equal and for 14 % worse.

6.2.1.2 Influence of Temporal Weights

So far, the temporal weights have been assumed to be constant. In the literature, this is also the most common case (Pepe and Lanari, 2006, Fornaro et al., 2011), besides non-linear statistical costs according to Chen (2001). Since the phase unwrapping problem should be solved further as an LP, linear temporal costs are required. In the following two possibilities are tested. On the one hand,

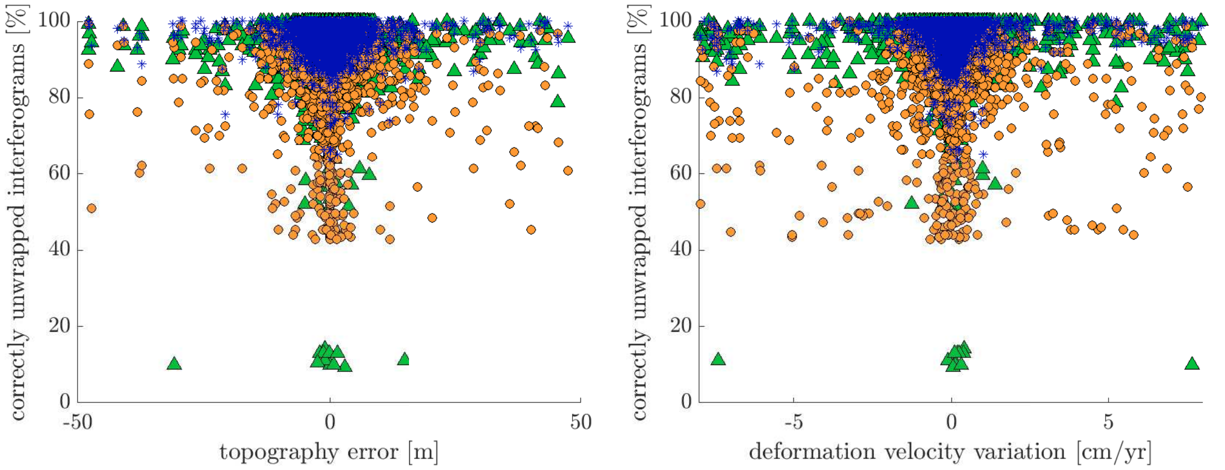

(a) correctness depending on the topography error

(b) correctness depending on the deformation velocity variation

Figure 6.12: Percentage of correctly unwrapped interferograms per phase gradient for a noise level of 0.8 rad. The results differ in the choice of spatial weighting factors. The green triangles are the results with conventional weights, the orange points with *Weights 2* and the blue stars with *Weights 3*. Constant weights are used for the temporal phase unwrapping.

Weights 2, cf. (6.17) are used for the temporal weights. Since the same spatial phase gradient is considered for the temporal phase unwrapping in time, the Euclidean distance $L_{\Delta x_{kl}}$ of the phase gradient is irrelevant. The weight depends only on the phase gradient. Phase gradients which are considered over a longer temporal or spatial baseline or which include a temporal deformation are larger and are thus weighted down. On the other hand, a similar weighting which is carried out when finding the starting solution by means of a two-step weighted least squares adjustment according to Zhang et al. (2014), cf. (6.5), is used as temporal weights. The weight depends directly on the temporal and spatial baseline. Since the weighting must also be an integer value, the weight is increased by a power of ten, rounded and potentiated to base 2, resulting in the fourth analyzed weighting function

$$\boxed{\underline{\textit{Weight 4:}}\quad p^{\Delta t_{\alpha\beta}}(\Delta t_{\alpha\beta}, \Delta b_{\perp,\alpha\beta}) = 2^{\lfloor |\frac{4\pi}{\lambda}\Delta t_{\alpha\beta}\cdot\frac{4\pi}{\lambda}\frac{\Delta b_{\perp,\alpha\beta}}{r\sin(\theta)}|^{-1}\cdot 10\rceil}.} \tag{6.19}$$

So *Weights 2* and *Weights 4* are used as weights to temporally unwrap the phase gradients of the simulated D-InSAR stack and compared with the results using constant temporal weights.

Figure 6.13 shows the percentage of correctly unwrapped phase gradients after temporal phase unwrapping depending on the noise level per SAR image. The green bars symbolize the results with constant temporal weights, the orange bars with *Weights 2* and the blue bars with *Weights 4*. It can be seen, especially for the higher noise levels, that the *Weights 2* lead to a higher percentage of correctly unwrapped phase gradients compared to the other two weightings. *Weights 4* which include the direct relation to the spatial and temporal baselines seem to work less well.

The idea now is to combine the temporal *Weights 2* with the previously investigated spatial weights. The results are shown in Fig. 6.14. Again, the percentage of correctly unwrapped phase gradients is shown depending on the noise level. The green bars show the results when using

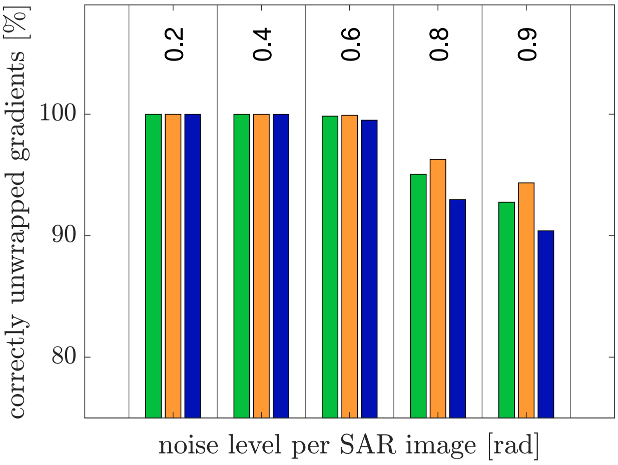

Figure 6.13: Percentage of correctly unwrapped phase gradients for simulated D-InSAR stack after temporal phase unwrapping depending on the noise level which is added per SAR image. The green bars are the results using constant temporal weights, the orange bars are the results using *Weights 2* as temporal weights and the blue bars using *Weights 4* as temporal weights.

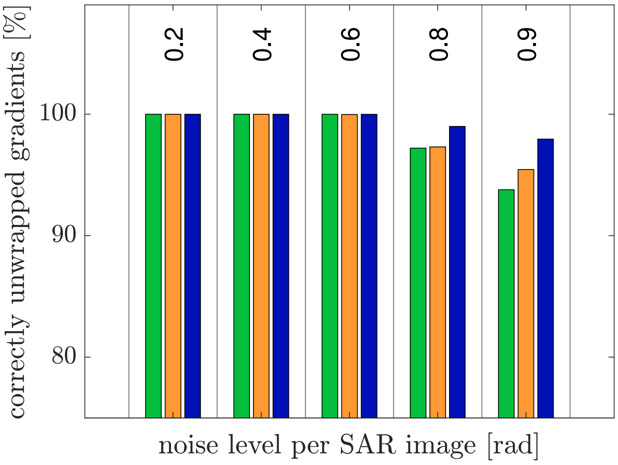

Figure 6.14: Percentage of correctly unwrapped phase gradients for simulated D-InSAR stack after temporal and spatial phase unwrapping depending on the noise level which is added per SAR image. For the temporal phase unwrapping *Weights 2* are used. The green bars are the results using the conventional spatial weights, for the orange bars *Weights 2* and for the blue bars *Weights 3* are used as spatial weights.

conventional spatial weights, the orange bars when using *Weights 2* and the blue bars when using *Weights 3*. In contrast to the results shown in Fig. 6.10, *Weights 2* are used as temporal weights instead of constant temporal weights. Here, again, only the results from a noise level above 0.6 rad are interesting. Previously, almost 100 % of the phase gradients are correctly reconstructed in all cases. For a noise level above 0.6 rad, it can be seen that the inclusion of different temporal weights has led to a further improvement. Especially for the spatial *Weights 2*, the accuracy increases from 96.3 % to 97.3 % at a noise level of 0.8 rad and from 93.9 % to 95.4 % at a noise level of 0.9 rad. For the conventional weights the percentage increases from 96.7 % to 97.2 % (noise level 0.8 rad) and from 92.9 % to 93.8 % (noise level 0.9 rad). For *Weights 3* the improvements are not as significant, from 98.5 % to 99.0 % (noise level 0.8 rad) and from 97.1 % to 97.9 % (noise level 0.9 rad).

However, with spatial *Weights 2* the problem remains that errors occur especially with phase gradients with large motion model parameters. For the noise level of 0.8 rad, Fig. 6.15 again shows the percentage of correctly unwrapped interferograms per phase gradient depending on the estimated topography errors and the estimated deformation velocity variations. The results are shown as green triangles when conventional spatial weights are used, as orange points when spatial *Weights 2* are used, and as blue stars when spatial *Weights 3* are used. In contrast to the results in Fig. 6.12, where constant temporal weights were assumed, an improvement can be seen, but the problem already described remains.

It can be concluded that *Weights 3* have proven to be a good alternative to conventional spatial weights at all noise levels. Even at a high noise level of 0.9 rad, which represents a worst case scenario, an improvement is observed. *Weights 2* are most unsuitable for the choice of spatial weights. For this simulated D-InSAR stack it is not possible to reconstruct the simulated settlement depression with *Weights 2*. Large motions are always down weighted and thus these phase gradients are changed during the spatial phase unwrapping. However, the introduction of *Weights 2* as temporal weights has proven to be suitable and has led to a further increase in the percentage of correctly unwrapped phase gradients.

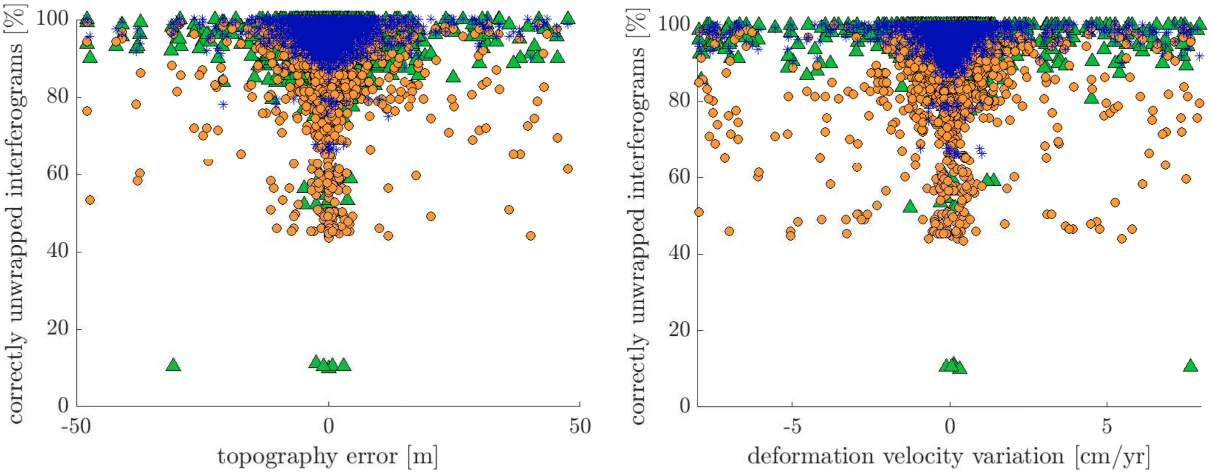

(a) correctness depending on the topography error **(b)** correctness depending on the deformation velocity variation

Figure 6.15: Percentage of correctly unwrapped interferograms per phase gradient for a noise level of 0.8 rad. For the temporal phase unwrapping *Weights 2* are chosen. The green triangles show the results based on the conventional spatial weights. The orange squares are the results using *Weights 2* and the blue bars using *Weight 3* as spatial weights.

6.3 Case Study 1: ERS-1/-2 D-InSAR Stack of the Lower-Rhine-Embayment

In this section, the EMCF algorithm and the above described ideas of improvement, which have already been verified on the basis of simulated data, are tested and applied to the analysis of real data. The test region is the Lower-Rhine-Embayment in the southwest of North Rhine-Westphalia, Germany, bounded by the cities Aachen and Cologne in the west and east and Mönchengladbach and Euskirchen in the north and south. Characteristic for the Lower-Rhine-Embayment are the mining regions. The coal mine Sophia-Jacoba in the mining region Erkelenz and the coal mine Emil Mayrisch in the mining region Aachen had been extracted underground until 1992 and 1997, respectively (Boje et al., 2008). The consequent rise of the groundwater level in the pits results in an elevation of the Earth's surface. In contrast, the three still active open-cast mines Garzweiler, Hambach and Inden in the Rhineland brown coal mining area are causing subsidence of the Earth's surface. Thus, the region is in a continuous motion. Regular monitoring measurements of these ground movements are therefore necessary. The aim is to detect these deformations with help of a multitemporal D-InSAR analysis.

6.3.1 Data Basis and Data Processing

The considered data set consists of the previously mentioned 64 SAR images collected by ERS-1/-2. These data cover the Lower-Rhine-Embayment from May 1992 to December 2000. They are stacked together to 161 D-InSAR images. The temporal data distribution is already shown in Fig. 2.8b. This triangulation is optimized according to Pepe et al. (2015). Again, pixels are defined as coherent if they have a coherence value greater than or equal to 0.7 in at least 80 % of interferograms. For the whole ERS-1/-2 scene this is the case for n =143 474 pixels defining m =430 115 arcs and r =286 643 triangles.

To detect the ground deformation in a large scale the SBAS method is used. The SBAS processing is carried out with the RSG Software. As already described in Section 2.3.2, the phase unwrapping is done twice to reduce phase unwrapping errors. However, this step remains a critical task in the analysis (Pepe and Lanari, 2006). Since it has been shown that the inclusion of the temporal information leads to considerably better results, the two-step EMCF algorithm is used. The state of the art in the RSG software is the estimation of the motion model using the conventional method. In this section the alternative method by maximizing the EPC function will be tested. Furthermore, various weight functions will be analyzed, afterwards. For this purpose, the phase unwrapping is performed twice externally in MATLAB© after all preprocessing steps from the coregistration of the individual SAR images to the wrapped, multilooked and multitemporally filtered differential interferograms have been completed in RSG. The unwrapped phase gradients are again included in RSG for the final SBAS analysis resulting in the deformation time series of the individual pixels, projected in vertical height changes with respect to (2.39). Since the phase gradients represent temporal and spatial double differences, both a temporal and a spatial reference must be chosen to overcome the datum defect. The spatial reference is a pixel in Cologne, since it can be assumed that the region in Cologne is stable. The first SAR observation in May 1992 is chosen as temporal reference.

Figure 6.16a shows the mean deformation velocity map of the stable pixels using the conventional EMCF approach. It can be seen that the Earth's surface around the still active open-cast mines Garzweiler and Hambach subsides in a range from -6 to $-8\,\mathrm{cm/yr}$. On the contrary, closing the mines Sophie-Jacoba in the mining region Erkelenz in 1997 and Emil Mayrisch in the mining region Aachen in 1992 still causes the Earth's surface to rise by a few cm/yr. On a more detailed examination of the results, the figure shows isolated irregularities and jumps that may indicate a phase unwrapping error. Therefore, some individual pixels in the highlighted test regions 1 to 8 will be considered in more detail below.

For comparison purposes, the leveling data measured by GeoBasis NRW in a four-year cycle are used. Each campaign is evaluated in an individual adjustment following Halsig et al. (2013). Data from 1993 to 2001 are used to ensure that the evaluations are in the same time span as the ERS-1/-2 data. The leveling observations are relative height differences, so that the system has also a rank defect, however, this time only in space. To solve this problem, the system is forced to a total of four reference points. These points should preferably not be located in a deformation area and should be distributed over the area. In this evaluation the reference points are in Viersen, Cologne, Aachen and Rheinbach. The results are estimated normal heights of 2472 leveling points measured in all epochs. A mean deformation velocity map is shown in Fig. 6.16b. The leveling data also show the lowering of the region around the still active open-cast mines and the lifting of the mining regions Erkelenz and Aachen around the mines Sophia-Jacoba and Emil Mayrisch. The individual subsidence above the mine Sophia-Jacoba cannot be explained geologically and indicates irregularities in the leveling data.

6.3.2 Influence of the Estimated Motion Model

To investigate the influence of the motion model, the final SBAS analysis is performed again. However, now the motion model is estimated using the alternative way by maximizing the EPC function. To maximize the EPC function simulated annealing (Algorithm 3) is used in one case and the modified algorithm (Algorithm 4) in the other case. The resulting mean deformation velocity maps are very similar to the one shown in Fig. 6.16a. This first of all shows that both methods work. The occurring subsidence in the area around the active open-cast mines and the uplift in the

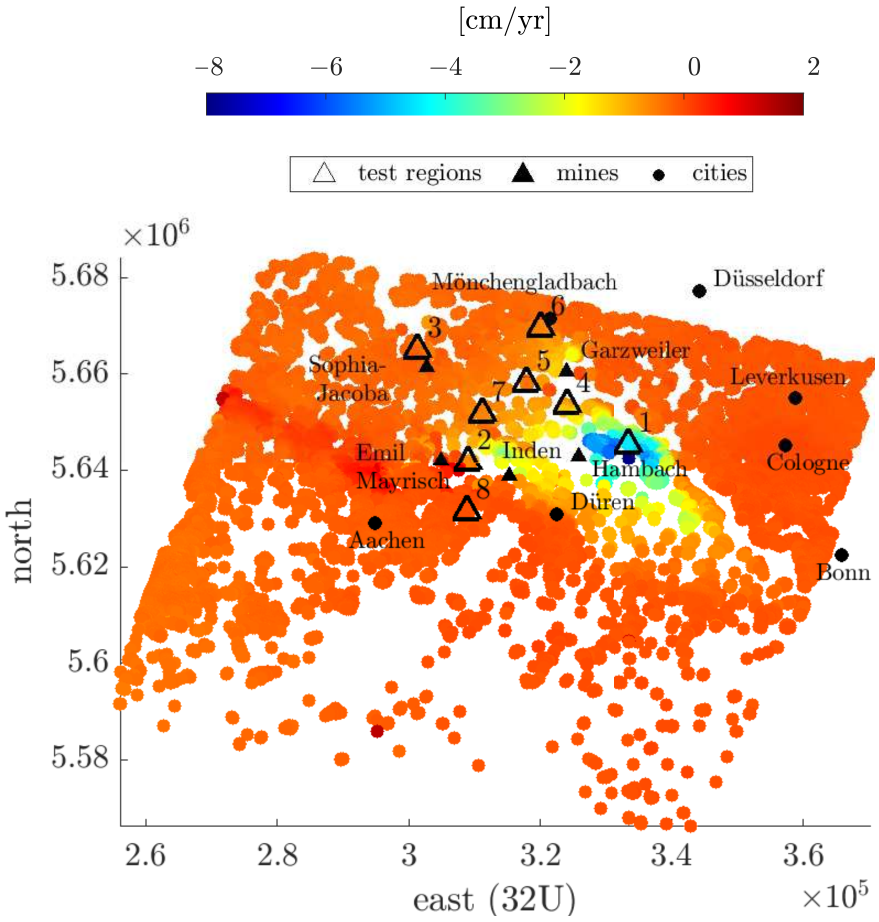

(a) conventional approach

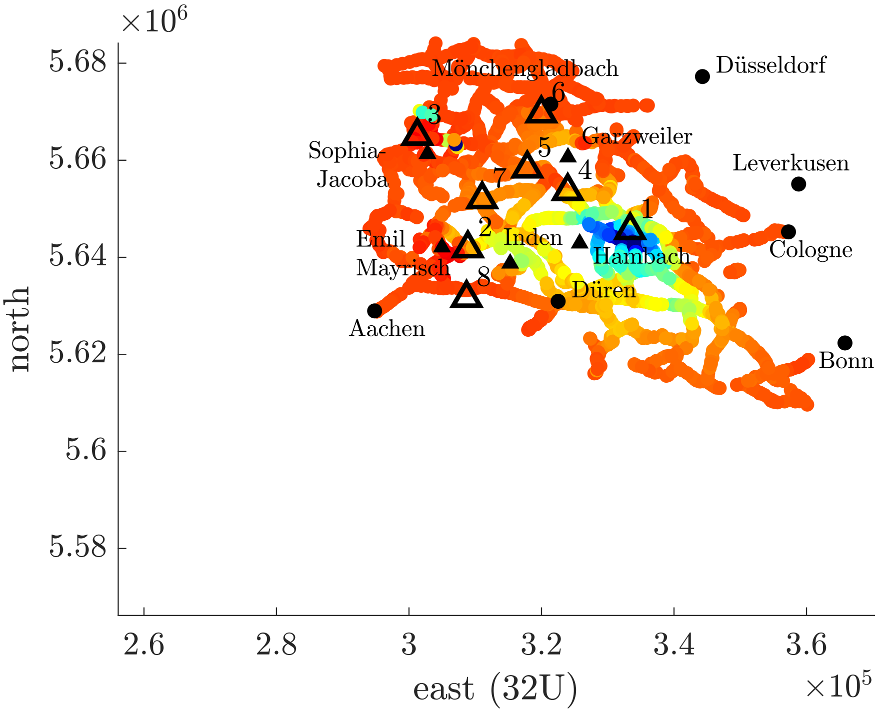

(b) leveling data

Figure 6.16: Mean deformation velocity map of the Lower-Rhine-Embayment based on ERS-1/-2 data from May 1992 to December 2000 and based on the leveling data from 1993 to 2001. The deformation model for the phase unwrapping in Fig. 6.16a is estimated using the conventional approach for pixels with a coherence value greater than 0.7 in at least 80 % of interferograms. The highlighted test regions 1 to 8 are examined in more detail as time series in Figs. 6.18 to 6.20.

area around the closed mines can be detected. The average differences comparing the conventional EMCF approach with the EMCF approach using Algorithm 3 and using Algorithm 4 is for both cases 0.002 cm/yr. For only 0.2 % of the pixels a difference of more than 0.1 cm/yr occurs. In order to be able to compare the results with each other, other criteria have to be found.

Looking at the estimated EPC values per phase gradient after the first phase unwrapping, it is noticeable that the EPC values are generally very high, in 80 % of the cases the value is higher or equal to 0.8, see Fig. 6.17. The dark blue histogram shows the EPC values when using the conventional method and the light blue histogram when using Algorithm 3 or respectively Algorithm 4. Since the EPC value is below the threshold value of 0.3 in only 0.01 % of the cases, there are almost no differences between these two methods. The histogram shows that the EPC value can be further increased using Algorithm 3 or 4 in contrast to the conventional method.

Since the true phase is not known, the accuracy of the results cannot be assessed as easily as with the simulated data. The following subsections therefore focus on determining criteria that can compare the results and verify the accuracy of the results.

6.3.2.1 Smoothness in Space

A criterion for evaluating whether there are errors in the results is to consider the smoothness of the results in space. If large movements from pixel to pixel are excluded, pixels whose movements deviate from their surrounding pixels indicate possible phase unwrapping errors or incorrectly assumed motion model parameters. Therefore, a Root Mean Square (RMS) error is calculated for each pixel x_j in space. For each pixel $x_j \in \mathcal{M}$ there is a deformation time series $h_{x_j}^{t_\alpha}, \ \forall t_\alpha \in \mathcal{M}'$. This deformation time series is compared to the deformation time series of the set $\mathcal{M}_{x_j}$ of m_{x_j} pixels within a radius of 300 m around x_j. If at least 5 pixels lie within this radius, the difference is squared and averaged over the number of m_{x_j} pixels. Then, the average over all m' time acquisition is taken to obtain one RMS value for each pixel

$$RMS_{x_j} = \frac{1}{m'} \sum_{t_\alpha \in \mathcal{M}'} \sqrt{\sum_{x_k \in \mathcal{M}_{x_j}} (h_{x_k}^{t_\alpha} - h_{x_j}^{t_\alpha})^2 / m_{x_j}}, \quad \forall x_j \in \mathcal{M}. \tag{6.20}$$

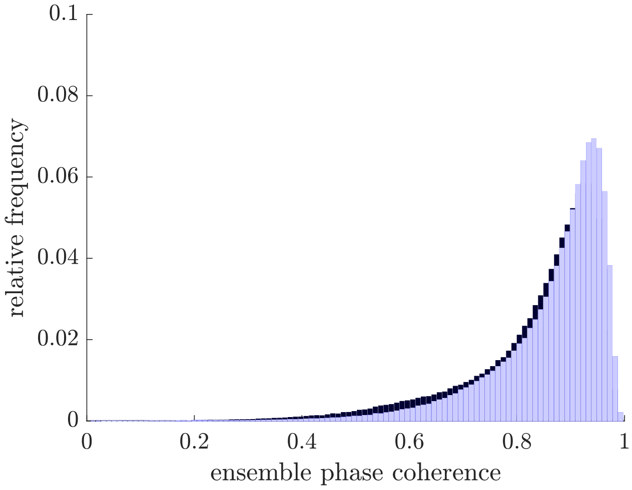

Figure 6.17: Relative frequency of occurring EPC values based on ERS-1/-2 data and using different methods to estimate the motion model parameters. The dark blue histogram is the result using the conventional method and the light blue histogram using Algorithm 3 or respectively Algorithm 4. There are almost no differences between Algorithms 3 and 4.

In this way, RMS values can be determined for a total of 98.7 % of pixels. Table 6.3 shows a summary of the RMS values for the different methods used to estimate the motion model parameters. The RMS values are classified into different orders of magnitude. It turns out very well that with the conventional method individual pixels have RMS values larger than the wavelength λ. Such large jumps are untypical and clearly indicate irregularities in the results. If individual pixels deviate from their neighboring pixels by a whole or half wavelength, this can indicate that a phase unwrapping error has occurred. By using the alternative Algorithm 3, the number of pixels with an RMS error greater than λ can be reduced from 8 to 1 and the number of pixels with an RMS error between λ and $\lambda/2$ from 45 to 10. Using Algorithm 4, no pixel has an RMS value greater than λ and only 9 pixels have values between λ and $\lambda/2$. Similar results can also be seen in the other classifications. It can be shown that the use of the alternative methods lead to smoother results in space, which is expressed in smaller RMS values. Using Algorithm 4, the RMS values can be further reduced. This shows that the number of phase unwrapping errors can be minimized using this method.

This conclusion will be further verified in the following by looking at individual deformation time series. In this context, pixels with very different RMS values depending on the method used to estimate the motion model are of particular interest.

6.3.2.2 Single Pixel Evaluations

Figures 6.18 to 6.20 give a more detailed view of the test regions 1 to 8 marked in Fig. 6.16a. The deformation time series of five pixels located in these test regions are shown from May 1992 to December 2000. The green triangles are the results using the conventional approach to estimate the motion model parameters. The results of the alternative Algorithm 3 are shown as blue squares and the results of the alternative Algorithm 4 as red points. To evaluate the results, the closest leveling point, shown as black squares, is added. In order to indicate the trend of the deformation time series, data from 2005 are represented in addition to the level data from 1993, 1997 and 2001.

When comparing interferometric data and leveling data sets, the problem of different spatial and temporal resolution and the problem of different temporal reference points occur. With the exception of test region 8, the nearest leveling point is at most 300 m away from the interferometric data. It can therefore be assumed that all examined data show similar behavior, since no abrupt deformation changes are expected. At test region 8 the nearest leveling point is 1600 m away from the interferometric data. The comparison of these two data sets should therefore be considered with caution. In general, correctly comparing the data would also have to take into account that the D-InSAR data observe only movements in LOS and the leveling data refer to vertical height changes. The used projection of the D-InSAR data into vertical height change is only allowed if the horizontal movement is assumed to be zero. However, since only ERS-1/-2 data from descending orbits are available, this assumption is necessary.

Table 6.3: RMS error in space with respect to pixels located in a radius of 300 meters, where at least 5 pixels must be within this radius. The RMS is classified and listed for different options to estimate the motion model parameters.

motion model	$RMS > \lambda$	$\lambda > RMS > \lambda/2$	$\lambda/2 > RMS > \lambda/4$	$RMS < \lambda/4$
conventional	8	45	255	141411
Algorithm 3	1	10	124	141584
Algorithm 4	0	9	122	141588

The time offset is compensated by linearly interpolating the leveling data piecewise over time according to Esch et al. (2019b). For each coherent pixel, a local offset is calculated using a weighted average. The weights are chosen so that heights that are close to the leveling points are weighted more strongly and the weights between the leveling points decrease quadratically. Figures 6.18 to 6.20 show the corresponding deformation time series after applying the local offset. The reader is reminded that the vertical axes of the plots were chosen differently, since the examined pixels show differently strong motions.

First, pixels are considered where both the conventional and the alternative methods show comparable results that also agree well with the leveling data. Figure 6.18a examines pixels in Thorr, Bergheim next to the still active open-cast mine Hambach. Brown coal mining causes the surface of the surrounding areas to subside. This can also be seen in the Fig. 6.18a. All data sets and methods show that the Earth's surface decreased by a few decimeters between 1992 and 2001, respectively 2005. The pixels in test region 2 are located in Aldenhoven, Düren in the basin of the mining region Aachen near the mine Emil Mayrisch, see Fig. 6.18b. Coal was mined there until 1992, as can be seen from the corresponding subsidence of the ground which slowly decreases at the end of 2000. The subsequent rise in the groundwater level causes a renewed uplift which is already becoming apparent at the end of the D-InSAR data. Again all methods, the conventional and both alternative methods, provide identical results and agree with the leveling data. The third considered test region is located in Wassenberg, Heinsberg near the mining region Erkelenz next to the mine Sophia-Jacoba, see Fig. 6.18c. Coal mining took place there until 1997. The resulting subsidence is reflected much more strongly in the D-InSAR data than in the leveling data. The following flooding of the mine galleries led to a renewed uplift of the Earth's surface which becomes clearly visible in the temporally more highly resolved D-InSAR data in 2000. Once again, all methods lead to nearly the same motion model.

Now pixels are considered where different motion parameters are estimated using the conventional and the alternative methods, which is also reflected in different RMS values. In test region 4, pixels in Kirchherten, Bedburg between the two active open-cast mines Garzweiler and Hambach are considered, see Fig. 6.19a. Similar to the pixels in test region 1, brown coal mining causes the Earth's surface to sink by a few centimeters. One pixel, however, shows a very extreme subsidence. In this case, the conventional method fails. Looking at the corresponding phase gradients and the estimated motion model parameters, it becomes clear that wrong motion model parameters are estimated with the conventional method. Table 6.4a shows the estimated deformation velocity variations and the estimated topography errors as well as the corresponding EPC values for the phase gradients where the conspicuous pixel is involved. The values are listed for the conventional method, Algorithm 3 and Algorithm 4. At phase gradient 4 the conventional method estimates a too extreme deformation velocity variation. The corresponding EPC value of 0.3 is extremely low which also indicates that the method fails. This is also reflected in the high RMS value calculated to the nearest 19 pixels within a radius of 300 meters. The RMS value is greater than the wavelength λ. The alternative Algorithms 3 and 4 show better results. The RMS values are below $\lambda/4$. Both methods are identical, since Algorithm 4 is only relevant if an EPC value below 0.3 occurs. Since this is not the case, in both cases the maximum is determined by simulated annealing. The obtained results fit better with the neighboring pixels and the leveling data.

Similar results can be seen in test regions 5 and 6. Figure 6.19b shows pixels in Holzweiler, Erkelenz next to the active mine Garzweiler. The open-cast mining again leads to a subsidence of the area. However, it is clearly visible that the conventional method indicates a strong uplift at one pixel. This behavior deviates clearly from the neighboring pixels, which is reflected in a high RMS

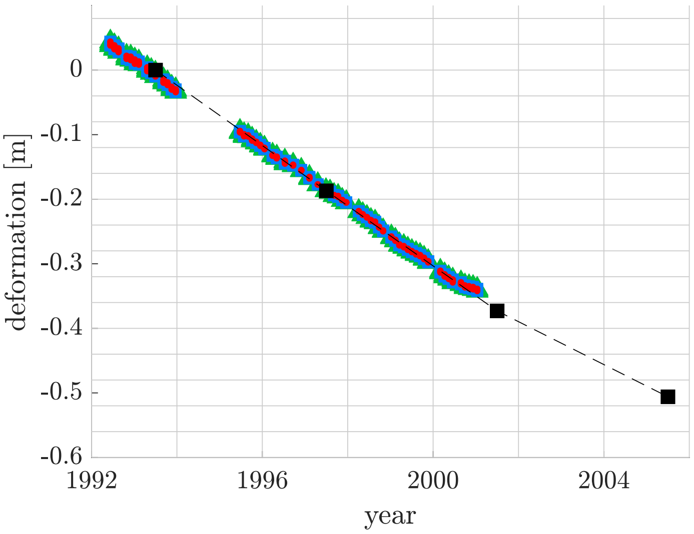

(a) test region 1: Thorr, Bergheim

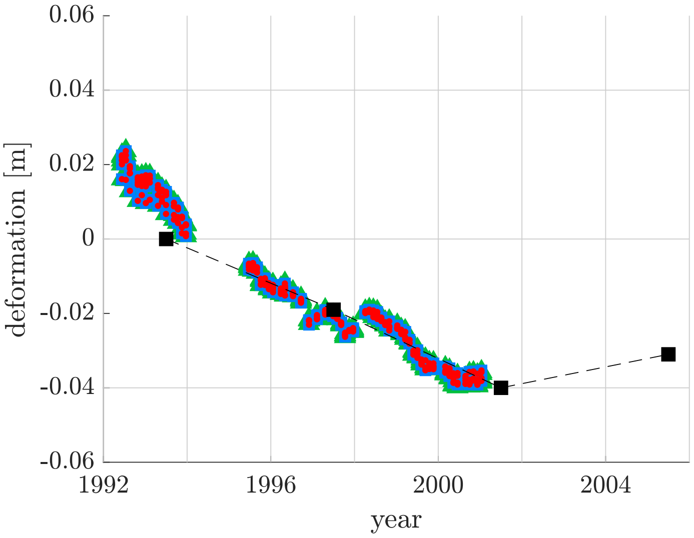

(b) test region 2: Aldenhoven, Düren

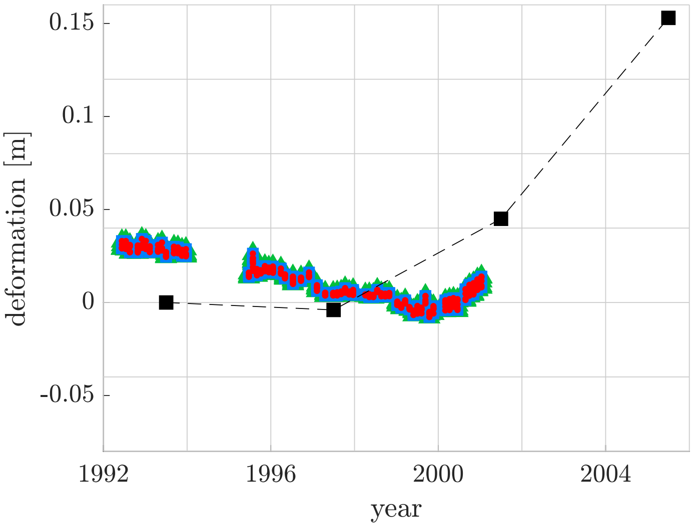

(c) test region 3: Wassenberg, Heinsberg

Figure 6.18: Deformation time series of five pixels lying in each of the highlighted test regions 1 to 3 shown in Fig. 6.16a. The green triangles are the results using the conventional approach, the blue squares using Algorithm 3 and the red points using Algorithm 4. For comparison the black squares indicate the data from the closest leveling point.

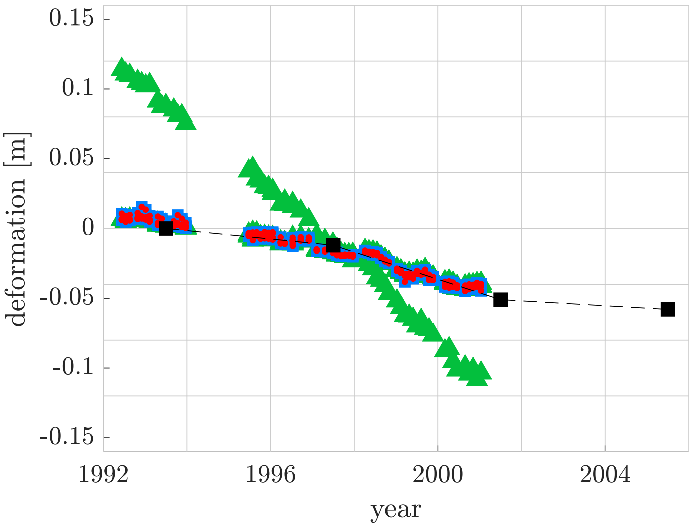

(a) test region 4: Kirchherten, Bedburg

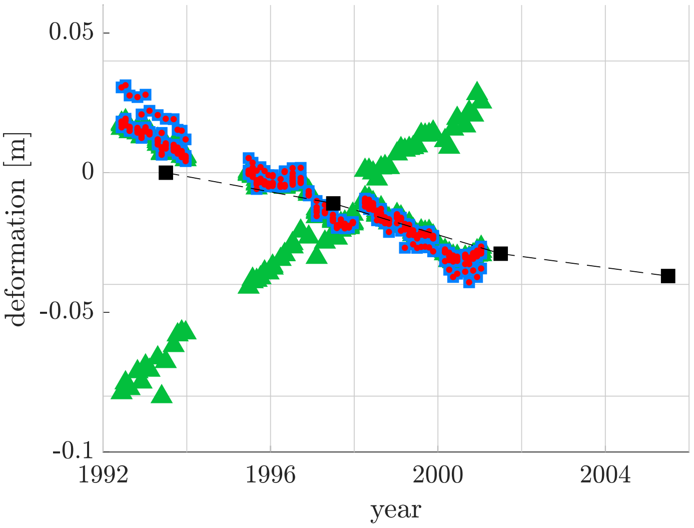

(b) test region 5: Holzweiler, Erkelenz

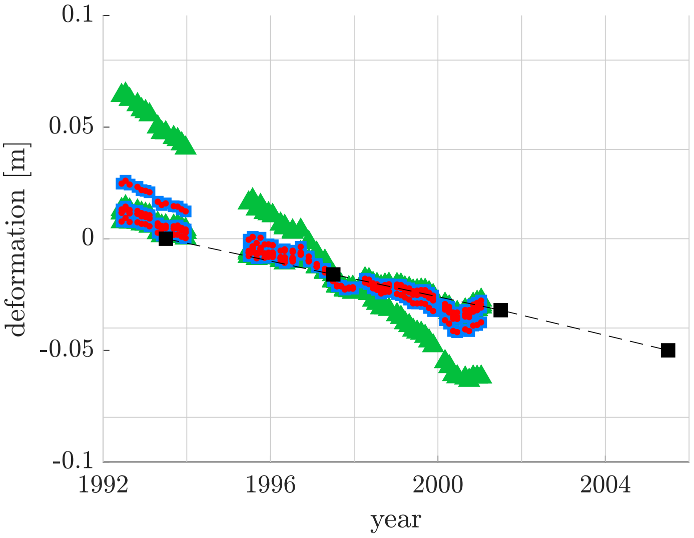

(c) test region 6: Rheydt, Mönchengladbach

Figure 6.19: Deformation time series of five pixels lying in each of the highlighted test regions 4 to 6 shown in Fig. 6.16a. The green triangles are the results using the conventional approach, the blue squares using Algorithm 3 and the red points using Algorithm 4. For comparison the black squares indicate the data from the closest leveling point.

Table 6.4: Motion model parameters belonging to the phase gradients of the conspicuous pixels in the test region 4 to 8, cf. Figs 6.19a to 6.20b. The motion model parameters are estimated with the conventional and the alternative approach using simulated annealing (Algorithm 3) and the modified algorithm (Algorithm 4).

(a) Kirchherten

idx	conventional			Algorithm 3			Algorithm 4		
	v[cm/yr]	Δh[m]	EPC	v[cm/yr]	Δh[m]	EPC	v[cm/yr]	Δh[m]	EPC
1	0.0	-5	0.35	0.0	-2	0.38	0.0	-2	0.38
2	0.0	0	0.37	-0.1	0	0.39	-0.1	0	0.39
3	0.0	5	0.34	0.0	4	0.35	0.0	4	0.35
4	2.0	-50	0.03	0.1	-0	0.41	0.1	-0	0.41
5	0.0	5	0.35	-0.1	2	0.42	-0.1	2	0.42
6	0.0	0	0.38	-0.1	2	0.41	-0.1	2	0.41

(b) Holzweiler

idx	conventional			Algorithm 3			Algorithm 4		
	v[cm/yr]	Δh[m]	EPC	v[cm/yr]	Δh[m]	EPC	v[cm/yr]	Δh[m]	EPC
1	3.5	40	0.07	-1.0	-0	0.30	-1.0	-0	0.30
2	1.0	-25	0.10	0.3	3	0.37	0.3	3	0.37
3	-3.5	-45	0.07	0.3	1	0.37	0.3	1	0.37
4	2.0	-45	0.16	-0.3	-3	0.33	-0.3	-3	0.33

(c) Rheydt

idx	conventional			Algorithm 3			Algorithm 4		
	v[cm/yr]	Δh[m]	EPC	v[cm/yr]	Δh[m]	EPC	v[cm/yr]	Δh[m]	EPC
1	-1.0	-5	0.37	-0.2	-1	0.66	-0.2	-1	0.66
2	1.0	0	0.42	0.2	0	0.67	0.2	0	0.67
3	0.5	-5	0.46	0.2	-1	0.59	0.2	-1	0.59
4	0.5	0	0.51	-0.3	0	0.67	-0.3	0	0.67
5	1.0	5	0.25	0.3	-1	0.58	0.3	-1	0.58
6	-0.5	0	0.57	-0.2	2	0.69	-0.2	2	0.69

(d) Gevenich

idx	conventional			Algorithm 3			Algorithm 4		
	v[cm/yr]	Δh[m]	EPC	v[cm/yr]	Δh[m]	EPC	v[cm/yr]	Δh[m]	EPC
1	0.5	5	0.21	7.5	9	0.26	-0.1	0	0.24
2	-3.5	-5	0.16	0.8	1	0.23	0.2	-3	0.16
3	0.0	-25	0.08	7.5	9	0.28	-0.2	-0	0.24
4	-0.5	0	0.20	-1.7	-3	0.24	0.1	0	0.23
5	0.0	0	0.24	0.9	3	0.26	0.1	-2	0.25

(e) Eschweiler

idx	conventional			Algorithm 3			Algorithm 4		
	v[cm/yr]	Δh[m]	EPC	v[cm/yr]	Δh[m]	EPC	v[cm/yr]	Δh[m]	EPC
1	0.0	0	0.89	0.0	0	0.89	0.0	0	0.89
2	0.0	0	0.93	0.0	-1	0.93	0.0	-1	0.93
3	0.0	0	0.95	0.0	1	0.95	0.0	1	0.95
4	0.0	0	0.91	0.0	0	0.91	0.0	0	0.91
5	-0.5	0	0.56	-0.1	0	0.61	-0.1	0	0.61

value, larger than λ. Looking at the associated phase gradients in Table 6.4b, the reason can be found in the high deformation velocity variations estimated using the conventional method. Here, again, very low EPC values arise. Algorithms 3 and 4 estimate motion model parameters that produce EPC values greater than 0.3, so there are no differences between the two methods. In addition, the results fit better to the neighboring pixels expressed by low RMS values, below $\lambda/4$. Moreover, the results are consistent with the leveling data. Figure 6.19c shows pixels in Rheydt, Mönchengladbach within the basin of the still active open-cast mine Garzweiler. The pixels in this region decrease and again the conventional method fails at one pixel. This results in an RMS value greater than $\lambda/2$. Table 6.4c shows the corresponding estimated parameters, where the conventional method estimates too large deformation velocities. The results of the alternative methods fit better to the neighboring pixels (RMS$<\lambda/4$) and better to the leveling data. The corresponding EPC values are good with approx. 0.6, so there are no differences between Algorithms 3 and 4.

Test region 7 provides an example where Algorithm 4 shows its effect. Figure 6.20a shows pixels in Gevenich, Linnich in the area of influence of the active open-cast mines. These lead to a subsidence of the area. Depending on the used method, a different behavior can be recognized for one pixel. The estimated motion model parameters of the corresponding phase gradients are listed in Table 6.4d. Remarkable are the extremely low EPC values which result from the estimated motion model parameters. Using Algorithm 3, all EPC values are below the threshold of 0.3. So it can be assumed that the estimation is not reliable. Thus, Algorithm 4 uses the local maximum around zero found by the Nelder-Mead method. The extreme values, such as those that occur for phase gradients 1 and 3 using Algorithm 3, are avoided. Algorithm 3 results in an RMS value greater than λ for the conspicuous pixel. Using Algorithm 4, the value is smaller $\lambda/2$ and the result fits better to the neighboring pixels and also better to the leveling data. Using the conventional method, a slightly too large movement is estimated, especially for the phase gradient 2. In the deformation time series, it is noticeable that the pixel also deviates significantly more from the neighboring pixels (RMS greater $\lambda/2$) than with Algorithm 4. In this case, Algorithm 4 delivers the best results.

The last considered test region is located in Eschweiler, Aachen near the still active open-cast mine Inden and near the mine region Aachen with the closed mine Emil Mayrisch. The closest leveling point is 1600 m away. This is also shown by the fact that the leveling points show a slight increase of the Earth's surface, whereas the interferometric data show no movement or rather a slight decrease. This is due to the fact that the leveling point is more in the basin of the closed mine Email Mayrisch and the interferometric data 1600 m southeast and therefore more in the basin of the still active open-cast mine Inden. However, it is noticeable that one pixel in the D-InSAR data shows a significantly different behavior towards the neighboring pixels. All methods, both the conventional and the two alternative Algorithms 3 and 4, indicate a strong decrease of the pixel. Looking at the estimated motion model parameters of the associated phase gradients in Table 6.4e, it can be seen that the estimated deformation velocities are some mm/yr and the corresponding EPC values are 0.5-0.6 on average. If one now considers the estimated deformation velocities of the phase gradients that belong to the neighboring pixels, it can be seen that these are almost zero and that the associated EPC values are greater than 0.8. So it can happen that even with Algorithm 4 wrong movements are still estimated which do not fit to the neighboring pixels. These errors can be further minimized by weighting the phase gradients of the neighboring pixels, which were obviously estimated more reliably due to the higher EPC values, with a higher factor. The influence of the weights will now be discussed in the following section.

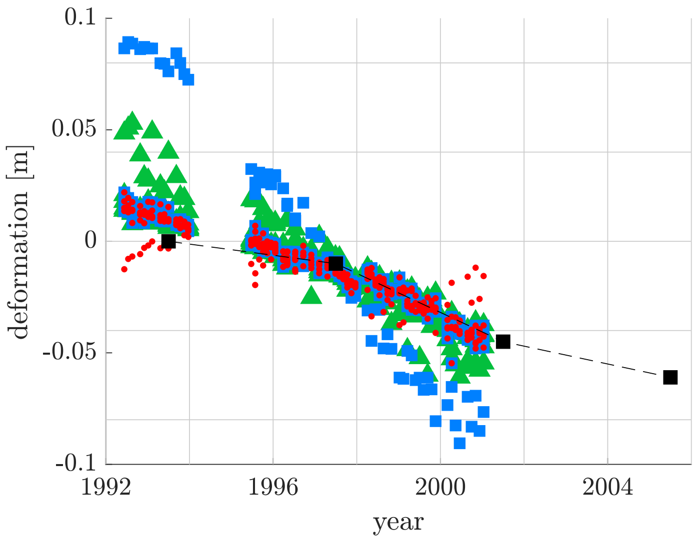

(a) test region 7: Gevenich, Linnich

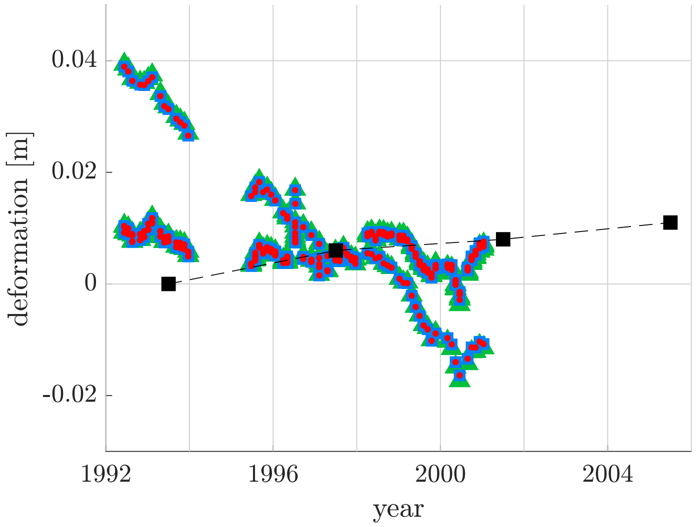

(b) test region 8: Eschweiler, Aachen

Figure 6.20: Deformation time series of five pixels lying in each of the highlighted test regions 7 and 8 shown in Fig. 6.16a. The green triangles are the results using the conventional approach, the blue squares using Algorithm 3 and the red points using Algorithm 4. For comparison the black squares indicate the data from the closest leveling point.

6.3.3 Influence of the Weights

On the basis of the simulated data, it could already be shown that the choice of weights has an influence on the phase unwrapping result. For the temporal phase unwrapping constant weights can be assumed or the weights are set in dependence of the phase gradients, see *Weights 2*, cf. (6.17). For the spatial phase unwrapping it is possible to choose between the conventional weights depending on the temporal costs, *Weights 2* or the EPC based *Weights 3*, cf. (6.18). Coherence based *Weights 1*, cf. (6.16), are an additional option. To investigate only the influence of the weights, the motion model is estimated using Algorithm 4, as it has proven to be the best. As with the simulated data, the influence of spatial weights will be investigated first, followed by the influence of temporal weights.

6.3.3.1 Influence of Spatial Weights

To validate the results, the RMS is calculated again for each pixel in space. The results of the different spatial weights are shown in Table 6.5. To remember, weights that are constant over time

Table 6.5: RMS error in space with respect to pixels located in a radius of 300 meters, where at least five pixels must be in this radius. The RMS is classified and listed for different spatial weights. The temporal weights are assumed to be constant in all cases.

weights	$RMS > \lambda$	$\lambda > RMS > \lambda/2$	$\lambda/2 > RMS > \lambda/4$	$RMS < \lambda/4$
conventional	0	9	122	141588
Weights 1	0	16	150	141553
Weights 2	0	8	112	141599
Weights 3	0	8	107	141604

are assumed in all cases. It can be seen that *Weight 1* clearly has the highest RMS values. With this choice of weights, the results are not smooth in space and in sum 16 pixels have RMS values between one and half a wavelength. Since the RMS value refers to a radius of 300 m, such jumps are rather unlikely and indicate phase unwrapping errors. With *Weights 2*, these jumps can be slightly minimized to 8 compared to 9 for the conventional weighting. A more significant reduction of the RMS can be seen in the value range from $\lambda/2$ to a $\lambda/4$ .The number can be reduced from 122 to 112 by using *Weights 2* instead of the conventional ones. However, the smallest RMS values result from *Weights 3*. Thus, with help of the RMS values, it can be observed that on the basis of the real data the use of *Weights 3* lead to an improvement with regard to the conventional weighting. This will be further validated by single pixel analysis.

For the single pixel analysis, especially pixels where differences in the resulting deformation time series result from the choice of spatial weights are considered more closely. First, the 8 previously considered test regions are investigated. For the pixels in test regions 1, 3, 4, 6 and 7 there are no significant differences, so that a closer examination is omitted here. It should be remarked, however, that some of these pixels have significant movements, which can also be reproduced using *Weights 2*. At first, this is in contrary to the previous statement that large movements cannot be reproduced by means of this weighting. If, however, one considers the temporal phase gradients in these regions, it becomes apparent that the phase gradients already fulfill the spatial constraints. The choice of spatial weights therefore has no influence here.

The situation is different for the pixels in test regions 2, 5 and 8. For these test regions, the deformation time series for a total of five pixels are shown again in Fig. 6.21. The green triangles show the results when using the conventional weights, the light blue squares when using *Weights 1*, the orange points when using *Weights 2*, and the dark blue points when using *Weights 3*. As a reference the deformation time series of the nearest leveling point are drawn again as black squares.

Test region 2 shows pixels in Aldenhoven, Düren, near the mine Emil Mayrisch which was closed in 1992, see Fig. 6.21a. The estimated motion model parameters fit well and clearly show that the Earth's surface subsides until the end of 2000 as a result of the mining that took place. The corresponding EPC values are on average 0.9 and the temporal costs are 0, so that the weights are very high for both *Weights 3* and the conventional weights. The coherence values are also very high resulting in very high *Weights 1*. *Weights 2* are the smallest which can explain why the resulting deformation time series results in the lowest rate of subsidence. This confirms the previously established assumption that *Weights 2* cannot reproduce deformations as well. In this case, however, the lower rate of subsidence is better suited to the leveling data.

In test region 5, displayed in Fig. 6.21b, pixels in Holzweiler, Erkelenz near the still active mine Garzweiler are shown. The open-cast mining leads to a subsidence of the surrounding area. One

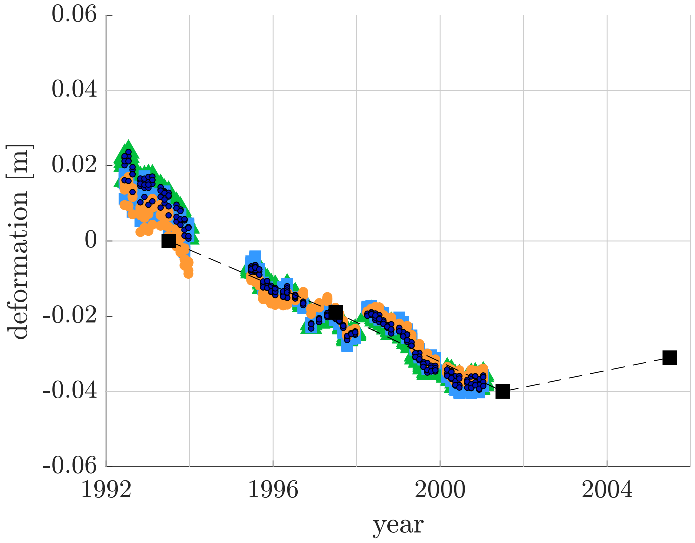

(a) test region 2: Aldenhoven, Düren

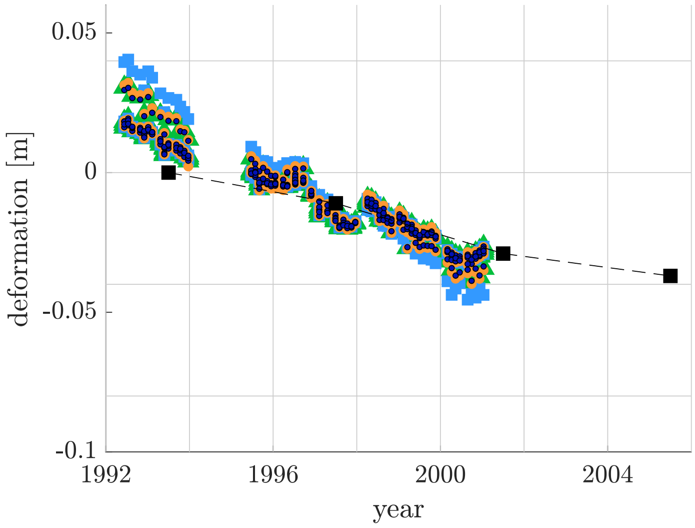

(b) test region 5: Holzweiler, Erkelenz

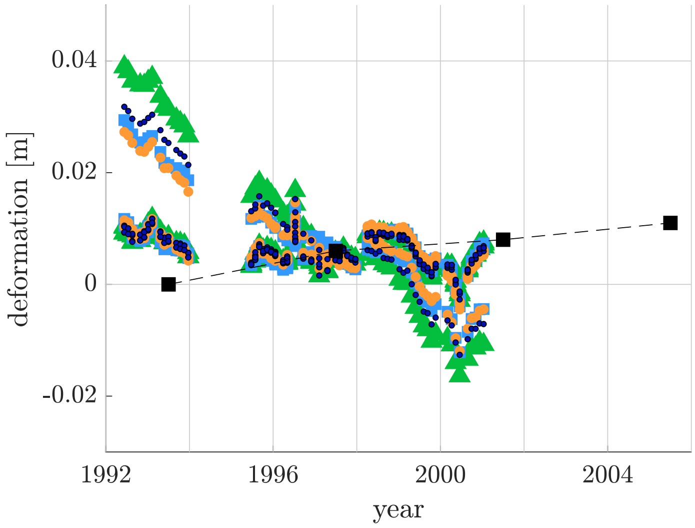

(c) test region 8: Eschweiler, Aachen

Figure 6.21: Deformation time series of five pixels lying in each of the test regions. The analysis is done with different spatial weights. For the temporal weights constant values are assumed. The green triangles are the results using the conventional spatial weights, for the light blue squares *Weights 1* are used, for the orange points *Weights 2* and for the dark blue points *Weights 3*.

pixel now shows a much stronger lowering when using *Weights 1*. The corresponding phase gradients of this pixel also show a larger motion than the phase gradients of the surrounding pixels. The corresponding EPC values are on average 0.34 and the temporal costs are over 20. *Weights 3* and the temporal costs are therefore rather low. For the surrounding phase gradients, which show less movement and where the EPC values are on average 0.9 and the temporal costs are on average zero, the corresponding weights are therefore very high. *Weights 2* also trust the less strong movements, so that for all three cases, conventional, *Weights 3* and *Weights 2*, there is no difference. The situation regarding *Weights 1* is now different. For all phase gradients, also for the one with a larger movement, the coherence values and thus the weights are high. So all phase gradients, regardless of large or less large, are equally trusted. This can explain why in this case one pixel has a much stronger decrease than the surrounding pixels.

Test region 8 shows pixels in Eschweiler, Aachen near the still active mine Inden and the closed mine Emil Mayrisch in the mine region Aachen, see Fig. 6.21c. The nearest leveling point is 1600 m away towards the closed mine Emil Mayrisch. The leveling point thus shows an elevation of the Earth's surface, whereas the interferometric data show a decrease. It can be clearly seen that one pixel does not match its neighboring pixels. The conventional weighting shows the largest deviation. For the corresponding phase gradients the movement is estimated too high in comparison to the surrounding phase gradients. The EPC values of the overestimated motion model are on average 0.5-0.6. For the surrounding phase gradients, which have a less large motion, the EPC value is greater than 0.8. These phase gradients are therefore more familiar with *Weights 3*, so that the remarkable pixel is pulled down. This works even better with *Weights 1* and *Weights 2*. This is not surprising with *Weights 2*, since large phase gradients are generally less familiar with this weighting. In this case, these large phase gradients also show lower coherence values, so that *Weights 1* also work well.

Finally, the pixel is examined which has an RMS value smaller than $\lambda/2$ for *Weights 2* and *3* and an RMS value larger than $\lambda/2$ for the conventional weighting, see Table 6.5. It is a pixel in Odenkirchen, Mönchengladbach about 4 km south of the region in Rheydt investigated in test region 8. The related deformation time series is shown in Fig. 6.22. It can be clearly seen that for the conventional weights and *Weights 1* and *2*, there is a conspicuous pixel that decreases too much. The RMS value is 0.028 m for the conventional weights, 0.025 m for *Weights 1* and 0.016 m for *Weights 2*. *Weights 3* can lower the RMS value of this pixel to 0.003 m, so that it optimally matches the neighboring pixels. In this case, the phase gradients of the conspicuous pixel were not sufficiently down-weighted by *Weights 2*. There is an improvement compared to the conventional weighting, but *Weights 3* fit even better in this case.

It can be concluded that the spatial weights of course only have an influence when the temporally unwrapped phase gradients in this region do not fulfill the spatial constraints. With all four tested spatial weights, conventional, *Weights 1*, *Weights 2* and *Weights 3*, it is therefore possible to detect a settlement in the region around the active open-cast mines Garzweiler, Hambach and Inden and an uplift around the closed mines Sophie-Jacoba and Emil Mayrisch. However, *Weights 1* provides the worst results. The results are not smooth in space and occasionally show more jumps than with conventional weights. Consequently, the coherence value does not seem to be a good criterion. Although it indicates the correlation between the two signals of the SAR images used for interferogram generation, it does not indicate the degree of reliability of the temporally unwrapped phase gradients in which an estimated motion model is already involved. The reliability of the motion model is reflected in the EPC value. This value seems to be very suitable as a spatial weight. In contrast to the conventional weighting, which is based on the temporal costs, spatially smoother results can be

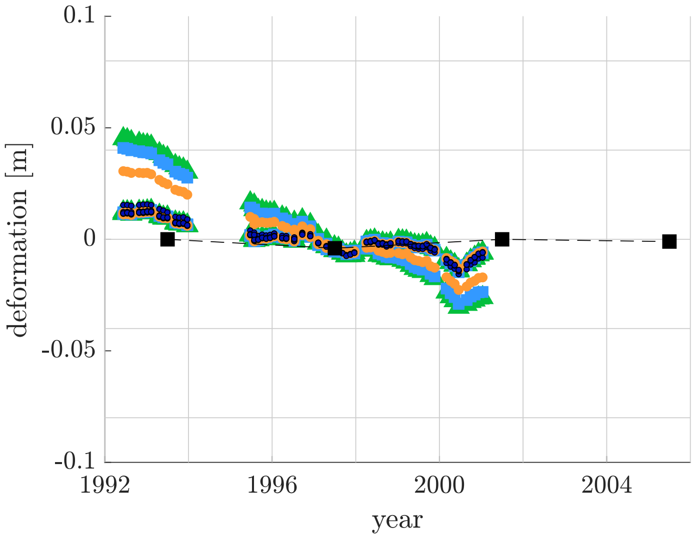

Figure 6.22: Deformation time series of five pixels lying in the test region 9. The analysis is done with different spatial weights. For the temporal weights constant values are assumed. The green triangles are the results using the conventional spatial weights, for the light blue squares *Weights 1* are used, for the orange points *Weights 2* and for the dark blue points *Weights 3*.

achieved using *Weights 3*. *Weights 2* trust small gradients which show almost no movement stronger than large gradients. In the test region studied here, this weighting is also very well suited. In the cases where the spatial constraints are not fulfilled, the assumption that no or only a very small movement occurs is usually correct.

6.3.3.2 Influence of Temporal Weights

After studying the spatial weights, the influence of the temporal weights is analyzed. Therefore, *Weights 2* are used in the temporal phase unwrapping instead of the previously assumed constant temporal weights. For the spatial weights, a choice is made between the conventional weights, *Weights 2* and *Weights 3*. *Weights 1* are neglected as they have already been found to be less suitable. In all cases, the motion model is estimated by maximizing the EPC function using Algorithm 4. The modified observations $\boldsymbol{\chi}^{\boldsymbol{\Delta t}}_{\Delta x_{kl}}$ entering the temporal phase unwrapping, cf. (5.12), are therefore the same in all cases. Since the EPC values are usually very high, i.e. the motion model fits the observations very well, the modified observations already fulfill the temporal constraints for the most part. In 77.9 % of the cases the phase gradient is already consistent in time, so all temporal constraints are fulfilled, and in 18.9 % of the cases an inconsistency occurs only in less than 5 temporal triangles. Thus, the influence of the temporal weights is rather small.

This is also reflected in the RMS values in Table 6.6. The RMS values for different spatial weights are shown, whereby in contrast to the values in Table 6.5 *Weights 2* are used as temporal

Table 6.6: RMS error in space with respect to pixels located in a radius of 300 m, where at least five pixels must be in this radius. The RMS is classified and listed for different spatial weights. For the temporal phase unwrapping *Weights 2* are used.

weights	$RMS > \lambda$	$\lambda > RMS > \lambda/2$	$\lambda/2 > RMS > \lambda/4$	$RMS < \lambda/4$
conventional	0	9	126	141584
Weights 2	0	9	107	141603
Weights 3	0	8	107	141604

weights instead of constant weights. A comparison of the two tables shows that there are no large differences. With the conventional spatial weights, a change in the temporal weights tends to lead to a moderate deterioration. With constant temporal weights, the RMS value at 122 pixels is between $\lambda/2$ and $\lambda/4$ and with *Weights 2* as temporal weights the number rises to 126. If *Weights 2* are used both in space and in time, the RMS value at 9 pixels is between λ and $\lambda/2$ and at 107 pixels between $\lambda/2$ and $\lambda/4$. With constant temporal weights, the numbers are 6 and 112, respectively. With *Weights 3* as spatial weights, there is no difference or the differences lie within a value range of less than one and a half centimeter.

Figures 6.23 and 6.24 show the deformation time series of the test regions 2, 5, 8 and 9 analogous to Figs. 6.21 and 6.22. The only difference is that *Weights 2* are used as temporal weights instead of constant ones. The green triangles again show the results for conventional spatial weights, the orange points for *Weights 2* also as spatial weights and the dark blue points for *Weights 3* as spatial

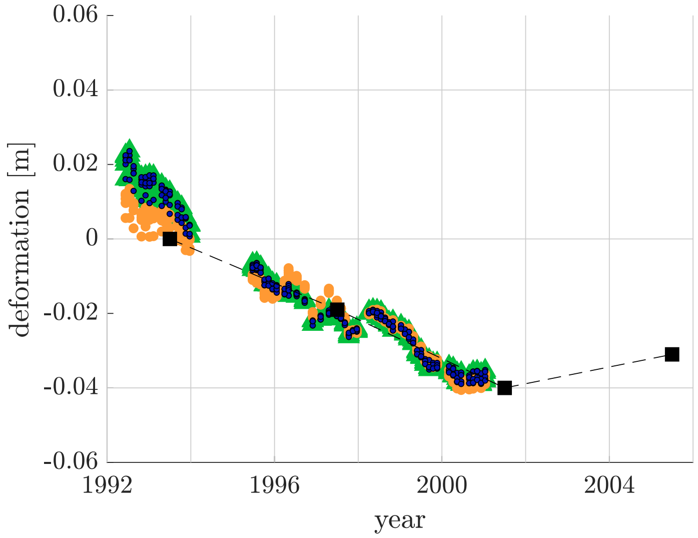

(a) test region 2: Holzweiler, Erkelenz

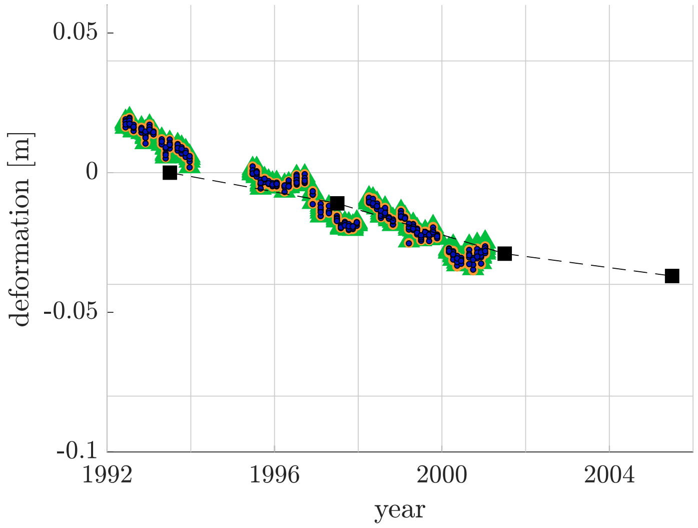

(b) test region 5: Holzweiler, Erkelenz

Figure 6.23: Deformation time series of five pixels lying in each of the highlighted test regions 2 and 5. The analysis is done with different spatial weights. The temporal weights are based on *Weights 2*. The green triangles are the results using the conventional spatial weights, the orange points are the results using *Weights 2* also as spatial weights and for the dark blue points *Weights 3* are used as spatial weights. For comparison the black squares indicate the data from the closest leveling point.

weights. Looking at test region 2, see Figs. 6.21a and 6.23a, there is almost no difference. Only at the boundaries of the data gap around 1994 and towards the end of the time series minimal differences can be observed. At test region 5, see Figs. 6.21b and 6.23b, *Weights 2* as temporal weights result in deformation time series of the neighboring pixels all matching very well in themselves and with the leveling data. Especially the offsets of the conspicuous pixel occurring at the boundaries of the time series and directly after the data gap can be fixed. However, the differences are very small and lead to an improvement of the RMS value of this pixel by about 0.8 cm only. In test region 8, see Figs. 6.21c and 6.24a, *Weights 2* as temporal weights also partly lead to an improvement. The results when using *Weights 2* or *Weights 3* as spatial weights fit better to the neighboring pixels, so that the RMS value can be improved by 0.7 cm or 1.0 cm. When conventional spatial weights are used, no significant difference can be detected. Test region 9, see Fig. 6.22 and 6.24b, looks a little different. Using *Weights 2* as temporal weights results in a slight deterioration compared to

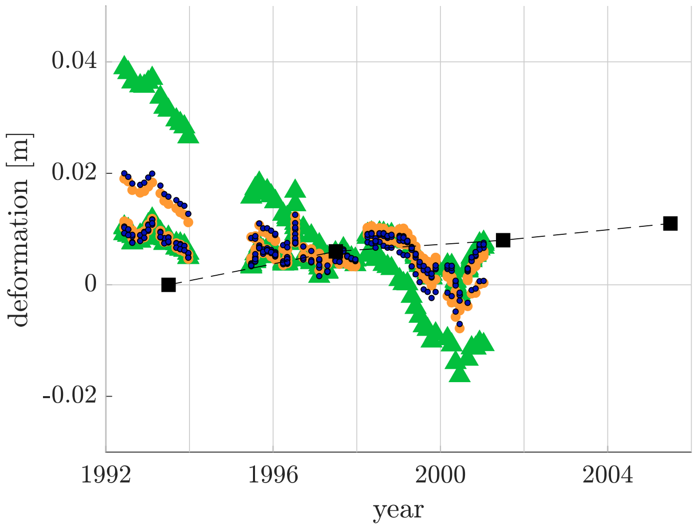

(a) test region 8: Eschweiler, Aachen

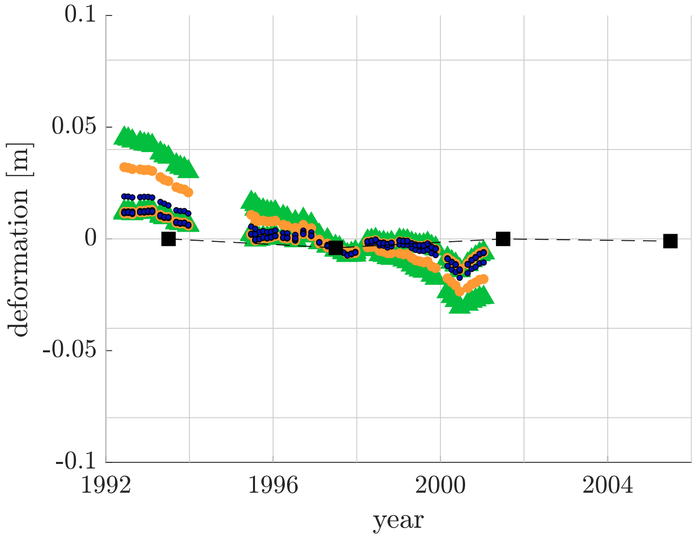

(b) test region 9: Odenkirchen, Mönchengladbach

Figure 6.24: Deformation time series of five pixels lying in each of the highlighted test regions 8 and 9. The analysis is done with different spatial weights. The temporal weights are based on the *Weights 2*. The green triangles are the results of using the conventional spatial weights, the orange points are the results of using *Weights 2* also as spatial weights and for the dark blue points *Weights 3* are used as spatial weights. For comparison the black squares indicate the data from the closest leveling point.

the constant temporal weights. The RMS value increases by 0.1 cm for *Weights 2* and by 0.3 cm for *Weights 3* as spatial weights. With the conventional spatial weights again no significant difference can be noticed.

6.4 Summary

It can be concluded that all discussed ideas lead to an improvement when applied to simulated and to real data of the ERS-1/-2 stack. The alternative approach for estimating the motion model parameters by maximizing the EPC function can prevent some phase unwrapping errors in contrast to the conventional method by estimating the cost of the temporal LP iteratively. Maximization the EPC function using Algorithm 4, which is a modified algorithm that combines simulated annealing and the Nelder-Mead method, has proven to be the most appropriate method. It is very robust even with a high noise level. The alternative approach also has the advantage that the motion model can be estimated independently of the temporal phase unwrapping. The temporal phase unwrapping only needs to be solved once. With the conventional approach the temporal LP has to be solved iteratively several times depending on the choice and discretization of the search space for the motion model parameters. Consequently, the alternative method also provides a considerable advantage in terms of run time.

The analysis of the choice of spatial weights has shown that *Weights 2* and *3* have led to an improvement. *Weights 2* are phase and length dependent, so that large phase gradients get a low weight and with *Weights 3* the EPC value is relevant. Phase gradients where the estimated motion model fits well with the observations, i.e. where the EPC value is high, become more reliable in spatial phase unwrapping. They therefore receive a high weight. For conventional weights, the result of the temporal phase unwrapping is important. If the temporal costs are high, the phase gradient is less reliable and the weight in the spatial phase unwrapping is low. The alternative spatial *Weights 2* and *3* lead to better, spatially smoother deformation time series compared to the conventional weights. Furthermore, the alternative weights have the advantage that they are independent of the temporal phase unwrapping.

The modified observations entering the temporal phase unwrapping already fulfill the temporal constraints for the most part. Thus, the temporal weights do not have a very large influence when applied to the real data. With the conventional method the temporal weights are assumed to be constant. This is also a widely used procedure (Pepe and Lanari, 2006, Fornaro et al., 2011). Alternatively, *Weights 2*, which are different in time for a phase gradient, are used as temporal weights. In sum, however, the different temporal weights only have a very small influence on the finally estimated deformation time series. In some cases the results are smoother, so that an improvement can be expected when compared to the constant temporal weights, but in some cases they are also less smooth. Thus, in the following, constant temporal weights will be assumed, as this is also the standard case.

In this chapter, the EMCF algorithm could be modified in such a way that the temporal phase unwrapping only has to be performed once and that the spatial weights are independent from the solution of the temporal phase unwrapping. This modification is the second main objective of this thesis, which is thus fulfilled. With the help of these modifications it is now possible to combine the EMCF algorithm, which runs in two steps, into a one-step three dimensional approach.

7. One-Step Three Dimensional Phase Unwrapping Approach

So far, the phase unwrapping problem has been seen as a stepwise problem, solving first the temporal and afterwards the spatial phase unwrapping. Therefore, the three dimensional problem is recast into two smaller dimensional problems. A two-step solution is never optimal in contrast to a global one-step solution (Imperatore et al., 2015). So the goal of this work is to develop a three dimensional phase unwrapping approach that solves both the temporal and the spatial phase unwrapping in one single step. Furthermore, the approach should be easy to integrate into the SBAS workflow. The following considerations refer again to a multitemporal D-InSAR stack with a set $\mathcal{M}'$ of m' SAR images at times $t_1, t_2, \dots, t_{m'}$ resulting in a set $\mathcal{N}'$ of n' D-InSAR images according to the SBAS method which define a set $\mathcal{R}'$ of r' triangles in the temporal/ perpendicular baseline plane. For evaluation, the same set $\mathcal{M}$ of m stable pixels is used in each interferogram. On its basis a Delaunay triangulation is generated in the azimuth/ range plane with a set $\mathcal{N}$ of n gradients and a set $\mathcal{R}$ of r triangles.

When the one-step three dimensional approach is developed, it becomes apparent that the previously identified alternative approaches have not only led to an improvement of the two-step EMCF approach, but that these ideas of improvement are now essential for this global approach. Temporal and spatial phase unwrapping are no longer performed sequentially, so the results of the temporal LP cannot be used to estimate the motion model parameters and to calculate weights for the spatial phase unwrapping. Once the problem has been defined and further refined, it is applied in a closed loop simulation scenario and later on real data. The aspects of the developed one-step three dimensional approach have already been published in Esch et al. (2020).

7.1 Problem Formulation

Costantini et al. (2012) have defined the phase unwrapping in general as the integration of finite multitemporal differences. As mentioned in Chapter 5, the observation itself is a so called double difference in time and space resulting in the functional model

$$\phi_{x_l}^{t_\beta} - \phi_{x_l}^{t_\alpha} - (\phi_{x_k}^{t_\beta} - \phi_{x_k}^{t_\alpha}) - 2\pi k_{\Delta x_{kl}}^{\Delta t_{\alpha\beta}} = \psi_{\Delta x_{kl}}^{\Delta t_{\alpha\beta}} \tag{7.1}$$

for one phase gradient $\psi_{\Delta x_{kl}}^{\Delta t_{\alpha\beta}}$ between two pixels x_k and x_l computed from two SAR images at times t_α and t_β. Inserting relationship (4.1) for each pixel at each time and considering that the wrapped phase gradient $\psi_{\Delta x_{kl}}^{\Delta t_{\alpha\beta}}$ is already a wrapped value in a range from $-\pi$ to π, this results in the functional model

$$k_{x_l}^{t_\beta} - k_{x_l}^{t_\alpha} - k_{x_k}^{t_\beta} + k_{x_k}^{t_\alpha} - k_{\Delta x_{kl}}^{\Delta t_{\alpha\beta}} = -\lfloor \frac{\psi_{x_l}^{t_\beta} - \psi_{x_l}^{t_\alpha} - \psi_{x_k}^{t_\beta} + \psi_{x_k}^{t_\alpha}}{2\pi} \rceil . \tag{7.2}$$

So the observations are the wrapped phases at each single SAR images and at each pixel. The phase unwrapping step follows after several filtering steps, such as multilooking, which are applied individually to each interferogram. As mentioned in Chapter 5, it holds that

$$\langle \psi_{x_l}^{t_\beta} - \psi_{x_l}^{t_\alpha} - \psi_{x_k}^{t_\beta} + \psi_{x_k}^{t_\alpha} \rangle_{-\pi,\pi} \neq \psi_{\Delta x_{kl}}^{\Delta t_{\alpha\beta}} . \tag{7.3}$$

Therefore, the phase values per SAR image and per pixel are included as observations and not the measured wrapped phase gradients. Since the phase unwrapping is applied to the multilooked images, this approach is difficult to integrate into the SBAS workflow.

The idea now is to define a one-step three dimensional phase unwrapping approach on the basis of the interferometric, multilooked and multitemporally filtered phase gradients which can easily be integrated into the already existing SBAS workflow as implemented in the RSG software. Therefore, the two steps, temporal and spatial phase unwrapping, are combined in a single step. However, before the phase unwrapping step is done, it is necessary to estimate a motion model to make the phase unwrapping step easier (Pepe and Lanari, 2006). Thus, the phase unwrapping refers to the modified observations $\boldsymbol{\chi}_{\boldsymbol{\Delta x}}^{\boldsymbol{\Delta t}}$ collected to one vector, whereby all observations of one spatial phase gradient in time follow one after the other resulting in

$$\boldsymbol{\chi}_{\boldsymbol{\Delta x}}^{\boldsymbol{\Delta t}} = \begin{bmatrix} \chi_{\Delta x_{kl}}^{\Delta t_{\alpha\beta}} & \chi_{\Delta x_{kl}}^{\Delta t_{\beta\gamma}} & \chi_{\Delta x_{kl}}^{\Delta t_{\gamma\alpha}} & \dots & \chi_{\Delta x_{lm}}^{\Delta t_{\alpha\beta}} & \chi_{\Delta x_{lm}}^{\Delta t_{\beta\gamma}} & \chi_{\Delta x_{lm}}^{\Delta t_{\gamma\alpha}} & \dots \end{bmatrix}^T . \tag{7.4}$$

So, the one-step three dimensional phase unwrapping approach can be defined as

$$\boxed{\begin{aligned} &\text{Objective function:} \quad C_{3\mathrm{D}}(\boldsymbol{x}) = \underbrace{\begin{bmatrix} \boldsymbol{p}_{\boldsymbol{\Delta x}}^{\boldsymbol{\Delta t}\,T} & \boldsymbol{p}_{\boldsymbol{\Delta x}}^{\boldsymbol{\Delta t}\,T} \end{bmatrix}}_{\boldsymbol{c}_{3\mathrm{D}}^T} \underbrace{\begin{bmatrix} \boldsymbol{k}_{\boldsymbol{\Delta x}}^{\boldsymbol{\Delta t},+} \\ \boldsymbol{k}_{\boldsymbol{\Delta x}}^{\boldsymbol{\Delta t},-} \end{bmatrix}}_{\boldsymbol{x}} \dots \min \\ &\text{Constraint:} \quad \begin{bmatrix} \boldsymbol{B}_{3\mathrm{D}}^T & -\boldsymbol{B}_{3\mathrm{D}}^T \end{bmatrix} \underbrace{\begin{bmatrix} \boldsymbol{k}_{\boldsymbol{\Delta x}}^{\boldsymbol{\Delta t},+} \\ \boldsymbol{k}_{\boldsymbol{\Delta x}}^{\boldsymbol{\Delta t},-} \end{bmatrix}}_{\boldsymbol{x}} = \underbrace{-\left\lfloor \frac{\boldsymbol{B}_{3\mathrm{D}}^T \boldsymbol{\chi}_{\boldsymbol{\Delta x}}^{\boldsymbol{\Delta t}}}{2\pi} \right\rceil}_{\boldsymbol{b}_{3\mathrm{D}}} \\ &\text{Variable:} \quad \boldsymbol{x} \in \mathbb{Z}_{\geq 0} \end{aligned}} \tag{7.5}$$

with one single but high dimensional constraint matrix $\boldsymbol{B}_{3\mathrm{D}}^T \in \mathbb{Z}^{r'\cdot n + r \cdot n' \times n' \cdot n}$ which contains both, the temporal and the spatial constraints for all modified observations $\boldsymbol{\chi}_{\boldsymbol{\Delta x}}^{\boldsymbol{\Delta t}}$. Figure 7.1 shows an example of the structure of the global constraint matrix for a small sample stack consisting of $n' = 6$ interferograms between which a total of $r' = 3$ temporal constraints can be generated and $n = 5$ spatial phase gradients between which $r = 2$ spatial constraints must be fulfilled. The dimension of the constraint matrix $\boldsymbol{B}_{3\mathrm{D}}^T$ is therefore $3 \cdot 5 + 2 \cdot 6 \times 5 \cdot 6 = 27 \times 30$.

For an entire D-InSAR stack, the constraint matrix is thus very quickly expanded to a high dimension in the order of $\boldsymbol{B}_{3\mathrm{D}}^T \in \mathbb{Z}^{10^6 \times 10^6}$. But as seen in the example it is sparse with three entries for each row. The disadvantage of this global three dimensional approach is that the structure no longer corresponds to a three dimensional network, since the observations represent double differences in time and space. The already mentioned two independent networks in the azimuth/ range and temporal/ perpendicular baseline plane provide the data basis. Thus, the above described LP can no longer be solved as a network flow problem. Due to special properties: totally unimodular constraint matrix $\boldsymbol{B}_{3\mathrm{D}}^T$, integer weights $\boldsymbol{c}_{3\mathrm{D}}^T$ and an integer right-hand side vector $\boldsymbol{b}_{3\mathrm{D}}$, the problem can be solved using a standard LP solver, ideally accounting for the sparsity.

As the conditions refer to the modified observations $\boldsymbol{\chi}_{\boldsymbol{\Delta x}}^{\boldsymbol{\Delta t}}$, the motion model parameters have to be estimated before the phase unwrapping step. It is of particular importance at this point that an alternative approach has been examined in Section 6.1. This approach is independent of the solution of the temporal LP. The motion model parameters are estimated by maximizing the EPC function using Algorithm 4 which combines simulated annealing and the Nelder-Mead method.

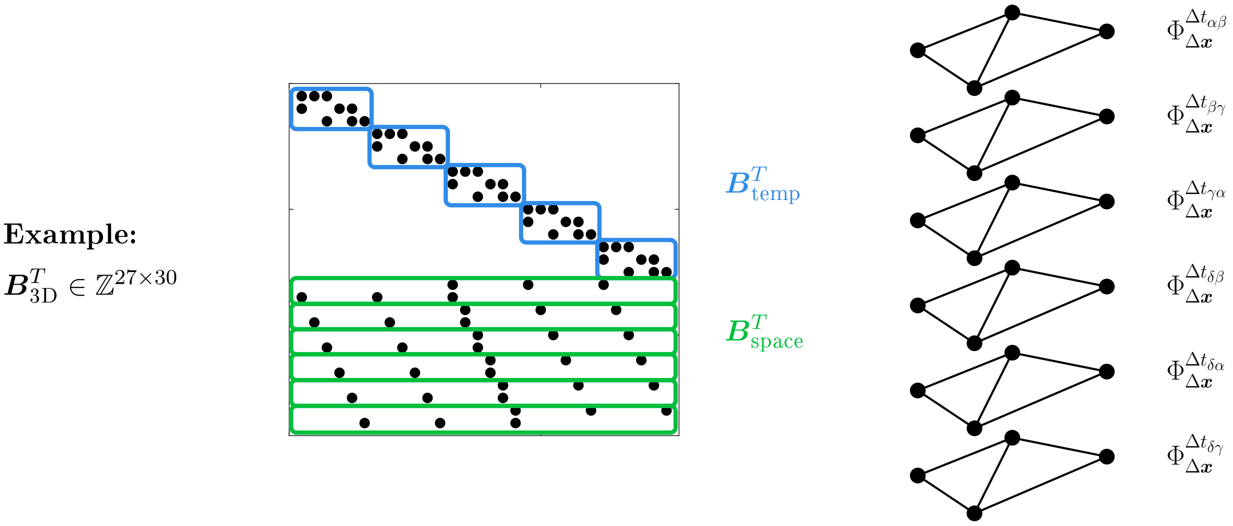

Figure 7.1: Exemplary structure of global constraint matrix for a small D-InSAR stack consisting of 6 interferograms between which a total of 3 temporal constraints can be generated and 5 spatial gradients between which 2 spatial constraints must be fulfilled.

Another topic is the choice of the weights. Here, again, it is of particular importance that weights that are independent of the solution of the temporal LP were examined previously in Section 6.2. It has been demonstrated that *Weights 2*. cf. (6.17), and *Weights 3*, cf. (6.18), are suitable to use as spatial weights. In time, *Weights 2* are also useful, but when applied to the real data, it has been shown that they have a minor influence. Sometimes smoother results can be achieved, but sometimes also less smooth results. Thus, constant temporal weights will be assumed here as it is also the standard case. With the one-step three dimensional approach, one weight $p^{\Delta t_{\alpha\beta}}_{\Delta x_{kl}}$ is needed for one interferometric phase gradient or, to be more correct, for one modified interferometric phase gradient $\chi^{\Delta t_{\alpha\beta}}_{\Delta x_{kl}}$. Thus, it is no longer possible to distinguish between temporal and spatial weights. The use of *Weights 2* in space and constant temporal weights is consequently not possible. *Weights 3*, however, which are based on the EPC values, are constant for one phase gradient in time. Therefore, *Weights 3* are used as weighting function for the one-step three dimensional phase unwrapping approach.

Theoretically, the approach is now completely defined. However, the problem of temporal inconsistency and the associated rounding problem occurred during the application, so that the problem must be further refined.

7.2 Temporal Inconsistency

A posteriori filtering steps which are done for each interferogram separately, like the multilooking, lead to temporally inconsistent interferograms. Thus, the temporal constraints for one phase gradient $\boldsymbol{\phi}^{\Delta \boldsymbol{t}}_{\Delta x_{kl}}$ are not necessarily fulfilled, so that

$$\boldsymbol{B}^T_{\mathrm{temp}} \boldsymbol{\phi}^{\Delta \boldsymbol{t}}_{\Delta x_{kl}} \neq \boldsymbol{0} \tag{7.6}$$

holds. This problem is already addressed in Imperatore et al. (2015). The temporal inconsistency is compensated by an additional term $\boldsymbol{D}^{\Delta \boldsymbol{t}}_{x_j}$, so that the temporal constraint becomes

$$\boldsymbol{B}^T_{\mathrm{temp}} \boldsymbol{k}^{\Delta \boldsymbol{t}}_{\Delta x_{kl}} = -\frac{\boldsymbol{B}^T_{\mathrm{temp}}(\boldsymbol{\chi}^{\Delta \boldsymbol{t}}_{\Delta x_{kl}} + \boldsymbol{A}_{\mathrm{primal,space}} \boldsymbol{D}^{\Delta \boldsymbol{t}}_{x_j})}{2\pi} \tag{7.7}$$

with the modified observations $\boldsymbol{\chi}_{\Delta x_{kl}}^{\Delta \boldsymbol{t}}$ which include the motion model parameters and the arc-to-node incidence matrix $\boldsymbol{A}_{\text{primal,space}}$ of the primal graph in the spatial plane. For the case $\boldsymbol{D}_{x_j}^{\Delta \boldsymbol{t}}$ unequal to zero it is difficult to find a solution (Imperatore et al., 2015). A rounding operator is therefore introduced, as with the EMCF algorithm, so that the temporal constraint results in

$$\boldsymbol{B}_{\text{temp}}^T \boldsymbol{k}_{\Delta x_{kl}}^{\Delta \boldsymbol{t}} = \underbrace{-\lfloor \frac{\boldsymbol{B}_{\text{temp}}^T \boldsymbol{\chi}_{\Delta x_{kl}}^{\Delta \boldsymbol{t}}}{2\pi} \rceil}_{\boldsymbol{b}_{\text{temp}}} . \tag{7.8}$$

A rounding operation always includes errors. It is not clear if rounding down or up represents the truth. Therefore, the rounding can lead to conflicts in the constraints, if the problem is defined in a one-step three dimensional approach as desired in this work.

When formulating the problem in a one-step three dimensional approach, it must therefore be taken into account that these contradictions are compensated by so called slack variables. The temporal constraints for the phase gradient between the pixels x_k and x_l are thus extended to

$$\boldsymbol{B}_{\text{temp}}^T \boldsymbol{k}_{\Delta x_{kl}}^{\Delta \boldsymbol{t}} + \boldsymbol{1}_{[r'\cdot n + r \cdot n' \times r' \cdot n]} \boldsymbol{y} = \underbrace{-\lfloor \frac{\boldsymbol{B}_{\text{temp}}^T \boldsymbol{\chi}_{\Delta x_{kl}}^{\Delta \boldsymbol{t}}}{2\pi} \rceil}_{\boldsymbol{b}_{\text{temp}}} . \tag{7.9}$$

There is one slack variable y for each temporal constraint. With the help of these slack variables the temporal inconsistency of the data is compensated. However, the inclusion of the slack variables is not intended to replace the estimation of a phase ambiguity factor. It must be expensive to insert such slack variables. Therefore, the objective function must also be adapted accordingly. Overall, the one-step three dimensional LP can be defined as

ONE-STEP THREE DIMENSIONAL APPROACH:

$$\text{Objective function:}\quad C_{3\text{D}}(\boldsymbol{x}) = \underbrace{\begin{bmatrix} \boldsymbol{p}_{\boldsymbol{\Delta x}}^{\boldsymbol{\Delta t}\,T} & \boldsymbol{p}_{\boldsymbol{y}}^T & \boldsymbol{p}_{\boldsymbol{\Delta x}}^{\boldsymbol{\Delta t}\,T} & \boldsymbol{p}_{\boldsymbol{y}}^T \end{bmatrix}}_{\boldsymbol{c}_{3\text{D}}^T} \underbrace{\begin{bmatrix} \boldsymbol{k}_{\boldsymbol{\Delta x}}^{\boldsymbol{\Delta t},+} \\ \boldsymbol{y}^+ \\ \boldsymbol{k}_{\boldsymbol{\Delta x}}^{\boldsymbol{\Delta t},-} \\ \boldsymbol{y}^- \end{bmatrix}}_{\boldsymbol{x}} \ldots \min$$

$$\text{Constraint:}\quad [\underbrace{\boldsymbol{B}_{3\text{D}}^T \quad \boldsymbol{B}_{\boldsymbol{y}}^T}_{\boldsymbol{B}_{3\text{D},\boldsymbol{y}}^T} \quad \underbrace{-\boldsymbol{B}_{3\text{D}}^T \quad -\boldsymbol{B}_{\boldsymbol{y}}^T}_{-\boldsymbol{B}_{3\text{D},\boldsymbol{y}}^T}] \underbrace{\begin{bmatrix} \boldsymbol{k}_{\boldsymbol{\Delta x}}^{\boldsymbol{\Delta t},+} \\ \boldsymbol{y}^+ \\ \boldsymbol{k}_{\boldsymbol{\Delta x}}^{\boldsymbol{\Delta t},-} \\ \boldsymbol{y}^- \end{bmatrix}}_{\boldsymbol{x}} = \underbrace{-\lfloor \frac{\boldsymbol{B}_{3\text{D}}^T \boldsymbol{\chi}_{\boldsymbol{\Delta x}}^{\boldsymbol{\Delta t}}}{2\pi} \rceil}_{\boldsymbol{b}_{3\text{D}}} \tag{7.10}$$

$$\text{Variable:}\quad \boldsymbol{x} \in \mathbb{Z}_{\geq 0}$$

with the constraint matrix $\boldsymbol{B}_{\boldsymbol{y}}^T \in \mathbb{Z}^{r'\cdot n + r\cdot n' \times r' \cdot n}$ which consists of an identity matrix for the temporal constraints and has only zero columns for the spatial constraints. Thus, the whole constraint matrix $\boldsymbol{B}_{3\text{D},\boldsymbol{y}}^T$ expands to a dimension of $r'\cdot n + r \cdot n' \times n' \cdot n + r' \cdot n$. For the above example the whole constraint matrix $\boldsymbol{B}_{3\text{D},\boldsymbol{y}}^T$ gets a size of $27 \times 30 + 3 \cdot 5 = 45$, see Fig. 7.2. However, the matrix is very sparse again, so that there are a maximum number of four non-zero entries per row. The weights of the slack variables $\boldsymbol{p}_{\boldsymbol{y}}^T$ must be chosen very high, so that it is more expensive to insert a slack variable than to estimate a phase ambiguity factor. The constraint matrix remains totally unimodular, so that the LP can still be solved with standard LP solvers resulting in integer parameters.

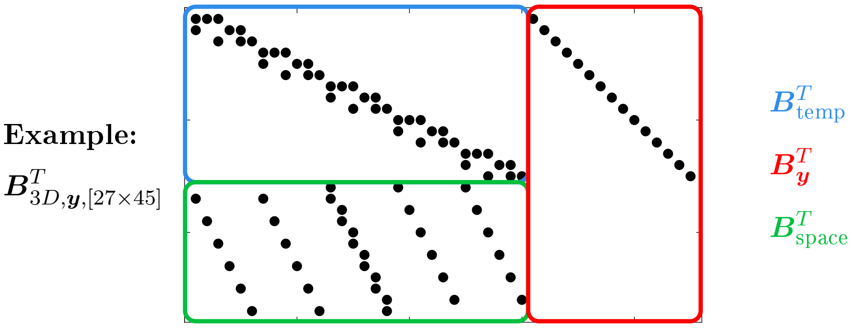

Figure 7.2: Exemplary structure of global constraint matrix with slack variables for a small D-InSAR stack consisting of 6 interferograms between which a total of 3 temporal conditions can be generated and 5 spatial gradients between which 2 spatial conditions must be fulfilled.

7.3 Application to Simulated Data

The new one-step three dimensional approach described in (7.10) will now be applied to the simulated D-InSAR stack. In advance, the motion model parameters are estimated by maximizing the EPC function using Algorithm 4. *Weights 3* are used for the phase ambiguity factors $\boldsymbol{p}^{\boldsymbol{\Delta t}}_{\boldsymbol{\Delta x}}$ and the weights of the slack variables $\boldsymbol{p}_{\boldsymbol{y}}$ are set to a very high value that is greater than the maximum of *Weights 3*, i.e. higher than 2^{10}. This ensures that it is always more expensive to insert a slack variable than a phase ambiguity factor. The results of the one-step three dimensional approach are compared with the results of the conventional two-step EMCF algorithm and with the results of the alternative two-step EMCF algorithm using Algorithm 4 and *Weights 3*.

Figure 7.3 shows the percentage of correctly unwrapped phase gradients depending on the noise level added per SAR image. The green bars correspond to the results of the conventional EMCF algorithm, the dark blue are the results using the alternative EMCF approach and finally, the results of the new one-step three dimensional approach are shown as orange bars. Up to a noise level of 0.6 rad there are no significant differences. Almost 100 % of the phase gradients are unwrapped correctly. From a noise level above 0.6 rad, however, it is clear that the one-step three dimensional approach leads to a further improvement compared to the alternative EMCF approach. The number of correctly unwrapped phase gradients can be increased from 98.5 % to 99.2 % with a noise level of 0.8 rad and from 97.1 % to 98.3 % with a noise level of 0.9 rad. For the EMCF algorithm with conventional methods, the proportion of correctly unwrapped phase gradients is 96.0 % (noise level 0.8 rad) and 88.1 % (noise level 0.9 rad), which is therefore the least.

The temporal consistency is checked for further investigation. Due to the slack variables, the results of the one-step three dimensional approach will not be completely consistent in time. As explained, this is not possible due to the preprocessing steps. However, it can be assumed that they are more consistent than with the two-step EMCF approach since the spatial phase unwrapping partially destroys the temporal consistency previously established in the temporal phase unwrapping. To check the temporal consistency, the total number of temporal inconsistencies for each unwrapped phase gradient is calculated

$$TINC_{\Delta x_{kl}} = \sum |\lfloor \frac{\boldsymbol{B}^T_{\text{time}} \tilde{\boldsymbol{\phi}}^{\boldsymbol{\Delta t}}_{\Delta x_{kl}}}{2\pi} \rceil| \quad \forall \Delta x_{kl} \in \mathcal{N} \tag{7.11}$$

and again summarized for all phase gradients resulting in

$$TINC = \sum_{\forall \Delta x_{kl} \in \mathcal{N}} TINC_{\Delta x_{kl}}. \tag{7.12}$$

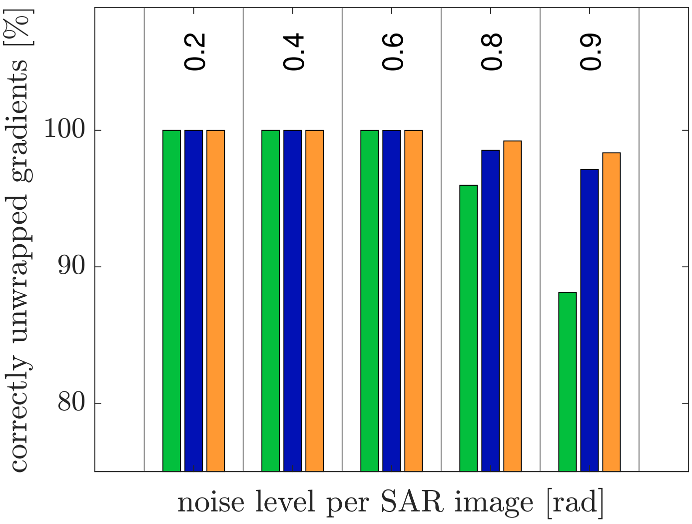

Figure 7.3: Percentage of correctly unwrapped phase gradients depending on the noise level added per SAR image. The green bars show the result of the conventional EMCF approach, the dark blue bars are the results using the alternative EMCF algorithm and the orange bars are the results using the one-step three dimensional approach.

The total sum of temporal inconsistencies is listed for the different noise levels and different phase unwrapping methods in Table 7.1. For comparison purposes, the temporal inconsistency of the reference data is given. The noise refers to the noise that is added to each SAR image. Consequently, the absolute total sum of temporal inconsistencies should remain the same regardless of the noise level. The table shows that this is the case with the one-step three dimensional approach. Independent of the noise level, the number is 127. With the alternative EMCF approach, temporal inconsistency can also be decreased compared to the conventional EMCF approach, but the one-step three dimensional approach clearly shows the most consistent results. Especially with the higher noise levels, it is noticeable that in the two-step approach the spatial phase unwrapping destroys the temporal consistency that was established in the previous temporal phase unwrapping to a large extent. Compared to the reference data, up to a noise level of 0.6 rad all phase unwrapping methods lead to temporally more consistent results. As a result, not all phase gradients are unwrapped correctly, only nearly 100 %. To solve the phase ambiguities, however, an additional assumption must be made. In this case the phase unwrapping problem is defined in such a way that the absolute number of inserted phase jumps should be minimal and according to the definition of the one-step three dimensional procedure the results should be temporally as consistent as possible. According to this definition, optimal results have been achieved in all cases. However, especially from a noise level above 0.6 rad it becomes apparent that the additional assumption of temporal consistency which is included in the one-step three dimensional approach leads to better results and is therefore valid.

Table 7.1: Number of total temporal inconsistencies for different noise levels. In addition to the reference, the number is listed for different phase unwrapping methods.

method	total number of temporal inconsistencies for different noise levels [rad]				
	0.2	0.4	0.6	0.8	0.9
reference	352	352	352	352	352
conventional EMCF approach	159	155	213	56110	259265
alternative EMCF approach	148	143	289	47714	107168
one-step three dimensional approach	127	127	127	127	127

7.4 Case Study 2: ERS-1/-2 D-InSAR Stack of the Lower-Rhine-Embayment

In the following, it will be tested if the additional assumption that the results should be temporally as consistent as possible leads to better results when applied to ERS-1/-2 real data. The test region is again the Lower-Rhine-Embayment with the deformation areas due to the still active open-cast mines and the already closed coal mines. The wrapped, multilooked and multitemporally filtered differential interferograms taken from RSG are again unwrapped twice using the one-step three dimensional approach and inserted into RSG again for the final SBAS analysis. The results are compared with the results from the EMCF algorithm, once using the conventional and once using the alternative approach with Algorithm 4 and *Weights 3*.

7.4.1 Data Basis

As before, the data consist of $m' = 64$ SAR images collected from May 1992 to December 2000 by ERS-1/-2. The temporal triangulation remains the same as in the study carried out previously in Section 6.3. A total of $n' = 161$ D-InSAR images are generated according to the SBAS method resulting in $r' = 98$ temporal constraints. Since the dimension of the whole condition matrix $\boldsymbol{B}^T_{3\mathrm{D},\boldsymbol{y}}$ in the one-step three dimensional approach grows to $r' \cdot n + r \cdot n' \times n' \cdot n + r' \cdot n$, a somewhat smaller spatial triangulation is built up due to a lack of computing capacity in the current test system. Therefore, the threshold for the definition of a coherent pixel is slightly increased. Instead of the 80 %, the pixels in 95 % of the interferograms must have a coherence value greater than 0.7. For the whole ERS-1/-2 scene this is the case for $m = 96\,531$ pixels defining $n = 289\,489$ arcs and $r = 192\,959$ triangles. Increasing the threshold to select the stable pixels reduces the noise level of the data accordingly. But as the simulated data has shown, the approach also works with higher noise, so the thresholds for selecting the pixels can be lowered again without any problems as long as the system has the computing capacity to solve the problem.

Figure 7.4 shows the mean deformation velocity map of the n stable pixels using the conventional EMCF approach. Analogous to the Case Study 1 in Section 6.3, it is clearly visible that the Earth's surface decreases from -6 to -8 cm/yr around the still active open-cast mines Garzweiler and Hambach. In contrast, the closing of the coal mines Sophie-Jacoba in the mining region Erkelenz and Emil Mayrisch in the mining region Aachen leads to an elevation of the Earth's surface of several cm/yr. The same can be seen when using the alternative EMCF approach. The average difference when comparing with Fig. 7.4 is 0.004 cm/yr. For only 0.5 % of the pixels a difference of more than 0.1 cm/yr occurs. Therefore, as in the first case study, other criteria have to be found to compare the results.

7.4.2 EMCF vs. One-Step Three Dimensional Approach

The phase unwrapping is now carried out twice again using the new one-step three dimensional approach. Compared with the alternative EMCF approach, the same motion model parameters and weights are used. The two results differ only in the fact that the alternative EMCF approach is performed in two steps and the new approach in a single step under the assumption that the results should be as consistent as possible in time, meaning that the temporal constraints should be fulfilled for the most part. The resulting mean deformation velocity map also looks very similar to the one shown in Fig. 7.4. As in the study in Section 6.3, it is difficult to verify the correctness of the results, as the real movement behavior is unknown. In the following, criteria such as temporal consistency

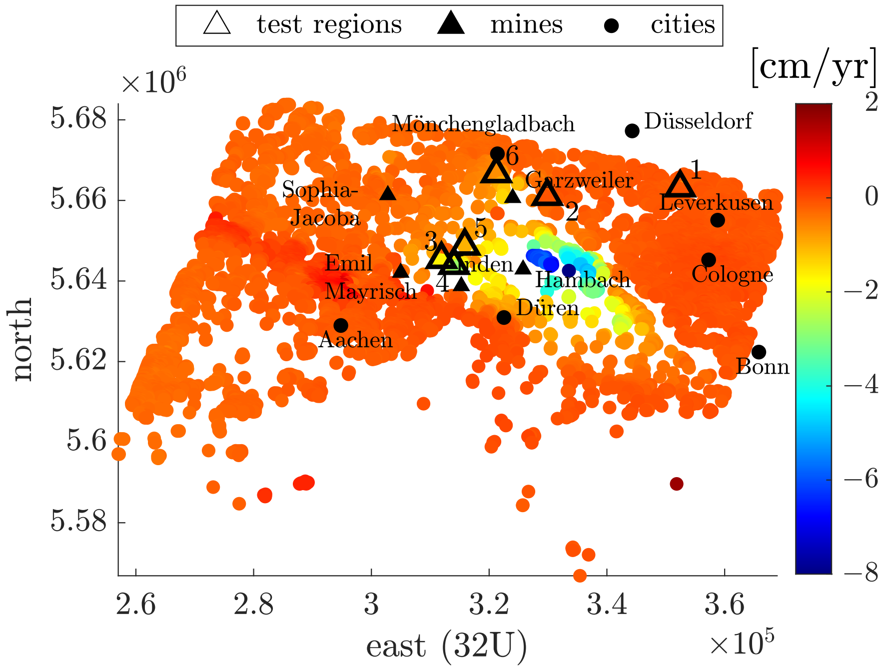

Figure 7.4: Mean deformation velocity map of the Lower-Rhine-Embayment based on ERS-1/-2 data from May 1992 to December 2000 for pixels with a coherence value greater than 0.7 in at least 95 % of interferograms and estimated using the conventional EMCF approach. The highlighted test regions 1 to 6 are examined in more detail as time series in Figs. 7.6 and 7.7.

and smoothness in space are examined and a comparison with the leveling data already used in Section 6.3 is made.

7.4.2.1 Temporal Consistency

As first criterion, the temporal consistency of the phase gradients is investigated. As reminder, the phase unwrapping is based on multitemporally filtered data (Pepe et al., 2015). These interferograms show increased coherence values compared to the original interferograms and they are more consistent in time. Thus, the phase unwrapping result should be as consistent as possible. The total sum of the temporal inconsistency is calculated according to (7.12) both after the first and after the second phase unwrapping step. After the second phase unwrapping, the unwrapped phase gradients are the observations previously excluded from the motion model, see Fig. 2.9. The values of the total sum of temporal inconsistencies are listed in Table 7.2 for the results using the conventional and the alternative EMCF approach and for the results using the one-step three dimensional approach. The values clearly show that the one-step three dimensional approach leads to much smaller temporal inconsistencies. The results are therefore more consistent in time. As with the simulated data, the alternative EMCF approach leads to lower temporal inconsistencies

Table 7.2: Number of total temporal inconsistencies for ERS-1/-2 data. The number is listed for different phase unwrapping methods after the first and the second phase unwrapping step in the SBAS workflow.

method	total number of temporal inconsistencies after	
	1st phase unwrapping	2nd phase unwrapping
conventional EMCF approach	16309	2947
alternative EMCF approach	15711	2810
one-step three dimensional approach	10491	938

compared to the conventional method. However, the two-step EMCF algorithm delivers clearly temporally more inconsistent results in contrast to the one-step three dimensional algorithm, since the spatial phase unwrapping, which is carried out after the temporal phase unwrapping independently for each individual interferogram, destroys the temporal consistency produced before.

7.4.2.2 Smoothness in Space

As in the study in Section 6.3, the smoothness in space is analyzed to verify the accuracy of the results. Therefore, the RMS of the deformation time series $h_{x_j}^{t_\alpha} \ \forall t_\alpha \in \mathcal{M}'$ is calculated for each pixel $x_j \in \mathcal{M}$ in space according to (6.20). All pixels in a radius of 300 m are again considered and the RMS is calculated if at least five pixels are within this radius. In this way, the RMS is calculated for 89.4 % of pixels for the results of the conventional and the alternative EMCF approach and for the results of the one-step three dimensional approach. Figure 7.5a shows the comparison between the conventional method and the one-step approach, where the difference is formed in such a way that positive differences indicate that the RMS value is lower when the one-step approach is used and the results are therefore smoother in space. The differences are mostly all close to zero. The histogram shows the relative frequencies, which in sum results in one. The bar around zero thus goes almost to one. However, it is exactly the range of interest, where the differences are not equal to zero. In order to make anything visible in this range, the histogram has been cut off. The RMS values differ also a few centimeters, for example 2.8 cm, which corresponds to half a wavelength and thus indicates phase unwrapping errors. It can be seen that the larger differences are in the positive range, so that the one-step three dimensional approach leads to a reduction of the RMS value. Figure 7.5b shows analogously the histogram of the differences between the alternative EMCF and the one-step three dimensional approach. Here again, the histogram is truncated at the top because the differences are mostly zero. Positive differences also mean that the one-step approach leads to lower RMS values than the alternative EMCF approach. However, it can be seen that the differences are very small and less than 1 cm. Consequently, by just comparing the RMS values, it is not possible to say which approach delivers better and which worse results.

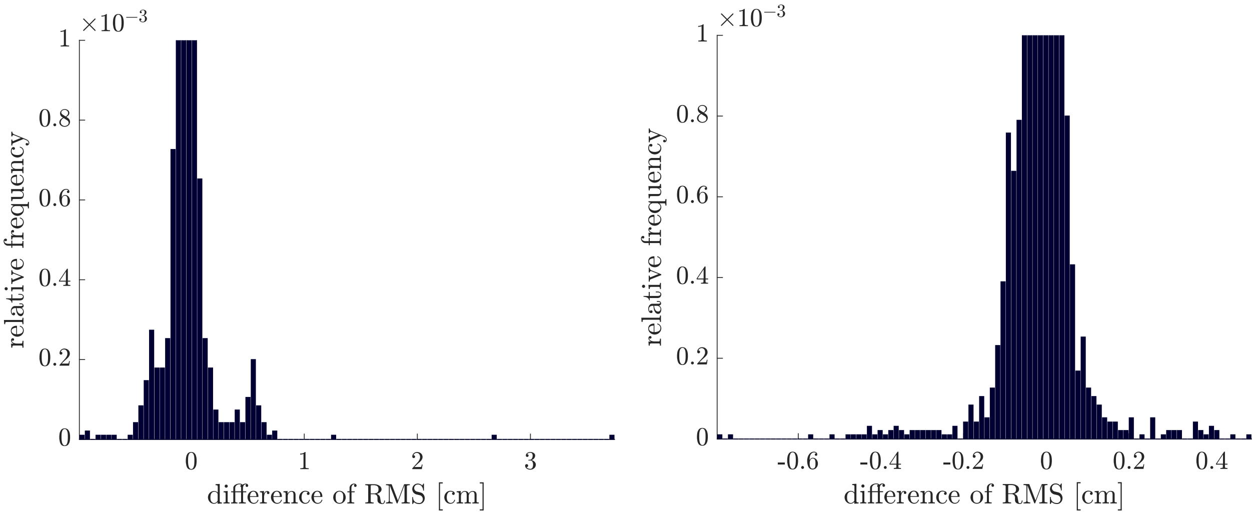

(a) RMS of conventional EMCF approach minus RMS of one-step three dimensional approach

(b) RMS of alternative EMCF approach minus RMS of one-step three dimensional approach

Figure 7.5: Difference of RMS values of the deformation time series estimated with the conventional and the alternative EMCF approach and with the one-step three dimensional approach.

7.4.2.3 Single Pixel Evaluations

For further validation, the time series of individual pixels are analyzed and compared with the closest leveling point. It is preferred to take a closer look at test regions in which a significant movement takes place and in which differences between the individual methods arise. A total of six test regions are analyzed, which are highlighted in Fig. 7.4. The deformation time series of five pixels located in this test regions are shown in Figs. 7.6 and 7.7 from May 1992 to December 2000. The green triangles are the results using the conventional EMCF methods, the dark blue points are the results using the alternative EMCF approach and the results of the one-step three dimensional approach are shown as orange points. To evaluate the results, the closest leveling point, shown as black squares, is added. In order to indicate the trend of the deformation time series, data from 2006 are represented in addition to the level data from 1993, 1997 and 2001. As in the study in Section 6.3, the nearest leveling point is at most 300 m away from the interferometric data so that it can be assumed that all examined data show similar behaviors. The different occurring temporal reference points are compensated by transferring the interferometric data to the leveling data with help of a local offset, calculated according to Esch et al. (2019b).

Test region 1 examines pixels in Mohnheim at the Rhine. It is a region where movement is almost non-existent, see Fig. 7.6a. Based on the leveling data, a slight elevation of the Earth's surface in the range of one centimeter can be observed after 2001. Within this test region, however, there is a pixel at which the RMS value using the conventional EMCF method is 3.84 cm, so greater than half the wavelength, see Fig. 7.5a. For comparison with the other two methods the RMS value of this pixel is 0.10 cm in both cases. The reason is that the motion model parameters of the corresponding phase gradients are estimated too highly when using the conventional method. With this method the pixel seems to experience a strong subsidence of the Earth's surface. Using Algorithm 4 more realistic motion model parameters are obtained that match the neighboring pixels and the leveling data better. There are no differences between the alternative EMCF and the one-step three dimensional approach. Table 7.3a once again examines the temporal inconsistencies. The total number of temporal inconsistencies is calculated for the phase gradients which include the conspicuous pixel where the conventional method estimates too much motion. The number is listed in the table after both the first and the second phase unwrapping step. After the first phase unwrapping, it becomes clear that the results of the conventional EMCF algorithm are not temporally consistent. The total number of temporal inconsistencies is 56. If the alternative EMCF algorithm or the one-step approach is used, the number can be reduced to 26 or 24. After the second phase unwrapping, the data is consistent in all cases. However, these are the phase gradients already reduced by the motion model. The possibly erroneous motion model is then added again after the phase unwrapping, see Fig. 2.9.

A similar example is shown in test region 2, see Fig. 7.6b, where pixels are shown in Gustorf, Grevenbroich. Here, again, there is almost no movement. Only on the basis of the leveling data from 2001 an elevation of the Earth's surface by about one centimeter can be observed. However, again one pixel shows a strong decrease when using the conventional method, which does not fit to the surrounding pixels and the leveling data. The RMS value of this pixel is 2.77 cm. Using the alternative EMCF approach, the RMS can be reduced to 0.34 cm and using the one-step three dimensional approach even further to 0.11 cm. Looking at the temporal inconsistencies in Table 7.3b, it can be seen once again that due to the incorrect motion model, the temporal inconsistencies are actually high with a value of 15 using the conventional EMCF approach. When using the other two methods, which are based on Algorithm 4 and *Weights 3*, a temporal inconsistency occurs only at one phase gradient. After the second phase unwrapping, all phase gradients are again temporally consistent.

So far, the observable differences between the methods are based on different motion model parameters. This demonstrates once again that Algorithm 4 leads to improved results when compared to the conventional method. However, it is of interest to see how the one-step three dimensional phase unwrapping differs from the alternative EMCF algorithm to validate the performance of the one-step approach. For this purpose, the following four test regions are considered.

Test region 3 shows pixels in Koslar, Jülich near the still active open-cast mine Inden. The resulting subsidence of the Earth's surface is visible both in the interferometric and in the leveling data, see Fig. 7.6c. Especially at the beginning of the D-InSAR time series it becomes apparent that the results based on the alternative EMCF algorithm, represented as dark blue points, show a significant difference of about 2 cm in contrast to the other two methods. This jump is more of an unnatural behavior and indicates a phase unwrapping error. This does not occur in the corresponding RMS values, since all pixels show this behavior and the pixels fit together. However, if one looks at the temporal inconsistencies of the associated phase gradients in Table 7.3c, it becomes apparent again that the one-step three dimensional approach provides the most consistent results in time. The temporal inconsistencies are conspicuously high after the second phase unwrapping step when using the alternative EMCF approach. The spatial phase unwrapping carried out in the second step caused these temporal inconsistencies resulting in the unnatural behavior at the beginning of the deformation time series.

The next test region 4 is in Jülich itself. The open-cast mine Inden, which is still active, causes a subsidence of the Earth's surface there as well. D-InSAR data and leveling data fit together well again, see Fig. 7.7a. This time the results of the alternative EMCF algorithm show a jump of about 2 cm at the end of the time series compared to the other two methods. This is also not visible in the RMS values, since all surrounding points show this jump. The conventional EMCF and the one-step approach show nearly the same results, in both cases temporaly consistent in contrast to the alternative EMCF approach, see Table 7.3d.

Test region 5 shows pixels in Mersch, Jülich, also near the open-cast mine Inden. Both the interferometric and the leveling data show a subsidence of the Earth's surface, see Fig. 7.7a. As already shown several times, the results of the one-step three dimensional approach are more consistent in time. This is also the case in this example, see Table 7.3e. This example is intended to show that this temporal consistency can also lead to more noisy results. The figure shows that the deformation time series of the one-step three dimensional approach initially deviate slightly from the original movement pattern. This also leads to a slightly higher RMS value, which is 0.68 cm for this pixel and 0.46 m for the other two methods. However, the differences are in the millimeter range and the actual motion pattern can also be reproduced with the one-step three dimensional approach.

The last test region is in Odenkirchen, Mönchengladbach. This region also shows a slight subsidence of the Earth's surface, see Fig. 7.7c. In this example all problems discussed before occur. Starting with the conventional EMCF algorithm, it becomes apparent that one pixel has a slightly different behavior than the surrounding pixels. The RMS value of this pixel is 1.42 cm. The reason can be found in incorrectly estimated motion model parameters of the corresponding phase gradients. This also results in a temporal inconsistency after the first phase unwrapping, see Table 7.3f. Using the alternative EMCF algorithm, the RMS value of this conspicuous pixel can be reduced to 0.36 cm. But also here a temporal inconsistency is inserted by the two-step procedure. The situation is different with the one-step three dimensional approach. The results are temporally consistent and the RMS value of the pixel can be further reduced to 0.16 cm.

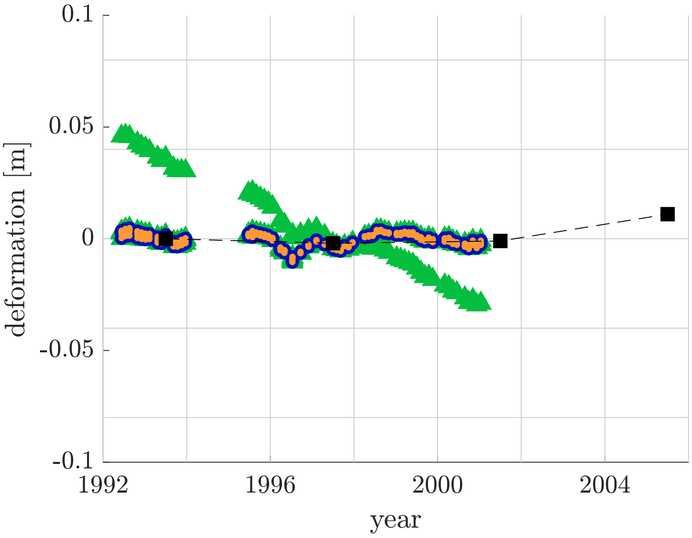

(a) test region 1: Monheim at the Rhine, Mettmann

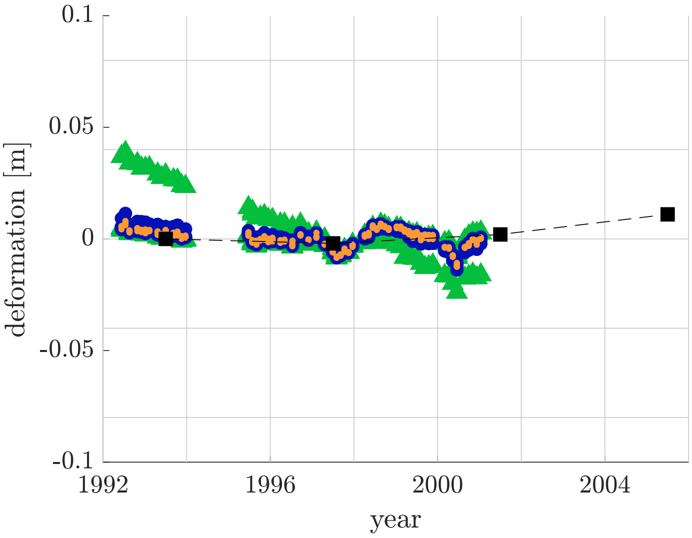

(b) test region 2: Gustorf, Grevenbroich

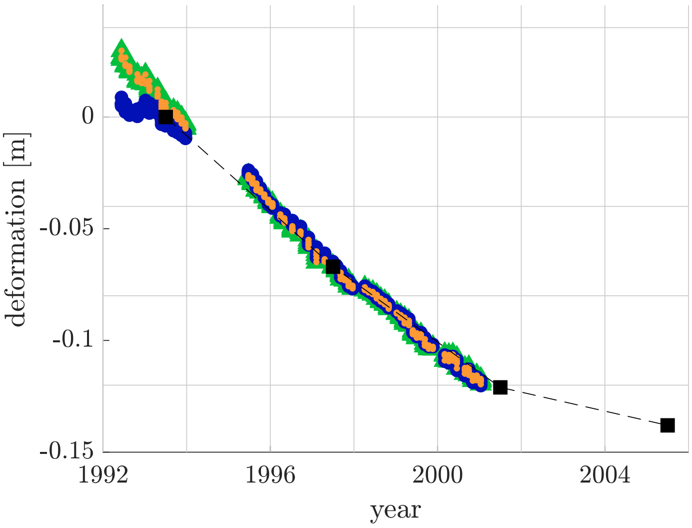

(c) test region 3: Koslar, Jülich

Figure 7.6: Deformation time series of five pixels lying in each of the six highlighted test regions 1, 2 and 3 shown in Fig. 7.4. The green triangles are the results using the conventional EMCF approach, the dark blue points are the results using the alternative EMCF approach and the orange points using the one-step three dimensional approach. For comparison the black squares indicate the data from the closest leveling point.

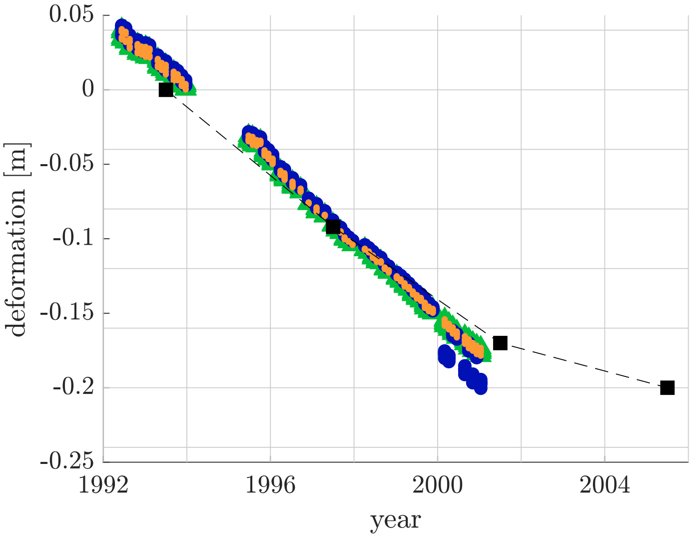

(a) test region 4: Jülich

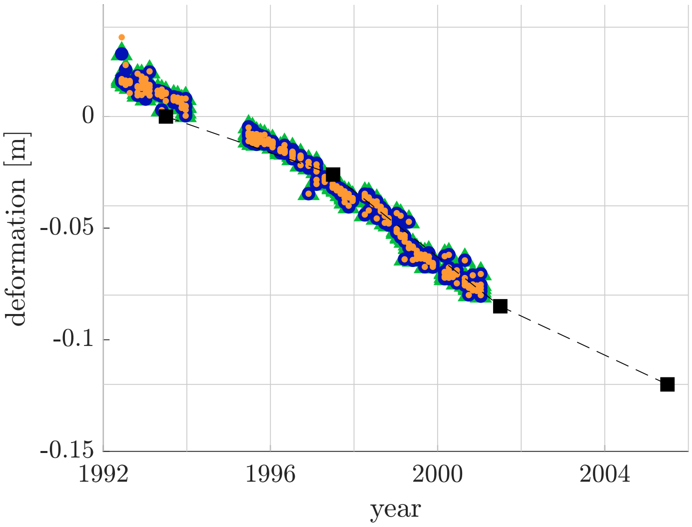

(b) test region 5: Mersch, Jülich

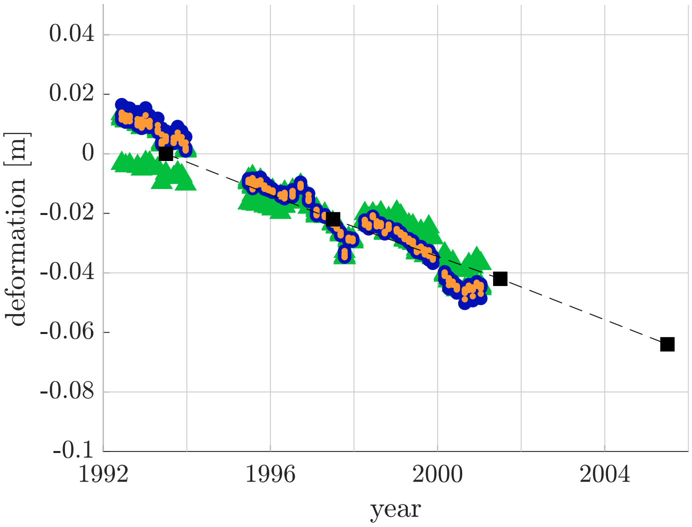

(c) test region 6: Odenkirchen, Mönchengladbach

Figure 7.7: Deformation time series of five pixels lying in each of the six highlighted test regions 4, 5 and 6 shown in Fig. 7.4. The green triangles are the results using the conventional EMCF approach, the dark blue points are the results using the alternative EMCF approach and the orange points using the one-step three dimensional approach. For comparison the black squares indicate the data from the closest leveling point.

Table 7.3: Number of total temporal inconsistencies of the phase gradients belonging to the conspicuous pixels in the test region 1 to 6, cf. Figs 7.6a to 7.7c. The number is listed after the first and the second phase unwrapping step in the SBAS workflow. The phase unwrapping is done with the conventional and the alternative EMCF approach and with the one-step three dimensional approach.

(a) Monheim at the Rhine

method	total number of temporal inconsistencies after 1st phase unwrapping	2nd phase unwrapping
conventional EMCF approach	56	0
alternative EMCF approach	26	0
one-step three dimensional approach	24	0

(b) Gustorf

method	total number of temporal inconsistencies after 1st phase unwrapping	2nd phase unwrapping
conventional EMCF approach	15	3
alternative EMCF approach	1	0
one-step three dimensional approach	1	0

(c) Koslar

method	total number of temporal inconsistencies after 1st phase unwrapping	2nd phase unwrapping
conventional EMCF approach	2	0
alternative EMCF approach	1	8
one-step three dimensional approach	0	0

(d) Jülich

method	total number of temporal inconsistencies after 1st phase unwrapping	2nd phase unwrapping
conventional EMCF approach	0	0
alternative EMCF approach	2	3
one-step three dimensional approach	0	0

(e) Mersch

method	total number of temporal inconsistencies after 1st phase unwrapping	2nd phase unwrapping
conventional EMCF approach	1	2
alternative EMCF approach	1	2
one-step three dimensional approach	1	1

(f) Odenkirchen

method	total number of temporal inconsistencies after 1st phase unwrapping	2nd phase unwrapping
conventional EMCF approach	1	0
alternative EMCF approach	1	0
one-step three dimensional approach	0	0

7.5 Summary

It can be concluded that a one-step three dimensional phase unwrapping approach has been successfully defined which can be integrated into the SBAS workflow on the basis of multilooked and multitemporally filtered wrapped phase gradients. When the spatial and temporal constraints are combined into a single large constraint matrix, it has been shown that there possibly arise conflicts in the constraints. This is due to the multilooked data. Since the multilooking is performed separately for each interferogram, the data do not exactly fulfill the temporal constraints. This problem can be avoided by inserting slack variables. These slack variables compensate the temporal inconsistency of the data. Since inserting a slack variable is not intended to replace the estimation of a phase ambiguity factor, the slack variables must be integrated into the objective function with a high weight. Therefore, the one-step three dimensional approach is based on the assumption that the phase gradients should be as consistent as possible in time.

Both on the basis of the simulated data and on the basis of the ERS-1/-2 real data, it has been shown that this assumption is justified. The resulting deformation time series reflects the essential movement patterns, i.e. the subsidence in the areas of the active open-cast mines Hambach, Inden and Garzweiler and the uplift in the already closed mine regions Aachen and Erkelenz. Compared to the two-step EMCF algorithm, the results are temporally more consistent and the analysis of single pixels has shown that the movement pattern partly fits better to the leveling data. Based on the findings of Chapter 6, it was possible to successfully fulfill the third and final main objective of this thesis, to formulate a one-step three dimensional algorithm that takes into account the temporal inconsistencies of the multilooked data.

8. Conclusion and Outlook

8.1 Conclusion

One of the critical steps during the SBAS analysis is the solution of the integer phase ambiguity factors which is done in the context of phase unwrapping. Within this thesis a contribution is made to improve the phase unwrapping step. The current state of the art to multitemporally unwrap the phases of a D-InSAR stack is the EMCF algorithm. Input variables are double differences in space and time. The inclusion of the temporal information provided by the D-InSAR stack, significantly improves the phase unwrapping compared to the spatial phase unwrapping which is based on one single interferogram only. The EMCF algorithm works in two steps: the temporal and the spatial phase unwrapping. Within the temporal phase unwrapping a spatial phase gradient is considered in all interferograms and a linear motion model is estimated first to calculate modified observations. These modified observations have less phase ambiguities than the original observations, which simplifies the phase unwrapping and is essential for its success. Subsequently, the temporally unwrapped phase gradients are used to perform the spatial phase unwrapping for each individual interferogram. Therefore, the three dimensional problem is divided into two problems of smaller dimension, each defined as weighted L_1-norm problem and solvable as LP. However, solving in two steps is not optimal, as the spatial phase unwrapping in the second step destroys the temporal constraints that are fulfilled for each phase gradient in the temporal phase unwrapping. Therefore, an approach was developed in this thesis which performs the temporal and spatial phase unwrapping in one single step. This approach can easily be integrated into the SBAS workflow. Furthermore, the approach is able to deal with multilooked and therefore temporally inconsistent data. This is especially important with noisy data.

The development of the one-step approach required some preliminary work. Since solving the three dimensional phase unwrapping in one single step involves the solution of a very large LP, it was necessary to understand in detail how the phase unwrapping problem looks like. The LP has special properties so that the results are integer values and using a special ILP solver is not necessary. The problem can be formulated in different ways and due to its special structure it can be solved by means of general LP solvers as well as by network flow solvers. This thesis gives a detailed and consistent overview and discusses different formulations and types of solutions, in this case related to the spatial phase unwrapping. However, the transition to the temporal phase unwrapping is straightforward and analogous conclusions can be derived. It was shown that all formulations lead to the same results. Differences only arise if the solution is not unique. However, looking at the complexity, the formulation referred to in this thesis as PROBLEM 1 and PROBLEM 3 is the most efficient. The problem is presented as a constrained weighted L_1-norm problem and is solved once using a general LP solver and once using a network flow solver. Based on this knowledge, the temporal as well as the spatial phase unwrapping can be set up and solved efficiently within the EMCF algorithm.

To solve the temporal and spatial phase unwrapping in one step, it was necessary to improve the EMCF algorithm. The estimation of the motion model, which is needed to calculate the modified and less ambiguous observations, is conventionally done iteratively. For a predefined search space and discretization, the temporal LP is solved several times and the solution that generates the lowest costs is considered as optimal. In this thesis, an alternative approach to estimate the motion model parameters was developed, where the EPC function is maximized by a modified approach combining simulated annealing and the Nelder-Mead method, defined as Algorithm 4. The efficiency and performance of this approach was demonstrated on simulated data with different noise levels from very good to worst case scenarios as well as on real data of the Lower-Rhine-Embayment. The alternative approach is independent of the solution of the temporal phase unwrapping, so that the temporal LP has to be solved once in contrast to the conventional iteratively way. Consequently, besides improved phase unwrapping results, the run time can also be reduced significantly. A second modification concerns the choice of weights. Conventionally, the spatial weights, required for setting up the spatial LP in the second step, depend on the costs of the temporal LP. High temporal costs lead to low spatial weights because the phase gradient is considered unreliable. To establish a one-step three dimensional approach, the spatial costs must be independent of the solution of the temporal phase unwrapping. For this purpose, different weighting functions were investigated, both for the spatial and for the temporal weights, which are conventionally considered to be constant. It was found that EPC based spatial weights, referred to as *Weights 3*, are a good alternative. The temporal weights do not have a very large influence, so that constant weights in time are still assumed. Choosing EPC based spatial weights, it was shown on the basis of the simulated data that the percentage of correctly unwrapped phase gradients can be further increased. An improvement can also be seen on the basis of the real data, the results are spatially smoother. In this way, an alternative EMCF approach was developed in the thesis, which estimates the motion model by maximizing the EPC function using a modified algorithm (Algorithm 4) and uses EPC based spatial weights (*Weights 3*).

Based on the preliminary work, a one-step three dimensional approach was defined. This approach can easily be integrated into the SBAS workflow and works on the basis of multilooked and multitemporally filtered phase gradients. The multilooked data lead to the fact that the temporal constraints are not exactly fulfilled. To compensate this problem, slack variables for the temporal constraints were inserted. These slack variables are highly weighted in the objective function to avoid that the insertion of slack variables replaces the estimation of phase ambiguities. Thus, the phase unwrapping can be solved multitemporally in one step by solving a single high dimensional weighted L_1-norm problem. The disadvantage in contrast to the EMCF algorithm is that the problem can no longer be solved as a network flow problem. However, due to certain properties, the problem can still be solved with LP solvers, resulting in integer parameters. The new developed one-step approach has shown its performance on the basis of simulated data, especially in worst case scenarios with high noise. But also on the basis of real ERS-1/-2 data it was clearly shown that the final results of the RSG software are more consistent if the interferometric phases are unwrapped externally using the self-developed approach.

8.2 Outlook

In this thesis a conscious choice was made to use the ERS-1/-2 data. Especially with these older data the phase unwrapping is more complex due to a lower spatial and temporal resolution compared to newer sensors. So especially with these data phase unwrapping errors can often be found and there is an increased potential for improvement. Moreover, the older data are of particular interest with regard to long-term evaluations. Nevertheless, it should be noted that all the approaches presented and discussed in this thesis can be applied one-to-one to other newer sensors such as TerraSAR-X or Sentinel-1.

So far, the evaluation of real data has been limited to a smaller data set in which only pixels with a coherence value greater than or equal to 0.7 in 95% of the interferograms were evaluated. Thus, the noise level of the data is very low. Although it was clearly shown that the new approach led to much more consistent results, the deformation time series of the individual pixels compared to the two-step EMCF algorithm did not differ significantly. The simulated data showed that the one-step approach shows its performance especially at high noise levels. Consequently, the new approach is well suited to also include less coherent pixels in the evaluation. Thus, spatially more dense results can be achieved. However, this leads to the fact that the weighted L_1-norm problem takes on a very high dimension. This requires larger computing resources which were not available in the context of this thesis. The dimension of the problem will also increase rapidly when the presented one-step three dimensional approach is applied to newer sensors, since TerraSAR-X and Sentinel-1 data have a higher spatial and temporal resolution. The current literature shows that there are research projects in this field, so that the solution of such complex problems is quite feasible. One possibility to apply the approach also to higher dimensional systems can be the transition to massively parallel computers as well as the further investigation and analysis of the special structure of the constraint matrix with respect to its efficiency, cf. Breuer et al. (2018). Furthermore, it would be conceivable to use a region growing based technology, similar to Yang et al. (2013) or Ojha et al. (2015), a hierarchical algorithm (Carballo and Fieguth, 2002) or a tiling strategy (Chen and Zebker, 2002).

In the course of this work, it could be shown that the stepwise solution is not optimal. However, if one is forced to use the two-step EMCF algorithm due to a lack of computing capacity, it is advisable, especially with noisy data, to use the alternative EMCF algorithm developed here. In addition to a more robust estimation of the motion model, the run time can be reduced significantly. Also, here, the potential to include more and less coherent pixels in the evaluation becomes apparent, resulting in spatially more dense results in the future. Even if the motion model parameters cannot be estimated reliably, this can be recognized by low EPC values, so that these areas are down-weighted with the new weighting.

Nevertheless, it has to be mentioned that there is no phase unwrapping algorithm that can be used for all scenarios. The approach presented here estimates the deformation parameters by maximizing the EPC function. This function includes a linear motion model. This means that the proposed approach assumes that the phase gradients move linearly with time. If non-linear motion components are present, the EPC function has to be extended by this non-linear effect to estimate realistic deformation model parameters.

A. Connection between Primal and Dual Linear Problems using the Tucker Diagram

This chapter is intended to give an overview of how to derive the dual LP of a primal LP. The following primary minimization problem is given in its standard form with three primal variables x_1, x_2 and x_3 and two constraints

$$\text{Objective function:} \quad c_1x_1 + c_2x_2 + c_3x_3 \ldots \min \tag{A.1}$$

$$\text{Constraint:} \quad B_{11}x_1 + B_{12}x_2 + B_{13}x_3 \geq b_1 \tag{A.2}$$

$$B_{21}x_1 + B_{22}x_2 + B_{23}x_3 \geq b_2 \tag{A.3}$$

$$\text{Variable:} \quad x_1, x_2, x_3 \in \mathbb{R}_{\geq 0}. \tag{A.4}$$

Every LP can be brought into this standard form. Each equation can be represented by two inequalities and each $\leq -$ inequality can be transformed into a $\geq -$ inequality by multiplication with minus one. In the same way every maximization task can be transformed into a minimization task by multiplication with minus one.

To obtain the dual LP of the primal LP given in standard form, the Tucker diagram in Table A.1 is used. The primal problem is read from left to right and the dual problem from top to bottom.

The dual LP is obtained by transposing the coefficients of the constraints B_{ij}, exchanging the role of the constant right-hand side vector b_i with the role of the coefficients of the object function c_j, changing the direction of the inequalities and turning a minimization problem into a maximization problem. This results in the following corresponding dual maximization problem with two dual variables y_1 and y_2 and three constraints

$$\text{Objective function:} \quad y_1b_1 + y_2b_2 \ldots \max \tag{A.5}$$

$$\text{Constraint:} \quad B_{11}y_1 + B_{21}y_2 \leq c_1 \tag{A.6}$$

$$B_{12}y_1 + B_{22}y_2 \leq c_2 \tag{A.7}$$

$$B_{13}y_1 + B_{23}y_2 \leq c_3 \tag{A.8}$$

$$\text{Variable:} \quad y_1, y_2 \in \mathbb{R}_{\geq 0}. \tag{A.9}$$

The dual of the dual LP will again result in the primal LP.

Table A.1: Tucker diagram to show the connection between dual and primal LPs, based on (Dantzig, 1963, p. 125).

	primal						
	variables	$x_1 \geq 0$	$x_2 \geq 0$	$\ldots$	$x_n \geq 0$	relation	constants
dual	$y_1 \geq 0$	B_{11}	B_{12}	$\ldots$	B_{1n}	$\geq$	b_1
	$y_2 \geq 0$	B_{21}	B_{22}	$\ldots$	B_{2n}	$\geq$	b_2
	$\vdots$	$\vdots$		$\ldots$	$\vdots$	$\vdots$	$\vdots$
	$y_r \geq 0$	B_{r1}	B_{r2}	$\ldots$	B_{rn}	$\geq$	b_r
	relation	$\leq$	$\leq$	$\ldots$	$\leq$		max
	constants	c_1	c_2	$\ldots$	c_n	min	

B. Lists

List of Symbols and Terms

SAR Image

$\phi_{x_j}^{t_\alpha}$	unwrapped phase at pixel x_j in SAR image at time t_α
$\psi_{x_j}^{t_\alpha} = \langle \phi_{x_j}^{t_\alpha} \rangle_{2\pi}$	measured wrapped phase at pixel x_j in SAR image at time t_α
$k_{x_j}^{t_\alpha}$	phase ambiguity factor at pixel x_j in SAR image at time t_α

with the following relationship

$$\phi_{x_j}^{t_\alpha} = \psi_{x_j}^{t_\alpha} + 2\pi k_{x_j}^{t_\alpha} \tag{B.1}$$

Differential Interferogram

$\Delta t_{\alpha\beta}$	temporal baseline between the two SAR images at times t_α and t_β
$\Delta b_{\alpha\beta}$	spatial baseline between the two orbits of the two SAR images at times t_α and t_β
$\Delta b_{\perp,\alpha\beta}$	orthogonal spatial baseline between the two orbits of the two SAR images at times t_α and t_β
$\phi_{x_j}^{\Delta t_{\alpha\beta}} = \phi_{x_j}^{t_\beta} - \phi_{x_j}^{t_\alpha}$	unwrapped interferometric phase at pixel x_j
$\psi_{x_j}^{\Delta t_{\alpha\beta}} = \langle \psi_{x_j}^{t_\beta} - \psi_{x_j}^{t_\alpha} \rangle_{2\pi}$	measured wrapped interferometric phase at pixel x_j
$k_{x_j}^{\Delta t_{\alpha\beta}}$	phase ambiguity factor of interferometric phase at pixel x_j

with the following relationship

$$\phi_{x_j}^{\Delta t_{\alpha\beta}} = \psi_{x_j}^{\Delta t_{\alpha\beta}} + 2\pi k_{x_j}^{\Delta t_{\alpha\beta}} \tag{B.2}$$

Δx_{kl}	gradient between the pixels x_k and x_l
$\phi_{\Delta x_{kl}}^{\Delta t_{\alpha\beta}} = \phi_{x_l}^{\Delta t_{\alpha\beta}} - \phi_{x_k}^{\Delta t_{\alpha\beta}}$	unwrapped interferometric phase gradient
$\psi_{\Delta x_{kl}}^{\Delta t_{\alpha\beta}} = \langle \psi_{x_l}^{\Delta t_{\alpha\beta}} - \psi_{x_k}^{\Delta t_{\alpha\beta}} \rangle_{2\pi}$	measured wrapped interferometric phase gradient
$k_{\Delta x_{kl}}^{\Delta t_{\alpha\beta}}$	phase ambiguity factor of interferometric phase gradient

with the following relationship

$$\phi_{\Delta x_{kl}}^{\Delta t_{\alpha\beta}} = \psi_{\Delta x_{kl}}^{\Delta t_{\alpha\beta}} + 2\pi k_{\Delta x_{kl}}^{\Delta t_{\alpha\beta}} \tag{B.3}$$

Graph in the Azimuth/ Range Plane

$\mathcal{M}$	set of nodes given by the stable pixels in the interferogram
m	number of nodes, equal to the number of stable pixels in the interferogram
$\mathcal{N}$	set of arcs given by the phase gradients in the interferogram
n	number of arcs, equal to the number of phase gradients in the interferogram
$\mathcal{R}$	set of triangles given by the constraints in the spatial phase unwrapping
r	number of triangles, equal to the number of constraints in the spatial phase unwrapping

Graph in the Temporal/ Orthogonal Spatial Baseline Plane

$\mathcal{M}'$	set of nodes given by the SAR images
m'	number of nodes, equal to the number of SAR images
$\mathcal{N}'$	set of arcs given by the interferograms
n'	number of arcs, equal to the number of interferograms
$\mathcal{R}'$	set of triangles given by the constraints in the temporal phase unwrapping
r'	number of triangles, equal to the number of constraints in the temporal phase unwrapping

Problem Formulations for the Spatial Phase Unwrapping

PROBLEM 1	constraint L_1-norm problem formulated as LP and defined in (4.16)
PROBLEM 2	parametric L_1-norm problem formulated as LP and defined in (4.23)
PROBLEM 3	constraint L_1-norm problem formulated as network flow problem and defined in (4.24)
PROBLEM 4	parametric L_1-norm problem formulated as network flow problem and defined in (4.26)

Used Methods to Estimate The Motion Model Parameters

Algorithm 1	grid search algorithm to maximize the EPC function, defined in Section 6.1 on p. 69
Algorithm 2	Nelder Mead algorithm to maximize the EPC function, defined in Section 6.1 on p. 71
Algorithm 3	simulated annealing to maximize the EPC function, defined in Section 6.1 on p. 72
Algorithm 4	modified algorithm combining simulated annealing and Nelder Mead, defined in Section 6.1 on p. 78

Used Weighting Functions to Set Up the Phase Unwrapping Problem

Weights 1	coherence based weights, defined in (6.16)
Weights 2	phase and length based weights, defined in (6.17)
Weights 3	EPC based weights, defined in (6.18)
Weights 4	weights directly depending on the temporal and spatial baseline between the two SAR images, defined in (6.19)

List of Abbreviations

AFM	Ambiguity Function Method
DEM	Digital Elevation Model
D-InSAR	Differential Interferometric Synthetic Aperture Radar
EMCF	Extended Minimum Cost Flow
EPC	Ensemble Phase Coherence
ERS	European Remote Sensing
ESA	European Space Ageny
FPP	Fringe Projection Profilometry
GNSS	Global Navigation Satellite System
ILP	Integer Linear Program
InSAR	Interferometric Synthetic Aperture Radar
LAMBDA	Least Squares Ambiguity Decorrelation Adjustment
LOS	Line of Sight
LP	Linear Program
MCF	Minimum Cost Flow
MILP	Mixed Integer Linear Program
MRI	Magnetic Resonance Imaging
PSI	Persistent Scatterer Interferometry
radar	radio detection and ranging
RMS	Root Mean Square
RSG	Remote Sensing Software Graz
SAR	Synthetic Aperture Radar
SBAS	Small BAseline Subset
SNAPHU	Statistical-cost Network-flow Algorithm for PHase Unwrapping
SRTM	Shuttle Radar Topography Mission
StaMPS	Stanford Method for Persistent Scatterers
SVD	Singular Value Decomposition
TOPS	Terrain Observation with Progressive Scans

List of Figures

List of Tables

Acknowledgements

Writing this thesis would not have been possible without the support of the following people.

First of all, I would like to express my gratitude to my Ph.D. supervisor Wolf-Dieter Schuh, who offered me the great chance to perform my Ph.D. studies in the Theoretical Geodesy (TG) group at the Institute of Geodesy and Geoinformation of the University of Bonn. Thank you for your guidance, the discussions and freedom that gave me the opportunity to build my own line of research. In addition, I want to thank Jan-Henrik Haunert and Mathias Schardt for both agreeing to be a referee of this thesis and for providing valuable inputs and kind supports.

My thanks also go to DIGITAL Institute for Information and Communication Technology of Joanneum Research in Graz for the provision of the RSG software, as well as the assistance with software problems. Particularly, I am very grateful to Karlheinz Gutjahr, who always had an open ear for my problems regarding InSAR and especially regarding the RSG software. Our discussions and your ideas and comments helped significantly to improve my work.

I also want to acknowledge the European Space Agency (ESA-Project ID 17055) for provision of the ERS-1/-2 data and GEOBasis NRW for the leveling data.

Moreover, I would like to thank Joël Köhler for all the scientific and non-work related talks. Special thanks go to my roommate Jan Martin Brockmann. Thank you for proofreading my work, for helping me with numerous technical problems and thank you for always believing in my work. Thanks also to Till Schubert, Christian Neyers and Johannes Korte and all colleagues in the Astronomical, Physical and Mathematical Geodesy (APMG) group for the wonderful time and the nice working atmosphere.

On a personal note, I would like to express my heartfelt gratitude to my family and friends, in particular, my parents Walter and Doris as well as my brother Thomas for supporting me and believing in me throughout my life. I would also like to thank my sister-in-law Monika, my godchild Jonas and my niece Lara. You have contributed to this work in your very special way.

Last but not least, I would like to thank Moritz. Thank you for struggling through the proofreading of my work and thank you for your love, your continuous support and your unwavering patience!

Bibliography

O. Aichholzer, F. Aurenhammer, H. Krasser, and P. Braß. Pseudotriangulations from Surfaces and a Novel Type of Edge Flip. SIAM on Computing, 32(6):1621–1653, 2003. doi:10.1137/S0097539702411368.

R. Bamler and P. Hartl. Synthetic aperture radar interferometry. Inverse Problems, 14:1–54, 1998. doi:10.1088/0266-5611/14/4/001.

R. Bamler and B. Schättler. SAR Data Acquisition and Image Formation. In Geocoding: ERS-1 SAR Data and Systems, pages 53–102. Wichmann-Verlag, January 1993. ISBN 3-87907-247-7.

P. Berardino, G. Fornaro, R. Lanari, and E. Sansosti. A new algorithm for surface deformation monitoring based on small baseline differential SAR interferograms. IEEE Transactions on Geoscience and Remote Sensing, 40(11):2375–2383, November 2002. ISSN 0196-2892. doi:10.1109/TGRS.2002.803792.

D. P. Bertsekas and P. Tseng. A faster version of the RELAX code for solving minimum cost flow problems. Technical report, Massachusetts Institute of Technology, Laboratory for Information and Decision Systems, 1994.

D.P. Bertsekas and P. Tseng. Relaxation method for minimum cost ordinary network flow problems. Operations Research, 36, 02 1988. doi:10.1287/opre.36.1.93.

R. Boje, W. Gstirner, D. Schuler, and M. Spata. Leitnivellements in Bodenbewegungsgebieten des Bergbaus - Eine langfährige Kernaufgabe der Landesvermessung in Nordrhein-Westfalen. NÖV NRW, 3:33–42, 2008.

T. Breuer, M. Bussieck, K.K. Cao, F. Cebulla, F. Fiand, H.C. Gils, A. Gleixner, D. Khabi, T. Koch, D. Rehfeldt, and M. Wetzel. Optimizing large-scale linear energy system problems with block diagonal structure by using parallel interior-point methods. In N. Kliewer, J.F. Ehmke, and R. Borndörfer, editors, Operations Research Proceedings 2017, pages 641–647, Cham, 2018. Springer International Publishing. ISBN 978-3-319-89920-6.

G.F. Carballo and Paul Fieguth. Hierarchical network flow phase unwrapping. IEEE Transactions on Geoscience and Remote Sensing, 40:1695 – 1708, 09 2002. doi:10.1109/TGRS.2002.800279.

W. G. Carrara, R. S. Goodman, and R. M. Majewski. Spotlight Synthetic Aperture Radar: Signal Processing Algorithms. Artech House, 1995. ISBN 978-0-89006-728-4.

C. W. Chen. Statistical-Cost Network-Flow Approaches to Two-Dimensional Phase Unwrapping for Radar Interferometry /. PhD thesis, Stanford University. Department of Electrical Engineering, 2001.

C. W. Chen and H. A. Zebker. Phase unwrapping for large sar interferograms: statistical segmentation and generalized network models. IEEE Transactions on Geoscience and Remote Sensing, 40(8):1709–1719, 2002.

M. Costantini. A phase unwrapping method based on network programming. In Fringe 96 Workshop ERS SAR Interferometry, pages 261–272, Zurich, 1997. ISBN 92-9092-307-5.

M. Costantini. A novel phase unwrapping method based on network programming. IEEE Transactions on Geoscience and Remote Sensing, 36(3):813–821, May 1998. ISSN 0196-2892. doi:10.1109/36.673674.

M. Costantini and P. Rosen. Generalized phase unwrapping approach for sparse data. In International Geoscience and Remote Sensing Symposium (IGARSS), volume 1, pages 267–269 vol.1, February 1999. ISBN 978-0-7803-5207-0. doi:10.1109/IGARSS.1999.773467.

M. Costantini, F. Malvarosa, and F. Minati. A General Formulation for Redundant Integration of Finite Differences and Phase Unwrapping on a Sparse Multidimensional Domain. IEEE Transactions on Geoscience and Remote Sensing, 50(3):758–768, March 2012. ISSN 0196-2892. doi:10.1109/TGRS.2011.2162630.

C. C. Counselman and S. A. Gourevitch. Miniature Interferometer Terminals for Earth Surveying: Ambiguity And Multipath with Global Positioning System. IEEE Transactions on Geoscience and Remote Sensing, GE-19(4):244–252, October 1981. ISSN 1558-0644. doi:10.1109/TGRS.1981.350379.

M. Crosetto, O. Monserrat, M. Cuevas-González, N. Devanthéry, and B. Crippa. Persistent Scatterer Interferometry: A review. ISPRS Journal of Photogrammetry and Remote Sensing, 115:78–89, May 2016. ISSN 0924-2716. doi:10.1016/j.isprsjprs.2015.10.011.

N. D. Curet. A primal-dual simplex method for linear programs. Operations Research Letters, 13 (4):233–237, May 1993. ISSN 0167-6377. doi:10.1016/0167-6377(93)90045-I.

J. C. Curlander and R. N. McDonough. Synthetic Aperture Radar: Systems and Signal Processing. Wiley, November 1991. ISBN 978-0-471-85770-9.

A. Currie and M. A. Brown. Wide-swath SAR. IEE Proceedings F - Radar and Signal Processing, 139(2):122–135, April 1992. ISSN 0956-375X. doi:10.1049/ip-f-2.1992.0016.

R. Cusack, N. Papdakis, K. Martin, and M. Brett. A new robust 3D phase-unwrapping algorithm applied to fMRI field maps for the undistortion of EPIs. Neuroimage, 13:103–103, June 2001. doi:10.1016/S1053-8119(01)91446-6.

G. Dantzig. Linear Programming and Extensions. Princeton University Press, 1963. ISBN 978-1-4008-8417-9.

F. De Zan and A. Monti Guarnieri. Topsar: Terrain observation by progressive scans. IEEE Transactions on Geoscience and Remote Sensing, 44(9):2352–2360, 2006.

J. Edmonds and R. Giles. A min-max relation for submodular functions on graphs. CORE Discussion Papers RP 301, Université catholique de Louvain, Center for Operations Research and Econometrics (CORE), January 1977.

M. Eineder, M. Hubig, and B. Milcke. Unwrapping large interferograms using the minimum cost flow algorithm. In IGARSS '98. Sensing and Managing the Environment. 1998 IEEE International Geoscience and Remote Sensing. Symposium Proceedings, volume 1, pages 83–87, July 1998. doi:10.1109/IGARSS.1998.702806.

C. Esch, J. Köhler, K. Gutjahr, and W.-D. Schuh. On the Analysis of the Phase Unwrapping Process in a D-InSAR Stack with Special Focus on the Estimation of a Motion Model. Remote Sensing, 11(19):2295, January 2019a. doi:10.3390/rs11192295.

C. Esch, J. Köhler, K. Gutjahr, and W.-D. Schuh. 25 Jahre Bodenbewegungen in der Niederrheinischen Bucht – Ein kombinierter Ansatz aus D-InSAR und amtlichen Leitnivellements. ZfV - Zeitschrift für Geodäsie, Geoinformation und Landmanagement, zfv 3/2019, June 2019b. ISSN 1618-8950. doi:10.12902/zfv-0257-2019.

C. Esch, J. Köhler, K. Gutjahr, and W.-D. Schuh. One-Step Three Dimensional Phase Unwrapping Approach Based on Small Baseline Subset Interferograms. Remote Sensing, 2020. (accepted for publication).

M. Even and K. Schulz. Cost Functions for Phase Unwrapping with Redundant Integration of Finite Differences. In EUSAR 2014, 10th European Conference on Synthetic Aperture Radar, pages 1037–1040, June 2014.

A. Ferretti, C. Prati, and F. Rocca. Permanent scatterers in SAR interferometry. IEEE Transactions on Geoscience and Remote Sensing, 39(1):8–20, January 2001. ISSN 0196-2892. doi:10.1109/36.898661.

A. Ferretti, A. Fumagalli, F. Novali, C. Prati, F. Rocca, and A. Rucci. A New Algorithm for Processing Interferometric Data-Stacks: SqueeSAR. IEEE Transactions on Geoscience and Remote Sensing, 49(9):3460–3470, September 2011. ISSN 0196-2892. doi:10.1109/TGRS.2011.2124465.

G. Fornaro, A. Pauciullo, and D. Reale. A Null-Space Method for the Phase Unwrapping of Multitemporal SAR Interferometric Stacks. IEEE Transactions on Geoscience and Remote Sensing, 49(6):2323–2334, June 2011. ISSN 0196-2892. doi:10.1109/TGRS.2010.2102767.

V. S. Frost, J. A. Stiles, K. S. Shanmugan, and J. C. Holtzman. A Model for Radar Images and Its Application to Adaptive Digital Filtering of Multiplicative Noise. IEEE Transactions on Pattern Analysis and Machine Intelligence, PAMI-4(2):157–166, March 1982. ISSN 0162-8828. doi:10.1109/TPAMI.1982.4767223.

D. R. Fulkerson. An Out-of-Kilter Method for Minimal-Cost Flow Problem. Journal of The Society for Industrial and Applied Mathematics, 9, March 1961. doi:10.1137/0109002.

A. K. Gabriel and R. M. Goldstein. Crossed orbit interferometry - Theory and experimental results from SIR-B. International Journal of Remote Sensing, 9:857–872, May 1988. ISSN 0143-1161. doi:10.1080/01431168808954901.

A. K. Gabriel, R. M. Goldstein, and H. A. Zebker. Mapping small elevation changes over large areas: Differential radar interferometry. Journal of Geophysical Research: Solid Earth, 94(B7): 9183–9191, July 1989. ISSN 2156-2202. doi:10.1029/JB094iB07p09183.

S. Geman and D. Geman. Stochastic Relaxation, Gibbs Distributions, and the Bayesian Restoration of Images. IEEE Transactions on Pattern Analysis and Machine Intelligence, PAMI-6(6):721–741, 1984.

D. C. Ghiglia and M. D. Pritt. Two-Dimensional Phase Unwrapping: Theory, Algorithms, and Software. Wiley, 1998. ISBN 978-0-471-24935-1.

D. C. Ghiglia and L. A. Romero. Robust two Dimensional weighted and unweighted phase unwrapping that uses fast transforms and iterative methods. Journal of The Optical Society of America A, 11:107–117, January 1994. doi:10.1364/JOSAA.11.000107.

R. M. Goldstein and C. L. Werner. Radar interferogram filtering for geophysical applications. Geophysical Research Letters, 25(21):4035–4038, November 1998. ISSN 1944-8007. doi:10.1029/1998GL900033.

R. M. Goldstein, H. A. Zebker, and C. L. Werner. Satellite Radar Interferometry: Two-Dimensional Phase Unwrapping. Radio Science, 23, September 1988. doi:10.1029/RS023i004p00713.

R. E. Gomory. Outline of an algorithm for integer solutions to linear programs. Bulletin of the American Mathematical Society, 64(5):275–278, September 1958. ISSN 0002-9904, 1936-881X.

J. Gondzio. Interior point methods 25 years later. European Journal of Operational Research, 218 (3):587–601, May 2012. ISSN 0377-2217. doi:10.1016/j.ejor.2011.09.017.

J. W. Goodman. Statistical Properties of Laser Speckle Patterns. In J. C. Dainty, editor, Laser Speckle and Related Phenomena, Topics in Applied Physics, pages 9–75. Springer Berlin Heidelberg, Berlin, Heidelberg, 1975. ISBN 978-3-662-43205-1. doi:10.1007/978-3-662-43205-1_2.

L. C. Graham. Synthetic interferometer radar for topographic mapping. Proceedings of the IEEE, 62(6):763–768, June 1974. ISSN 0018-9219. doi:10.1109/PROC.1974.9516.

S. Halsig, A. Ernst, and W.-D. Schuh. Ausgleichung von Höhennetzen aus mehreren Epochen unter Berücksichtigung von Bodenbewegungen. ZfV - Zeitschrift für Geodäsie, Geoinformation und Landmanagement, zfv 4/2013, 2013.

R. F. Hanssen. Radar Interferometry: Data Interpretation and Error Analysis. Remote Sensing and Digital Image Processing. Springer Netherlands, 2001. ISBN 978-0-7923-6945-5.

E. Hervet, R. Fjortoft, P. Marthon, and A. Lopes. Comparison of wavelet-based and statistical speckle filters. In SAR Image Analysis, Modeling, and Techniques, volume 3497, pages 43–54, November 1998. doi:10.1117/12.331361.

A. Hooper. Persistent Scatter Radar Interferometry for Crustal Deformation Studies and Modeling of Volcanic Deformation. PhD thesis, Department of Geophysics and the Commitee on Graduate Studies of Stanford University, January 2006.

A. Hooper and H. A. Zebker. Phase unwrapping in three dimensions with application to INSAR time series. Journal of the Optical Society of America. A, Optics, image science, and vision, 24: 2737–47, October 2007. doi:10.1364/JOSAA.24.002737.

A. Hooper, H. A. Zebker, P. Segall, and B. Kampes. A new method for measuring deformation on Volcanoes and other natural terrains using InSAR Persistent Scatterers. Geophyiscal Research Letters, 31:1–5, December 2004. doi:10.1029/2004GL021737.

A. Hooper, P. Segall, and H. A. Zebker. Persistent scatterer InSAR for crustal deformation analysis, with application to Volcán Alcedo, Galápagos. Journal of Geophysical Research, 112, July 2007. doi:10.1029/2006JB004763.

J. M. Huntley. Three-dimensional noise-immune phase unwrapping algorithm. Applied Optics, 40 (23):3901–3908, August 2001. ISSN 2155-3165. doi:10.1364/AO.40.003901.

P. Imperatore, A. Pepe, and R. Lanari. Multichannel Phase Unwrapping: Problem Topology and Dual-Level Parallel Computational Model. IEEE Transactions on Geoscience and Remote Sensing, 2015. doi:10.1109/TGRS.2015.2430619.

D. Just and R. Bamler. Phase statistics of interferograms with applications to synthetic aperture radar. Applied Optics, 33(20):4361–4368, July 1994. ISSN 2155-3165. doi:10.1364/AO.33.004361.

B. M. Kampes. Displacement Parameter Estimation Using Permanent Scatterer Interferometry. PhD thesis, TU Delft, 2005.

N. Karmarkar. A new polynomial-time algorithm for linear programming. Combinatorica, 4(4): 373–395, December 1984. ISSN 1439-6912. doi:10.1007/BF02579150.

S. Kirkpatrick, C. D. Gelatt, and M. P. Vecchi. Optimization by Simulated Annealing. Science, 220 (4598):671–680, May 1983. ISSN 0036-8075, 1095-9203. doi:10.1126/science.220.4598.671.

D. T. Kuan, A. A. Sawchuk, T. C. Strand, and P. Chavel. Adaptive Noise Smoothing Filter for Images with Signal-Dependent Noise. IEEE Transactions on Pattern Analysis and Machine Intelligence, PAMI-7(2):165–177, March 1985. ISSN 0162-8828. doi:10.1109/TPAMI.1985.4767641.

R. Lanari, O. Mora, M. Manunta, J. J. Mallorquí, P. Berardino, and E. Sansosti. A small-baseline approach for investigating deformations on full-resolution differential SAR interferograms. IEEE Transactions on Geoscience and Remote Sensing, 42:1377–1386, 2004. doi:10.1109/TGRS.2004.828196.

A. H. Land and A. G. Doig. An automatic method for solving discrete programming problems. Econometrica, 28(3):497–520, 1960.

J. Lee. Digital Image Enhancement and Noise Filtering by Use of Local Statistics. IEEE Transactions on Pattern Analysis and Machine Intelligence, PAMI-2(2):165–168, March 1980. ISSN 0162-8828. doi:10.1109/TPAMI.1980.4766994.

J.-S. Lee, K. W. Hoppel, S. A. Mango, and A. R. Miller. Intensity and phase statistics of multilook polarimetric and interferometric SAR imagery. IEEE Transactions on Geoscience and Remote Sensing, 32(5):1017–1028, September 1994. ISSN 0196-2892. doi:10.1109/36.312890.

C. E. Lemke. The dual method of solving the linear programming problem. Naval Research Logistics Quarterly, 1(1):36–47, March 1954. ISSN 1931-9193. doi:10.1002/nav.3800010107.

F. K. Li and R. M. Goldstein. Studies of multibaseline spaceborne interferometric synthetic aperture radars. IEEE Transactions on Geoscience and Remote Sensing, 28(1):88–97, January 1990. ISSN 0196-2892. doi:10.1109/36.45749.

Q. Lin, J. F. Vesecky, and H. A. Zebker. New approaches in interferometric SAR data processing. IEEE Transactions on Geoscience and Remote Sensing, 30(3):560–567, May 1992. ISSN 0196-2892. doi:10.1109/36.142934.

K. Liu, Y. Wang, D. L. Lau, Q. Hao, and L. G. Hassebrook. Dual-frequency pattern scheme for high-speed 3-D shape measurement. Optics Express, 18(5):5229–5244, March 2010. ISSN 1094-4087. doi:10.1364/OE.18.005229.

A. Lopes, E. Nezry, R. Touzi, and H. Laur. Maximum A Posteriori Speckle Filtering And First Order Texture Models In Sar Images. In 10th Annual International Symposium on Geoscience and Remote Sensing, pages 2409–2412, May 1990. doi:10.1109/IGARSS.1990.689026.

N. Metropolis, A. W. Rosenbluth, M. N. Rosenbluth, A. H. Teller, and E. Teller. Equation of State Calculations by Fast Computing Machines. Journal of Chemical Physics, 21:1087–1092, June 1953. ISSN 0301-0104. doi:10.1063/1.1699114.

R. K. Moore, J. P. Claassen, and Y.h. Lin. Scanning Spaceborne Synthetic Aperture Radar with Integrated Radiometer. IEEE Transactions on Aerospace and Electronic Systems, AES-17(3):410–421, May 1981. ISSN 0018-9251. doi:10.1109/TAES.1981.309069.

J. A. Nelder and R. Mead. A Simplex Method for Function Minimization. The Computer Journal, 7(4):308–313, January 1965. ISSN 0010-4620. doi:10.1093/comjnl/7.4.308.

J. Nocedal and S. Wright. Numerical Optimization. Springer Series in Operations Research and Financial Engineering. Springer-Verlag, New York, 2 edition, 2006. ISBN 978-0-387-30303-1. doi:10.1007/978-0-387-40065-5.

J. E. Odegard, H. Guo, M. Lang, C. S. Burrus, R. O. Wells, M. L. Novak, and M. Hiett. Wavelet Based SAR Speckle Reduction and Image Compression. Proceedings of SPIE - The International Society for Optical Engineering, 2487, 1995. doi:10.1117/12.210843.

C. Ojha, M. Manunta, R. Lanari, and A. Pepe. The Constrained-Network Propagation (C-NetP) Technique to Improve SBAS-DInSAR Deformation Time Series Retrieval. IEEE Journal of Selected Topics in Applied Earth Observations and Remote Sensing, 8(10):4910–4921, 2015.

A. Pepe and R. Lanari. On the Extension of the Minimum Cost Flow Algorithm for Phase Unwrapping of Multitemporal Differential SAR Interferograms. IEEE Transactions on Geoscience and Remote Sensing, 44(9):2374–2383, September 2006. ISSN 0196-2892. doi:10.1109/TGRS.2006.873207.

A. Pepe, Y. Yang, M. Manzo, and R. Lanari. Improved EMCF-SBAS Processing Chain Based on Advanced Techniques for the Noise-Filtering and Selection of Small Baseline Multi-Look DInSAR Interferograms. IEEE Transactions on Geoscience and Remote Sensing, 53(8):4394–4417, August 2015. ISSN 0196-2892. doi:10.1109/TGRS.2015.2396875.

M. D. Pritt. Phase unwrapping by means of multigrid techniques for interferometric SAR. IEEE Transactions on Geoscience and Remote Sensing, 34(3):728–738, May 1996. ISSN 0196-2892. doi:10.1109/36.499752.

T. Ranchin and F. Cauneau. Speckle reduction in synthetic aperture radar imagery using wavelets. In Mathematical Imaging: Wavelet Applications in Signal and Image Processing, volume 2034, pages 432–442. International Society for Optics and Photonics, November 1993. doi:10.1117/12.162083.

M. F. Salfity, P. D. Ruiz, J. M. Huntley, M. J. Graves, R. Cusack, and D. A. Beauregard. Branch cut surface placement for unwrapping of undersampled three-dimensional phase data: Application to magnetic resonance imaging arterial flow mapping. Applied Optics, 45(12):2711–2722, April 2006. ISSN 2155-3165. doi:10.1364/AO.45.002711.

G. Sansoni, M. Carocci, and R. Rodella. Three-dimensional vision based on a combination of gray-code and phase-shift light projection: Analysis and compensation of the systematic errors. Applied Optics, 38(31):6565–6573, November 1999. ISSN 2155-3165. doi:10.1364/AO.38.006565.

G. Schreier. Geometrical properties of SAR images. In SAR Geocoding: Data and Systems, pages 103–134. Karlsruhe: Wichmann, 1993.

A. Schrijver. Theory of Linear and Integer Programming. John Wiley & Sons, Inc., New York, USA, 1986. ISBN 978-0-471-98232-6.

M. Schwaebisch. Die SAR-Interferometrie zur Erzeugung digitaler Geländemodelle. Technical Report 95-25, DLR, Abtl. Operative Planung, Köln, January 1995.

M. Schwaebisch and D. Geudtner. Improvement of phase and coherence map quality using azimuth prefiltering: Examples from ERS-1 and X-SAR. In 1995 International Geoscience and Remote Sensing Symposium, IGARSS '95. Quantitative Remote Sensing for Science and Applications, volume 1, pages 205–207 vol.1, July 1995. doi:10.1109/IGARSS.1995.519691.

M. S. Seymour and I. G. Cumming. Maximum likelihood estimation for SAR interferometry. In Proceedings of IGARSS '94 - 1994 IEEE International Geoscience and Remote Sensing Symposium, volume 4, pages 2272–2275 vol.4, August 1994. doi:10.1109/IGARSS.1994.399711.

A. P. Shanker and H. A. Zebker. Edgelist phase unwrapping algorithm for time series InSAR analysis. Journal of the Optical Society of America A, 27:605–612, March 2010. doi:10.1364/JOSAA.27.000605.

M. I. Skolnik. Introduction to Radar Systems. McGraw-Hill, January 1980. ISBN 978-0-07-057909-5.

X. Su and W. Chen. Reliability-guided phase unwrapping algorithm: A review. Optics and Lasers in Engineering, 42(3):245–261, September 2004. ISSN 0143-8166. doi:10.1016/j.optlaseng.2003.11.002.

X. Su and Q. Zhang. Dynamic 3-D shape measurement method: A review. Optics and Lasers in Engineering, 48(2):191–204, February 2010. ISSN 0143-8166. doi:10.1016/j.optlaseng.2009.03.012.

P. J. G. Teunissen. The least-squares ambiguity decorrelation adjustment: A method for fast GPS integer ambiguity estimation. Journal of Geodesy, 70:65–82, November 1995. doi:10.1007/BF00863419.

R. Touzi, A. Lopes, J. Bruniquel, and P. W. Vachon. Coherence estimation for SAR imagery. IEEE Transactions on Geoscience and Remote Sensing, 37(1):135–149, January 1999. ISSN 0196-2892. doi:10.1109/36.739146.

J. Tribolet. A new phase unwrapping algorithm. IEEE Transactions on Acoustics, Speech, and Signal Processing, 25(2):170–177, 1977. doi:10.1109/TASSP.1977.1162923.

R. J. Vanderbei. Linear Programming: Foundations and Extensions. International Series in Operations Research & Management Science. Springer, 2 edition, 2001. ISBN 978-1-4614-7629-0.

R. J. Wilson. Introduction to Graph Theory. John Wiley & Sons, Inc., 1986. ISBN 0-470-20616-0.

Y. Yang, A. Pepe, M. Manzo, F. Casu, and R. Lanari. A region-growing technique to improve multi-temporal dinsar interferogram phase unwrapping performance. Remote Sensing Letters, 4, 10 2013. doi:10.1080/2150704X.2013.826835.

X. Yin and W. Busch. Nutzung der Sentinel-1 Aufnahmekonfigurationen zur Ableitung von Bodenbewegungskomponenten im Rahmen eines radarinterferometrischen Bodenbewegungsmonitorings. In Tagungsband: GeoMonitoring 2018. Clausthal-Zellerfeld, pages 119–138, 2018.

H. A. Zebker and Y. Lu. Phase unwrapping algorithms for radar interferometry: Residue-cut, least-squares, and synthesis algorithms. JOSA A, 15(3):586–598, March 1998. ISSN 1520-8532. doi:10.1364/JOSAA.15.000586.

K. Zhang, Z. Li, G. Meng, and Y. Dai. A very fast phase inversion approach for small baseline style interferogram stacks. ISPRS Journal of Photogrammetry and Remote Sensing, 97:1–8, November 2014. doi:10.1016/j.isprsjprs.2014.08.002.

M. Zhang, Q. Chen, T. Tao, S. Feng, Y. Hu, H. Li, and C. Zuo. Robust and efficient multi-frequency temporal phase unwrapping: Optimal fringe frequency and pattern sequence selection. Optics Express, 25:20381, August 2017. doi:10.1364/OE.25.020381.

D. Zheng, Q. Kemao, F. Da, and H. S. Seah. Ternary Gray code-based phase unwrapping for 3D measurement using binary patterns with projector defocusing. Applied Optics, 56(13):3660–3665, May 2017. ISSN 2155-3165. doi:10.1364/AO.56.003660.